University of Groningen

Gluon-induced quarkonium production in transverse-momentum-dependent factorisation

Bor, Jelle

DOI:
10.33612/diss.1191891247

IMPORTANT NOTE: You are advised to consult the publisher's version (publisher's PDF) if you wish to cite from it. Please check the document version below.

Document Version
Publisher's PDF, also known as Version of record

Publication date:
2025

Link to publication in University of Groningen/UMCG research database

Citation for published version (APA):
Bor, J. (2025). *Gluon-induced quarkonium production in transverse-momentum-dependent factorisation: applications to the LHC and EIC.* [Thesis fully internal (DIV), University of Groningen]. University of Groningen. https://doi.org/10.33612/diss.1191891247

Copyright
Other than for strictly personal use, it is not permitted to download or to forward/distribute the text or part of it without the consent of the author(s) and/or copyright holder(s), unless the work is under an open content license (like Creative Commons).

The publication may also be distributed here under the terms of Article 25fa of the Dutch Copyright Act, indicated by the “Taverne” license. More information can be found on the University of Groningen website: https://www.rug.nl/library/open-access/self-archiving-pure/taverne-amendment.

Take-down policy
If you believe that this document breaches copyright please contact us providing details, and we will remove access to the work immediately and investigate your claim.

Downloaded from the University of Groningen/UMCG research database (Pure): http://www.rug.nl/research/portal. For technical reasons the number of authors shown on this cover page is limited to 10 maximum.

Download date: 10-02-2025

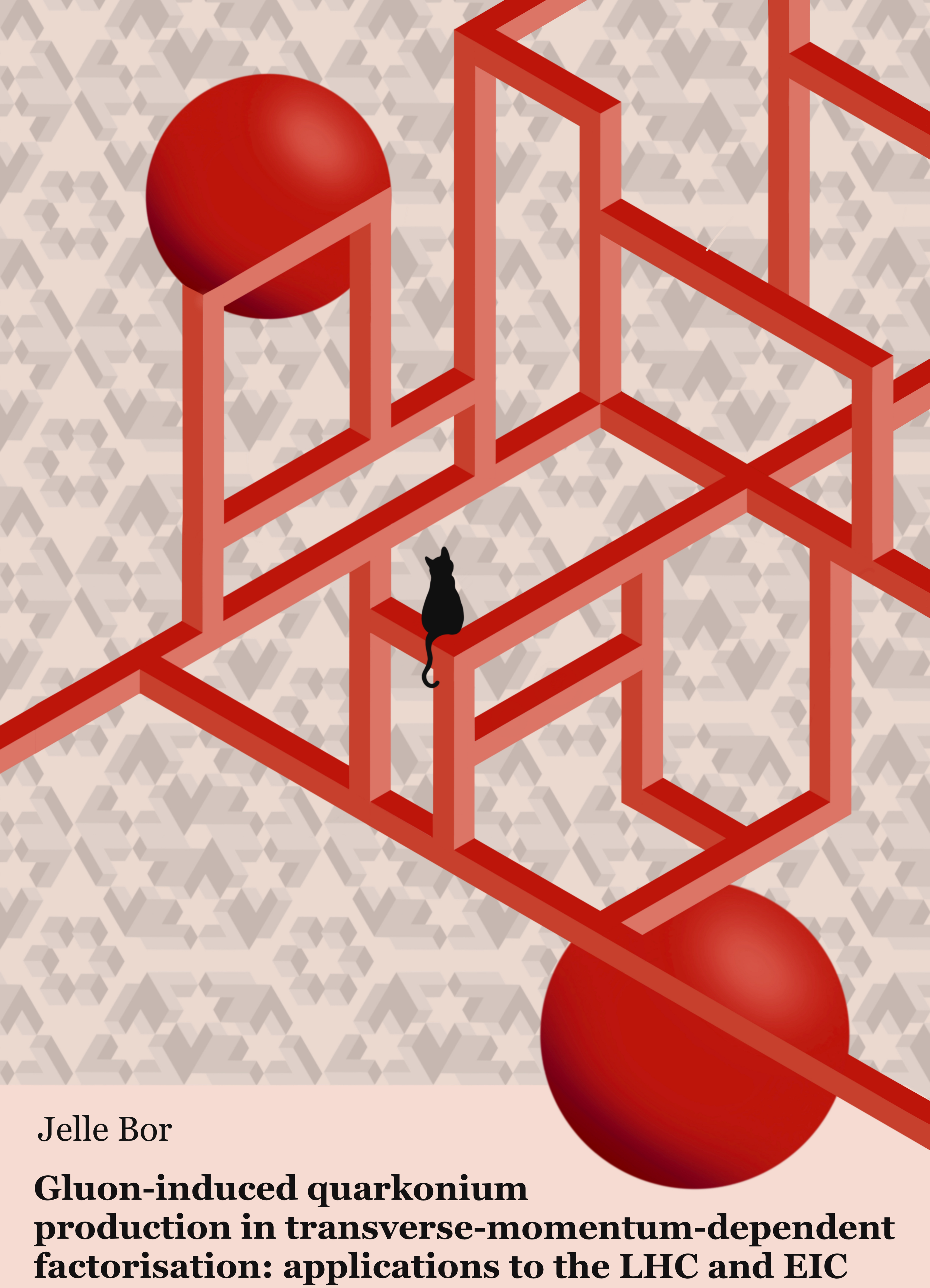

Jelle Bor

Gluon-induced quarkonium production in transverse-momentum-dependent factorisation: applications to the LHC and EIC

rijksuniversiteit
groningen

université
PARIS-SACLAY

Gluon-induced quarkonium production in transverse-momentum-dependent factorisation: applications to the LHC and EIC

PhD thesis

to obtain the degree of PhD at the
University of Groningen
on the authority of the
Rector Magnificus Prof. J.M.A. Scherpen
and in accordance with
the decision by the College of Deans

and

to obtain the degree of Doctor in Physics
at the University Paris-Saclay

Double PhD degree

This thesis will be defended in public on

Tuesday 11 February 2025 at 16.15 hours

by

Jelle Bor

born on 13 September 1994

Supervisor

Prof. D. Boer

Co-supervisor

Dr. J.-P. Lansberg

Assessment Committee

Prof. A. Kulesza
Prof. A. Szczurek
Prof. R.G.E. Timmermans
Prof. S. Wallon

Composition du jury

Prof. E. Pallante	Présidente
Prof. A. Kulesza	Rapporteur
Prof. A. Szczurek	Rapporteur
Dr. K.A.M. de Bruyn	Examinateur
Prof. R.G.E. Timmermans	Examinateur
Prof. S. Wallon	Examinateur

École doctorale n°576 : particules hadrons énergie et noyau : instrumentation, image, cosmos et simulation (PHENIICS)

Spécialité de doctorat : Physique des Particules

Unité de recherche : Université Paris-Saclay, CNRS, IJCLab, 91405, Orsay, France

Référent : Faculté des Sciences d'Orsay

The research presented in this thesis was conducted at the Van Swinderen Institute for Particle Physics and Gravity, University of Groningen, and Laboratoire de Physique des 2 Infinis Irène Joliot-Curie, Université Paris-Saclay.

Cover design: Jelle Bor

Contents

"Ik χ*, ik* χ*, wat jij niet* χ *... "*

1

Introduction

The structure of matter has fascinated humans for centuries. For example, already in ancient Greece, Anaxagoras (c. 500-428 BC) proposed that changes in matter result from different arrangements of indivisible particles, while Empedocles (c. 494-434 BC) explained the complexity of all matter in terms of four elements: earth, air, fire, and water. Leucippus (c. 470–360 BC) and his student Democritus (c. 460–370 BC) developed a more sophisticated philosophical foundation known as atomism. They proposed that the physical universe consists of atoms and void that have always existed, with the diversity of matter arising from infinitely many variations in the shapes, arrangements, and positions of atomic clusters. Although we now know their ideas differed significantly from reality, it is fascinating that they speculated about the fundamental building blocks of the universe in terms of 'atomos', which means uncuttable.

Centuries later, in 1766, Cavendish discovered the chemical element hydrogen by recognising its elemental nature, although others, such as Boyle, had prepared hydrogen gas for many years prior. At the beginning of the 19th century, Dalton introduced atomic theory, proposing that each chemical element has a characteristic type of atom that differs in properties from atoms of all other elements, and that atoms of different elements can combine to form compounds, later introduced as molecules by Avogadro in 1811. In 1838, Laming first hypothesised the existence of an indivisible unit of electric charge to explain the chemical properties of atoms, which Stoney named the 'electron' in 1891. By 1897 Thomson had identified the electron as a particle (much later identified as part of the lepton family). Meanwhile, in 1869, Mendeleev published his periodic table, organising atoms, which were then understood as the building blocks of nature.

About 40 years later, in 1911, Rutherford, Marsden and Geiger discovered the dense nucleus of the atom. However, the planetary model of the atom of Rutherford, in which electrons orbiting a solar-like nucleus, was problematic because it predicts that atoms would be unstable as classical mechanics suggests they would emit radiation and collapse. In 1913, Bohr resolved this issue by incorporating the quantum theory of Planck from 1900, proposing that electrons occupy fixed orbits with specific energies, based on their angular momentum being an integer multiple of the reduced Planck constant. Not long after, in 1919, Rutherford provided evidence for the proton, and in 1932, Chadwick discovered the neutron. These two particles, known as nucleons, make up the core of atoms, with the number of protons determining the chemical element.

To explain that not all electrons in an atom are in the lowest energy state, Pauli formulated the exclusion principle in 1925, which states that no two electrons in the same quantum system can share the same quantum state, i.e. quantum numbers. Later that year, Uhlenbeck and Goudsmit proposed spin, an intrinsic form of angular momentum, as a property of electrons. Although initially opposed to spin, Pauli inferred its existence in 1927 based on the results of the Stern–Gerlach experiment conducted in 1922. In this experiment, silver atoms with no orbital angular momentum were passed through an inhomogeneous magnetic field, and their deflection was measured. The reaction between sulfur from the cigar of Stern and the silver atoms on the detection plate made it clear that the atoms exhibited two distinct intrinsic angular momentum states. Hence, the exclusion principle states that two electrons in the same orbital must have opposite spins. Meanwhile, quantum mechanics was advancing with the formulation of matrix mechanics by Heisenberg and wave mechanics by Schrödinger, based on the idea from Broglie that matter can have wavelike properties. The existence of spin was later supported by the spin-statistics theorem of Pauli in 1940, which states that fermions, e.g. electrons and nucleons, have half-integer spins, while bosons, e.g. photons, have integer spins.

In 1932, Heisenberg introduced the concept of isospin, analogous to spin, to account for the fact that nucleons have nearly identical masses and experience the same strong interaction between them. This led to the interpretation of protons and neutrons as two states of the same particle. He assigned them to an isospin-$1/2$ doublet that transforms under the $SU(2)$ symmetry group, introducing a new quantum number to describe these particles. Although the neutron has a slightly greater mass due to isospin breaking (now understood to result from the mass difference between up and down valence quarks as well as the effects of electromagnetic interactions), the approximate symmetry remains useful. The small deviations from perfect symmetry can be treated using perturbation theory, which accounts for the subtle differences between the nearly degenerate states.

Isospin symmetry also proved valuable in the study of pions, discovered in 1947, which were classified as part of an isospin-1 triplet. However, during the 1950s and 1960s, a growing number of strongly interacting particles, called hadrons (including nucleons and pions), were detected in particle detectors, after the invention of the bubble chamber in 1952. The sheer number of these particles made it increasingly unlikely that they were all fundamental building blocks of matter. To bring order to this ‘particle zoo’, Gell-Mann and Ne’eman independently began classifying them by their mass and various quantum numbers: electric charge, isospin, and strangeness (introduced to explain the unusually slow decay of some particles such as kaons). This organisational scheme, known as the eightfold way, is based on a $SU(3)$ symmetry. In this framework, baryons (including nucleons), belong to octet and decuplet representations, while mesons, including pions, belong to octet and singlet representations. In 1964, Gell-Mann and Zweig, shortly after defending his PhD thesis under the supervision of Feynman, independently proposed that baryons and mesons are not elementary particles but are instead bound states of hypothetical particles called quarks, which obey a $SU(3)$ symmetry known as flavour. According to this theory, hadrons are composed of three types of quarks: up (u), down (d), and strange (s); spin-1/2 constituents that each carry a fractional electric charge. Mesons were defined as quark-antiquark pairs, while (anti)baryons were identified as bound states of three (anti)quarks.

A major success of the quark model was the accurate prediction by Gell-Mann of the existence, mass, and decay products of the Ω^-, which was observed in 1964. The Ω^-, composed of three strange quarks with parallel spins and no orbital angular momentum, appeared to violate the generalised exclusion principle of Pauli. This issue was first noted by Struminsky and a similar problem was identified for the Δ^{++}. Around 1965, Greenberg, and Han and Nambu independently proposed a solution by introducing a new quantum number for quarks, which is now known as colour. This colour charge can take one of three forms: red, blue, or green. It was also theorised that quarks interact by exchanging vector gauge bosons, i.e. gluons, and that hadrons are colour neutral.

In the early days of the quark model, there was no experimental evidence for the existence of quarks or gluons, so it was initially viewed as a mathematical framework for categorising hadrons based on their properties. However, the idea arose that if quarks and gluons do exist, they must be confined within hadrons. To investigate this, the Stanford Linear Accelerator Center (SLAC) began measuring elastic electron-proton scattering, followed by deep inelastic scattering (DIS) in 1967, studying electron-proton collisions of the form $e + p \to e + X$. Unexpectedly, large-angle deviations were observed, prompting Feynman to propose the parton model in 1969. This model suggest that the electron elastically scatters off one point-like, approximately free, constituent of the proton, called a parton, through the exchange of a virtual photon, such that the inelastic interaction of the electron with the proton is the incoherent sum of all the elastic scatterings between the electron and the constituents. The partons were naturally identified with the three constituent quarks of the proton: uud. This model predicted a behaviour in the scattering cross-section known as Bjorken scaling, where the structure functions, encoding information about the internal structure of the proton, depend only on x: the collinear momentum fraction of the parton taken from the proton. SLAC experiments initially confirmed this scaling. However, to match experimental data more accurately, it became necessary to include a sea of quark-antiquark pairs and gluons inside the proton as shown in Fig. 1.1, violating Bjorken scaling. The original three quarks are then reinterpreted as valence quarks, and the internal composition of the proton, as probed by the electron, is seen to change with x on which we elaborate below. Indeed, this is currently our understanding of the constituents of hadrons. We note that this view of the proton aligns with findings that valence quarks account for only a small fraction of its spin, while the distribution of the remaining spin among other contributions is an unsolved problem to this day.

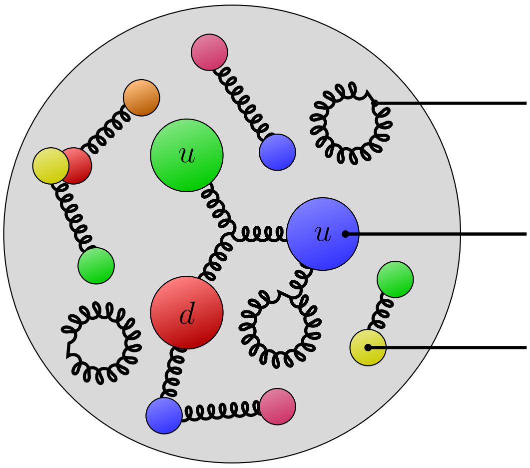

Gluons
bind everything together
and are omnipresent

Valence quarks
net quark content of the proton
that give its overall charge

Quark-antiquark pairs
transient and can have any flavour

Figure 1.1: Impression of the interior of a colour-neutral proton. The flavours of the valence quarks define the hadron as a proton. Due to the nature of the strong force it also contains a swirling sea of quarks, antiquarks and gluons. Its constituents are also called partons.

The experimental evidence that partons are confined within hadrons initially appeared inconsistent with the fact that high-energy electrons seemed to interact with what behaved like freely moving partons. This apparent contradiction is resolved by quantum chromodynamics (QCD), a quantum field theory (QFT) developed in 1973 by Gell-Mann, Fritzsch, and Leutwyler. This was a few years after Weinberg and Salam independently formulated the QFT in 1967 and 1968, respectively, that describes the electroweak force: a unified description of the electromagnetic and weak forces, with its gauge symmetry spontaneously broken through the Higgs mechanism. A QFT merges classical field theory, special relativity and quantum mechanics. In QCD the charge associated with the strong force is colour. QCD is similar to quantum electrodynamics (QED), which describes the electromagnetic force. The foundation of QED was established by Dirac in 1927 and later independently refined by Feynman, Schwinger, and Tomonaga, who were awarded the Nobel Prize in 1965 for their contributions. Unlike QED, QCD is a non-Abelian theory, also known as Yang-Mills theory. This means that the force carriers in QCD, the gluons, carry colour charge themselves, allowing them to interact with both quarks and other gluons. In 1973, Gross and Wilczek, independently of Politzer, discovered a key property of QCD known as asymptotic freedom, which 't Hooft had already observed in 1972: the coupling constant decreases at high energies, enabling perturbative calculations of hadronic cross sections. These kind of predictions have been experimentally verified with high precision. At low energies, however, the coupling becomes strong, consistent with the phenomenon of confinement; our knowledge on nonperturbative physics relies on fits to experimental data and lattice QCD, a numerical method to explore the nonperturbative regime of QCD. The result: the force between partons grows as they are separated, and when the distance between two partons becomes large enough, it becomes energetically favourable to create new colour-neutral hadrons, rather than allowing the coloured partons to exist freely. Lattice QCD supports the existence of confinement, although there is still no general mathematical proof for it. For more details on QCD we refer to App. A.

As the understanding of the strong interaction became more understood in the 1970s, yet another series of particles were discovered. In 1974, two groups at SLAC and Brookhaven National Laboratory (BNL) simultaneously announced the discovery of a new particle: the J/ψ meson, whose name is a combination of the names given to it by the two collaborations. This event marked the beginning of the so-called 'November Revolution'. The identification of the J/ψ as one of the lowest bound states of a charm-anticharm quark pair marked the discovery of the charm quark (c). Since $e^+ + e^-$ collisions at SLAC primarily involved the exchange of a virtual photon, the J/ψ was the most easily produced bound state because it has the same quantum numbers as the photon. The charm quark was first proposed by Glashow and Bjorken in 1964, and later shown to be essential in 1970 by the Glashow-Iliopoulos-Maiani mechanism, which explains the suppression of flavour-changing neutral currents in electroweak loop diagrams that would otherwise violate observed selection rules. The suppression occurs due to a small ratio m_u/m_c, which minimises these problematic contributions, suggesting the charm quark must be relatively heavy indeed. Furthermore, in 1973, Kobayashi and Maskawa proposed that a new doublet of heavy quarks was needed to explain charge-parity (CP) violation in electroweak decays. One of these was the bottom quark (b), discovered in 1977 at Fermilab in Υ mesons, which are similar to J/ψ mesons but consist of a bottom-antibottom quark pair. We note that the Υ meson played a crucial role in the lead-up to the experimental confirmation of gluons through the observation of three-jet events in 1979. The other, the top quark (t), was not discovered until 1995 at the Tevatron particle accelerator due to its extremely large mass of about 173 GeV, which placed it out of reach of earlier colliders. Interestingly, although the top quark is predominantly produced through strong interactions, it decays rapidly via the weak interaction into a W boson and a bottom quark, in a time much shorter than that of typical strong interactions. Because of this the top quark does not hadronise directly, offering a rare opportunity to study the properties of a bare quark.

During the 1970s and 1980s, numerous new flavour-neutral heavy-quark mesons, like J/ψ and Υ, were regularly detected in experiments, collectively referred to as quarkonium. In addition to these, open-charm and open-bottom mesons were discovered, consisting of a charm or bottom quark paired with a light quark: u-, d-, or s-quark. A notable feature of these heavy-quark mesons is that their masses are close to the masses of their constituent quarks, resulting in relatively small momentum between the quarks. This makes it possible to describe their binding using nonrelativistic potentials. Therefore, heavy-light mesons are analogous to hydrogen atoms, while quarkonium resembles positronium, which gave rise to its name. In particular, various models exist to describe heavy-quark mesons formation in collider experiments, but not all production data can be consistently explained, i.e. the relative contributions of different models to specific processes remain a topic of debate. Despite these uncertainties, heavy-quark mesons have become an important tool in several areas of high-energy physics, extending beyond the study of its own production mechanisms, e.g. open-bottom meson factories are used to study CP-violation and quarkonia are utilised as probes of the characteristics of the quark-gluon plasma, and to investigate the gluon content of the proton. In general, these particles are receiving a lot of attention as they can be used to investigate the perturbative and nonperturbative aspects of QCD, and their interplay, since much is still unknown about this.

In particular, we are interested in exploring the internal structure of nucleons in greater detail, which can be studied in collider experiments. To analyse specific QCD processes, factorisation frameworks that separate short-distance contributions from long-distance ones in the calculation of cross sections are used. The former can be perturbatively calculated through a systematic expansion in the strong coupling constant α_s, while the latter has to be parametrised in terms of nonperturbative functions, which need to be extracted from experiments. In the context of the parton model, these nonperturbative functions are known as parton distribution functions (PDFs), which describe the probability of finding a parton within a hadron as a function of x. The factorised description, where the PDFs are convoluted with a perturbative high-energy calculation, is valid when collinear factorisation holds. We note that the parametrisation of the hadron structure in terms of PDFs relies also on an expansion. The theoretical description of a specific final state requires a factorisation too, involving the use of another nonperturbative function for its hadronisation. Moreover, the parametrisation of the hadronisation procedure in terms of this function relies generally on an expansion as well. Therefore, the theoretical framework is structured as an expansion in α_s along with two other variables to apply the nonperturbative functions: one for the PDFs and another for the hadronisation process.

Once factorisation is established, theory and experiment can be directly compared to extract one-dimensional PDFs, provided the nonperturbative hadronisation process is already understood from other experiments. We note that experiments generally probe nonperturbative functions at different energy scales, so their scale evolution must also be considered. Over the past few decades, this iterative process has led to a solid understanding of PDFs, though some still exhibit significant uncertainties in certain kinematic regions. It is known that for large values of x, valence quarks dominate the composition of the proton. At smaller x, however, the sea of quark-antiquarks provides probabilities for also other flavoured quarks, while the internal structure of the proton becomes increasingly dominated by gluons, e.g. see [1]. The next step is naturally to understand higher-dimensional functions of the hadron structure, such as the three-dimensional transverse-momentum-dependent (TMD) PDFs (TMDPDFs, in short TMDs). These functions not only depend on x, but also on the two-dimensional transverse momentum (TM) of the parton and can be probed in processes when TMD factorisation is applicable. While currently quark TMDs are already quite well understood, hardly anything is known about the gluon TMDs experimentally.

Particularly, quarkonium production is a promising tool for probing gluon TMDs. Namely, it is predominantly driven by gluon fusion, as heavy quarks are primarily generated from gluons and are not intrinsically present in hadrons at small values of x. From an experimental viewpoint, these processes also exhibit a clean signature because certain quarkonia, like the J/ψ, are relatively easy to detect due to their large branching ratios in leptonic decay modes which enable the collection of numerous clean events in collider experiments. In particular, this thesis focuses on studying quarkonium production in both proton-proton collisions at the Large Hadron Collider (LHC) and in electron-proton collisions at the future Electron-Ion Collider (EIC) to investigate gluon TMDs. For further insights into what quarkonium production can reveal at the EIC we refer to [2].

Predictions for high-energy processes require factorisation which is process dependent and nontrivial. In particular, processes that produce final state coloured particles have difficulties, as radiation of soft-gluons to form a colour-neutral particle can lead to interactions with the initial state. Although TMD factorisation has not been explicitly proven for quarkonium production in electron-proton collisions, it has been proven to all order in perturbation theory for light hadron production in electron-proton collisions [3]. At leading order, the only difference between these processes lies in the underlying hard scattering: $\gamma^* q$ for light hadrons versus $\gamma^* g$ for quarkonium, where γ^* denotes a virtual photon, q a quark and g a gluon. However, this does not make a difference from the perspective of TMD factorisation, and neither does the mass of the final state hadron. Similarly, TMD factorisation is argued to hold for quarkonium production in proton-proton collisions, based on analogous processes [4, 5]. Nevertheless, the production of coloured particles in this process could be problematic. Taking this into account, it is not expected that any TMD factorisation-breaking effects occur for the processes discussed in this thesis. The latter is also assumed for the factorisation that describes the hadronisation. However, coloured quarkonium production suggests that final state TM smearing effects may arise, which are described by the TMD shape functions (TMDShFs). A large part of this thesis is focused on determining these functions as well, since they are essential to the theoretical description of the processes that we study and hardly anything is known about them currently. This is aimed to facilitate their experimental determination.

This thesis is organised as follows: Ch. 2, 3, and 4 provide a comprehensive overview of the theoretical framework for our studies of various processes, their features and uncertainties, which is applied in Ch. 5 and 6 where we present our conducted research.

In more detail, we examine the TMD partonic correlator in terms of gluon TMDs in Ch. 2 and explore its relationship to other correlators, especially the collinear correlator that is parametrised with PDFs. Additionally, we explain constraints on the gluon TMDs derived from the theoretical framework, including their process dependence. In Ch. 3 we provide an overview of various models for quarkonium production, with a particular focus on two models that are employed later on: one that allows only the production of colourless quarkonium, and another that includes the production of quarkonium from a coloured pair of quarks, both within the framework of nonrelativistic QCD. Then we have all the necessary ingredients to compute the theoretical differential cross sections for the processes studied in this thesis; we present their TMD results along with their particular features, covering single quarkonium production in proton-proton and electron-proton reactions, as well as quarkonium-pair production in proton-proton collisions for which LHCb data is available for comparison.

In Ch. 4 we explore possible approaches for TMD studies aimed at providing theoretical predictions for quarkonium production at the LHC and the EIC. In particular, one can employ parametrisations for the TMDs, or use the TMD-evolution formalism to relate them to the well-known PDFs, while the nonperturbative quarkonium hadronisation can be taken from experimental studies. Although both approaches to TMDs involve some unknown parametrisation, TMD evolution that follows from TMD factorisation is more predictive than directly parametrising the TMDs themselves. Therefore, we focus particularly on this approach while also examining its limitations.

Thereafter, we discuss that the TMDShFs are generally required for quarkonium production within TMD factorisation in Ch. 5. Specifically, we explain how we determine their leading-order functional form, relevant when the quarkonium is not colour neutral immediately after production, by solving the matching of the process within TMD and collinear factorisations. We also address that the TMDShFs should be universal, while noting that they are accompanied by a process-dependent (soft) factor.

In Ch. 6 we finally present numerical predictions for observables related to the processes under investigation. We evaluate various approaches for the nonperturbative component of TMD evolution, incorporating both standard parametrisations and our own developed model for it. Additionally, we conduct a thorough analysis of the uncertainties affecting our predictions. The highlight of this chapter is that good agreement with recent data on J/ψ-pair production at the LHC is found, although many questions remain and new issues have emerged. We end with an exploratory study of the complete TM spectrum of J/ψ production at the EIC.

In Ch. 7 we conclude the results and insights gained throughout this work. Moreover, we discuss where further research is needed, outlining potential directions for future investigations to build on our work and to address remaining questions.

2

The TMD gluon correlator

The partonic correlator that encapsulates the internal dynamics of the hadron cannot be computed through perturbation theory; instead, it is described by nonperturbative distribution functions. In particular, we are interested in the TMD gluon correlator parametrised by the poorly known three-dimensional gluon TMDs. This chapter is devoted to the understanding of this object, which enters the cross section of the processes we investigate in this thesis. Moreover, we elaborate on properties of the gluon TMDs that follow from the correlator definition. We start by giving a brief overview in Sec. 2.1 of the unintegrated correlator and gauge invariance. In Sec. 2.2 we explain light-cone coordinates that are commonly used for high-energy collisions and employed throughout the rest of this thesis. In Sec. 2.3 we discuss the parametrisation of the unintegrated gluon correlator and construct the TMD correlator in terms of the TMDs. Here we also explain relations with other types of correlators and distribution functions. Sec. 2.4 covers the bounds of gluon TMDs and Sec. 2.5 their process dependence that follows from the Wilson-line structure.

2.1 Unintegrated correlators and gauge invariance

We first introduce the definition of the quark-quark correlation matrix Φ in a hadron, that is given by

$$\Phi_{\alpha\beta}(k,P_h) \equiv \sum_X \int \frac{d^3P_X}{(2\pi)^3 dP_X^0} \langle P_h|\bar{\psi}_\beta(0)|X\rangle\langle X|\psi_\alpha(0)|P_h\rangle\, \delta^4(P_h-k-P_X)\,, \tag{2.1}$$

where k and P_h are the momenta of the quark and hadron, and α and β are the indices of the Dirac fields that describe an incoming and outgoing quark, respectively. Here flavour labels and colour (triplet) indices are omitted. The Dirac delta function reflects the momentum conservation of the process. The product of matrix elements gives the probability density for extracting a quark with momentum k from the hadron, leaving a remnant X with momentum P_X. Since X is a final state, we integrate over its phase space. Moreover, since it is not experimentally measured, we also perform a summation over all possible final states. Such processes are called inclusive, in contrast to exclusive processes. The delta function can facilitate the translation of the field ψ from position 0 to ξ. Therefore, after utilising the completeness relation for the unobserved final states, one can write:

$$\Phi_{\alpha\beta}(k,P_h) = \int \frac{d^4\xi}{(2\pi)^4}\, e^{ik\cdot\xi}\, \langle P_h|\bar{\psi}_\beta(0)\psi_\alpha(\xi)|P_h\rangle\,. \tag{2.2}$$

Since this correlator, depicted in Fig. 2.1, depends on the full four-momentum k, it is referred to as an unintegrated correlator.

Because the two quark fields reside at two different space-time positions, i.e. the matrix element is bilocal, Eq. 2.2 is not gauge invariant. Explicitly, under local $SU(3)$ transformations of QCD (see App. A), the quark fields transform as:

$$\psi_\alpha(\xi) \to V(\xi)\psi_\alpha(\xi)\,, \quad \bar{\psi}_\beta(0) \to \bar{\psi}_\beta(0)V^\dagger(0)\,. \tag{2.3}$$

Therefore, the complete correlator contains a gauge link $\mathcal{U}_{[0,\xi]}$ between the two fields to be gauge invariant, also called Wilson line, that transforms as

$$\mathcal{U}_{[0,\xi]} \to V(0)\mathcal{U}_{[0,\xi]}V^\dagger(\xi)\,, \tag{2.4}$$

and is defined as follows

$$\mathcal{U}_{[0,\xi]} = \mathcal{P}\exp\left(ig_s\int_0^\xi d\eta^\mu\, A_\mu(\eta)\right)\,, \tag{2.5}$$

where g_s is related to the strong coupling constant α_s through the relation $\alpha_s = g_s^2/4\pi$, and A is a four-vector field that describes a gluon. Upon expanding the exponent of the Wilson line it becomes evident that the path-ordering, denoted by the symbol $\mathcal{P}$, is required (for each term) because the group generators (contracted with the gluon fields) do not commute. Physically, a Wilson line reflects a sum over infinitely many gluon emissions which can be calculated explicitly. In principle, any possible path between 0 and ξ guarantees gauge invariance of the unintegrated correlator, yet the actual path that results from the summation of gluon exchanges in TMD correlators is dictated by the particular process at hand as discussed in Sec. 2.5.

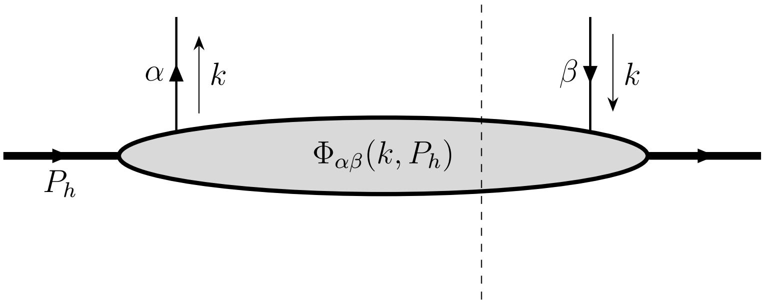

Figure 2.1: The definition of the unintegrated quark correlator. The figure is split by a dotted line, called the final-state cut, into an amplitude (all that is to the left of the cut) and a conjugate amplitude (all that is to the right of the cut).

The gluon-gluon correlation matrix is obtained by replacing the quarks in Fig. 2.1 with gluons. However, employing the gluonic fields A in the correlator is not convenient because of their gauge transformations. Instead, one uses the field strength tensor $F_{\mu\nu}$, that transforms as:

$$F_{\mu\nu} \to V F_{\mu\nu} V^\dagger \,. \tag{2.6}$$

Therefore, two Wilson lines enter the gluon correlator. Including the hadron spin S_h, the unintegrated gluon correlator is written as

$$\Gamma^{\mu\nu;\rho\sigma}(k, P_h, S_h) = \int \frac{d^4\xi}{(2\pi)^4}\, e^{ik\cdot\xi}\, \langle P_h, S_h | F^{\mu\nu}(0) \mathcal{U}_{[0,\xi]} F^{\rho\sigma}(\xi) \mathcal{U}'_{[\xi,0]} | P_h, S_h \rangle \,, \tag{2.7}$$

where the summation over colour (octet) indices is understood.

2.2 Light-cone coordinates

In high-energy scattering it is convenient to work with light-cone coordinates [6]. A four-vector $a = (a^0, a^1, a^2, a^3)$ is then represented as $a = (a^+, a^-, \mathbf{a}_T)$, where $a^\pm = (a^0 \pm a^3)/\sqrt{2}$ (note that $a^\pm = a_\mp$) and $\mathbf{a}_T = (a^1, a^2)$. The inner product between two four-vectors a and b is given by: $a \cdot b = g^{\mu\nu} a_\mu b_\nu = a^+ b^- + a^- b^+ - \mathbf{a}_T \cdot \mathbf{b}_T$. Defining light-like vectors $n_+ = (1, 0, \mathbf{0})$ and $n_- = (0, 1, \mathbf{0})$, such that $n_+ \cdot n_- = 1$ (note that $n_+^2 = n_-^2 = 0$), a four-vector can be decomposed as: $a^\mu = a^+ n_+^\mu + a^- n_-^\mu + a_T^\mu$. In the latter $a_T = (0, 0, \mathbf{a}_T)$ is defined, therefore $a_T^2 = -\mathbf{a}_T^2$. In terms of n_+ and n_-, the parton and hadron momenta, and the space-like hadron-spin vector, e.g. for a spin-1/2 proton of mass M_h, can be written as:

$$P_h^\mu = P_h^+ n_+^\mu + \frac{M_h^2}{2P_h^+} n_-^\mu \,, \tag{2.8}$$

$$k^\mu = x P_h^+ n_+^\mu + k^- n_-^\mu + k_T^\mu \,, \tag{2.9}$$

$$S^\mu = S_L \frac{P_h^+}{M_h} n_+^\mu - S_L \frac{M_h}{2P_h^+} n_-^\mu + S_T^\mu \,. \tag{2.10}$$

The hadron moves along the $\hat{z}$ axis and satisfies the on-shell condition: $P_h^2 = M_h^2$. The collinear momentum fraction of the parton is defined as $x = k^+/P_h^+$. Typically,

$P_h^+ \sim \mu_H$, where μ_H is the hard scale in the process. Therefore, P_h^- becomes negligible compared to its plus component in the high-energy limit when P_h becomes light-like. The spin vector has three independent parameters, namely S_L and the two transverse components of S_T; they characterise longitudinal and transverse polarisation, respectively. The parameters obey $0 \leq S_L^2, \mathbf{S}_T^2 \leq 1$, such that $S_L^2 + \mathbf{S}_T^2 = 1$. Besides, $P_h \cdot S_h = 0$. Utilising the $n_\pm$ vectors, the transverse tensors $g_T^{\mu\nu}$ and $\epsilon_T^{\mu\nu}$ are defined as

$$g_T^{\mu\nu} = g^{\mu\nu} - n_+^{\{\mu} n_-^{\nu\}}, \tag{2.11}$$

$$\epsilon_T^{\mu\nu} = \epsilon^{n_+ n_- \mu\nu}, \tag{2.12}$$

where the symmetrisation operator is used: $p^{\{\mu}q^{\nu\}} = p^\mu q^\nu + p^\nu q^\mu$. The non-zero components are $g_T^{11} = g_T^{22} = -1$ and $\epsilon_T^{12} = -\epsilon_T^{21} = 1$.

2.3 The parametrisation of the gluon correlator

The unintegrated gluon correlator presented in Eq. 2.7 can be parametrised in terms of Lorentz structures. These structures need to be antisymmetric in μ, ν as well as in ρ, σ, which follows from the antisymmetric nature of the field strength tensor. They can be built from the Levi-Civita tensor ϵ, the metric tensor g, and the available vectors k, P_h and S_h. The different Lorentz structures are then accompanied by nonperturbative amplitudes X_i (also called coefficient functions) with mass dimension $[X_i] = -4$, and the hadron mass M_h can be used to give the terms the correct dimension: $[\Gamma] = -2$. As the spin vector appears linearly in the spin density matrix, as shown in Sec. 2.4, it can at most occur linearly in the parametrisation. Besides, the correlator is constrained by requirements that arise from hermiticity and parity, given by

$$\Gamma^{\mu\nu;\rho\sigma}(k, P_h, S_h) = \Gamma^{\rho\sigma;\mu\nu *}(k, P_h, S_h)\,, \tag{2.13}$$

$$\Gamma^{\mu\nu;\rho\sigma}(k, P_h, S_h) = \Gamma_{\mu\nu;\rho\sigma}(\bar{k}, \bar{P}_h, -\bar{S}_h)\,, \tag{2.14}$$

where $\bar{k} = (k^0, -k^i)$. Hermiticity ensures that the amplitudes X_i are real and parity conservation forbids the presence of parity-odd terms, i.e only odd numbers of Levi-Civita tensors can be combined with the axial vector S_h. With these constraints, the following parametrisation is found for an unpolarised hadron [7,8]

$$\begin{aligned}\Gamma_U^{\mu\nu;\rho\sigma}(k, P_h) = {} & M_h^2 X_1 \epsilon^{\mu\nu\alpha\beta}\epsilon^{\rho\sigma}{}_{\alpha\beta} \\ & + X_2 P_h^{[\mu} g^{\nu][\rho} P_h^{\sigma]} + X_3 k^{[\mu} g^{\nu][\rho} k^{\sigma]} \\ & + (X_4 + iX_5) P_h^{[\mu} g^{\nu][\rho} k^{\sigma]} + (X_4 - iX_5) k^{[\mu} g^{\nu][\rho} P_h^{\sigma]} \\ & + \frac{X_6}{M_h^2} P_h^{[\mu} k^{\nu]} P_h^{[\rho} k^{\sigma]}\,, \end{aligned} \tag{2.15}$$

where the antisymmetrisation operator is employed: $p^{[\mu}q^{\nu]} = p^\mu q^\nu - p^\nu q^\mu$. The subscript of the correlator denotes the polarisation of the hadron. Time-reversal invariance imposes a third condition when applicable

$$\Gamma^{\mu\nu;\rho\sigma *}(k, P_h, S_h) = \Gamma_{\mu\nu;\rho\sigma}(\bar{k}, \bar{P}_h, \bar{S}_h)\,, \tag{2.16}$$

which implies that $X_5^* = -X_5$ for Eq. 2.15. For this reason such an amplitude is called T-odd and must vanish when time reversal can be used as a constraint. Consequently, unlike hermiticity and parity, time reversal does not impose constraints on the parametrisation of the correlator in terms of distribution functions. We note that since Wilson lines transform under time reversal, it relates two different correlators with different Wilson lines as explained in Sec. 2.5.

The light-cone coordinates show their usefulness when the correlation functions are used in a calculation of a hard-scattering process. Hence, power counting in the hard scale tells one that the most important contributions from $\Gamma^{\mu\nu;\rho\sigma}$ are the ones with the largest possible number of '+'-indices. The remaining indices are transverse to generate non-zero terms at a specific order. Particularly, $\Gamma^{+\mu;+\nu}$ is referred to as twist two, followed by $\Gamma^{+\mu;+-}$ and $\Gamma^{\mu\nu;\rho+}$, referred to as twist three, etc. So, Eq. 2.15 at leading twist becomes:

$$\Gamma_U^{+\mu;+\nu}(k,P_h) = (P_h^+)^2 \bigg\{ -g_T^{\mu\nu}[X_2 + 2xX_4 + x^2 X_3] + \frac{k_T^\mu k_T^\nu}{M_h^2} X_6 \bigg\} . \tag{2.17}$$

Due to suppressed powers of P_h^+ in higher-order contributions, the expansion is similar to an expansion in the inverse hard scale, like twist expansion in the operator product expansion of deep inelastic scattering [9]. This explains the naming convention used in this context.

The TMD correlator can be obtained by integrating the unintegrated correlator over k^-

$$\begin{aligned} P_h^+\,\Gamma^{\mu\nu}(x,\mathbf{k}_T) &\equiv \int dk^-\,\Gamma^{+\mu;+\nu}(k,P_h,S_h) \\ &= \int \frac{d\xi^- d^2\boldsymbol{\xi}_T}{(2\pi)^3}\, e^{ik\cdot\xi}\, \langle P_h,S_h|F^{+\mu}(0)\mathcal{U}_{[0,\xi]}F^{+\nu}(\xi)\mathcal{U}'_{[\xi,0]}|P_h,S_h\rangle\bigg|_{\xi^+=0} , \end{aligned} \tag{2.18}$$

where a conventional factor of P^+ is introduced. It can be rewritten as

$$\begin{aligned} \Gamma^{\mu\nu}(x,\mathbf{k}_T) &= \frac{1}{P_h^+}\int dk^-\,\Gamma^{+\mu;+\nu}(k,P_h,S_h) \\ &= \frac{M_h^2}{2(P_h^+)^2}\int [d\sigma d\tau]\,\Gamma^{+\mu;+\nu}(k,P_h,S_h) , \end{aligned} \tag{2.19}$$

where one usually introduces

$$[d\sigma d\tau] \equiv d\sigma d\tau\, \delta\bigg(\tau - x\sigma + x^2 + \frac{\mathbf{k}_T^2}{M_h}\bigg) , \tag{2.20}$$

with the dimensionless invariants σ and τ, given by:

$$\sigma \equiv \frac{2k\cdot P_h}{M_h^2} , \quad \tau \equiv \frac{k^2}{M_h^2} . \tag{2.21}$$

The gluon TMDs are then related to the amplitudes as follows

$$x f_1(x,\mathbf{k}_T^2) = M_h^2 \int [d\sigma d\tau] \bigg(X_2 + 2xX_4 + x^2 X_3 + \frac{\mathbf{k}_T^2}{2M_h^2} X_6 \bigg) , \tag{2.22}$$

$$x h_1^{\perp}(x,\mathbf{k}_T^2) = M_h^2 \int [d\sigma d\tau]\, X_6 , \tag{2.23}$$

where the symmetric traceless tensor of rank-2 (i.e. the number of open indices)

$$k_T^{\mu\nu} = k_T^{\mu} k_T^{\nu} + \frac{1}{2}\mathbf{k}_T^2 g_T^{\mu\nu}\,, \tag{2.24}$$

is used to ensure that the tensors that accompany the TMDs transform according to an irreducible representations of the Lorentz group, i.e. are independent Lorentz structures that do not mix under Lorentz transformations. So, the following parametrisation for the TMD gluon correlator in terms of TMDs is found:

$$\Gamma_U^{\mu\nu}(x,\mathbf{k}_T) = \frac{x}{2}\bigg\{ -g_T^{\mu\nu}\, f_1(x,\mathbf{k}_T^2) + \bigg(\frac{k_T^{\mu} k_T^{\nu}}{M_h^2} + g_T^{\mu\nu}\frac{\mathbf{k}_T^2}{2M_h^2}\bigg) h_1^{\perp}(x,\mathbf{k}_T^2)\bigg\}\,. \tag{2.25}$$

It contains the unpolarised gluon TMD f_1 and the linearly polarised gluon TMD $h_1^{\perp}$ examined in the phenomenological studies conducted in this thesis. For completeness, the longitudinally and transversely polarised hadron integrated correlators in terms of TMDs are given by [7,8]:

$$\Gamma_L^{\mu\nu}(x,\mathbf{k}_T) = \frac{x}{2}\bigg\{ i\epsilon_T^{\mu\nu} S_L\, g_{1L}(x,\mathbf{k}_T^2) + \frac{\epsilon_T^{k_T\{\mu} k_T^{\nu\}}}{2M_h^2} S_L\, h_{1L}^{\perp}(x,\mathbf{k}_T^2)\bigg\}\,, \tag{2.26}$$

$$\begin{aligned}\Gamma_T^{\mu\nu}(x,\mathbf{k}_T) = \frac{x}{2}\bigg\{ & g_T^{\mu\nu}\frac{\epsilon_T^{k_T S_T}}{M_h}\, f_{1T}^{\perp}(x,\mathbf{k}_T^2) + i\epsilon_T^{\mu\nu}\frac{k_T\cdot S_T}{M_h}\, g_{1T}(x,\mathbf{k}_T^2) \\ & - \frac{\epsilon_T^{k_T\{\mu} S_T^{\nu\}} + \epsilon_T^{S_T\{\mu} k_T^{\nu\}}}{4M_h}\, h_{1T}(x,\mathbf{k}_T^2) + \frac{\epsilon_T^{k_T\{\mu} k_T^{\nu\}}}{2M_h^2}\frac{k_T\cdot S_T}{M_h}\, h_{1T}^{\perp}(x,\mathbf{k}_T^2)\bigg\}\,.\end{aligned} \tag{2.27}$$

The letters f, g, and h indicate unpolarised, circularly polarised, and linearly polarised gluons TMDs due to the Lorentz structures g_T^{ij}, ϵ_T^{ij} and k_T^{ij} they accompany, respectively. We note that the nomenclature of the TMDs adopted here is in analogy to the ones for quarks [10]. Besides, in correspondence to the transversity function for quarks, the following function is usually defined:

$$h_1 \equiv h_{1T} + \frac{\mathbf{k}_T^2}{2M_h^2} h_{1T}^{\perp}\,. \tag{2.28}$$

We note that in [8] the analysis of [7] was extended by including a light-like vector n in the parametrisation ($n\cdot\xi = 0$), that can enter upon the consideration of staple-like Wilson lines as explained in Sec. 2.5. Nevertheless, it was found that these structures do not give rise to any new leading-twist TMDs. Additionally, the parametrisation of the gluon correlator for a spin-1 hadron was as well performed by them. Prior the gluon correlators, the quark correlators were studied in a similar way by a parametrisation in terms of Dirac matrices. For their expressions for spin-1/2 as well as spin-1 hadrons we refer to [11].

The collinear correlator can be obtained by integrating again, over TM $\mathbf{k}_T$:

$$\begin{aligned}\Gamma^{\mu\nu}(x) &\equiv \int d^2\mathbf{k}_T\, \Gamma^{\mu\nu}(x,\mathbf{k}_T) \\ &= \frac{1}{P_h^+}\int \frac{d\xi^-}{2\pi}\, e^{ik\cdot\xi}\, \langle P_h, S_h| F^{+\mu}(0)\mathcal{U}_{[0,\xi]} F^{+\nu}(\xi)\mathcal{U}'_{[\xi,0]} |P_h, S_h\rangle\bigg|_{\xi^+=\xi_T=0}\,.\end{aligned} \tag{2.29}$$

Explicitly, one finds

$$\Gamma^{\mu\nu}(x) = \frac{x}{2}\Big\{ - g_T^{\mu\nu}\, f_1(x) - i\epsilon_T^{\mu\nu}\, S_L\, g_{1L}(x)\Big\}\,, \tag{2.30}$$

where $f_1(x) = \int d^2\mathbf{k}_T\, f_1(x, \mathbf{k}_T^2)$ and $g_{1L}(x) = \int d^2\mathbf{k}_T\, g_{1L}(x, \mathbf{k}_T^2)$ are the one-dimensional PDFs. Therefore, TMDs are also called unintegrated PDFs. We note that only TMDs without k_T-dependent tensors survive. Besides, in contrast to quark transversity, h_1 vanishes upon integration over TM, i.e. it has no collinear counterpart [12]. In Table 2.1 the gluon TMDs are summarised by hadron and gluon polarisations and we have indicated which functions are T-odd, i.e. that contain T-odd amplitudes, and which ones have a collinear counterpart. We note that gaps in the table are due to the lack of specific Lorentz structures that arise at leading twist.

The PDFs have been extensively investigated in various fixed-target and collider experiments, and will be utilised in the TMD studies presented in this thesis, i.e. $f_1^i(x)$ simply provides the probability for finding a (unpolarised) parton i with collinear momentum fraction x inside the hadron, while for the TMDs also their TM needs to be taken into account. These functions must be normalised in a way such that the valence quark content of the hadron is respected, this is called the number sum rule, i.e. for the proton:

$$\int_0^1 dx\,\big(f_1^u(x) - f_1^{\bar{u}}(x)\big) = 2\,, \quad \int_0^1 dx\,\big(f_1^d(x) - f_1^{\bar{d}}(x)\big) = 1\,. \tag{2.31}$$

In the latter the antiquark distributions have to be subtracted to avoid infinities arising form the sea quarks. Besides, they also satisfy the momentum sum rule. This rule dictates that the total fractional momentum carried by the partons is unity:

$$\sum_{a=q,\bar{q},g} \int_0^1 dx\, x f_1^a(x) = 1\,. \tag{2.32}$$

It turns out that when $\mu_H \gg M_h$, quarks and antiquarks only contribute to approximately half of the total momentum, with the remaining half being carried by gluons that pronounces their importance. The implicit scale dependence of the PDFs, as well as for TMDs, will be discussed later in this thesis. We note that, as done here, we added from next chapter onwards a superscript to the distributions functions to mark the parton associated to it.

Upon integrating Eq. 2.29 over k^+ one finds the local hadronic matrix elements:

$$P_h^+ \int dk^+\, \Gamma^{\mu\nu}(x) = \int d^4k\, \Gamma^{+\mu;+\nu}(k, P_h, S_h) = \langle P_h, S_h | F^{+\mu}(0) F^{+\nu}(0) | P_h, S_h\rangle\,. \tag{2.33}$$

The trace of this quantity is precisely the energy momentum tensor: $\langle T^{\mu\nu}\rangle \equiv \langle P_h | T^{\mu\nu} | P_h\rangle = 2P_h^\mu P_h^\nu$. So, the integration of the parametrisation $\Gamma^{\mu\nu}$ in terms of the gluon distribution $f_1(x)$ in Eq. 2.30 over x gives

$$2(P_h^+)^2 \int_0^1 dx\, x f_1(x) = \langle P_h, S_h | T^{++} | P_h, S_h\rangle\,, \tag{2.34}$$

Table 2.1: Overview of the leading-twist gluon TMDs for unpolarised (U) and polarised (L or T) hadrons. The functions indicated in red also occur as collinear PDFs, and the ones in blue are T-odd. The historical names of the equivalent quark TMDs (unpolarised, chiral and transverse quarks) are enclosed in parentheses, although for the quark case the TMDs in bottom row have the opposite time-reversal symmetry and transversity has a collinear counterpart as well [13].

		Parent hadron polarisation		
		Unpolarised	Longitudinal	Transverse
Gluon polarisation	Unpolarised	f_1 (Number density)		$f_{1T}^{\perp}$ (Sivers)
	Circular		g_{1L} (Helicity)	g_{1T} (Worm-gear)
	Linear	$h_1^{\perp}$ (Boer-Mulders)	$h_{1L}^{\perp}$ (Worm-gear)	h_1 (Transversity) $h_{1T}^{\perp}$ (Pretzelosity)

where the restriction $-1 \leq x \leq 1$ and the symmetry relation $f_1(-x) = -f_1(x)$ are employed. Since the right-hand side is only the gluonic part of the energy momentum tensor, it follows that the normalisation of the correlator is in agreement with the momentum sum presented in Eq. 2.32, namely:

$$0 \leq \int_0^1 dx\, x f_1(x) \leq 1\,. \tag{2.35}$$

For completeness, we mention that there also exist generalised TMDs (GTMDs) that depend on more kinematical variables. These are interesting because these contain more information on the internal structure of the hadron. However, their correlator parametrisation will require more terms to describe all the possible interactions. To study these correlators a different family of processes is used, namely exclusive processes where one measures the momentum shift denoted by Δ of e.g. the proton. Note that there is no final-state cut in such processes; a correlator represents then an amplitude rather than a squared amplitude. Through Fourier transforms, the Δ dependence translates into a dependence in the position of partons inside the proton, bringing information that is complementary to those encoded in momentum-dependent correlators. The Δ dependence is divided in light-cone coordinates too: its '+'-component via the shift fraction $2\xi = \Delta^+/P_h^+$ called skewness (its physical region corresponds to $-1 \leq \xi \leq 1$), the transverse component $\boldsymbol{\Delta}_T$ and the '$-$'-component being fixed by the on-shell condition of the proton. Fig. 2.2 presents some types of multidimensional correlators and the connections between them, from the most general fully unintegrated correlator, to the one-dimensional collinear PDF. Integrating the full correlator over k^- gives a GTMD that still depends both on three-dimensional partonic momenta and the proton momentum shift. Integrating over transverse partonic momentum $\mathbf{k}_T$ will give a generalised parton distribution (GPD), while taking the forward limit $\Delta = 0$ will give a TMD. Naturally, enforcing the forward limit on

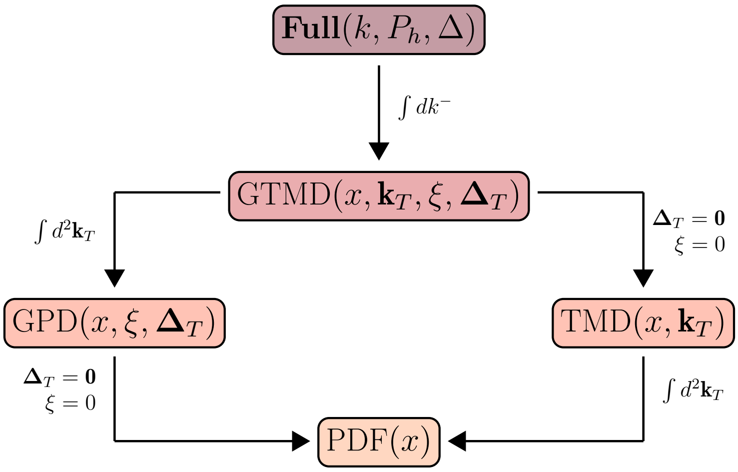

Figure 2.2: Overview of some types of multidimensional parton correlators and the relations between them.

a GPD or integrating a TMD over $\mathbf{k}_T$ must result in a PDF, although matching the two requires specific care [14, 15]. For a more complete review of the proton structure landscape and different types of correlators we refer to [16].

The distribution functions discussed above can be utilised in single-parton scattering (SPS) processes. However, in proton-proton collisions resulting in a two-particle final state, such as the production of quarkonium pairs, one should also consider the particles to originate from two distinct hard scatterings. This is called double-parton scattering (DPS), in which each hard scattering takes place with one parton from the double-parton distribution (DPD). The two interactions are separated by a finite distance in the plane transverse to the colliding proton momenta, such that a DPD depends not only on the momentum fractions of two partons, but also on the transverse distance between them. Our understanding of multi-parton distribution functions, like DPDs, is currently not yet as developed as our knowledge of SPS distribution functions (especially when compared to PDFs), but are extensively studied in recent years, e.g. for TMD DPS see [17]. Although it really depends on the kinematic region, when the momentum fractions become small a DPD is expected to grow roughly like the square of an ordinary SPS distribution function (up to some normalisation) [18]. Therefore, the importance of DPS compared to SPS is increased in the small-x region, and hence cannot probably be neglected in the case of gluon fusion to a two-particle final state. DPS contributions are further discussed for quarkonium-pair production in Sec. 6.3.

2.4 Positivity bounds

In order to make the hadron spin explicit, the TMD correlator can be written as [7]

$$\Gamma^{\mu\nu}(x, \mathbf{k}_T; S_h) = \operatorname{Tr}\left(\rho(\mathbf{S}_h)\, N^{\mu\nu}(x, \mathbf{k}_T)\right) = \rho_{s's}(\mathbf{S}_h)\, N^{ij}_{ss'}(x, \mathbf{k}_T)\,, \tag{2.36}$$

where s, s' label the hadronic polarisation states. This form of the correlator is examined as it can be used to establish constraints on the nonperturbative TMDs. Γ can be seen as a 2×2 matrix in the two gluon polarisations, and N can be understood as a 4×4 matrix in gluon $\otimes$ hadron-spin space. $\rho(\mathbf{S}_h)$ is the spin density matrix for a spin-1/2 particle characterised by the spin vector $\mathbf{S}_h = (S_L, \mathbf{S}_T)$, in its rest frame given by

$$\rho(\mathbf{S}_h) = \frac{1}{2}\big(\mathbf{1} + \mathbf{S}_h \cdot \boldsymbol{\sigma}\big) \tag{2.37}$$

where $\boldsymbol{\sigma} = (\sigma_1, \sigma_2, \sigma_3)$ are the well-known Pauli matrices. It should not matter which basis is used, whether it be the (real) linear polarisations or circular polarisations for the gluons, for instance. Adopting the latter as is usually done, e.g.

$$|\pm\rangle = \frac{1}{\sqrt{2}}(\mp|1\rangle + i|2\rangle)\,, \tag{2.38}$$

one obtains the following matrix elements

$$\begin{aligned}
\Gamma^{++} &= \frac{1}{2}\big(\Gamma^{11} + \Gamma^{22}\big) + \mathfrak{Im}\{\Gamma^{12}\}\,,\\
\Gamma^{+-} &= -\frac{1}{2}\big(\Gamma^{11} - \Gamma^{22}\big) - i\mathfrak{Re}\{\Gamma^{12}\}\,,\\
\Gamma^{-+} &= -\frac{1}{2}\big(\Gamma^{11} - \Gamma^{22}\big) + i\mathfrak{Re}\{\Gamma^{12}\}\,,\\
\Gamma^{--} &= \frac{1}{2}\big(\Gamma^{11} + \Gamma^{22}\big) - \mathfrak{Im}\{\Gamma^{12}\}\,,
\end{aligned} \tag{2.39}$$

where $\mathbf{k}_T$ in the explicit expressions is conveniently expressed in terms of its polar coordinates $|\mathbf{k}_T|$ and ϕ. Besides, using the density matrix, Eq. 2.36 can be written as:

$$\begin{aligned}
\Gamma^{\mu\nu} = {}& \frac{1}{2}\big(N^{\mu\nu}_{++} + N^{\mu\nu}_{--}\big) + \frac{S_L}{2}\big(N^{\mu\nu}_{++} - N^{\mu\nu}_{--}\big)\\
& + \frac{S_T^1}{2}\big(N^{\mu\nu}_{+-} + N^{\mu\nu}_{-+}\big) + \frac{iS_T^2}{2}\big(N^{\mu\nu}_{+-} - N^{\mu\nu}_{-+}\big)\,.
\end{aligned} \tag{2.40}$$

In general, N has the following structure

$$N = \frac{x}{2}\begin{pmatrix} A & B \\ B^\dagger & C \end{pmatrix} \tag{2.41}$$

where the 2×2 blocks A and C are related by parity and the off-diagonal blocks B are Hermitian conjugates. For the explicit expression we refer to [7, 19]. To make the properties of the matrix N more apparent, one can write its elements in the following form

$$\begin{aligned}
N^{\mu\nu}_{ss'}(x, \mathbf{k}_T) &= \frac{1}{P_h^+}\int \frac{d\xi^- d^2\boldsymbol{\xi}_T}{(2\pi)^3}\, e^{ik\cdot\xi}\, \langle P_h; s|F^{+\mu}(0)F^{+\nu}(\xi)|P_h; s'\rangle\Big|_{\xi^+=0}\\
&= \frac{1}{P_h^+}\sum_n \langle P_n|F^{+\mu}(0)|P_h; s\rangle^* \langle P_n|F^{+\nu}(0)|P_h; s'\rangle\\
&\quad \times \delta(P_n^+ - (1-x)P_h^+)\, \delta^2(\mathbf{P}_{nT} + \mathbf{k}_T)\,,
\end{aligned} \tag{2.42}$$

where a complete set of momentum eigenstates is inserted. This equation infers that N is positive-semidefinite or, equivalently, that the eigenvalues of N in must be ≥ 0. From its 2×2 principal minors the following positivity bounds are derived:

$$|g_{1L}| \leq f_1\,, \tag{2.43}$$

$$\frac{\mathbf{k}_T^4}{4M_h^4}\left[(h_{1L}^\perp)^2+(h_1^\perp)^2\right]\leq(f_1+g_{1L})(f_1-g_{1L})\,, \tag{2.44}$$

$$\frac{|\mathbf{k}_T|}{M_h}|h_1|\leq f_1+g_{1L}\,, \tag{2.45}$$

$$\frac{|\mathbf{k}_T|^3}{2M_h^3}|h_{1T}^\perp|\leq f_1-g_{1L}\,, \tag{2.46}$$

$$\frac{\mathbf{k}_T^2}{M_h^2}\left[(f_{1T}^\perp)^2+g_{1T}^2\right]\leq(f_1+g_{1L})(f_1-g_{1L})\,. \tag{2.47}$$

For spin-0 hadrons the parametrisation of the correlator in Eq. 2.25 is given by the only two functions. Then there is no spin density matrix, meaning that $\Gamma = N$, such that one simply needs to compute the eigenvalues of the Γ_U, that results in the single bound:

$$\frac{\mathbf{k}_T^2}{2M_h^2}|h_1^\perp|\leq f_1\,. \tag{2.48}$$

This inequality also follows from Eq. 2.44 upon omitting the TMDs related to the polarisation of the hadron. We note that the positivity bounds for gluon TMDs in higher-spin hadrons can be derived similarly, e.g. the spin-1 case is derived in [19]. Furthermore, for positivity bounds of quark TMDs we refer to [20] for spin-1/2 hadrons, and to [21] for spin-1 hadrons.

Since the positivity bounds are derived from the operator definition of the correlator, they serve as a test of the TMD formalism. Moreover, these bounds are useful as a method to obtain a rough estimate of certain TMDs, e.g. by saturating the bounds. In turn, such estimates could be used for evaluating certain observables of a specific process.

2.5 Wilson lines and process dependence

As explained in Sec. 2.1, ensuring gauge invariance of the correlator requires the inclusion of Wilson lines, which account for collinear and soft gluon emissions. In the collinear case, e.g. Eq. 2.29, the Wilson line that bridges the nonlocality is given by

$$\mathcal{U}^N_{[0,\xi^-;\mathbf{0}]}=\mathcal{P}\exp\left(ig_s\int_0^{\xi^-}d\eta^-\,A^+(\eta^+=0,\,\eta^-,\,\boldsymbol{\eta}=\mathbf{0})\right), \tag{2.49}$$

which runs along the minus direction with respect to the hadron as indicated by the superscript N. Specifically, two such lines are needed for the collinear gluon correlator. We note that the integration path is fixed which implies that these Wilson lines are uniquely determined. Therefore, PDFs are universal, i.e. independent of the hard-scattering event so that they can be extracted from one process and used in others. For this reason, and the fact that they only depend on the variable x, the PDFs are the most conveniently to study and therefore the most well-known. Besides, in the $A^+ = 0$ light-cone gauge, the collinear Wilson lines reduce to unity and can be even omitted.

However, the Wilson lines for the TMD correlators are no longer unique, because the fields are not only separated in the minus direction but also in the transverse

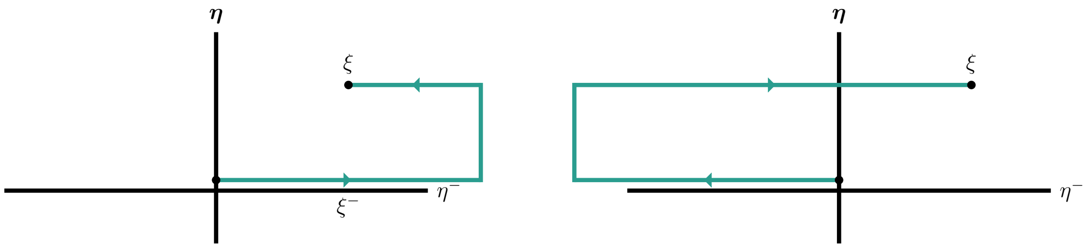

Figure 2.3: The integration paths of the future-pointing Wilson line $\mathcal{U}^{[+]}_{[0,\xi]}$ (left) and the past-pointing Wilson line $\mathcal{U}^{[-]}_{[0,\xi]}$ (right). The paths run along the light-front $\eta^+ = 0$ via plus or minus light-cone infinity, respectively.

directions. This means that the Wilson line necessarily includes a transverse piece [22, 23]. The two gauge links that are of importance for the considered processes in this thesis are the so-called future- and past-pointing gauge links, also known as staple-like Wilson lines, denoted by $\mathcal{U}^{[+]}_{[0,\xi]}$ and $\mathcal{U}^{[-]}_{[0,\xi]}$, respectively. They are constructed by

$$\mathcal{U}^{[\pm]}_{[0,\xi]} = \mathcal{U}^{N}_{[0,\pm\infty;\mathbf{0}]}\,\mathcal{U}^{T}_{[\pm\infty;\mathbf{0},\boldsymbol{\xi}]}\,\mathcal{U}^{N}_{[\pm\infty,\xi^-;\boldsymbol{\xi}]}\,, \tag{2.50}$$

and their integration paths are illustrated in Fig. 2.3. The links along the minus directions are given in Eq. 2.49 and the link along the transverse direction, indicated by the superscript T, is defined by:

$$\mathcal{U}^{T}_{[\pm\infty;\mathbf{0},\boldsymbol{\xi}]} = \mathcal{P}\exp\left(ig_s\int_{\mathbf{0}}^{\boldsymbol{\xi}} d\boldsymbol{\eta}\cdot\mathbf{A}(\eta^+ = 0,\, \eta^- = \pm\infty,\, \boldsymbol{\eta})\right). \tag{2.51}$$

We note that one can choose a gauge such that the staple-like Wilson line becomes unity, e.g. $\mathcal{U}^{[+]}_{[0,\xi]}$ (that will alter the other Wilson line accordingly, e.g. $\mathcal{U}^{[-]}_{[0,\xi]}$). However, it is not allowed for both of them to become unity simultaneously as can be inferred from the gauge invariant (rectangular) Wilson loop: $\mathcal{U}^{[\Box]} \equiv \mathcal{U}^{[+]}_{[0,\xi]}\mathcal{U}^{[-]}_{[\xi,0]}$.

Which staple-like Wilson lines are employed for the TMD gluon correlator depends on the direction of colour flow in the perturbative hard-scattering process. There are four possibilities with these lines, namely: $[+,+]$, $[-,-]$, $[+,-]$, and $[-,+]$. The $[-,-]$ structure appears in processes with colour flow annihilated within the initial state, such as quarkonium (-pair) production in proton-proton collisions ($g+g \to [Q\bar{Q}]$, where the brackets denote the quarks are bound) [24, 25]. The structure $[+,+]$, on the other hand, is related to colour flow into the final state, which is the case for quarkonium production in electron-proton collisions ($\gamma^* + g \to [Q\bar{Q}]$) [26]. The other Wilson lines, $[+,-]$, and $[-,+]$, appear in processes with $q+g \to q+g$ and $\bar{q}+g \to \bar{q}+g$ partonic contributions, respectively [27], in which the colour flow involves both initial and final states. For a comprehensive overview of the staple-like Wilson lines involved in various processes, such as quarkonium production, we refer to [28]. In general, when the hard-scattering process contains more coloured particles the colour flow gets more complicated, leading to more complicated link structures, e.g. Wilson loops, or even factorisation breaking of the process. Actually, for dijet and open heavy-quark pair production in hadron-hadron collisions ($g + g \to q + \bar{q}$) possible factorisation-breaking effects are expected [29, 30], although at small x these contributions may become suppressed [31, 32].

As pointed out before, time-reversal transformations relate correlators with time-reversed Wilson-line structures. Hence, TMDs in different processes can be related. This was initially argued in [33], while the comprehension came later. Considering staple-like Wilson lines, Eq. 2.16 can be written as

$$\Gamma^{[\pm,\pm]\mu\nu *}(x,\mathbf{k}_T) = \Gamma_{\mu\nu}^{[\mp,\mp]}(x,\mathbf{k}_T)\,, \quad \Gamma^{[\pm,\mp]\mu\nu *}(x,\mathbf{k}_T) = \Gamma_{\mu\nu}^{[\mp,\pm]}(x,\mathbf{k}_T)\,, \tag{2.52}$$

where Hermitian conjugation is implied for the second gauge link entry. So, the T-even and T-odd parts of Γ are given by

$$\Gamma^{(T\text{-even})}(x,\mathbf{k}_T) = \frac{1}{2}\left[\Gamma^{[+,+]}(x,\mathbf{k}_T) + \Gamma^{[-,-]}(x,\mathbf{k}_T)\right], \tag{2.53}$$

$$\Gamma'^{(T\text{-even})}(x,\mathbf{k}_T) = \frac{1}{2}\left[\Gamma^{[+,-]}(x,\mathbf{k}_T) + \Gamma^{[-,+]}(x,\mathbf{k}_T)\right], \tag{2.54}$$

$$\Gamma^{(T\text{-odd})}(x,\mathbf{k}_T) = \frac{1}{2}\left[\Gamma^{[+,+]}(x,\mathbf{k}_T) - \Gamma^{[-,-]}(x,\mathbf{k}_T)\right], \tag{2.55}$$

$$\Gamma'^{(T\text{-odd})}(x,\mathbf{k}_T) = \frac{1}{2}\left[\Gamma^{[+,-]}(x,\mathbf{k}_T) - \Gamma^{[-,+]}(x,\mathbf{k}_T)\right], \tag{2.56}$$

where the Lorentz indices are suppressed. It follows that the unpolarised and linearly polarised gluon T-even TMDs f_1 and $h_1^\perp$ are expected to be the same in both quarkonium (-pair) production in hadron-hadron collisions and quarkonium production in electron-hadron collisions, although their Wilson-line structures are different. On the contrary, T-odd TMDs in polarised hadron reactions (see Table 2.1) are expected to have a sign flip between these processes. This is a striking prediction of the TMD formalism. Additionally, it tells that for certain processes, TMDs are entirely independent of each other and encapsulate distinct information, e.g. $f_1^{[+,+]}$ cannot be related to $f_1^{[+,-]}$. Consequently, different experimental extractions provide complementary insights. We note that TMDs in a certain process are not Wilson line independent of course, e.g. distinctions relative to a direct straight line from 0 to ξ appears to be related to orbital angular momentum [34, 35].

3

Quarkonium production

Quarkonium production is a two-scale process, i.e. it consist out of two steps that occur at different energies: the high-energy scattering in which a heavy-quark pair is produced and their binding to a mass $M_{\mathcal{Q}}$. The former can be calculated using perturbative QCD, i.e. using Feynman graphs, while the latter requires a nonperturbative description (like the distribution functions). There are various models available for the hadronisation of the heavy-quark pair in the final state which rely on the factorisation of the constituent parts of the processes at different scales (with the hard scale μ_H much larger that the masses involved). In this chapter we discuss the most commonly used models for quarkonium production with particular focus on the colour-singlet model and the colour-octet mechanism within the framework of nonrelativistic QCD that are employed in this thesis. Moreover, by assuming factorisation of a process, we can then calculate the cross sections in terms of the TMDs that we want to probe. In Sec. 3.1 we discuss the current understanding of quarkonium and its formation methods. Furthermore, we show in Sec. 3.2 how to calculate the probability amplitude of quarkonium production by employing the Bethe-Salpeter wave function, i.e. that contains the hard scattering as well as the nonperturbative binding. Thereafter, we employ the correlator definition for unpolarised protons in terms of their gluon TMDs to calculate the differential cross sections of the processes investigated in this thesis. Particularly, we organise the studies as follows: single quarkonium hadroproduction (proton-proton collisions) in Sec. 3.3, single quarkonium photo- and electroproduction (photon-proton and electron-proton collisions) in Sec. 3.4, and quarkonium-pair hadroproduction in Sec. 3.5.

3.1 Binding the heavy-quark pair

The name quarkonium originates from its resemblance to positronium [36], discovered in 1951, which is a bound state composed of an electron and its corresponding antiparticle: the positron. The light-quark flavours (up, down, and strange) have respectively closely lying masses in contrast to the heavy-quark flavours (charm, bottom and top). This results in experimentally observed $[q\bar{q}]$ states, e.g. η, η', and π^0 mesons, that are actually quantum mechanical mixtures of light quark-antiquark flavour combinations. On the other hand, heavy-quark bound states are better defined in terms of their valence quark–antiquark content of a given flavour denoted by $[Q\bar{Q}]$, where the capital Q denotes that the quarks are heavy. The top quark is however too heavy to form a bound state as it decays through the electroweak interaction (a rare example of a weak process proceeding more quickly than a strong process). Therefore, quarkonium refers only to charmonium, $[c\bar{c}]$, and bottomonium, $[b\bar{b}]$, states.

Besides the mass, quarkonium actually exhibits two additional scales, $m_Q v$ and $m_Q v^2$, that are the momentum and the kinetic energy of the heavy quarks, respectively, where v is their relative velocity in the rest frame of the bound state. Unlike in the case of the proton, the mass of quarkonium is close to the masses of its valence quarks, i.e. $M_Q = 2m_Q$ up to small corrections. In particular, their ground state (η_Q) masses, $2984.1 \pm 0.4\,\text{MeV}$ and $9398.7 \pm 2.0\,\text{MeV}$ [37], are in accordance with twice the charm quark mass $m_c = 1.5\,\text{GeV}$ and twice the bottom quark mass $m_b = 4.7\,\text{GeV}$, considering the binding energy to be negligible. As such, the heavy quarks typically have a small relative velocity. Therefore, it is possible to use nonrelativistic potentials, like models of the hydrogen atom, to describe the binding between the heavy quarks and to study the spectroscopy of quarkonium.

The strong force is well described in the nonrelativistic regime by the Cornell potential [38, 39], among other models. It is a combination of a Coulombic potential at small distances in accordance with asymptotic freedom, and a linear potential at large distances describing the effect of confinement

$$V(r) = -C_F \frac{\alpha_s(1/r)}{r} + \sigma r \,, \tag{3.1}$$

where r is the distance between the quark and antiquark, α_s the strong coupling and σ the string tension of the flux tube formed by gluonic field lines between the quark and antiquark. The latter must be proportional to Λ^2_{QCD}, that is small such that only at large distances this term becomes important. The size of the bound state is determined by a balance between the kinetic energy and the potential energy

$$m_Q v^2 \sim \frac{\alpha_s(1/r)}{r} \,, \tag{3.2}$$

where we have used that the distance between the quarks is small. By noticing that the inverse of the momentum $m_Q v$ is the length scale for the size of the quarkonium state, we have that $v^2 \sim \alpha_s^2(m_Q v)$. This can be solved self-consistently, yielding for charmonium $v^2 \simeq 0.3$ and for bottomonium $v^2 \simeq 0.1$.

The naming of quarkonium is based on its quantum numbers J^{PC}, where J denotes the total angular momentum (the orbital angular momentum L plus spin S), P the parity and C the charge-parity [37, pp. 148–150]. The naive quark model relates these

Table 3.1: Schematic spectrum of quarkonium states and their naming, for charmonium up to the $D\bar{D}$ threshold, for bottomonium up to the $B\bar{B}$ threshold. The states in curly brackets have not been experimentally verified but are expected to exist based on their hierarchical structure. The states are sorted by J^{PC} (up to 2^{--}) and states with a higher total angular momentum are denoted with an extra subscript J. The excited states are presented above the ground states and for the explicit energies of the states we refer to [37, p. 1898, p. 2023]. We note that the η_Q states are the true ground states of quarkonium.

	0^{-+}	1^{--}	1^{+-}	0^{++}	1^{++}	2^{++}	2^{--}
	$\{\eta_b(3S)\}$	$\Upsilon(3S)$	$\{h_b(3S)\}$	$\{\chi_{b0}(3S)\}$	$\chi_{b1}(3P)$	$\chi_{b2}(3P)$	
	$\{\eta_b(2S)\}$	$\Upsilon(2S)$	$h_b(2P)$	$\chi_{b0}(2P)$	$\chi_{b1}(2P)$	$\chi_{b2}(2P)$	
$[b\bar{b}]$	$\eta_b(1S)$	$\Upsilon(1S)$	$h_b(1P)$	$\chi_{b0}(1P)$	$\chi_{b1}(1P)$	$\chi_{b2}(1P)$	$\Upsilon_2(1D)$
	$\eta_c(2S)$	$\psi(2\mathrm{S})$					
$[c\bar{c}]$	$\eta_c(1S)$	$J/\psi(1S)$	$h_c(1P)$	$\chi_{c0}(1P)$	$\chi_{c1}(1P)$	$\chi_{c2}(1P)$	

quantum numbers as follows: $P = (-1)^{L+1}$ and $C = (-1)^{L+S}$, which impose restrictions on the quantum numbers that are allowed for the bound $Q\bar{Q}$ states. In Table 3.1 the quarkonium states and their naming is summarised up to the lowest-lying thresholds for decay to a pair of ground state open-charm or open-bottom mesons, i.e. $D\bar{D}$ for charmonium and $B\bar{B}$ for bottomonium. For a complete picture of our current understanding of quarkonium we refer to the complete energy spectra in [37, p. 1898, p. 2023] and to the review of mesons containing two heavy quarks [37, pp. 985–993]. Usually, the spectroscopic notation of the state is added to the name, e.g. $J/\psi(1S)$, as for most quarkonium states it is known. However, when it is unknown, the energy in MeV is usually given between the brackets instead. In the spectra of [37, p. 1898, p. 2023] the most dominant hadronic decays, the location of higher-lying decay thresholds to a pair of open-charm/bottom mesons and some exotic quarkonium states are also incorporated. In particular, the closely related tetraquarks are included that consist out of a heavy-quark and antiquark with the same flavour, and additional up en down valence quarks (giving rise to isospin). These kind of hadronic states are possible in QCD as long as the bound state is colourless.

In general, the binding of quarks can result in colour-singlet (CS) or in colour-octet (CO) states, i.e. in a colourless bound state or a non-colourless bound state, respectively. Namely, in group theoretical terms, we have that for mesons, such as quarkonia:

$$\mathbf{3} \otimes \bar{\mathbf{3}} = \mathbf{8} \oplus \mathbf{1}\,. \tag{3.3}$$

However, in the CO case, the bound state needs to becomes colourless as only CS states can be observed physically. As mentioned before, there exist different models to describe the actual hadronisation procedure that takes place which have different advantages and disadvantages, and for a comparison of their applicability to data we refer to [40].

We begin by discussing the colour-evaporation model (CEM), proposed in 1977 [41, 42], which aims for describing quarkonium production. The CEM was actually improved in [43], but for simplicity we present here the original one. In the CEM, the cross section governing the creation of a quarkonium state $\mathcal{Q}$ is calculated by a nonperturbative fraction $F_{\mathcal{Q}}$ times the perturbative cross section that generates the heavy-quark pair with an invariant mass below the threshold for meson-pair decay at a mass $2m_{\text{thr}}$. Here, m_{thr} denotes the mass of the D-meson for charmonium and the mass of the B-meson for bottomonium. These fractions $F_{\mathcal{Q}}$ are assumed to be universal, allowing their determination from experimental data, which in turn enables the prediction of cross sections in different processes or kinematic regions. We note that the idea of universal nonperturbative factors enters every model discussed here. The cross section for the creation of heavy-quark pairs imposes constraints solely on the mass of the heavy-quark pair, i.e. there are no restrictions on the colour or spin of the pair. Subsequently, the pair is hypothesised to neutralise its colour through interaction with the collision-induced colour field, called 'colour evaporation'. In some versions of the CEM [44], it is further assumed that this colour-neutralisation process also randomises the spins of the quarks. The probability $F_{\mathcal{Q}}$ provides the likelihood that a heavy-quark pair with an invariant mass less than $2m_{\text{thr}}$ will bind to form the quarkonium state, that is zero if the invariant mass of the pair exceeds $2m_{\text{thr}}$. Therefore, the inclusive differential cross section can be written as

$$d\sigma_{\text{CEM}}(\mathcal{Q}+X) = F_{\mathcal{Q}} \times \int_{2m_Q}^{2m_{\text{thr}}} dm_{Q\bar{Q}} \, \frac{d\sigma(Q\bar{Q}+X)}{dm_{Q\bar{Q}}}, \tag{3.4}$$

where $m_{Q\bar{Q}}$ is the invariant mass of the heavy-quark pair. There is an implied sum over the colours and spins of the final state heavy-quark pair. This is where the model assumptions of colour evaporation and spin randomisation manifest themselves. We note that the CEM remains a rather phenomenological approach which does not rely (so far) on any proof of factorisation. For this reason, we have opted not to study this model.

The second model is the CS model (CSM), that was introduced around 1980 [45–47]. Basically, the CSM excludes CO state production. In this model the heavy-quark pair is directly projected onto a CS state where the quantum numbers of the pair do not evolve between the production of the pair and its formation of the bound state. In particular, one considers only the leading Fock-state (an element of a Fock space with a well-defined number of particles) of the bound state with $v = 0$ such that the momenta of the two heavy quarks become identical, i.e. the S-wave quarkonium states ($L = 0$). The inclusive differential cross section can then be obtained by the following factorisation

$$d\sigma_{\text{CSM}}(\mathcal{Q}[^{2S+1}S_J^1] + X) = d\sigma(Q\bar{Q}[^{2S+1}S_J^1] + X) \times |R(0)|^2 \tag{3.5}$$

where $R(0)$ is the nonperturbative universal radial wave function of a quarkonium state at the origin. This model can be as well employed for P-waves by using instead $R'(0)$ as will be shown in the next section. In order to the improve theory predictions one can either tune the value $R(0)$ by comparison with new data, or include higher-order α_s corrections in the high-energy scattering to the heavy-quark pair.

The third and final model we discuss, the CO mechanism (COM), was much later introduced within the framework of nonrelativistic QCD (NRQCD) in 1994 [49]. NRQCD, which is an effective field theory (EFT), stands as a subject of study in its

Table 3.2: Relative velocity scaling for S-waves and P-waves LDMEs up to order v^4 [48]. Here the naming of charmonium states is employed as an example.

	${}^1S_0^1$	${}^3S_1^1$	${}^1S_0^8$	${}^3S_1^8$	${}^1P_1^1$	${}^3P_0^1$	${}^3P_1^1$	${}^3P_2^1$	${}^1P_1^8$	${}^3P_0^8$	${}^3P_1^8$	${}^3P_2^8$
η_c	1		v^4	v^3					v^4			
J/ψ		1	v^3	v^4						v^4	v^4	v^4
h_c			v^2		v^2							
χ_{c0}				v^2		v^2						
χ_{c1}				v^2			v^2					
χ_{c2}				v^2				v^2				

own regard. Here we provide simply a short overview, since we only employ its results in this thesis. It is based on a hierarchy of scales: $m_Q v^2 \lesssim \Lambda_{\rm QCD} \ll m_Q v \ll m_Q$. The factorisation for the inclusive cross section in NRQCD is given by

$$d\sigma_{\rm NRQCD}(a+b \to \mathcal{Q}+X) = \sum_n C_n^{ab}(\Lambda) \times \langle \mathcal{O}_n^{\mathcal{Q}}(\Lambda)\rangle\,, \tag{3.6}$$

where $\langle \mathcal{O}_n^{\mathcal{Q}}\rangle \equiv \langle 0|\mathcal{O}_n^{\mathcal{Q}}|0\rangle$ are universal vacuum-expectation values (vevs) of four-fermion operators in NRQCD, evaluated in the rest frame of the quarkonium, i.e. the heavy-quark pair is produced in a point in the EFT. The latter are more commonly called the long-distance matrix elements (LDMEs). The short-distance, high-energy coefficients C_n^{ab} can be calculated in perturbation theory by matching amplitudes in NRQCD with those in full QCD. Both the short-distance and long-distance physics depend on Λ, the ultraviolet cut-off of the effective theory, i.e. the scale where the theory breaks down. The operators have a general form

$$\mathcal{O}_n^{\mathcal{Q}} = \chi^\dagger \kappa_n \psi \mathcal{P}^{\mathcal{Q}}(\Lambda) \psi^\dagger \kappa_n' \chi\,, \tag{3.7}$$

where ψ is the two-component Pauli spinor that annihilates a heavy quark and χ is the two-component spinor that creates a heavy antiquark. $\mathcal{P}^{\mathcal{Q}}$ is a projector onto Fock states that in the asymptotic future contain $\mathcal{Q}$ and X whose energies and momenta lie below the cut-off Λ:

$$\mathcal{P}^{\mathcal{Q}}(\Lambda) = \sum_X |\mathcal{Q}+X, t\to\infty\rangle\langle \mathcal{Q}+X, t\to\infty|\,. \tag{3.8}$$

The factors κ_n are direct products of a colour matrix (either the unit matrix or the matrix t^a with octet index a), a spin matrix (either the unit matrix or the Pauli matrix σ^i with triplet index i, respectively $S=0$ or 1), and a polynomial in the QCD covariant derivative and field strengths (increasing L and J of the heavy-quark bound state). Therefore, the summation in Eq. 3.6 is in $n = {}^{2S+1}L_J^c$, where c is the colour configuration of the quarkonium, i.e. $c=1$ or $c=8$ for CS and CO, respectively. With the inclusion of higher Fock-states, the CO states become colourless through soft-gluon emission taken into account by the LDMEs.

So, in NRQCD the heavy-quark pair can not only be produced in a CS state, but also in a CO state. Essentially, we can therefore rewrite the inclusive cross section as

$$d\sigma_{\rm NRQCD}(\mathcal{Q}+X) = \sum_n d\sigma(Q\bar{Q}[n]+X) \times \langle \mathcal{O}^{\mathcal{Q}}[n]\rangle\,, \tag{3.9}$$

where we have slightly altered the notation of the LDMEs, that contain all of the nonperturbative physics of the transition of a heavy-quark pair into a quarkonium state (in collinear factorisation). From the EFT it can be derived that LDMEs fall into a hierarchy according to their scaling with the relative velocity v, and as v is small the summation over the matrix elements can be truncated at a low order in v. In Table 3.2 one finds the velocity scaling rules for S- and P-waves. When one truncates at LO in v, one ends up with the CSM by identifying that $|R(0)|^2$ equals the corresponding LDME. We note that the COM has been introduced to address the issue of remaining infrared divergences in the decay of P-wave quarkonium states ($L = 1$) to $gq\bar{q}$ in the CSM [49, 50]. This additional divergence is removed with the inclusion of the CO state ${}^3S_1^8$, which within the framework of NRQCD has the same power counting in v^2 as the P-waves. The CO LDMEs bring however also difficulties as the emission of soft-gluons can alter the quantum numbers of the heavy-quark pair. Therefore, it is only possible to study the CS LDMEs from potential models and lattice calculations, while the CO ones are usually only determined by fits to experimental data. As a result, the present knowledge of CO LDMEs is not very accurate.

We note that another EFT named potential NRQCD [51] was introduced subsequent to NRQCD, which is based on a slightly different hierarchy of scales, namely: $\Lambda_{\text{QCD}} \ll m_Q v^2 \ll m_Q v \ll m_Q$. This situation only holds for very heavy quarkonium that is outside the scope of this thesis. Though, there are situations with a different relative size between Λ_{QCD} and $m_Q v^2$ where this theory can provide statements for less heavy quarkonium production [52].

Another approach to describe quarkonium production is through the use of nonperturbative fragmentation functions (FFs). In essence FFs are similar to the distribution functions discussed in Ch. 2 as they are defined by a correlator, e.g. $D^i(z)$, similar the PDF $f_1^i(x)$, provides the probability for producing a (unpolarised) hadron from a (unpolarised) parton i with collinear momentum fraction z. The difference is that for FFs time-reversal symmetry cannot be used as a constraint because of the explicit appearance of outgoing states $|P_h, S_h; X\rangle$ in the definition of the unintegrated correlator, e.g. the expression for gluon TMDFFs can be found in [7]. Usually the FFs are employed for light hadron states, but since NRQCD with NLO α_s short-distance calculations have not been able to fully describe all collinear experimental data of inclusive quarkonium production (especially polarised quarkonium is problematic), the fragmentation description of quarkonium was studied in [53–55]. In particular, they consider the following expression

$$d\sigma_{\text{FF}}(\mathcal{Q} + X) = d\sigma(i + X) \times D_{i\to\mathcal{Q}}(z) + d\sigma(Q\bar{Q} + X) \times D_{Q\bar{Q}\to\mathcal{Q}}(z)\,, \tag{3.10}$$

where $D_{i\to\mathcal{Q}}$ are single-parton FFs and $D_{Q\bar{Q}\to\mathcal{Q}}$ parton-pair FFs which give rise to the leading power and next-to-leading power contributions, respectively. The latter contribution is important and may even dominate over the leading power in certain kinematical regions. They found that these FFs can be evaluated analytically, i.e. expressed in terms of LDMEs with perturbative coefficients as in NRQCD, when the scale of the FFs is of the order of the invariant mass of the quarkonium. Therefore, quarkonium production is this way is not another model, but rather a different way of describing the production phenomenology. We will not utilise the fragmentation description in this thesis, but since we explore some relations to it in Sec. 5.3 we have presented it here for completeness.

3.2 Analysis of quarkonium production amplitudes

In Fig. 3.1 the formation of a bound $Q\bar{Q}$ state from a two particle initial state is schematically shown. The two particles a and b are understood from the process under investigation: they are both partons in hadroproduction, and a photon/electron and a parton in photo/electroproduction. They undergo a high-energy scattering after which a bound $Q\bar{Q}$ state is formed. The high-energy perturbative calculation through Feynman diagrams relies on the small coupling of α_s and α at the hard scale of the process, which provides the hard factor denoted by $\mathcal{H}$. The probability amplitude $\mathcal{M}$, including the binding of the heavy quarks, can be written as [56–59]

$$\begin{aligned}\mathcal{M}\big(a(p_1)+b(p_2)\to[Q\bar{Q}](^{2S+1}L_J^c;P)\big) &= \int\frac{d^4k}{(2\pi)^4}\,\mathrm{Tr}[\mathcal{O}(p_1,p_2;k)\,\Phi_{LS;J,J_z}(P,k)]\\ &= \frac{1}{\sqrt{m_Q}}\sum_{L_z,S_z}\sum_{s_1,s_2}\sum_{i,j}\int\frac{d^3\mathbf{k}}{(2\pi)^3}\,\langle s_1;s_2|S,S_z\rangle\,\langle LL_z;SS_z|J,J_z\rangle\,\psi_{LL_z}(\mathbf{k})\\ &\quad\times\,\langle 3i,\bar{3}j|c\rangle\,\mathcal{M}\big(a(p_1)+b(p_2)\to Q_i(P/2+k)+\bar{Q}_j(P/2-k)\big)\,, \qquad (3.11)\end{aligned}$$

with $2k$ being the relative momentum of the quarks and i,j the colour indices of the quark and antiquark, respectively. The orbital angular momentum eigenfunction is $\psi_{LL_z}(\mathbf{k})$ and the brackets denote the appropriate Clebsch-Gordan (CG) coefficients that project onto the specific quantum numbers of the bound state. The bound $Q\bar{Q}$ state obeys the on-shell condition: $P^2=M_{\mathcal{Q}}^2=4m_Q^2$. The mass dimension of the amplitudes is $[\mathcal{M}]=4-n$, where n is the total number of particles involved in the process, i.e. the sum of the incoming and outgoing particles. We point out that in this section the boldface momentum denotes a spatial three-vector, not the spatial TM two-vector employed throughout the rest of this thesis. Moreover, Eq. 3.11 is also applicable to processes involving additional initial and final state particles by altering the partonic amplitude that is part of $\mathcal{O}$. An example of this is shown in Sec. 5.1, where collinear J/ψ production in electron-proton collisions is discussed.

In the first line of Eq. 3.11 we have introduced the Bethe-Salpeter wave function of the produced bound amplitude, namely

$$\Phi_{LS;J,J_z}(P,k)=2\pi\,\delta\!\left(k^0-\frac{|\mathbf{k}|^2}{M_{\mathcal{Q}}}\right)\sum_{L_z,S_z}\psi_{LL_z}(\mathbf{k})\,\langle LL_z;SS_z|J,J_z\rangle\,\mathcal{P}_{SS_z}(P,k)\,, \qquad (3.12)$$

where the δ-function reflects its nonrelativistic nature. The amplitude $\mathcal{O}$ contains the hard factor and is calculated without including the heavy-quark legs of the final states that form the bound state, since they are absorbed into the definition of $\mathcal{P}_{SS_z}$ as shown below. Therefore, $\mathcal{O}$ is defined by

$$\langle 3i,\bar{3}j|c\rangle\,\mathcal{M}(a+b\to Q_i+\bar{Q}_j)=\bar{u}_i\!\left(\frac{P}{2}+k;s_1\right)\mathcal{O}_{ij}(p_1,p_2;k)\,v_j\!\left(\frac{P}{2}-k;s_2\right), \qquad (3.13)$$

which includes the colour projection of the bound state. It is important to note that when calculating the amplitude within TMD factorisation, the polarisation vectors of the initial states are also excluded from $\mathcal{O}$, as they are incorporated into the definitions of the TMDs. $\mathcal{P}_{SS_z}$ plays a role of a spin projection operator that is defined as

$$\mathcal{P}_{SS_z}(P,k)_{ji}=\frac{1}{\sqrt{m_Q}}\sum_{s_1,s_2}\langle s_1;s_2|S,S_z\rangle\,v_j\!\left(\frac{P}{2}-k;s_2\right)\bar{u}_i\!\left(\frac{P}{2}+k;s_1\right), \qquad (3.14)$$

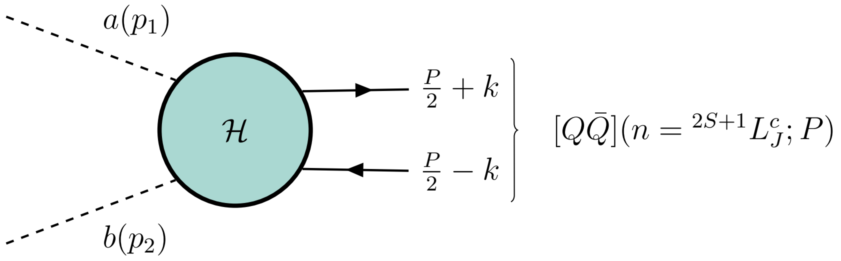

Figure 3.1: Production of a bound $Q\bar{Q}$ state by a two particle initial state. The particles a and b, with momentum p_1 and p_2, undergo a hard scattering after which they are bound to a particular state n with momentum P. The relative momentum k between the outgoing quark and antiquark is considered small for the production.

where the factor $m_Q^{-1/2}$ comes from the normalisation which can be derived from $[\Phi]=-2$. Therefore, Eq. 3.11 can be written in a more compact form, namely:

$$\mathcal{M}\big(a+b\to[Q\bar{Q}]({}^{2S+1}L_J^c;p_1,p_2;P)\big)=\sum_{L_z,S_z}\int\frac{d^3\mathbf{k}}{(2\pi)^3}\,\psi_{LL_z}(\mathbf{k})\,\langle LL_z;SS_z|J,J_z\rangle$$
$$\times\,\mathrm{Tr}[\mathcal{O}(p_1,p_2;k)\,\mathcal{P}_{SS_z}(P,k)]\,. \tag{3.15}$$

From the Dirac equation, $(\not{p}-m)\,u_s(p)=0$ and $(\not{p}+m)\,v_s(p)=0$, it follows that the spinors of the quark and antiquark with momentum p and mass m can be related to the corresponding ones evaluated at rest

$$u_s(p)=(\not{p}+m)\,u_s(0)\,,\quad v_s(p)=(-\not{p}+m)\,v_s(0)\,, \tag{3.16}$$

where here the subscript of the spinors denotes their spin. Considering the following Dirac spinors by taking into account that the quarks are of nonrelativistic nature

$$u_+(0)=\frac{1}{\sqrt{2m_Q}}\begin{pmatrix}1\\0\\0\\0\end{pmatrix},\ u_-(0)=\frac{1}{\sqrt{2m_Q}}\begin{pmatrix}0\\1\\0\\0\end{pmatrix},$$
$$v_+(0)=\frac{1}{\sqrt{2m_Q}}\begin{pmatrix}0\\0\\0\\1\end{pmatrix},\ v_-(0)=\frac{1}{\sqrt{2m_Q}}\begin{pmatrix}0\\0\\-1\\0\end{pmatrix}, \tag{3.17}$$

and the CG coefficients, Eq. 3.14 can be simplified, e.g.

$$\begin{aligned}\mathcal{P}_{00}(f,\bar{f})&=\frac{1}{\sqrt{m_Q}}\sum_{s_1,s_2}\langle\frac{1}{2}s_1;\frac{1}{2}s_2|00\rangle\,v(p_2;s_2)\,\bar{u}(p_1;s_1)\\&=\frac{1}{\sqrt{2m_Q}}[v_-(p_2)\,\bar{u}_+(p_1)-v_+(p_2)\,\bar{u}_-(p_1)]\\&=\frac{1}{\sqrt{2m_Q}}(-\not{p}_2+m_Q)[v_-(0)\,\bar{u}_+(0)-v_+(0)\,\bar{u}_-(0)](\not{p}_1+m_Q)\\&=\frac{1}{\sqrt{8m_Q^3}}(-\not{p}_1+m_Q)\left[-\gamma^5\frac{I+\gamma^0}{2}\right](\not{p}_2+m_Q)\,.\end{aligned} \tag{3.18}$$

The derivation for $S = 1$ is equivalent, whereby a factor of $\slashed{\epsilon}^*_{S_z}(I + \gamma^0)/2$ is found between the square brackets instead. The explicit form of the polarisation vector is given in Eq. 3.24 below (equivalent to $\epsilon^*_{L_z}$). Finally, the spin projection is approximated as

$$\mathcal{P}_{SS_z}(P,k) = \frac{1}{4\sqrt{M_Q^3}}(-\slashed{P} + 2\slashed{k} + M_Q)\,\Pi_{SS_z}\,(\slashed{P} + 2\slashed{k} + M_Q) + O(k^2)\,, \tag{3.19}$$

where:

$$\Pi_{SS_z} = \begin{cases} -\gamma^5 & S = 0 \\ \slashed{\epsilon}^*_{S_z} & S = 1 \end{cases}. \tag{3.20}$$

Eq. 3.15 can be Taylor expanded in powers of $|\mathbf{k}|$ around $\mathbf{k} = 0$ as the relative momentum of the quarks in the bound state is expected to be small. For this purpose, it is convenient to separate the Fourier transform of the wave function $\psi_{LL_z}(\mathbf{k})$ of the bound state into its radial and angular pieces

$$\int \frac{d^3\mathbf{k}}{(2\pi)^3} e^{i\mathbf{k}\cdot\mathbf{r}} \psi_{LL_z}(\mathbf{k}) = \hat{\psi}_{LL_z}(\mathbf{r}) = R_L\big(|\mathbf{r}|\big)\,Y_{LL_z}(\theta,\phi)\,, \tag{3.21}$$

where $R_L\big(|\mathbf{r}|\big)$ is the radial wave function, $Y_{LL_z}(\theta,\phi)$ a spherical harmonic and spherical coordinates are employed: $\mathbf{r} = \big(|\mathbf{r}|,\theta,\phi\big)$. For S-waves $(L = 0,\ J = 0,1)$ we obtain by expanding:

$$\int \frac{d^3\mathbf{k}}{(2\pi)^3} \psi_{00}(\mathbf{k}) = \frac{1}{\sqrt{4\pi}} R_0(0)\,. \tag{3.22}$$

However, for P-waves $(L = 1,\ J = 0,1,2)$ $R_1(0) = 0$. Therefore, we need to consider the linear term k^α in the expansion. For the wave function we can write:

$$\int \frac{d^3\mathbf{k}}{(2\pi)^3} ik^\alpha e^{i\mathbf{k}\cdot\mathbf{r}} \psi_{1L_z}(\mathbf{k}) = \frac{\partial}{\partial \mathbf{r}_\alpha} \hat{\psi}_{1L_z}(\mathbf{r}) = R_1'\big(|\mathbf{r}|\big)\,Y^\alpha_{1L_z}(\theta,\phi)\,. \tag{3.23}$$

This, together with the spherical harmonic

$$Y^\alpha_{1L_z}(\theta,\phi) = \sqrt{\frac{3}{4\pi}}\epsilon^{\alpha *}_{L_z} = \sqrt{\frac{3}{4\pi}} \begin{cases} (0,0,0,1) & L_z = 0 \\ (0,-\lambda,i,0)/\sqrt{2} & L_z = \lambda = \pm 1 \end{cases}, \tag{3.24}$$

gives:

$$\int \frac{d^3\mathbf{k}}{(2\pi)^3} k^\alpha \psi_{1L_z}(\mathbf{k}) = -i\epsilon^{\alpha *}_{L_z}(P)\sqrt{\frac{3}{4\pi}} R_1'(0)\,. \tag{3.25}$$

The polarisation vector $\epsilon^{\alpha *}_{L_z}(P)$ refers to the $L = 1$ bound state and $R_1'(0)$ is the derivative of radial wave function evaluated at the origin. Putting everything together, we obtain the following equations for the S- and P-wave amplitudes

$$\mathcal{M}[{}^{2S+1}S^c_J](p_1,p_2;P) = \frac{1}{\sqrt{4\pi}} R_0(0)\,\mathrm{Tr}[\mathcal{O}(p_1,p_2;0)\,\mathcal{P}_{SS_z}(P,0)]\,, \tag{3.26}$$

$$
\begin{aligned}
\mathcal{M}[{}^{2S+1}P_J^c](p_1,p_2;P) &= -i\sqrt{\frac{3}{4\pi}}R_1'(0)\sum_{L_z,S_z}\langle 1L_z;SS_z|J,J_z\rangle\,\epsilon^{\alpha *}_{L_z}(P)\\
&\quad\times\frac{\partial}{\partial k^\alpha}\,\mathrm{Tr}[\mathcal{O}(p,q;k)\,\mathcal{P}_{SS_z}(P,k)]\Big|_{k=0}\\
&= -i\sqrt{\frac{3}{4\pi}}R_1'(0)\sum_{L_z,S_z}\langle 1L_z;SS_z|J,J_z\rangle\,\epsilon^{\alpha *}_{L_z}(P)\\
&\quad\times\mathrm{Tr}[\hat{\mathcal{O}}_\alpha(0)\,\mathcal{P}_{SS_z}(P,0)+\mathcal{O}(p_1,p_2;0)\,\hat{\mathcal{P}}_{SS_z\alpha}(0)]\,,
\end{aligned}
\tag{3.27}
$$

where:

$$
\hat{\mathcal{O}}_\alpha(0)\equiv\frac{\partial}{\partial k^\alpha}\mathcal{O}(p_1,p_2;k)\Big|_{k=0}\,,\quad \hat{\mathcal{P}}_{SS_z\alpha}(0)\equiv\frac{\partial}{\partial k^\alpha}\mathcal{P}_{SS_z}(P,k)\Big|_{k=0}\,.
\tag{3.28}
$$

$\mathcal{P}_{SS_z}$ can be simplified further by considering its possible quantum numbers, using the anticommutator relations of the gamma matrices and the general identity of a polarisation vector: $P_\alpha\epsilon^\alpha(P)=0$. In the different cases we obtain

$$
\mathcal{P}_{00}=\frac{1}{2}\frac{1}{\sqrt{M_Q}}[\not{P}-M_Q]\gamma^5\,,
\tag{3.29}
$$

$$
\mathcal{P}_{1S_z}=-\frac{1}{2}\frac{1}{\sqrt{M_Q}}[\not{P}-M_Q]\not{\epsilon}^*_{S_z}\,,
\tag{3.30}
$$

$$
\hat{\mathcal{P}}_{00\alpha}=\frac{1}{\sqrt{M_Q}}\gamma_\alpha\frac{\not{P}}{M_Q}\gamma^5\,,
\tag{3.31}
$$

$$
\hat{\mathcal{P}}_{1S_z\alpha}=\frac{1}{2}\frac{1}{\sqrt{M_Q}}\left[\gamma_\alpha\not{\epsilon}^*_{S_z}\frac{\not{P}+M_Q}{M_Q}-\frac{\not{P}-M_Q}{M_Q}\not{\epsilon}^*_{S_z}\gamma_\alpha\right],
\tag{3.32}
$$

where we employed that $P\cdot k\sim O(k^2)$. Therefore, we find for the particular S-waves

$$
\mathcal{M}^{\mu\nu}[{}^1S_0^c](p_1,p_2;P)=\frac{1}{4}\frac{1}{\sqrt{\pi M_Q}}R_0(0)\,\mathrm{Tr}[\mathcal{O}^{\mu\nu}(\not{P}-M_Q)\gamma^5]\,,
\tag{3.33}
$$

$$
\mathcal{M}^{\mu\nu}[{}^3S_1^c](p_1,p_2;P)=-\frac{1}{4}\frac{1}{\sqrt{\pi M_Q}}R_0(0)\,\mathrm{Tr}[\mathcal{O}^{\mu\nu}(\not{P}-M_Q)\not{\epsilon}^*_{S_z}]\,,
\tag{3.34}
$$

and for the P-wave with $S=0$

$$
\begin{aligned}
\mathcal{M}^{\mu\nu}[{}^1P_1^c](p_1,p_2;P) &= -i\sqrt{\frac{3}{4\pi M_Q}}R_1'(0)\\
&\quad\times\mathrm{Tr}\left[\left(\epsilon^{\alpha *}_{L_z}\hat{\mathcal{O}}^{\mu\nu}_\alpha\frac{\not{P}-M_Q}{2}+\mathcal{O}^{\mu\nu}\not{\epsilon}^*_{L_z}\frac{\not{P}}{M_Q}\right)\gamma^5\right],
\end{aligned}
\tag{3.35}
$$

where the CG coefficients are just 1.

For the more difficult triplet P-wave amplitudes we have:

$$
\begin{aligned}
\mathcal{M}^{\mu\nu}[{}^3P_J^c](p_1,p_2;P) &= i\sqrt{\frac{3}{4\pi M_Q}}R_1'(0)\sum_{L_z,S_z}\langle 1L_z;SS_z|J,J_z\rangle\,\epsilon^{\alpha *}_{L_z}(P)\epsilon^{\beta *}_{S_z}(P)\\
&\times\mathrm{Tr}\left[\hat{\mathcal{O}}^{\mu\nu}_\alpha\frac{\not{P}-M_Q}{2}\gamma_\beta-\frac{1}{2}\hat{\mathcal{O}}^{\mu\nu}\left(\gamma_\alpha\gamma_\beta\frac{\not{P}+M_Q}{M_Q}-\frac{\not{P}-M_Q}{M_Q}\gamma_\beta\gamma_\alpha\right)\right].
\end{aligned}
\tag{3.36}
$$

In order to evaluate these we utilise the following relations of the CG coefficients

$$\sum_{L_zS_z}\langle 1L_z;1S_z|00\rangle\,\epsilon^{\alpha*}_{L_z}\epsilon^{\beta*}_{S_z} = \sqrt{\frac{1}{3}}\left(g^{\alpha\beta}-\frac{P^\alpha P^\beta}{M_{\mathcal{Q}}^2}\right), \tag{3.37}$$

$$\sum_{L_zS_z}\langle 1L_z;1S_z|1J_z\rangle\,\epsilon^{\alpha*}_{L_z}\epsilon^{\beta*}_{S_z} = -\frac{i}{M_{\mathcal{Q}}}\sqrt{\frac{1}{2}}\epsilon^{\alpha\beta\mu\nu}P_\mu\epsilon^*_{J_z\nu}(P)\,, \tag{3.38}$$

$$\sum_{L_zS_z}\langle 1L_z;1S_z|2J_z\rangle\,\epsilon^{\alpha*}_{L_z}\epsilon^{\beta*}_{S_z} = \epsilon^{\alpha\beta*}_{J_z}(P)\,, \tag{3.39}$$

where $\epsilon^{\nu}_{J_z}$ is the polarisation vector for a bound state with $J=1$ and $\epsilon^{\alpha\beta}_{J_z}$ the polarisation tensor for a bound state with $J=2$. The latter satisfies the following identities: $\epsilon^{\alpha\beta}_{J_z}(P)=\epsilon^{\beta\alpha}_{J_z}(P)$, $\epsilon^{\alpha}_{J_z\alpha}(P)=0$ and $P_\alpha\epsilon^{\alpha\beta}_{J_z}(P)=0$. When squaring the amplitude one can employ the tensor polarisation sum, that is given by

$$\sum_{\lambda=-2,-1,0,1,2}\epsilon^{\mu\nu}_{\lambda}(P)\epsilon^{\alpha\beta*}_{\lambda}(P) = \frac{1}{2}\left[\mathcal{Z}^{\mu\alpha}\mathcal{Z}^{\nu\beta}+\mathcal{Z}^{\mu\beta}\mathcal{Z}^{\nu\alpha}\right]-\frac{1}{3}\mathcal{Z}^{\mu\nu}\mathcal{Z}^{\alpha\beta}\,. \tag{3.40}$$

where $\mathcal{Z}^{\mu\nu}$ is the common vector polarisation sum given in Eq. A.25. Exploiting the cyclic identity of the trace and the symmetry of the individual terms, the following expressions for the remaining P-wave amplitudes are found:

$$\begin{aligned}\mathcal{M}^{\mu\nu}[{}^3P_0^c](p_1,p_2;P) &= i\frac{1}{\sqrt{4\pi M_{\mathcal{Q}}}}R_1'(0)\\ &\quad\times\mathrm{Tr}\left[\left(\gamma^\alpha\hat{\mathcal{O}}^{\mu\nu}_\alpha-\frac{\not{P}P^\alpha}{M_{\mathcal{Q}}^2}\hat{\mathcal{O}}^{\mu\nu}_\alpha\right)\frac{\not{P}-M_{\mathcal{Q}}}{2}-3\mathcal{O}^{\mu\nu}\right], \end{aligned}\tag{3.41}$$

$$\begin{aligned}\mathcal{M}^{\mu\nu}[{}^3P_1^c](p_1,p_2;P) &= -\sqrt{\frac{3}{8\pi M_{\mathcal{Q}}}}R_1'(0)\,\epsilon^{\alpha\beta\rho\sigma}\frac{P_\rho}{M_{\mathcal{Q}}}\epsilon^*_{J_z\sigma}(P)\\ &\quad\times\mathrm{Tr}\left[\gamma_\alpha\hat{\mathcal{O}}^{\mu\nu}_\beta\frac{\not{P}-M_{\mathcal{Q}}}{2}+\mathcal{O}^{\mu\nu}\frac{\not{P}}{M_{\mathcal{Q}}}\gamma_\alpha\gamma_\beta\right], \end{aligned}\tag{3.42}$$

$$\mathcal{M}^{\mu\nu}[{}^3P_2^c](p_1,p_2;P) = i\sqrt{\frac{3}{4\pi M_{\mathcal{Q}}}}R_1'(0)\,\epsilon^{\alpha\beta*}_{J_z}(P)\,\mathrm{Tr}\left[\gamma_\alpha\hat{\mathcal{O}}^{\mu\nu}_\beta\frac{\not{P}-M_{\mathcal{Q}}}{2}\right]. \tag{3.43}$$

We note that overall minus signs and factors of i are irrelevant in the end since the cross sections are proportional to the squared amplitude $\mathcal{M}\cdot\mathcal{M}^*$.

The formalism discussed in this section provides the description to compute the amplitudes of S- and P-wave quarkonium states in either a CS or CO configuration by choosing the specific hard interactions in the amplitude $\mathcal{O}$. By definition the $SU(3)$ CG coefficients are included in $\mathcal{O}$ defined in Eq. 3.13, that project out the colour configuration c of the quarkonium state. In particular, for CS and CO we have respectively that

$$\langle 3i,\bar{3}j|1\rangle = \frac{\delta_{ij}}{\sqrt{N_c}}\,,\quad \langle 3i,\bar{3}j|8\rangle = \sqrt{2}\,t^c_{ij}\,, \tag{3.44}$$

where the numerical factors come from their normalisation. Although increasingly more complicated, the amplitude for higher-L bound states could be obtained similarly, e.g. for D-waves see [59]. Moreover, since the radial wave functions at the origin and the derivatives thereof are related to the LDMEs of NRQCD as we will see, the amplitude of a particular state naturally shows their relative importance in v.

3.3 Hadroproduction in the TMD formalism

If TMD factorisation is valid for the inclusive process at hand, it follows from the correlator parametrisation in terms of light-cone coordinates that the TM of the parton p_T should be small with respect to the hard scale μ_H of the process. By momentum conservation this translates into the need for a small-q_T final state to probe TMDs in a certain process. On the other hand, if a large TM final state is generated, e.g. if the TM is generated by the recoil of another outgoing particle, one cannot probe the TM of the parton. Then the appropriate approach is to employ collinear factorisation instead to theoretically describe the process. Therefore, it is useful to define the low TM (LTM) region for which TMD factorisation is assumed and the high TM (HTM) region for which collinear factorisation is assumed. In particular, we have that $q_T \ll \mu_H$ for the LTM and $q_T \gg \Lambda_{\mathrm{QCD}}$ for the HTM, where $q_T = |\mathbf{q}_T|$. The HTM region will be addressed later in this thesis. In the remainder of this chapter the LTM differential cross sections are investigated that can be written as

$$\frac{d\sigma}{d^2\mathbf{q}_T} = \mathcal{H}(\mu_H) \times \mathcal{C}[w f_A f_B](\mathbf{q}_T) + Y(\mathbf{q}_T^2/\mu_H^2)\,, \tag{3.45}$$

where $\mathcal{C}[wf_Af_B]$ is the convolution of the nonperturbative TMD functions f_A and f_B, in particular two TMDs for a proton-proton collision, with a certain TMD weight w that is multiplied with the hard factor $\mathcal{H}$ (up to a certain order) and Y is the correction factor at large q_T (towards the HTM region). We note that for each process there can be also higher-twist terms that are power-suppressed like M_h/μ_H which are omitted in this equation.

In this section we discuss the results of [24], where they choose to inspect single $C = +$ quarkonium production in proton-proton scattering, i.e. the scalar particle η_Q, the pseudoscalar particle χ_{Q0}, and the tensor particle χ_{Q2}. The other vector quarkonia ($J = 1$) are not investigated because these states cannot be produced due to the Landau-Yang theorem [60, 61]: massive on-shell spin-1 particles cannot be produced by two massless on-shell spin-1 particles, i.e. their production from two gluons requires an additional gluon. Besides, χ_{Q1} production is suppressed due to conservation of helicity (the sign of the projection of the spin of a particle onto the direction of its momentum). We note that in Sec. 3.5 we explain how the helicities of the partonic gluons can be used to understand the specific form of the differential cross section found in double quarkonium production in proton-proton collisions, which is related to the single quarkonium production discussed here. It is important to notice that the hard scale of this process is set by the quarkonium mass: $\mu_H \sim M_Q$.

The LO α_s perturbative-QCD diagrams for quarkonium hadroproduction are shown in Fig. 3.2, where a gluon is taken out of each protons. These are the leading gluon-induced hard-scattering diagrams because every interaction introduces at least a small factor g_s in which perturbation theory is applied. As both gluons carry a colour charge, with colour index a and b, these diagrams are proportional to t^at^b. Therefore, from the trace of the colour that arises at amplitude level (see App. A), both CS and CO

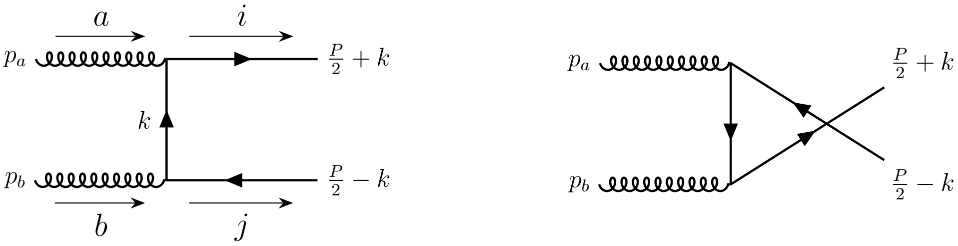

Figure 3.2: LO Feynman diagrams for $g + g \to Q + \bar{Q}$ that are constructed following the Feynman rules for QCD presented in App. A. In the left diagram the colour indices are made explicit.

states can be constructed at LO by taken into account the CG coefficients presented in Eq. 3.44. However, for this process we consider the CSM because the CO contributions for these particles are suppressed with respect to the CS contributions (see Table 3.2). Actually, for the χ_Q particles there are CO contributions of the same order v^2. Nevertheless, it can be argued that these matrix elements are suppressed reflected by the ratio $R^{\chi_{QJ}} \equiv m_Q^2 \langle \mathcal{O}^{\chi_{QJ}}[^3S_1^8]\rangle / \langle \mathcal{O}^{\chi_{QJ}}[^3P_J^1]\rangle$ [48], for which measurements are reasonably close to the estimated value from NRQCD: $R^{\chi_{c0}} \approx v^0/(2N_c) \approx 0.17$ [50]. The expectation from NRQCD is that the ratio R^{χ_b} should be comparable to R^{χ_c}. Besides, the triplet P-wave LDMEs can be related to each other by the heavy-quark spin-symmetry relations [49]

$$\langle \mathcal{O}^{\mathcal{Q}}[^3P_J^c]\rangle = (2J+1)\,\langle \mathcal{O}^{\mathcal{Q}}[^3P_0^c]\rangle + O(v^2)\,, \tag{3.46}$$

therefore, by assuming $\langle \mathcal{O}^{\chi_{Q2}}[^3S_1^8]\rangle \sim \langle \mathcal{O}^{\chi_{Q0}}[^3S_1^8]\rangle$, one can expect that $R^{\chi_{Q2}} \sim R^{\chi_{Q0}}/5$, i.e. $\langle \mathcal{O}^{\chi_{Q2}}[^3P_2^1]\rangle$ is even more dominant over $\langle \mathcal{O}^{\chi_{Q2}}[^3S_1^8]\rangle$ than the χ_{Q0} P-wave LDME. For a detailed investigation of (collinear) CO quarkonium hadroproduction we refer to [62, 63].

Employing the Feynman rules gives (see App. A) the following expressions for the amplitude $\mathcal{O}$:

$$\mathcal{O}^{\mu\nu} = -i\frac{\delta^{ab}}{\sqrt{N_c}}\frac{g_s^2}{2M_\mathcal{Q}^2}[\gamma^\nu(\not{P} - 2\not{p}_a + M_\mathcal{Q})\gamma^\mu - \gamma^\mu(\not{P} - 2\not{p}_a - M_\mathcal{Q})\gamma^\nu]\,, \tag{3.47}$$

$$\begin{aligned}\hat{\mathcal{O}}^{\mu\nu\alpha} = i\frac{\delta^{ab}}{\sqrt{N_c}}\frac{g_s^2}{M_\mathcal{Q}^2}\Bigg[&\frac{2p_a^\alpha}{M_\mathcal{Q}^2}[\gamma^\nu(\not{P} - 2\not{p}_a + M_\mathcal{Q})\gamma^\mu \\ &+ \gamma^\mu(\not{P} - 2\not{p}_a - M_\mathcal{Q})\gamma^\nu] - \gamma^\nu\gamma^\alpha\gamma^\mu - \gamma^\mu\gamma^\alpha\gamma^\nu\Bigg]\,. \end{aligned}\tag{3.48}$$

Using these in Eqs. 3.33, 3.34, 3.35, 3.41, 3.42 and 3.43, and calculating the traces we find the following non-zero amplitudes:

$$\mathcal{M}^{\mu\nu}[^1S_0^1](p_a, P) = -2\frac{\delta^{ab}}{\sqrt{N_c}}\frac{g_s^2}{\sqrt{\pi M_\mathcal{Q}^5}}\,R_0(0)\,\epsilon^{\mu\nu\rho\sigma}p_{a\rho}P_\sigma\,, \tag{3.49}$$

$$\mathcal{M}^{\mu\nu}[^3P_0^1](p_a, P) = -6\frac{\delta^{ab}}{\sqrt{N_c}}\frac{g_s^2}{\sqrt{\pi M_\mathcal{Q}^3}}\,R_1'(0)\left[g^{\mu\nu} - \frac{2}{M_\mathcal{Q}^2}P^\mu p_a^\nu\right], \tag{3.50}$$

$$\mathcal{M}^{\mu\nu}[^3P_2^1](p_a, P) = -4\frac{\delta^{ab}}{\sqrt{N_c}}\sqrt{\frac{3}{\pi M_\mathcal{Q}^3}}\,g_s^2\,R_1'(0)\,\epsilon_{J_z}^{\sigma\rho *}(P)\left[g_\sigma^\mu g_\rho^\nu - \frac{2}{M_\mathcal{Q}^2}g^{\mu\nu}p_{a\sigma}p_{a\rho}\right]. \tag{3.51}$$

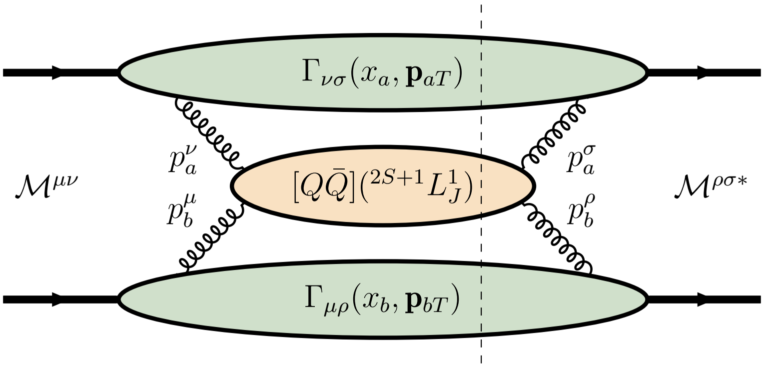

Figure 3.3: The LO gluon-induced inclusive cross section for $p + p \to [Q\bar{Q}] + X$ within TMD factorisation and the CSM. It consist out of the contraction of two TMD correlators and two amplitudes. The blob in the middle is where the quarkonium is formed from the hard scattering of the two partonic gluons.

We note that the TMD correlators in the cross section are proportional to the partonic polarisations: e.g. $\Gamma_{\nu\sigma} \sim \epsilon_\nu \epsilon_\sigma$, so that $p_a^\nu \Gamma_{\nu\sigma} \simeq (x_a P_a + \mathbf{p}_{aT})^\nu \Gamma_{\nu\sigma} = \mathbf{p}_{aT}^\nu \Gamma_{\nu\sigma}$ gives power-suppressed terms. Therefore, such terms are excluded from the amplitudes presented above.

The cross section for the process, shown in Fig. 3.3, is given by

$$\begin{aligned} d\sigma = {}& \frac{1}{2s} \frac{1}{N_g} \frac{d^3 P}{(2\pi)^3 2P^0} \int dx_a \, dx_b \, d^2\mathbf{p}_{aT} \, d^2\mathbf{p}_{bT} \, (2\pi)^4 \delta^4(p_a + p_b - P) \\ & \times \frac{1}{x_a^2 x_b^2} \Gamma_{\nu\sigma}(x_a, \mathbf{p}_{aT}) \, \Gamma_{\mu\rho}(x_b, \mathbf{p}_{bT}) \, \mathcal{M}^{\mu\nu}(p_a, P) \, \mathcal{M}^{\rho\sigma *}(p_a, P) \, , \end{aligned} \tag{3.52}$$

where $s = (P_a + P_b)^2$ is the total energy squared in the hadronic centre-of-mass frame, and the average over the colour state of the incoming gluons is taken: $N_g = N_c^2 - 1$. We employ the TMD gluon correlator for an unpolarised proton twice given in Eq. 2.25, which incorporates a factor of $1/2$ that accounts for the averaging over the initial spin states of the gluon. Considering light-cone kinematics in which $p_a^- = p_b^+ = 0$ (with a slight off-shellness for the gluons) and renaming the quarkonium momentum $P \equiv q$ for comparison with the process discussed hereafter, we re-express the delta function as

$$\begin{aligned} \delta^4(p_a + p_b - q) &= \delta(p_a^+ - q^+) \, \delta(p_b^- - q^-) \, \delta^2(\mathbf{p}_{aT} + \mathbf{p}_{bT} - \mathbf{q}_T) \\ &\approx \frac{2}{s} \, \delta\bigg(x_a - \frac{M_\mathcal{Q}}{\sqrt{s}} e^y \bigg) \, \delta\bigg(x_b - \frac{M_\mathcal{Q}}{\sqrt{s}} e^{-y} \bigg) \, \delta^2(\mathbf{p}_{aT} + \mathbf{p}_{bT} - \mathbf{q}_T) + O\bigg(\frac{q_T^2}{M_\mathcal{Q}^2} \bigg) \, , \end{aligned} \tag{3.53}$$

where y is the rapidity of the produced bound state with respect to the axis of the colliding hadrons. The phase-space element can be rewritten as:

$$\frac{d^3 q}{(2\pi)^3 2q^0} = \frac{dq^3 \, d^2\mathbf{q}_T}{(2\pi)^3 2q^0} = \frac{1}{16\pi^3} \, dy \, d^2\mathbf{q}_T \, . \tag{3.54}$$

Introducing the following LO relations from NRQCD [49, 59]

$$\frac{N_c}{2\pi} |R_0(0)|^2 = \frac{1}{2J+1} \langle \mathcal{O}^\mathcal{Q}[^{2S+1}S_J^1] \rangle \, , \tag{3.55}$$

$$\frac{3N_c}{2\pi}\,|R_1'(0)|^2 = \frac{1}{2J+1}\,\langle \mathcal{O}^{\mathcal{Q}}[{}^{2S+1}P_J^1]\rangle\,, \tag{3.56}$$

we find the differential cross sections at LO in α_s, v and leading twist

$$\frac{d\sigma(\eta_Q)}{dy\,d^2\mathbf{q}_T} = \frac{2}{9}\,\frac{\pi^3\alpha_s^2}{M_Q^3 s}\,\langle \mathcal{O}^{\eta_Q}[{}^1S_0^1]\rangle\,\mathcal{C}[f_1^g f_1^g]\,[1-R(\mathbf{q}_T^2)]\,, \tag{3.57}$$

$$\frac{d\sigma(\chi_{Q0})}{dy\,d^2\mathbf{q}_T} = \frac{8}{3}\,\frac{\pi^3\alpha_s^2}{M_Q^5 s}\,\langle \mathcal{O}^{\chi_{Q0}}[{}^3P_0^1]\rangle\,\mathcal{C}[f_1^g f_1^g]\,[1+R(\mathbf{q}_T^2)]\,, \tag{3.58}$$

$$\frac{d\sigma(\chi_{Q2})}{dy\,d^2\mathbf{q}_T} = \frac{32}{45}\,\frac{\pi^3\alpha_s^2}{M_Q^5 s}\,\langle \mathcal{O}^{\chi_{Q2}}[{}^3P_2^1]\rangle\,\mathcal{C}[f_1^g f_1^g]\,, \tag{3.59}$$

where $N_c = 3$ and:

$$R(\mathbf{q}_T^2) = \frac{\mathcal{C}[w_2 h_1^{\perp g} h_1^{\perp g}]}{\mathcal{C}[f_1^g f_1^g]}\,. \tag{3.60}$$

We introduced the convolutions of the TMDs as

$$\begin{aligned}\mathcal{C}[wff](x_a, x_b, \mathbf{q}_T^2) = \int d^2\mathbf{p}_{aT} \int d^2\mathbf{p}_{bT}\, \delta^2(\mathbf{p}_{aT} + \mathbf{p}_{bT} - \mathbf{q}_T)&\\ \times\, w(\mathbf{p}_{aT}, \mathbf{p}_{bT})\, f(x_a, \mathbf{p}_{aT}^2)\, f(x_b, \mathbf{p}_{bT}^2)\,,&\end{aligned} \tag{3.61}$$

with the TMD weight

$$w_2(\mathbf{p}_{aT}, \mathbf{p}_{bT}) = \frac{1}{4M_h^4}\left[2(\mathbf{p}_{aT}\cdot\mathbf{p}_{bT})^2 - \mathbf{p}_{aT}^2\mathbf{p}_{bT}^2\right], \tag{3.62}$$

which comes from the contraction of the tensor structures in front of $h_1^{\perp g}$ in the definition of the correlator. We note that the contribution of linearly polarised gluons described by $h_1^{\perp g}$ is suppressed in χ_{Q2} production. As a consequence, in leading order in v^2 the ratio of χ_{Q0} to χ_{Q2} cross section yields a direct probe of the ratio $R(\mathbf{q}_T^2)$. Other convolutions of TMDs (that have also different weights), and different ratios of them, emerge in this process by considering polarised protons, while the hard factors stay the same. These are studied in [64]. We also mention that the same convolutions occur in Higgs production which have been investigated (using TMD evolution) in [65–67].

3.4 Photo- and electroproduction

Single quarkonium production in electroproduction, $e(l) + p(P_h) \to e'(l') + [Q\bar{Q}](P) + X$, within the TMD formalism is similar to the computation presented in the previous section. We can just modify Fig. 3.2 slightly: taking $p_b \to p$ and $p_a \to q = l - l'$, an off-shell photon with its energy determined by the difference of the incoming and outgoing electron defined by $q^2 = -Q^2$. Since photoproduction is the limiting case in which the photon becomes on-shell, i.e. $Q = 0$, its results follow directly from the electroproduction results presented here. Particularly, we discuss the results of [26].

The amplitude $\mathcal{O}$ becomes

$$\mathcal{O}^{\mu\nu} = i\sqrt{2}\,\frac{e\,e_Q\,g_s\,\delta^{ab}}{2(M_{\mathcal{Q}}^2+Q^2)}[\gamma^\nu(\not{p}-\not{q}+M_{\mathcal{Q}})\gamma^\mu-\gamma^\mu(\not{p}-\not{q}-M_{\mathcal{Q}})\gamma^\nu]\,, \tag{3.63}$$

$$\begin{aligned}\hat{\mathcal{O}}^{\mu\nu\alpha} &= -i\sqrt{2}\,\frac{e\,e_Q\,g_s\,\delta^{ab}}{(M_{\mathcal{Q}}^2+Q^2)}\left[\frac{2p^\alpha}{(M_{\mathcal{Q}}^2+Q^2)}[\gamma^\nu(\not{q}-\not{p}-M_{\mathcal{Q}})\gamma^\mu\right.\\ &\quad\left.+\gamma^\mu(\not{q}-\not{p}+M_{\mathcal{Q}})\gamma^\nu]-\gamma^\nu\gamma^\alpha\gamma^\mu-\gamma^\mu\gamma^\alpha\gamma^\nu\right]\,,\end{aligned} \tag{3.64}$$

where e_Q is the fractional electric charge of the heavy quark. We note that the hard scale of electroproduction is not only determined by the quarkonium mass, but also by the photon virtuality. By comparing Eqs. 3.63 and 3.47, as well as Eqs. 3.64 and 3.48, we find that $\mu_H^2 \sim M_{\mathcal{Q}}^2 + Q^2$. However, a more detailed discussion of this relationship, and in general the hard scale dependence of processes, is provided in Ch. 4. In this case we produce CO quarkonium states by employing Eq. 3.44 instead of CS states because the LO hard scattering only provides one colour matrix, i.e. producing CS would result in the trace of just one colour matrix giving zero for all amplitudes. From Table 3.2 we find that these computations are of particular interest for producing vector quarkonium, e.g. the J/ψ and the Υ, although suppressed in v as compared to the CS LDMEs. At higher-order α_s^2 it is possible to produce the ${}^3S_1$ CS state for these quarkonia. More precisely, the CS contribution is suppressed relatively to the CO by a perturbative coefficient of the order α_s/π. Hence, together with the NRQCD scaling rules the CO configuration is enhanced by a factor $v^3\pi/\alpha_s$, already around 2 for $Q = 3$ GeV and grows with increasing Q. Furthermore, it is known that for large values of z, defined in Eq. 3.71, the CS term becomes negligible due to the dominance of the CO term [68]. Because the kinematical variable z is fixed to 1 in this analysis as we will see, it allows for a study concerning only CO contributions.

Similar as before, the non-zero amplitudes are found to be

$$\mathcal{M}^{\mu\nu}[{}^1S_0^8](q,P) = 2\sqrt{\frac{C_{S,0}}{M_{\mathcal{Q}}}}\,\delta^{ab}\,\frac{e\,e_Q\,g_s}{M_{\mathcal{Q}}^2+Q^2}\,\epsilon^{\mu\nu\rho\sigma}q_\rho P_\sigma\,, \tag{3.65}$$

$$\mathcal{M}^{\mu\nu}[{}^3P_0^8](q,P) = 2\sqrt{\frac{C_{P,0}}{3M_{\mathcal{Q}}}}\,\delta^{ab}\,\frac{e\,e_Q\,g_s}{M_{\mathcal{Q}}^2+Q^2}\,\frac{3M_{\mathcal{Q}}^2+Q^2}{M_{\mathcal{Q}}}\left[g^{\mu\nu}-\frac{2}{M_{\mathcal{Q}}^2+Q^2}P^\mu q^\nu\right], \tag{3.66}$$

$$\begin{aligned}\mathcal{M}^{\mu\nu}[{}^3P_1^8](q,P) &= 4i\sqrt{\frac{C_{P,1}}{2M_{\mathcal{Q}}}}\,\delta^{ab}\,\frac{e\,e_Q\,g_s}{(M_{\mathcal{Q}}^2+Q^2)^2}P^\rho\epsilon_{J_z}^{\sigma *}\frac{Q^2}{M_{\mathcal{Q}}^2}\\ &\quad\times\left[(M_{\mathcal{Q}}^2+Q^2)\epsilon_{\rho\sigma}{}^{\mu\nu}+2\epsilon_{\rho\sigma\alpha\beta}q^\alpha(P^\mu g^{\beta\nu}-g^{\beta\mu}P^\nu)\right],\end{aligned} \tag{3.67}$$

$$\begin{aligned}\mathcal{M}^{\mu\nu}[{}^3P_2^8](q,P) &= 4\sqrt{C_{P,2}M_{\mathcal{Q}}}\,\delta^{ab}\,\frac{e\,e_Q\,g_s}{M_{\mathcal{Q}}^2+Q^2}\,\epsilon_{J_z}^{\sigma\rho *}\\ &\quad\times\left[g_\sigma^\mu g_\rho^\nu-\frac{2}{M_{\mathcal{Q}}^2+Q^2}q_\sigma(g^{\mu\nu}q_\rho+P^\mu g_\rho^\nu-g_\rho^\mu P^\nu)\right],\end{aligned} \tag{3.68}$$

where we used $N_c = 3$ and defined:

$$C_{S,J} \equiv \frac{1}{4\pi}(N_c^2-1)\,|R_0(0)|^2 = \frac{1}{2J+1}\langle\mathcal{O}^{\mathcal{Q}}[{}^{2S+1}S_J^8]\rangle\,, \tag{3.69}$$

$$C_{P,J} \equiv \frac{3}{4\pi}(N_c^2-1)\,|R_1'(0)|^2 = \frac{1}{2J+1}\langle \mathcal{O}^{\mathcal{Q}}[{}^{2S+1}P_J^8]\rangle\,. \tag{3.70}$$

We note that latter equations are equivalent to Eq. 3.55 and Eq. 3.56 upon replacing $(N_c^2-1) \to 2N_c$ for CS states.

Before we continue with calculating the differential cross section, we remark that single quarkonium production in electron-proton scattering has some advantages with respect to proton-proton scattering. Namely, in this process we only probe one TMD at a time instead of two as there is only one proton involved. Moreover, due to the second hard scale Q, that is determined by the electron, we can investigate the process for a whole range of hard scales instead of only at the mass of the quarkonium that is produced. It was already mentioned in Sec. 2.3 that the TMDs like the PDFs have an implicit scale dependence, hence, with this processes one can probe the TMDs at different scales and thus use it to study how the TMDs evolve with this scale. TMD evolution is discussed in detail in Sec. 4.2.

However, the process studied here has also disadvantages. Aside from the fact that the peak in the spectrum from CO contributions has not been observed in any data and that at $z=1$ a diffractive signal is obtained [2] (first discussed in [69]), a further complication arises from the large uncertainties in the CO LDMEs. Moreover, TMD factorised expressions have to take into account the TMDShFs, which include smearing effects that can arise in the formation of quarkonium [70, 71]. This non-perturbative hadronic quantity describes the transition from the $Q\bar{Q}$ pair to a bound quarkonium state, i.e. it not only contains the formation of the bound state in terms of a LDME, but also the TM effects that can arise to produce the final state hadron, which generally change the momentum of the quarkonium. In particular, the required soft-gluon emission in CO quarkonium production is the reason for considering final state smearing to occur in this process, while at least for LO CS production the TMDShFs are expected to be absent. The complete relation between the TMDShFs and the LDMEs of NRQCD is not yet known as discussed in Ch. 5, where the LO TMDShFs for single quarkonium in photo- and electroproduction are investigated. As a first step we consider the transition to the colourless final state as infinitely narrow, i.e. as a delta function in TM, thereafter, we add the TMDShFs which convolute with TMDs. This process can therefore provide insight to the poorly known gluon TMDs, as well as to the unknown TMDShFs of which the CO LDMEs are part. A comparison of this process to open heavy-quark pair production in electron-proton collisions (neglecting final state smearing), ideally performed with the same kinematics, has been proposed as a approach to investigate the CO LDMEs as well [26, 72].

Since quarkonium production in the electron-proton scattering is similar to conventional semi-inclusive deep inelastic scattering (SIDIS), $e+p \to e' + h + X$, we employ the following kinematical variables

$$x_B = \frac{Q^2}{2P_h\cdot q}\,, \quad y = \frac{P_h\cdot q}{P_h\cdot l}\,, \quad z = \frac{P_h\cdot P}{P_h\cdot q}\,, \tag{3.71}$$

were x_B is the Bjorken-x variable, y the inelasticity variable and z the elasticity variable, the fraction of momentum of the (virtual) photon carried into the final state. We choose the reference frame such that both the photon in the reaction and the incoming proton move along the $\hat{z}$ axis. The azimuthal angle ϕ_T of the outgoing quarkonium is measured with respect to the lepton scattering plane ($\phi_l = \phi_{l'} = 0$).

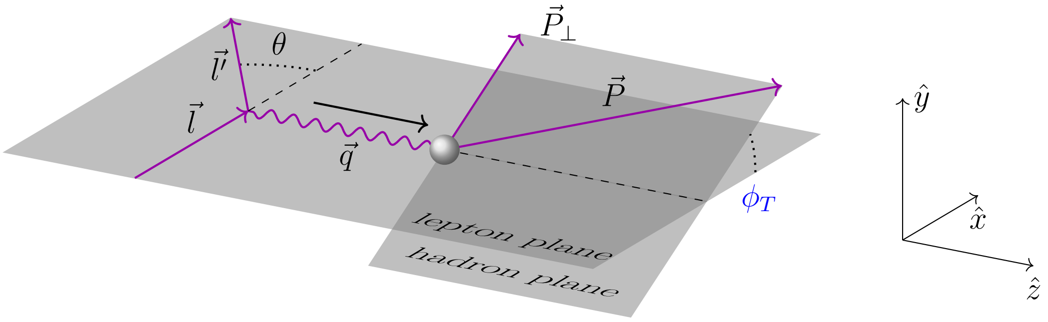

Figure 3.4: Visualisation of the azimuthal angle ϕ_T, the scattering angle θ, and the lepton and hadron scattering planes of quarkonium production in electron-proton collisions in the frame where the photon and proton have no TM.

Moreover, the electron scatters with an angle θ. Fig. 3.4 provides a visual overview of these planes and angles.

Compared to proton-proton collisions, the cross section is slightly altered for electron-proton collisions as shown in Fig. 3.5. We have now a leptonic tensor instead of a second TMD gluon correlator $\Gamma_{\nu\sigma}$. Therefore, the differential cross section with an extra outgoing electron becomes

$$
\begin{aligned}
d\sigma = {} & \frac{1}{2s}\,\frac{1}{N_g}\,\frac{d^3l'}{(2\pi)^3 2l'^0}\,\frac{d^3P}{(2\pi)^3 2P^0}\int dx\, d^2\mathbf{p}_T\,(2\pi)^4\delta^4(q+p-P) \\
& \times \frac{1}{x^2Q^4}\,L(l,q)_{\nu\sigma}\,\Gamma_{\mu\rho}(x,\mathbf{p}_T)\,\mathcal{M}^{\mu\nu}(q,P)\,\mathcal{M}^{\rho\sigma *}(q,P)\,, \qquad (3.72)
\end{aligned}
$$

where $s = (l+P_h)^2 \approx 2P_h\cdot l = 2P_h\cdot q/y = Q^2/(x_B y)$ is the total invariant mass squared and $Q^2 \approx 2\,l\cdot l'$. In addition, the invariant mass squared of the photon-target system is defined as $W^2 = (q+P_h)^2$, and can be expressed in terms of the other invariants: $W^2 = Q^2(1-x_B)/x_B = (1-x_B)ys$. The factor Q^{-4} in the differential cross section comes from the squared photon propagator. For an unpolarised massless electron, the leptonic tensor is given by (see e.g. [73])

$$
L^{\mu\nu}(l,q) = \frac{1}{2}e^2\,\mathrm{Tr}[\not{l}\gamma_\mu \not{l}'\gamma_\nu] = e^2[-g^{\mu\nu}Q^2 + 2(l^\mu l'^\nu + l^\nu l'^\mu)]\,, \qquad (3.73)
$$

where the factor $1/2$ comes from averaging over the initial spin states of the electron. The four-momenta P_h and q in light-cone coordinates are more involved than in the hadroproduction case. They can be written as:

$$
P_h^\mu = n_+^\mu + \frac{M_h^2}{2}n^\mu \approx n_+^\mu\,, \qquad q^\mu = -x_B n_+^\mu + \frac{Q^2}{2x_B}n^\mu \approx -x_B P_h^\mu + (P_h\cdot q)n^\mu\,. \qquad (3.74)
$$

Hence, we perform a decomposition of all the momenta in terms of $n_+^\mu = P_h^\mu$ (i.e. $P_h^+ = 1$ in Eq. 2.8) and $n^\mu = n_-^\mu = (q^\mu + x_B P_h^\mu)/P_h\cdot q$. The leptonic momenta can be written as

$$
l^\mu = \frac{1-y}{y}x_B P_h^\mu + \frac{1}{y}\frac{Q^2}{2x_B}n^\mu + \frac{\sqrt{1-y}}{y}Q\,\hat{l}_\perp^\mu\,, \qquad (3.75)
$$

$$
l'^\mu = \frac{1}{y}x_B P_h^\mu + \frac{1-y}{y}\frac{Q^2}{2x_B}n^\mu + \frac{\sqrt{1-y}}{y}Q\,\hat{l}_\perp^\mu\,, \qquad (3.76)
$$

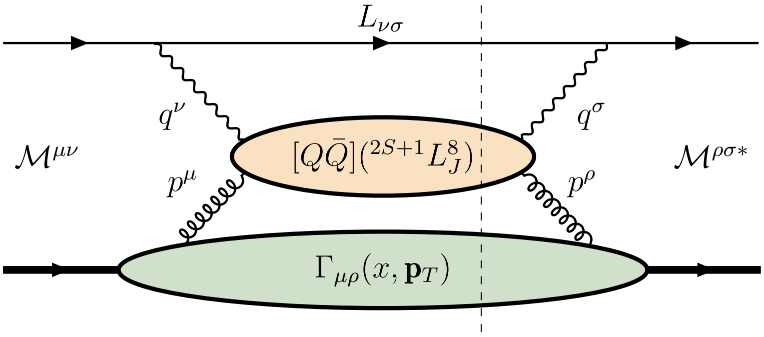

Figure 3.5: The LO gluon-induced inclusive cross section for $e + p \to e' + [Q\bar{Q}] + X$ within TMD factorisation and the COM. It is constructed by the contraction of the TMD correlator, the leptonic tensor and two amplitudes.

where $\hat{l}_\perp^\mu$ is the unit vector in the transverse direction of l with respect to the photon-proton axis. Similarly, the gluon momentum can be expanded as:

$$p^\mu = xP_h^\mu + p_T^\mu + (p \cdot P_h - xM_h^2)n^\mu \approx xP_h^\mu + p_T^\mu \,. \tag{3.77}$$

Lastly, the momentum of the quarkonium state is written as

$$P^\mu = z(P_h \cdot q)n^\mu + \frac{M_\mathcal{Q}^2 + \mathbf{P}_\perp^2}{2z\, P_h \cdot q} P_h^\mu + P_\perp^\mu \,, \tag{3.78}$$

where we introduced the subscript $\perp$ for the TM of the quarkonium. This distinction is made to highlight the difference with respect to the reference frame where the photon has TM q_T, i.e. the frame in which the hadrons do not possess TM. We note that all these momentum expressions above can be easily checked by squaring them.

As before, we evaluate first the delta function

$$\begin{aligned} \delta^4(p + q - P) &\approx \delta\left(x - x_B - \frac{M_\mathcal{Q}^2}{yzs}\right) \delta\big(P_h \cdot q - z(P_h \cdot q)\big)\, \delta^2(\mathbf{p}_T - \mathbf{P}_\perp) \\ &= \frac{2}{ys}\, \delta\left(x - x_B - \frac{M_\mathcal{Q}^2}{yzs}\right) \delta(1 - z)\, \delta^2(\mathbf{p}_T - \mathbf{P}_\perp) \,, \end{aligned} \tag{3.79}$$

from which it follows that:

$$x = x_B + \frac{M_\mathcal{Q}^2}{ys} = \frac{M_\mathcal{Q}^2 + Q^2}{ys} = x_B \frac{M_\mathcal{Q}^2 + Q^2}{Q^2} \,. \tag{3.80}$$

Moreover, since $z = 1$ the TM of the photon and the quarkonium in the two frames are equal: $q_T = P_\perp$. The phase-space elements can be rewritten as

$$\frac{d^3P}{(2\pi)^3 2P^0} = \frac{1}{16\pi^3} \frac{dz}{z} d^2\mathbf{P}_\perp \,, \tag{3.81}$$

and

$$\frac{d^3l'}{(2\pi)^3 2l'^0} = \frac{l'^0 dl'^0 d\Omega}{16\pi^3} = \frac{1}{16\pi^2}\, sy\, dx_B\, dy \,, \tag{3.82}$$

where $\Omega = 4\pi \sin^2(\theta/2)$ is the solid angle with apex angle 2θ. The latter equation is most conveniently derived in the target hadron rest frame where $Q^2 = 2l^0 l'^0(1-\cos\theta)$ such that $l'^0 = s(1-y)/(2M_h) = syx_B/\big(4l^0 \sin^2(\theta/2)\big)$.

With all these ingredients we can evaluate the unpolarised cross section in terms of gluon TMDs again. Specifically, we find for J/ψ production

$$\begin{aligned}\frac{d\sigma(J/\psi)}{dx_B\,dy\,dz\,d\mathbf{q}_T^2\,d\phi_T} = \frac{\alpha}{yQ^2}\Big\{&[1+(1-y)^2]\,\mathcal{F}_{UU,T} + 4(1-y)\,\mathcal{F}_{UU,L} \\ &+ 4(1-y)\cos 2\phi_T\,\mathcal{F}_{UU}^{\cos 2\phi_T}\Big\}\,,\end{aligned} \tag{3.83}$$

where,

$$\begin{aligned}\mathcal{F}_{UU,T} = 2\pi^2 &\frac{\alpha\alpha_s e_c^2}{M_\mathcal{Q}(M_\mathcal{Q}^2+Q^2)}\bigg[\langle\mathcal{O}^{J/\psi}[{}^1S_0^8]\rangle \\ &+ 4\frac{(7M_\mathcal{Q}^4+2M_\mathcal{Q}^2Q^2+3Q^4)}{M_\mathcal{Q}^2(M_\mathcal{Q}^2+Q^2)^2}\langle\mathcal{O}^{J/\psi}[{}^3P_0^8]\rangle\bigg]\,\delta(1-z)\,f_1^g(x,\mathbf{p}_T^2)\bigg|_{\mathbf{p}_T=\mathbf{q}_T}\,,\end{aligned} \tag{3.84}$$

$$\begin{aligned}\mathcal{F}_{UU,L} = 2\pi^2 &\frac{\alpha\alpha_s e_c^2}{M_\mathcal{Q}(M_\mathcal{Q}^2+Q^2)}\bigg[\frac{16Q^2}{(M_\mathcal{Q}^2+Q^2)^2}\langle\mathcal{O}^{J/\psi}[{}^3P_0^8]\rangle\bigg] \\ &\times\delta(1-z)\,f_1^g(x,\mathbf{p}_T^2)\bigg|_{\mathbf{p}_T=\mathbf{q}_T}\,,\end{aligned} \tag{3.85}$$

$$\begin{aligned}\mathcal{F}_{UU}^{\cos 2\phi_T} = \pi^2 &\frac{\alpha\alpha_s e_c^2}{M_\mathcal{Q}(M_\mathcal{Q}^2+Q^2)}\bigg[-\langle\mathcal{O}^{J/\psi}[{}^1S_0^8]\rangle \\ &+ 4\frac{3M_\mathcal{Q}^2-Q^2}{M_\mathcal{Q}^2(M_\mathcal{Q}^2+Q^2)}\langle\mathcal{O}^{J/\psi}[{}^3P_0^8]\rangle\bigg]\,\delta(1-z)\,\frac{\mathbf{p}_T^2}{2M_h^2}\,h_1^{\perp g}(x,\mathbf{p}_T^2)\bigg|_{\mathbf{p}_T=\mathbf{q}_T}\,,\end{aligned} \tag{3.86}$$

with $M_\mathcal{Q} = M_{J/\psi}$. Here we employed $\alpha = e^2/4\pi$ and the heavy-quark spin symmetry relations presented in Eq. 3.46. The first and second subscripts of the structure functions $\mathcal{F}$ denote the polarisation of the initial electron and proton, respectively, while the third one when present specifies the polarisation of the exchanged virtual photon; whenever relevant the angle associated to the function is added. We note that the dot product $q_T \cdot l \propto |\mathbf{q}_T|\cos\phi_T$ together with another term $q_T^2 = -\mathbf{q}_T^2$ generates the angular term $\cos 2\phi_T$ in the cross section.

As explained, the transition from the CO state into the true colourless hadronic final state is not fully described by the CO LDMEs solely. Including the general TMDShFs $\Delta^{[n]}$ in the differential cross section we obtain the following expressions for the structure functions

$$\mathcal{F}_{UU,T} = \sum_n \mathcal{H}_T^{[n]}\,\mathcal{C}[f_1^g\Delta^{[n]}](x,z,\mathbf{q}_T^2)\,, \tag{3.87}$$

$$\mathcal{F}_{UU,L} = \sum_n \mathcal{H}_L^{[n]}\,\mathcal{C}[f_1^g\Delta^{[n]}](x,z,\mathbf{q}_T^2)\,, \tag{3.88}$$

$$\mathcal{F}_{UU}^{\cos 2\phi_T} = \sum_n \mathcal{H}_{\cos 2\phi_T}^{[n]}\,\mathcal{C}[wh_1^{\perp g}\Delta_h^{[n]}](x,z,\mathbf{q}_T^2)\,, \tag{3.89}$$

where we have introduced the convolutions

$$\begin{aligned}\mathcal{C}[f_1^g \Delta^{[n]}](x,z,\mathbf{q}_T^2) &= \int d^2\mathbf{p}_T \int d^2\mathbf{k}_T\, \delta^2(\mathbf{p}_T + \mathbf{k}_T - \mathbf{q}_T) \\ &\quad \times f_1^g(x,\mathbf{p}_T^2)\, \Delta^{[n]}(z,\mathbf{k}_T^2)\,, \qquad (3.90)\\ \mathcal{C}[w h_1^{\perp g} \Delta_h^{[n]}](x,z,\mathbf{q}_T^2) &= \int d^2\mathbf{p}_T \int d^2\mathbf{k}_T\, \delta^2(\mathbf{p}_T + \mathbf{k}_T - \mathbf{q}_T) \\ &\quad \times w(\mathbf{p}_T,\mathbf{k}_T)\, h_1^{\perp g}(x,\mathbf{p}_T^2)\, \Delta_h^{[n]}(z,\mathbf{k}_T^2)\,, \qquad (3.91)\end{aligned}$$

similar to Eq. 3.61. The hard factors $\mathcal{H}$ can be easily extracted from Eqs. 3.84, 3.85 and 3.86. The TMD weight function $w(\mathbf{p}_T,\mathbf{k}_T)$ is constructed by contracting the TM of the produced quarkonium (hence the difference with respect to Eq. 3.62) with the tensor structure of the gluon correlator

$$w(\mathbf{p}_T,\mathbf{k}_T) = \frac{1}{2M_h^2(\mathbf{p}_T+\mathbf{k}_T)^2}\left[2(\mathbf{p}_T\cdot\mathbf{k}_T)^2 + \mathbf{p}_T^2\big(\mathbf{p}_T^2 - \mathbf{k}_T^2\big)\right], \qquad (3.92)$$

such that when $q_T = p_T$, one retrieves Eq. 3.86.

The TMDShFs can be thought of as a generalisation of the LDMEs from collinear factorisation in the HTM region. We have added the superscript h in Eq. 3.89 as we consider that the TMDShFs that convolute with $h_1^{\perp g}$ could in principal be unequal to the ones that convolute with f_1^g. The naive expectation is that the TMDShFs are proportional to the LDMEs, at least at LO:

$$\Delta_{(h)}^{[n]}(z,\mathbf{k}_T^2) \equiv \langle \mathcal{O}^{\mathcal{Q}}[n]\rangle\, \Delta_{(h)}(z,\mathbf{k}_T^2)\,. \qquad (3.93)$$

Although $z = 1$ for the process studied in this section, we note that we have included the corresponding delta function in the final state TMDShFs due to their comparability to FFs that depend on z (see Eq. 3.10), which is discussed later in this thesis. In absence of smearing $\Delta_{(h)}(z,\mathbf{k}_T^2) = \delta^2(\mathbf{k}_T)\,\delta(1-z)$ in Eq. 3.93, such that the previous equations without the TMDShFs are recovered.

The weighted average of the angle ϕ_T in the differential cross section can be calculated as follows:

$$\begin{aligned}\langle \cos 2\phi_T\rangle &= \frac{\int d\phi_T \cos 2\phi_T\, d\sigma(\phi_T)}{\int d\phi_T\, d\sigma(\phi_T)} \\ &= \frac{1}{2}\, \frac{\sum_n 4(1-y)\, \mathcal{H}^{[n]}_{\cos 2\phi_T}\, \mathcal{C}[w h_1^{\perp g}\Delta_h^{[n]}]}{\sum_n \left([1+(1-y)^2]\, \mathcal{H}_T^{[n]} + 4(1-y)\, \mathcal{H}_L^{[n]}\right) \mathcal{C}[f_1^g \Delta^{[n]}]}\,. \qquad (3.94)\end{aligned}$$

This observable is interesting to study experimentally alongside the cross section, as it also provides insights into the TMDShFs and the TMDs. Indeed, the azimuthal asymmetry arises due to the presence of linearly polarised gluons inside an unpolarised proton. In absence of smearing we can write

$$\langle \cos 2\phi_T\rangle = \frac{2(1-y)\, \mathcal{F}_{UU}^{\cos 2\phi_T}}{[1+(1-y)^2]\, \mathcal{F}_{UU,T} + 4(1-y)\, \mathcal{F}_{UU,L}}\, R \equiv \mathcal{A}\, R\,, \qquad (3.95)$$

with

$$R \equiv \frac{\mathcal{C}[w h_1^{\perp g}\Delta_h]}{\mathcal{C}[f_1^g \Delta]} \Rightarrow \frac{\mathbf{q}_T^2}{2M_h^2}\frac{h_1^{\perp g}}{f_1^g}\,, \qquad (3.96)$$

Table 3.3: LMDE values for J/ψ production from various studies. The charm quark mass in this table is set to 1.5 GeV.

	$\langle \mathcal{O}^{J/\psi}[^3S_1^1]\rangle$ (GeV^3)	$\langle \mathcal{O}^{J/\psi}[^1S_0^8]\rangle$ (10^{-2} GeV^3)	$\langle \mathcal{O}^{J/\psi}[^3S_1^8]\rangle$ (10^{-2} GeV^3)	$\langle \mathcal{O}^{J/\psi}[^3P_0^8]\rangle/m_c^2$ (10^{-2} GeV^3)
BK [74]	1.32	4.50 ± 0.72	0.312 ± 0.093	-0.538 ± 0.16
CMSWZ [75]	1.16	8.9 ± 0.98	0.30 ± 0.12	0.56 ± 0.21
SV [76]	1.2	1.8 ± 0.87	0.13 ± 0.13	1.8 ± 0.87
BCKL [77]	-	9.9 ± 2.2	1.1 ± 1.0	0.49 ± 0.44

where we have redefined the structure functions, i.e. we removed the TMDs from their definitions given in Eqs. 3.84, 3.85 and 3.86 (including the $\mathbf{q}_T^2/(2M_h^2)$ term from $\mathcal{F}_{UU}^{\cos 2\phi_T}$). We note that the positivity bound outlined in Eq. 2.48 implies that $|R| \leq 1$.

For numerical calculations different extractions of J/ψ LDMEs are available. Table 3.3 provides a summary of these values from selected studies, that are derived from fits to data from Tevatron, Relativistic Heavy Ion Collider (RHIC), and LHC. Most of these results are obtained from NLO analyses, except for the SV set, which is based on a LO calculation. We note that, although the BK set is the only one that describes J/ψ photoproduction data well [2], the negative value of $\langle \mathcal{O}^{J/\psi}[^3P_0^8]\rangle$ results in negative cross sections for certain values of Q when used in the LO calculation presented in this section, and is therefore not utilised by us. Moreover, the relevant CO LDME values from BCKL are comparable to those from CMSWZ, but exhibit larger uncertainties.

In Fig. 3.6 the behaviour of the asymmetry hard factor $\mathcal{A}$ defined in Eq. 3.95, in case no smearing occurs, is shown as a function of y, where we used the central values of the CMSWZ LDMEs as an example and $M_{J/\psi} = 3.1$ GeV (employed throughout the rest of the thesis). $|\mathcal{A}| = |\langle \cos 2\phi_T\rangle|$ when the positivity bound is saturated, i.e. it actually is the upper bound of the average azimuthal angle for a specific y. In general, it turns out that $\mathcal{A}$ depends very strongly on the specific set of CO LDMEs adopted, but it always vanish in the limit $y \to 1$ and maximises when $y \to 0$. Since $|\langle \cos 2\phi_T\rangle| \leq 1$ and $|R| \leq 1$, the LDMEs must be such that $|\mathcal{A}| \leq 1$ and the denominator of $\mathcal{A}$ should be greater or equal to zero, which are important constraints to impose on LDME extractions at EIC. These constraints are not satisfied by the BK set for $2.5M_Q^2 \gtrsim Q^2$, but that seems a problem of applying LDMEs that were obtained from a NLO analysis in a LO computation.

It should be noted that, in our investigations, we indirectly sum over the quarkonium polarisations in the calculation of the cross sections for both proton-proton and electron-proton collisions by projecting the amplitudes of the quarkonium states onto $|J, J_z\rangle$. Although we do not present any numerical predictions for polarised quarkonium production reactions in this thesis, we explain some polarised LO electron-proton collisions to unpolarised as well as polarised J/ψ in App. B for completeness. In such calculations similar hard factors like $\mathcal{A}$ can be determined for J/ψ (or for Υ with the appropriate LDMEs).

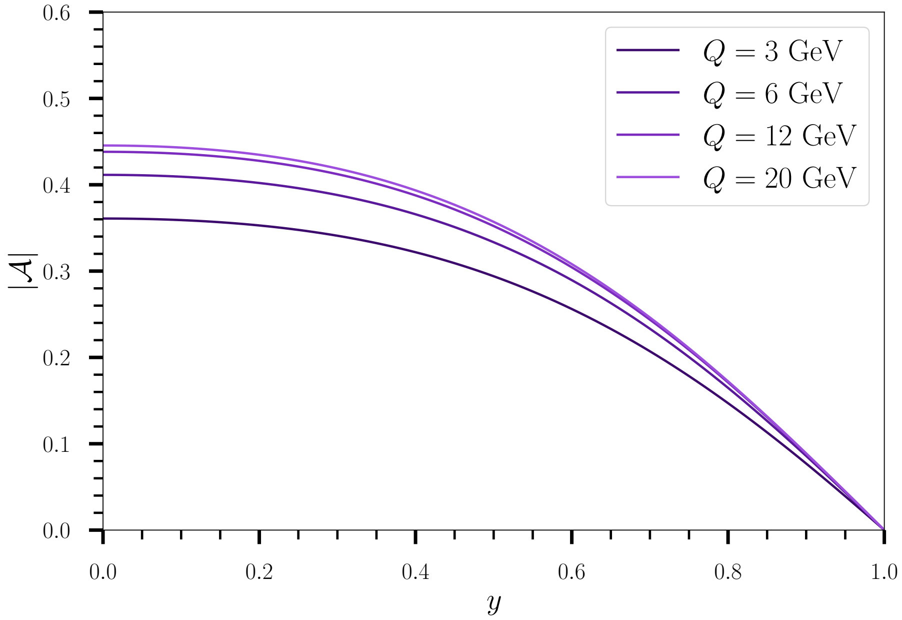

Figure 3.6: The absolute value of the asymmetry hard factor $\mathcal{A}$ as a function of y in unpolarised J/ψ electroproduction. Here we employed the central values of the CMSWZ LDMEs [75].

3.5 Quarkonium-pair hadroproduction

The last process we investigate is this thesis is quarkonium-pair production in unpolarised proton-proton collisions in the TMD regime where we employ again the CSM. The differential cross section of the reaction of interest is shown in Fig. 3.7. Not only are CO contributions suppressed in v since both the CO and the CS yields appear at the same order in α_s, they can also likely break TMD factorisation. Namely, in the case of CO production one expects gluonic interactions between the initial and final state. Besides, it is expected that for CO TM effects from soft-gluon radiation need to be taken into account by TMDShFs, like for TMD single quarkonium production in electron-proton collisions. So, although one probes convolutions of two TMDs, it is expected that at LO it does not have the problem that TMDShFs enter the process (likewise for single quarkonium production in proton-proton collisions). In particular, we are interested when two J/ψ mesons are produced, as these are most easily detected, allowing for the recording of a large number of events in the detector (note that in this case the Landau-Yang theorem is not applicable). Indeed, new measurements of J/ψ-pair production have been made recently available by the LHCb collaboration [78]. Hence, this process emerges as currently the most promising one for probing gluon TMDs, as it allows for direct comparison between experimental data and theoretical predictions, which is performed in Sec. 6.3.

Processes involving two particles in the final state offer advantages when compared to those involving only a single detected particle. Because the TM of the final state needs to be small for the cross section to be sensitive to TMD effects, single-particle final states tend to remain close to the beam axis, making them in general more challenging to detect due to a large background and triggering requirements. However, when two particles are produced nearly back-to-back, they can each possess significant

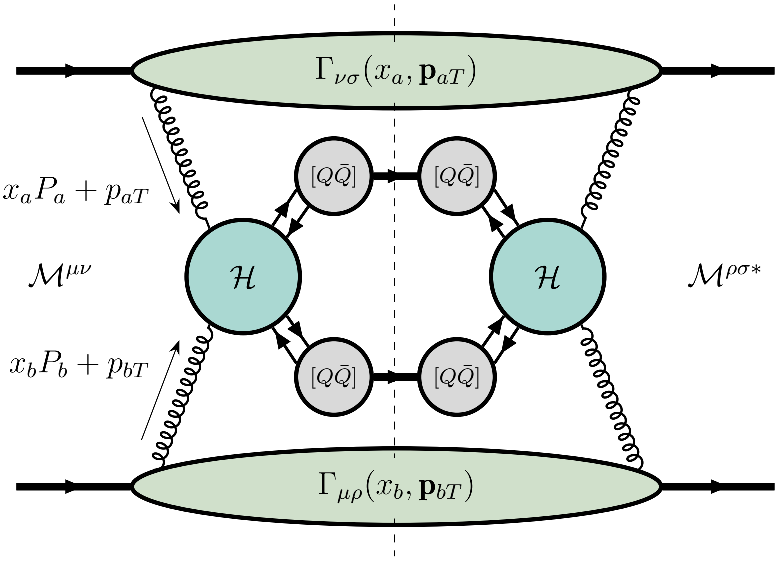

Figure 3.7: The LO gluon-induced inclusive cross section for $p+p \to [Q\bar{Q}]+[Q\bar{Q}]+X$ within TMD factorisation and the CSM.

individual transverse momenta that collectively contribute to a small overall TM in order to stay in the LTM region for TMD factorisation. Moreover, unlike single quarkonium production in proton-proton collisions where the hard scale is determined by its mass, the invariant mass of the quarkonium-pair $M_{\mathcal{Q}\mathcal{Q}}$ can be tuned with their individual momenta. The latter allows one to study the scale evolution of the TMDs like single quarkonium in electroproduction.

For this process it is convenient to work with the helicity formalism. Then the differential cross section can be calculated from contracting helicity correlators with helicity amplitudes, which can be derived from the usual correlators and amplitudes as shown in App. C. In [25] this procedure was performed for this process utilising the LO α_s^4 uncontracted amplitudes from [79]. They found that the differential cross section in the case of two unpolarised protons can be written as

$$\begin{aligned}\frac{d\sigma(J/\psi + J/\psi)}{dM_{\mathcal{Q}\mathcal{Q}}\, dy_{\mathcal{Q}\mathcal{Q}}\, d^2\mathbf{q}_T\, d\Omega} &= \frac{\sqrt{M_{\mathcal{Q}\mathcal{Q}}^2 - 4M_{\mathcal{Q}}^2}}{(2\pi)^2 8s\, M_{\mathcal{Q}\mathcal{Q}}^2} \\ &\quad \times \Big\{ \mathcal{F}_1(\theta_{CS}, M_{\mathcal{Q}\mathcal{Q}})\, \mathcal{C}[f_1^g f_1^g] + \mathcal{F}_2(\theta_{CS}, M_{\mathcal{Q}\mathcal{Q}})\, \mathcal{C}[w_2 h_1^{\perp g} h_1^{\perp g}] \\ &\quad + \big\{ \mathcal{F}_3(\theta_{CS}, M_{\mathcal{Q}\mathcal{Q}})\, \mathcal{C}[w_3 f_1^g h_1^{\perp g}] + \mathcal{F}_3'(\theta_{CS}, M_{\mathcal{Q}\mathcal{Q}})\, \mathcal{C}[w_3' h_1^{\perp g} f_1^g] \big\} \cos 2\phi_{CS} \\ &\quad + \mathcal{F}_4(\theta_{CS}, M_{\mathcal{Q}\mathcal{Q}})\, \mathcal{C}[w_4 h_1^{\perp g} h_1^{\perp g}] \cos 4\phi_{CS} \Big\}\,, \end{aligned} \tag{3.97}$$

with $d\Omega = d(\cos\theta_{CS})\, d\phi_{CS}$, where θ_{CS} and ϕ_{CS} are the Collins-Soper angles that are defined in the Collins-Soper reference frame shown in Fig. 3.8. The rapidity of the quarkonium-pair $y_{\mathcal{Q}\mathcal{Q}}$ is defined in the hadron centre-of-mass frame, i.e.

$$x_{a,b} = \exp(\pm y_{\mathcal{Q}\mathcal{Q}})\, M_{\mathcal{Q}\mathcal{Q}}/\sqrt{s}\,, \tag{3.98}$$

similar to single quarkonium production (where we take $y_{\mathcal{Q}\mathcal{Q}} \to y$ and $M_{\mathcal{Q}\mathcal{Q}} \to \mu_H$). We note that it is evident from the overall factor of the differential cross section that

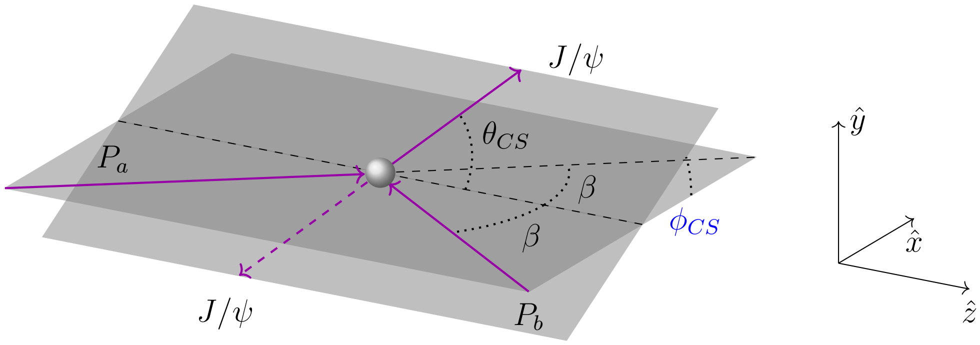

Figure 3.8: Illustration of $p+p \to J/\psi + J/\psi$ in the Collins-Soper reference frame in which the angles θ_{CS} and ϕ_{CS} are defined.

$M_{\mathcal{Q}\mathcal{Q}} > 2M_{\mathcal{Q}}$. The definition of the convolutions is given in Eq. 3.61. Besides the TMD weight w_2 defined in Eq. 3.62, we have that:

$$w_3 = \frac{1}{2M_h^2 \mathbf{q}_T^2}\left[\mathbf{p}_{bT}^2 \mathbf{q}_T^2 - 2(\mathbf{p}_{bT}\cdot\mathbf{q}_T)^2\right], \quad w_3' = \frac{1}{2M_h^2 \mathbf{q}_T^2}\left[\mathbf{p}_{aT}^2 \mathbf{q}_T^2 - 2(\mathbf{p}_{aT}\cdot\mathbf{q}_T)^2\right] \tag{3.99}$$

$$w_4 = 2\left(\frac{\mathbf{p}_{aT}\cdot\mathbf{p}_{bT}}{2M_h^2} - \frac{(\mathbf{p}_{aT}\cdot\mathbf{q}_T)(\mathbf{p}_{bT}\cdot\mathbf{q}_T)}{M_h^2 \mathbf{q}_T^2}\right)^2 - \frac{\mathbf{p}_{aT}^2 \mathbf{p}_{bT}^2}{4M_h^4}\,. \tag{3.100}$$

For the specific analytic expressions of the hard factors $\mathcal{F}_i(\theta_{CS}, M_{\mathcal{Q}\mathcal{Q}})$ we refer to [25]. We point out that strictly the nonperturbative factor $\langle \mathcal{O}^{J/\psi}[^3S_1^1]\rangle^2$ should not be included in $\mathcal{F}_i$. However, for this process only, we continue this practice for convenience. The hard factors contain the information on the helicities of the partonic gluons. In particular, we have two helicity amplitudes that are shown in Fig. 3.9, which lead to four different combinations of squared amplitudes. Namely, $\mathcal{F}_1$ corresponds to no helicity change within the squared amplitude as both gluons are unpolarised, while $\mathcal{F}_3 = \mathcal{F}_3'$ contain a single helicity flip of one linearly polarised gluon. On the other hand, $\mathcal{F}_2$ corresponds to a double helicity flip for which the two gluons of one amplitude have the same helicity, while $\mathcal{F}_4$ corresponds to a double flip with initial state gluons of opposite helicities. Again, the weight factors arise due to the contraction of the TM prefactors in front of $h_1^{\perp g}$ in the parametrisation of the correlator. Moreover, within the helicity formalism, the TM prefactors also generate a phase for $\mathcal{F}_3$ and $\mathcal{F}_4$ that translates directly into the $\cos(n\phi_{CS})$-terms of the differential cross section, with $n = 2, 4$. For a figure presenting squared helicity amplitudes see [80].

The two-particle final state is used to define the azimuthal angle ϕ_{CS} which is most naturally distinguished as an interesting observable because this asymmetry is directly related to gluon TMDs, like in single quarkonium production in electron-proton collisions as discussed before. Namely, by calculating its average, similar to Eq. 3.94, one can identify two azimuthal modulations [25]

$$\langle \cos 2\phi_{CS}\rangle = \frac{1}{2}\frac{\mathcal{F}_3\big(\mathcal{C}[w_3 f_1^g h_1^{\perp g}] + \mathcal{C}[w_3' h_1^{\perp g} f_1^g]\big)}{\mathcal{F}_1\,\mathcal{C}[f_1^g f_1^g] + F_2\,\mathcal{C}[w_2 h_1^{\perp g} h_1^{\perp g}]}\,, \tag{3.101}$$

and:

$$\langle \cos 4\phi_{CS}\rangle = \frac{1}{2}\frac{\mathcal{F}_4\,\mathcal{C}[w_4 h_1^{\perp g} h_1^{\perp g}]}{\mathcal{F}_1\,\mathcal{C}[f_1^g f_1^g] + \mathcal{F}_2\,\mathcal{C}[w_2 h_1^{\perp g} h_1^{\perp g}]}\,. \tag{3.102}$$

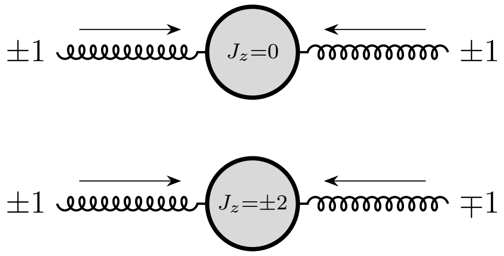

Figure 3.9: Helicity amplitudes induced by two gluons: the signs denote their spin and the arrows the direction of their momentum. The $J_z = \pm 2$ amplitudes generate azimuthal modulations in the cross section of the process.

The positivity bound for the gluon TMDs in Eq. 2.48 implies that the convolutions must obey

$$\begin{aligned} |\mathcal{C}[w_3 f_1^g h_1^{\perp g}]| \leq \mathcal{C}[f_1^g f_1^g]\,, &\quad |\mathcal{C}[w_3' h_1^{\perp g} f_1^g]| \leq \mathcal{C}[f_1^g f_1^g]\,, \\ |\mathcal{C}[w_2 h_1^{\perp g} h_1^{\perp g}]| \leq \mathcal{C}[f_1^g f_1^g]\,, &\quad |\mathcal{C}[w_4 h_1^{\perp g} h_1^{\perp g}]| \leq \mathcal{C}[f_1^g f_1^g] \end{aligned} \tag{3.103}$$

such that upper bounds for the modulations are obtained:

$$|\langle \cos 2\phi_{CS} \rangle| \leq \frac{|\mathcal{F}_3|}{|\mathcal{F}_1| - |\mathcal{F}_2|}\,, \quad |\langle \cos 4\phi_{CS} \rangle| \leq \frac{1}{2}\frac{|\mathcal{F}_4|}{|\mathcal{F}_1| - |\mathcal{F}_2|}\,. \tag{3.104}$$

In Fig. 3.10 we show the hard factors over the whole $\cos{(\theta_{CS})}$ region for two different values of $M_{J/\psi\, J/\psi}$ as an example. Although the polynomial structure of the hard factors in terms of $\cos\theta_{CS}$ are complicated, one can observe some trends. We see that $\mathcal{F}_1$ has a relatively large magnitude compared to $\mathcal{F}_3$ and $\mathcal{F}_4$, and decreases with increasing M_{QQ} (until at some point it does not change much any more). $\mathcal{F}_2$ behaves similarly: it is close to zero for large M_{QQ}, but increases (more and more) rapidly at the maxima of $\cos\theta_{CS}$ when decreasing M_{QQ}. The numerators of the modulations have a different shape as a function of $\cos\theta_{CS}$. $\mathcal{F}_3$ first increases in magnitude when increasing $\mathcal{M}_{QQ}$ (although not visible from Fig. 3.10), but (continuously) decreases thereafter. On the other hand, the magnitude of $\mathcal{F}_4$ only increases with increasing M_{QQ} (until at some point it does not change any more like $\mathcal{F}_1$). Moreover, from the fact that $\mathcal{F}_4$ is negative for some values of $\cos\theta_{CS}$ (depending on M_{QQ}) a sign flip for $\cos 4\phi_{CS}$ is predicted with respect to θ_{CS}, so choosing bins in θ_{CS} must be done with care. We note that both $\mathcal{F}_3$ and $\mathcal{F}_4$ are zero for $M_{J/\psi\, J/\psi} = 2M_{J/\psi}$.

One can neglect $\mathcal{F}_2\,\mathcal{C}[w_2 h_1^{\perp g} h_1^{\perp g}]$ in the azimuthal modulations [25], in the case that $|\cos\theta_{CS}| \leq 0.5$ or when M_{QQ} is large. Indeed, it is expected that in collider experiments most of the data are found at small $\cos\theta_{CS}$ and not too small M_{QQ}. Such a restriction is useful to simplify computations, e.g. it can be used to make sure that the upper bounds of the modulations in Eq. 3.104 cannot become larger than unity; that can occur due to the minus sign in front of $\mathcal{F}_2$ in the denominator of Eq. 3.104 that originates from the unknown sign of $\mathcal{C}[w_2 h_1^{\perp g} h_1^{\perp g}]$.

The behaviour of the modulations becomes slightly more evident when choosing a $\cos{(\theta_{CS})}$-bin, i.e. we perform an extra integration in the numerator and denominator of Eqs. 3.101 and 3.102. The corresponding upper bounds are shown in Fig. 3.11, where we see that the maximum of the $\cos{(2\phi_{CS})}$-modulation first grows with increasing

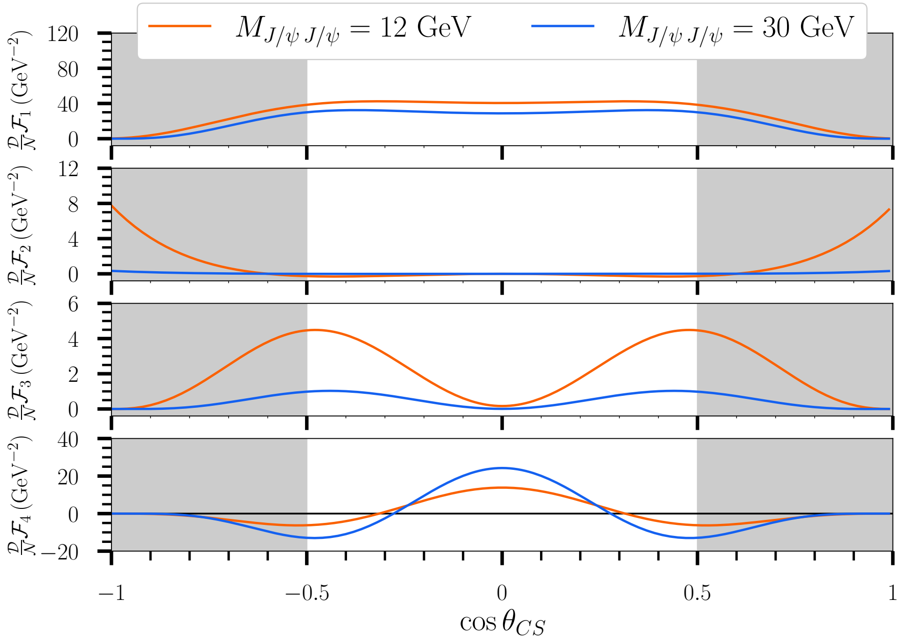

Figure 3.10: Isolated hard factors as a function of $\cos\theta_{CS}$ for two different invariant masses $M_{J/\psi\,J/\psi}$ as an example. We note that the factors are multiplied with an overall factor $\mathcal{D}/\mathcal{N}$ from [25] that cancel out in the modulations. The grey area denotes the region where $|\cos\theta_{CS}| \geq 0.5$, in which $\mathcal{F}_2$ becomes non-negligible.

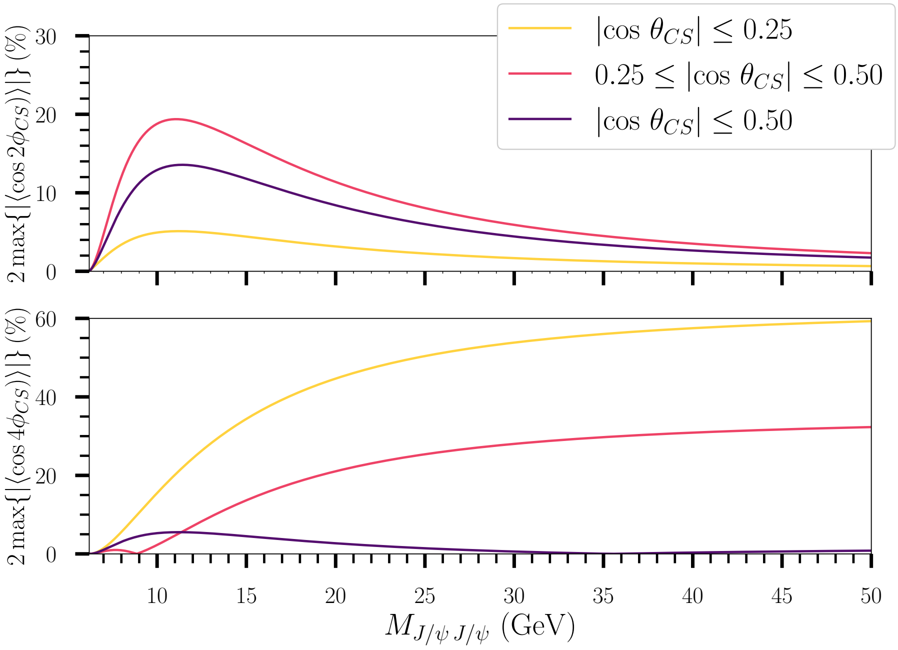

Figure 3.11: Upper bounds of the $\cos(2\phi_{CS})$-modulation (above) and $\cos(4\phi_{CS})$-modulation (below) as a function of $M_{J/\psi}$ for different $\cos(\theta_{CS})$-bins.

M_{QQ} and thereafter decreases towards zero, although the specific shape and magnitude depend on the bin choice. For the $\cos(4\phi_{CS})$-modulation we observe instead that it goes towards a certain asymptotic value, as well as by first crossing the horizontal axis. Therefore, the $\cos(\theta_{CS})$-bin choice for the modulations is crucial to make predictions.

Although the sign of $h_1^{\perp g}$ is unknown, it is typically assumed to be positive in models. Regardless of its sign, the theory predicts that a sign flip of the $\cos(4\phi_{CS})$-modulations with respect to M_{QQ} (or with respect to another bin) occurs. We note that the $\mathcal{C}[w_3 f_1^g h_1^{\perp g}]$ and $\mathcal{C}[w_3' h_1^{\perp g} f_1^g]$ convolution that enter the $\cos(2\phi_{CS})$-modulation provide a way to determine the sign of $h_1^{\perp g}$, while $\mathcal{C}[w_4 h_1^{\perp g} h_1^{\perp g}]$ that enters the $\cos(4\phi_{CS})$-modulation can allow one to extract $h_1^{\perp g}$ independently of f_1^g (when $F_2\,\mathcal{C}[w_2 h_1^{\perp g} h_1^{\perp g}]$ is negligible and $\mathcal{C}[f_1^g f_1^g]$ is extracted), but not its sign.

In principle, all differential cross sections and modulations presented in this chapter can be measured in current LHC and future EIC experiments to try to extract the nonperturbative TMDs by comparing to theory expressions. However, a step further would be to provide actual numerical predictions for observables in collider experiments. In the following chapter possible approaches for this are discussed and investigated.

4

Approaches to TMD studies

Recently, there has been a significant development in extracting quark TMDs from experimental SIDIS and Drell-Yan (DY) lepton-pair production data [81–84]: in SIDIS the hadron formation goes through quark fragmentation and in DY a quark and an antiquark annihilate creating a virtual photon or a Z-boson (at higher energies), which decays into a pair of oppositely-charged leptons perturbatively, i.e. $p + p \to l + \bar{l} + X$. Specifically, they extracted values for the parametrisations of the unknown nonperturbative components of the TMDs by employing TMD evolution. However, not much is known about the gluon TMDs experimentally, although from a theoretical point of view it is expected that data of inclusive quarkonium production is likely to make their extraction possible. Besides the studies investigated in Ch. 3, many others have appeared about this topic already [85–93]. Furthermore, back-to-back heavy-quark pair production in both proton-proton and electron-proton collisions [94]; and η_Q-pair [95], quarkonium plus photon [96], quarkonium plus virtual photon or Z [97] in proton-proton collisions; and J/ψ plus jet [98, 99], J/ψ plus photon [100], D-meson plus jet [101] and J/ψ plus pion [102] in electron-proton collisions, have been put forward as gluon TMD probes too. The electron-proton processes mentioned above are expected to be measurable at the future EIC, but one must still wait for a while for it to become operational. The proton-proton processes on the other hand can be measured at the ongoing LHC experiment, where the current challenge lies in achieving sufficient statistical significance and resolution at LTM (also for Higgs production). In the meantime, there are multiple ways to study processes with gluon TMDs in greater detail. In particular, we distinguish two approaches: one can either fully parametrise the TMDs, as explained in Sec. 4.1, or employ TMD evolution in which only their nonperturbative part is parametrised, as discussed in Sec. 4.2.

4.1 Parametrisations of TMDs

A useful approach is to assume that the nonperturbative unpolarised gluon TMD has a simple Gaussian dependence on TM [103]

$$f_1^g(x, \mathbf{p}_T^2; \mu) = \frac{f_1^g(x; \mu)}{\pi \langle p_T^2 \rangle} \exp\left(- \frac{\mathbf{p}_T^2}{\langle p_T^2 \rangle} \right), \tag{4.1}$$

where $\langle p_T^2 \rangle$ is the width parameter, such that the integral over TM gives the unintegrated collinear PDF f_1^g by its definition in Eq. 2.30. We note that the dependence on the scale μ with mass dimension $[\mu] = 1$, that comes from the renormalisation of the PDF, is made explicit from now on. Moreover, $\langle p_T^2 \rangle$ is taken independent of x, i.e. the x behaviour is solely determined by the PDF. Since there is no collinear version of $h_1^{\perp g}$ it is completely unknown on the other hand, but one can saturate its positivity bound given in Eq. 2.48. This makes it possible to describe $h_1^{\perp g}$ by a simple Gaussian expression too. Another model, where the bound is satisfied, but not saturated, is [104]

$$h_1^{\perp g}(x, \mathbf{p}_T^2; \mu) = \frac{2M_h^2}{\langle p_T^2 \rangle} \frac{(1-r)}{r} \frac{f_1^g(x; \mu)}{\pi \langle p_T^2 \rangle} \exp\left(1 - \frac{1}{r} \frac{\mathbf{p}_T^2}{\langle p_T^2 \rangle} \right), \tag{4.2}$$

where $r < 1$. Initially a model of this type was explored in [105]. The usual value taken for the input parameter r is 2/3, as it maximises the second moment of $h_1^{\perp g}$, i.e. the variance of the Gaussian function. We note that even less is known about the TMDShFs, therefore there is no conventional parametrisation for these functions at present.

These TMD parametrisations can be used to analytically compute the convolutions in the cross sections that appear. In particular, employing Eq. 3.61 we have for unpolarised proton-proton collisions that:

$$\mathcal{C}[f_1^g f_1^g] = \frac{f_1^g(x_a; \mu) f_1^g(x_b; \mu)}{2\pi \langle p_T^2 \rangle} \exp\left(- \frac{1}{2} \frac{\mathbf{q}_T^2}{\langle p_T^2 \rangle} \right). \tag{4.3}$$

By employing the Gaussian r-dependent model for $h_1^{\perp g}$ (with $r = 2/3$), which we define as Model 1, expressions for the other convolutions are found:

$$\begin{aligned} \mathcal{C}[w h_1^{\perp g} h_1^{\perp g}] &= \frac{f_1^g(x_a; \mu) f_1^g(x_b; \mu)}{32\pi \langle p_T^2 \rangle^3} \frac{(r-1)^2}{r} \\ &\quad \times \left[8r^2 \langle p_T^2 \rangle^2 - 8r \langle p_T^2 \rangle \mathbf{q}_T^2 + \mathbf{q}_T^4 \right] \exp\left(2 - \frac{1}{2r} \frac{\mathbf{q}_T^2}{\langle p_T^2 \rangle} \right), \qquad (4.4) \\ \mathcal{C}[w_3 f_1^g h_1^{\perp g}] &= \frac{f_1^g(x_a; \mu) f_1^g(x_b; \mu)}{\pi \langle p_T^2 \rangle^2} \frac{(r-1) r^2}{(r+1)^3} \mathbf{q}_T^2 \exp\left(1 - \frac{1}{r+1} \frac{\mathbf{q}_T^2}{\langle p_T^2 \rangle} \right), \qquad (4.5) \\ \mathcal{C}[w_4 h_1^{\perp g} h_1^{\perp g}] &= \frac{f_1^g(x_a; \mu) f_1^g(x_b; \mu)}{32\pi \langle p_T^2 \rangle^3} \frac{(r-1)^2}{r} \mathbf{q}_T^4 \exp\left(2 - \frac{1}{2r} \frac{\mathbf{q}_T^2}{\langle p_T^2 \rangle} \right). \qquad (4.6) \end{aligned}$$

Saturating the positivity bound for $h_1^{\perp g}$, which we define as Model 2, gives instead the following expressions:

$$\begin{aligned}
\mathcal{C}[w_2 h_1^{\perp g} h_1^{\perp g}] &= \frac{f_1^g(x_a;\mu) f_1^g(x_b;\mu)}{2\pi\langle p_T^2\rangle} \left\{ \left[4 - 3\, e^{\frac{\mathbf{q}_T^2}{2\langle p_T^2\rangle}} \right] \exp\left(-\frac{\mathbf{q}_T^2}{\langle p_T^2\rangle} \right) \right. \\
&\quad \left. + \frac{4}{\langle p_T^2\rangle} \mathbf{q}_T^2 \left[\mathrm{EI}\left(-\frac{\mathbf{q}_T^2}{\langle p_T^2\rangle} \right) - \frac{1}{2}\, \mathrm{EI}\left(-\frac{\mathbf{q}_T^2}{2\langle p_T^2\rangle} \right) \right] \right\}, \qquad (4.7) \\
\mathcal{C}[w_3 f_1^g h_1^{\perp g}] &= -\frac{f_1^g(x_a;\mu) f_1^g(x_b;\mu)}{2\pi\langle p_T^2\rangle \mathbf{q}_T^2} \\
&\quad \times \left[\left(\mathbf{q}_T^2 - 2\langle p_T^2\rangle \right) e^{\frac{\mathbf{q}_T^2}{2\langle p_T^2\rangle}} + 2\langle p_T^2\rangle \right] \exp\left(-\frac{\mathbf{q}_T^2}{\langle p_T^2\rangle} \right), \qquad (4.8) \\
\mathcal{C}[w_4 h_1^{\perp g} h_1^{\perp g}] &= \frac{f_1^g(x_a;\mu) f_1^g(x_b;\mu)}{2\pi\langle p_T^2\rangle \mathbf{q}_T^4} \\
&\quad \times \left[\left(\mathbf{q}_T^4 - 8\langle p_T^2\rangle^2 \right) e^{\frac{\mathbf{q}_T^2}{2\langle p_T^2\rangle}} + 4\langle p_T^2\rangle \left(\mathbf{q}_T^2 + 2\langle p_T^2\rangle \right) \right] \exp\left(-\frac{\mathbf{q}_T^2}{\langle p_T^2\rangle} \right), \qquad (4.9)
\end{aligned}$$

where we make use of the exponential integral:

$$\mathrm{EI}(x) = \int_{-\infty}^{x} dt\, \frac{e^t}{t}\,. \qquad (4.10)$$

In all these equations it is used that $\langle p_{aT}^2\rangle = \langle p_{bT}^2\rangle \equiv \langle p_T^2\rangle$.

We recall that all TMD expressions are applicable only when $q_T \ll \mu_H$. Hence, in order to stay within the TMD regime one usually defines $q_{T,\max} = \mu_H/2$, e.g. for η_c hadroproduction discussed in Sec. 3.3 we have that $q_{T,\max} = M_{\eta_c}/2 \approx 1.5\,\mathrm{GeV}$. Therefore, we expect the model approach and in particular a Gaussian fall-off of $h_1^{\perp g}$ at $q_T \sim \mu_H$ to be unrealistic: one rather expects a power-law fall-off that would result from a perturbative collinear treatment [106]. In practice, this difference may not matter much, as the contribution from linearly polarised gluons in the tail region are expected to be quite small. Given that no experimental constraints have been imposed on the gluon TMDs so far, an alternative model can also be adopted.

In Fig. 4.1 we show the behaviour of Eqs. 4.1 and 4.2, where the PDFs are factored out, thereby eliminating their μ dependence. Increasing (or decreasing) the value of $\langle p_T^2\rangle$ increases (or decreases) the width of the TMDs and decreases (or increases) the value of f_1^g at $p_T = 0\,\mathrm{GeV}$, hence the magnitude of the TMDs. Similarly, increasing r broadens $h_1^{\perp g}$ as well. Although it is likely scale dependent, $\langle p_T^2\rangle = 1.0\,\mathrm{GeV}^2$ is chosen, which is often considered to be a realistic value for gluon-induced single charmonium production. This is because this value has been found to provide an accurate description of the unpolarised cross section data for J/ψ production in proton-proton collisions [90, 107], while for quark induced SIDIS a smaller value of $0.25\,\mathrm{GeV}^2$ was found [108]. Generally, for bottomonium larger values are expected such that not too much of the Gaussian $h_1^{\perp g}$ tail lies within the TMD regime.

An example of the Gaussian convolutions is shown in Fig. 4.2, where we investigate their ratio with respect to Eq. 4.3 for a (larger) value of $\langle p_T^2\rangle$ that is relevant for J/ψ-pair production (which generally exbibits a larger scale than single quarkonium production). The latter number was found in [25] from fitting $\mathcal{C}[f_1^g f_1^g]$ to normalised J/ψ-pair production data at $\sqrt{s} = 13\,\mathrm{TeV}$ with $\langle M_{J/\psi\, J/\psi}\rangle = 8\,\mathrm{GeV}$ from LHCb [109],

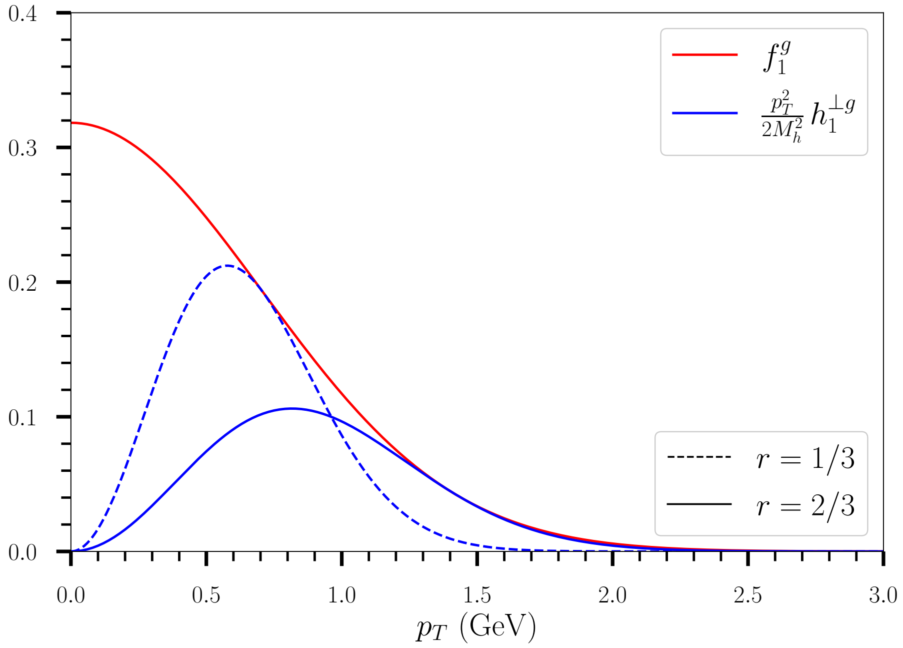

Figure 4.1: Gaussian models for the TMDs f_1^g and $h_1^{\perp g}$, divided by $f_1^g(x)$, as a function of p_T in units of GeV^{-2} with $\langle p_T^2 \rangle = 1.0\,\text{GeV}^2$ as an example.

which will be explained in more detail in Sec. 6.3. We note that in the large-q_T limit all the convolutions become zero due to their Gaussian nature and, again, that the dependence of the PDFs is factored out. In Model 1 the ratios all tend toward zero as the Gaussian convolutions containing $h_1^{\perp g}$ are all steeper than $\mathcal{C}[f_1^g f_1^g]$ in the large-q_T limit. This is a consequence of the presence of the factor r in the argument of the p_T-exponential in Eq. 4.2. In Model 2, however, the Gaussian convolutions containing $h_1^{\perp g}$ are as broad as $\mathcal{C}[f_1^g f_1^g]$ in the large-q_T limit. Therefore, they actually become all identical to $\mathcal{C}[f_1^g f_1^g]$, making their ratio equal to 1 (up to a minus sign for $\mathcal{C}[w_3 f_1^g h_1^{\perp g}]$). Hence, ensuring a maximal size for the azimuthal modulations. We note that $\mathcal{C}[w_2 h_1^{\perp g} h_1^{\perp g}]/\mathcal{C}[f_1^g f_1^g]$ is the only non-zero ratio for the models at $q_T = 0\,\text{GeV}$: in Model 1 it is $e^2/27 = 0.27$, while in Model 2 it is 1. Hence, $\mathcal{C}[w_2 h_1^{\perp g} h_1^{\perp g}]$ is the only convolution involving $h_1^{\perp g}$ that contributes to the ϕ_{CS}-independent part of the differential cross section.

Furthermore, we point out that $\int d^2\mathbf{q}_T\, (\mathbf{q}_T^2)^\alpha\, \mathcal{C}[w_2 h_1^{\perp g} h_1^{\perp g}] = 0$ for $\alpha = 0,\, 1$, independent of the model. The case of $\alpha = 0$ implies that linearly polarised gluons do not affect the q_T-integrated cross section. The case of case of $\alpha = 1$ implies that the convolution must have at least two nodes as a function of q_T, i.e. it has to flip sign at least twice as can be observed in Fig. 4.2. This distinctive double-node feature can be used to experimentally demonstrate the presence of the linear polarisation of the gluons when part of the TMD regime.

The behaviour of the TMD Gaussian convolutions as function of $\langle p_T^2 \rangle$ naturally follows the behaviour of the individual TMDs that are discussed above: increasing $\langle p_T^2 \rangle$ increases the width of the ratios (and the other way around), while the values at $q_T = 0\,\text{GeV}$ stay the same. It shifts the value at which the ratios in Model 1 peak to larger q_T (the magnitude stays the same), while it makes the ratios in Model 2 slower, at larger q_T, to reach their maximal value. We note that the large-q_T behaviour of

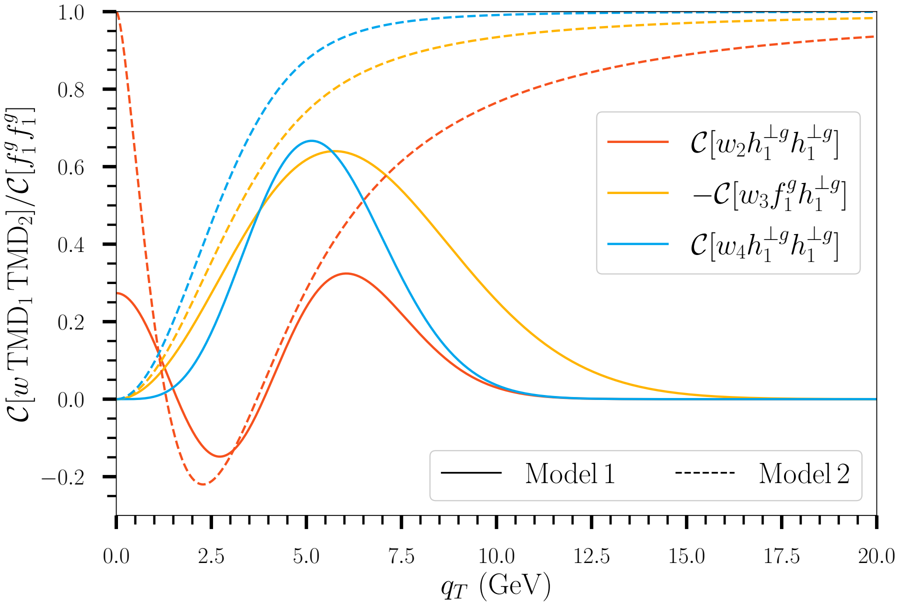

Figure 4.2: Ratios of TMD Gaussian convolutions in unpolarised hadron-hadron collisions as a function of p_T with $\langle p_T^2 \rangle = 3.3\,\mathrm{GeV}^2$ as an example. Two different Gaussian models of $h_1^{\perp g}$ are employed: Model 1 is the r-dependent model given in Eq. 4.2 with $r = 2/3$ and Model 2 is the saturation of the positivity bound given in Eq. 2.48 with Eq. 4.1.

the ratios and the convolutions discussed here are expected not to be observable since $q_{T,\max} = 4\,\mathrm{GeV}$ in this example, i.e. a larger hard scale or a smaller value for $\langle p_T^2 \rangle$ (like in Fig. 4.1 for single quarkonium production) would in that regard be more useful.

The Gaussian TMDs can of course be used to make predictions of the azimuthal modulations as well. In Fig. 4.3 we show such a prediction for J/ψ production in electron-proton collisions without smearing following Eq. 3.95. We utilise the value of $\langle p_T^2 \rangle$ for the Gaussian TMDs that was employed in Fig. 4.1 and the central values of the CMSWZ LDMEs [75] that were employed in Fig. 3.6. However, for this prediction we also need the (central) gluon PDF that depend on x and the scale μ as additional integration is performed in the numerator and denominator (determined by the other kinematic values). Here, and in the rest of this thesis, we employ the LO MSHT20 extraction of the PDFs [1]. We point out that, although the performance of PDF sets from major collaborations varies depending on the process, they currently perform equally well across all available data [110]. In the figure we observe that the Gaussian model predicts an asymmetry that should be measurably large. Moreover, we have again that r and $\langle p_T^2 \rangle$ alter the position of the peak and its width like the TMDs themselves, while the magnitude of the $(2\phi_{CS})$-modulation remains unchanged as it is determined by the integration ranges.

In Fig. 4.4 we employ the TMD Gaussian models for the modulations in J/ψ-pair hadroproduction in two different $\cos(\theta_{CS})$-bins. The values of M_{QQ} investigated are in line with the LHCb measurements [78], namely: 6.6, 7.9 and 11.0 GeV. In contrast to the previous example, the PDFs cancel in the modulations as no additional integration is performed for comparison with the TMD-evolution results presented in Sec. 6.3. Besides, each prediction is plotted up to $q_{T,\max} = M_{QQ}/2$ to show

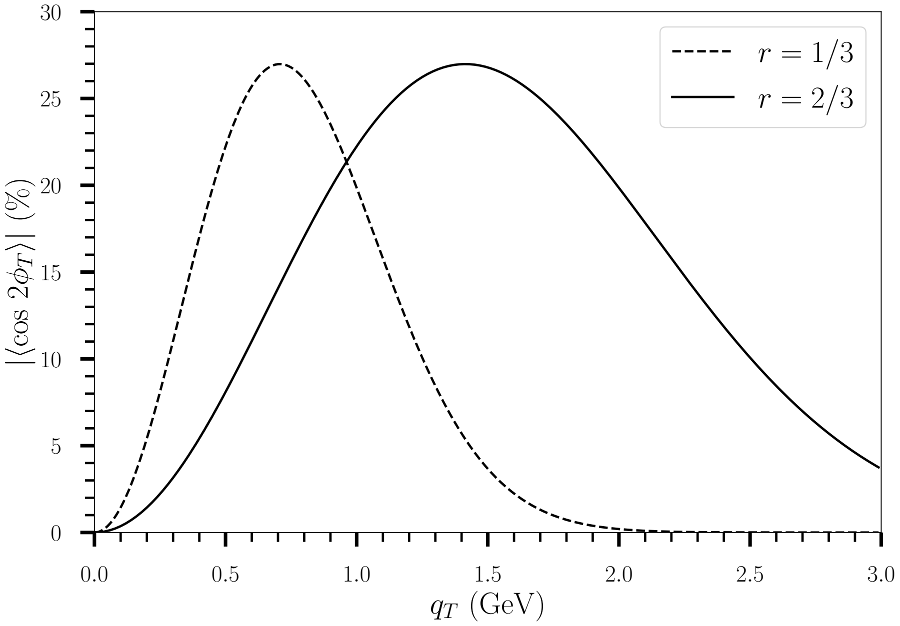

Figure 4.3: An example prediction for the $\cos(2\phi_T)$-asymmetry in unpolarised J/ψ electroproduction at $z = 1$ as function of q_T, without smearing, using Gaussian TMDs. Here we employed the central values of the CMSWZ LDMEs [75] and $\sqrt{s} = 45\,\mathrm{GeV}$. Also $M_p = 938\,\mathrm{MeV}$ is employed, and an additional integration over $0.1 \le y \le 0.9$ and $0.0001 \le x_B \le 0.9$ is performed determining $\mu = Q$ following [89].

the observable in the TMD regime. We observe that the $\cos(2\phi_{CS})$-modulation is largest in the $0.25 \le |\cos\theta_{CS}| \le 0.50$ bin, while the $\cos(4\phi_{CS})$-modulation is best observed in the $|\cos\theta_{CS}| \le 0.25$ bin. A notable difference between these two is that the $M_{J/\psi\, J/\psi} = 6.6\,\mathrm{GeV}$ prediction is almost zero in the latter. Indeed, a sign flip of the $\cos(4\phi_{CS})$-modulations with respect to M_{QQ} can be observed when taking the $\cos(\theta_{CS})$-bin to be $0.25 \le |\cos\theta_{CS}| \le 0.50$ as discussed in Sec. 3.5. In general, for large M_{QQ} it is also possible to observe this sign flip between the two considered bins.

We also show the corresponding upper bounds of the modulations in Fig. 4.4 such that we see that Model 2 is approaching the upper bound at large q_T naturally. We note that the sign in front of $|\mathcal{F}_2|$ in the denominator of Eq. 3.104 is now positive set by the positive sign of $h_1^{\perp g}$ in the Gaussian model. When a smaller $\langle p_T^2 \rangle$ is taken, Model 2 will approach the upper bound value earlier, at smaller q_T, and more of the Gaussian shape of the Model 1 will be visible within the TMD regime (and the other way around), equivalent to the behaviour of the ratio of the convolutions as discussed before. We note that in the $\cos(4\phi_{CS})$-modulations more of the Gaussian shape is observed with respect to the $\cos(2\phi_{CS})$-modulations, especially visible for large M_{QQ}.

Similarly, Gaussian models for other TMDs in polarised interactions can be constructed, e.g. for the gluon Sivers function see [111], but since our focus is solely on f_1^g and $h_1^{\perp g}$ these are not discussed. For completeness, we briefly mention the existence of another model. This spectator model is based on the assumption that the remainders after the emission of a parton from the hadron are treated as a single spectator particle. The hadron-parton-spectator coupling is then described by an effective vertex containing two form factors in which the spectator mass can take a continuous range of values described by a spectral function. The parameters of this model are subsequently determined by reproducing the PDFs obtained in global fits. For details we refer to [112–114].

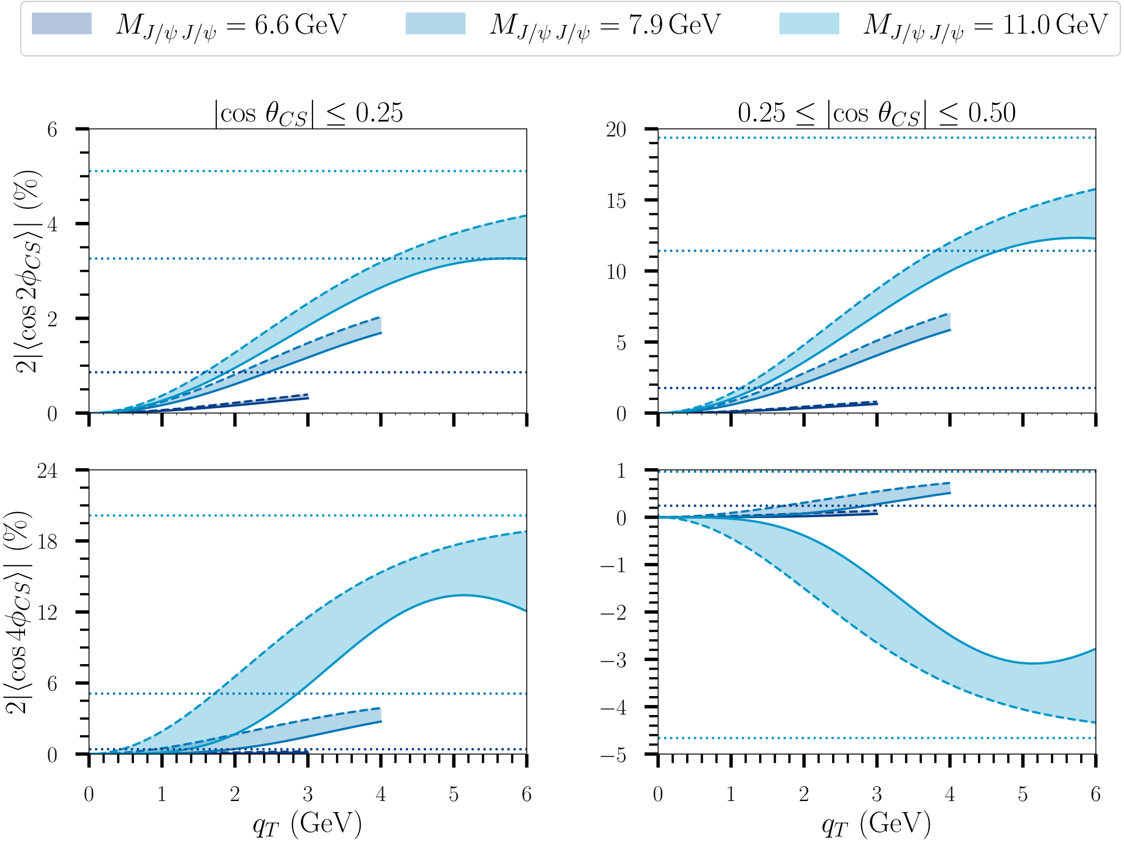

Figure 4.4: The $\cos(2\phi_{CS})$- and $\cos(4\phi_{CS})$-modulations in unpolarised J/ψ-pair hadroproduction as a function of q_T for different values of $M_{J/\psi\,J/\psi}$ in two different θ_{CS}-bins, $|\cos\theta_{CS}| \leq 0.25$ (left column) and $0.25 \leq |\cos\theta_{CS}| \leq 0.25$ (right column), by using Gaussian TMDs. We employ the model parametrisations as in Fig. 4.2. Model 1 predictions are shown with solid lines and Model 2 predictions with dashed lines. Also the corresponding upper bounds of the modulations are shown with dotted lines.

4.2 TMD evolution

A more sophisticated approach to study TMDs is to make use of evolution to the scale where we can relate the large TM part of TMDs to the well-known collinear PDFs. Although more involved, we consider TMD evolution, that originates from the Collins-Soper-Sterman formalism [115–120] for formulating TMD factorisation (updated in [3]), to be more reliable than the simple parametrisations discussed in the previous section. Beyond tree level the TMDs (and the TMDShFs or TMDFF) present in the form of convolutions and the perturbative hard factor become scale dependent (like the PDFs) which makes evolution possible [115, 118]. Implementing evolution of TMD functions is more easily done in impact-parameter space, where convolutions become simple products as we will see. In general, we can rewrite Eq. 3.45 as follows:

$$\frac{d\sigma}{d^2\mathbf{q}_T} = \int d^2\mathbf{b}_T\, e^{-i\mathbf{b}_T\cdot\mathbf{q}_T}\, \hat{W}(\mathbf{b}_T,\mu_H) + Y(\mathbf{q}_T^2/\mu_H^2)\,. \tag{4.11}$$

While the natural hard scales of the process under investigation were identified in Ch. 3, we note that there actually exists some freedom in selecting μ_H. In the electron-proton case this scale can be dependent on $M_{\mathcal{Q}}$ or Q, or a combination of both, such that $\mu_H = f(M_{\mathcal{Q}}, Q)$ with $f(M_{\mathcal{Q}}, Q) \gtrsim \mu_{NP}$, where μ_{NP} is the nonperturbative scale that is discussed below. Instead, in the proton-proton collision case the hard scale is a function of the (invariant) quarkonium mass only: $\mu_H = f(M_{\mathcal{Q}(\mathcal{Q})})$. Since in all cases our interest is in the region where q_T is small compared to the hard scale, TM dependence in μ_H is neglected (unlike e.g. dijet production). $\hat{W}$ consists of the following factors

$$\hat{W}(\mathbf{b}_T,\mu_H) = w\, \hat{f}_A(\mathbf{b}_T;\zeta_A,\mu)\, \hat{f}_B(\mathbf{b}_T;\zeta_B,\mu)\, \mathcal{H}(\mu_H;\mu)\,, \tag{4.12}$$

where $\hat{f}_A$ and $\hat{f}_B$ are Fourier transforms of TMD functions that depend on kinematic variables of the specific process (not explicitly shown), the spatial $\mathbf{b}_T$, the renormalisation scale μ and the rapidity variable ζ. We note that the hard factor $\mathcal{H}$ is instead independent of $\mathbf{b}_T$. As we have seen, the operator definition of the TMDs involve gauge links, which arises from summation of all insertions of gluons that are not power-suppressed. These gauge links have light-like pieces which lead to light-cone divergences: divergent contributions for infinite negative rapidity $y = 1/2 \ln p^+/p^-$, i.e. zero '+'-momentum. ζ arises due to the required regularisation of the latter. As a regularisation, the path can be taken off the light-cone, specified by some finite rapidity. For example, the rapidity variable for two TMDs in the proton-proton case is defined as [3, pp. 562–563]

$$\zeta_A = M_A^2 x_A^2 e^{2(y_A - y_s)}\,, \quad \zeta_B = M_B^2 x_B^2 e^{2(y_s - y_B)}\,, \tag{4.13}$$

where $y_{A/B}$ denotes the rapidity of the hadrons. The dependence on the arbitrary cut-off y_s cancels in the cross section, which only depends on the combination $\zeta_A\zeta_B$, where $\zeta_A \approx \zeta_B \approx \mu_H^2$.

We first Fourier transform our TMD functions f_1^g, $h_1^{\perp g}$ and $\Delta_{(h)}^{[n]}$ as follows

$$\hat{f}_1^g(x,\mathbf{b}_T^2) \equiv \int d^2\mathbf{p}_T\, e^{i\mathbf{b}_T\cdot\mathbf{p}_T}\, f_1^g(x,\mathbf{p}_T^2)\,, \tag{4.14}$$

$$\hat{h}_1^{\perp g}(x,\mathbf{b}_T^2) \equiv \int d^2\mathbf{p}_T\, \frac{(\mathbf{b}_T\cdot\mathbf{p}_T)^2 - \frac{1}{2}\mathbf{b}_T^2\mathbf{p}_T^2}{\mathbf{b}_T^2 M_h^2}\, e^{i\mathbf{b}_T\cdot\mathbf{p}_T}\, h_1^{\perp g}(x,\mathbf{p}_T^2)\,, \tag{4.15}$$

$$\hat{\Delta}_{(h)}^{[n]}(z,\mathbf{b}_T^2) \equiv \int d^2\mathbf{k}_T\, e^{i\mathbf{b}_T\cdot\mathbf{k}_T}\, \Delta_{(h)}^{[n]}(z,\mathbf{k}_T^2)\,. \tag{4.16}$$

such that the factors of $(2\pi)^2$ are included in their inverse Fourier transforms. To simplify the notation, we have omitted here their dependence on μ and ζ. If we change the Cartesian variables (k_T^x, k_T^y) to polar ones (k_T, ϕ), the angular integrals can be expressed in terms of Bessel functions of the first kind:

$$J_n(z) = \frac{1}{\pi}\int_0^\pi d\phi \cos\left(z\sin\phi - n\phi\right) = \frac{i^{-n}}{\pi}\int_0^\pi d\phi\, e^{iz\cos\phi}\cos\left(n\phi\right). \tag{4.17}$$

When n is even this function is symmetric. Employing this and Eq. 3.61 we can write:

$$
\begin{aligned}
\mathcal{C}[f_1^g f_1^g](x_a, x_b, \mathbf{q}_T^2) &= \frac{1}{(2\pi)^2} \int d^2\mathbf{b}_T \, e^{-i\mathbf{b}_T\cdot\mathbf{q}_T} \\
&\times \int d^2\mathbf{p}_{aT} \, e^{i\mathbf{b}_T\cdot\mathbf{p}_{aT}} f_1^g(x_a, \mathbf{p}_{aT}^2) \int d^2\mathbf{p}_{bT} \, e^{i\mathbf{b}_T\cdot\mathbf{p}_{bT}} \, f_1^g(x_b, \mathbf{p}_{bT}^2) \\
&= \int_0^\infty \frac{db_T}{2\pi} \, b_T \, J_0(b_T \, q_T) \, \hat{f}_1^g(x_a, \mathbf{b}_T^2) \, \hat{f}_1^g(x_b, \mathbf{b}_T^2) \,.
\end{aligned}
\tag{4.18}
$$

Similarly, Eq. 3.90 becomes:

$$
\mathcal{C}[f_1^g \Delta^{[n]}](x, z, \mathbf{q}_T^2) = \int_0^\infty \frac{db_T}{2\pi} \, b_T \, J_0(b_T \, q_T) \, \hat{f}_1^g(x, \mathbf{b}_T^2) \, \hat{\Delta}^{[n]}(z, \mathbf{b}_T^2). \tag{4.19}
$$

The convolutions containing a weight function are more difficult to evaluate. Here we consider $\mathcal{C}[w h_1^{\perp g} \Delta_h^{[n]}]$ given in Eq. 3.91 as an example

$$
\begin{aligned}
\mathcal{C}[w h_1^{\perp g} \Delta_h^{[n]}](x, z, \mathbf{q}_T^2) &= \frac{1}{(2\pi)^2} \frac{1}{2M_h^2 \mathbf{q}_T^2} \int d^2\mathbf{b}_T \, e^{-i\mathbf{b}_T\cdot\mathbf{q}_T} \\
\times \, \mathbf{q}_T^k \mathbf{q}_T^l \int d^2\mathbf{p}_T \, e^{i\mathbf{b}_T\cdot\mathbf{p}_T} \, &\mathbf{p}_T^i \mathbf{p}_T^j \left[2\delta^{ki}\delta^{lj} - \delta^{kl}\delta^{ij}\right] h_1^{\perp g}(x, \mathbf{p}_T^2) \, \hat{\Delta}_h^{[n]}(z, \mathbf{b}_T^2) \,.
\end{aligned}
\tag{4.20}
$$

where i, j, k and l are transverse indices. We express the TM integral as a function of the impact-parameter components

$$
\int d^2\mathbf{p}_T \, e^{i\mathbf{b}_T\cdot\mathbf{p}_T} \, \mathbf{p}_T^i \mathbf{p}_T^j \, h_1^{\perp g}(x, \mathbf{p}_T^2) = A \, \delta^{ij} + B \left(\mathbf{b}_T^i \mathbf{b}_T^j - \frac{\mathbf{b}_T^2}{2} \delta^{ij}\right), \tag{4.21}
$$

where the product of the two terms is zero. The solutions are found by contracting on both sides with $(\mathbf{b}_T^i \mathbf{b}_T^j - \mathbf{b}_T^2 \, \delta^{ij}/2)$ and δ^{ij}:

$$
\begin{aligned}
A &= \frac{1}{2} \int d^2\mathbf{p}_T \, e^{i\mathbf{b}_T\cdot\mathbf{p}_T} \, \mathbf{p}_T^2 \, h_1^{\perp g}(x, \mathbf{p}_T^2) \\
&= \pi \int_0^\infty dp_T \, p_T^3 \, J_0(b_T \, p_T) \, h_1^{\perp g}(x, \mathbf{p}_T^2) \,,
\end{aligned}
\tag{4.22}
$$

$$
\begin{aligned}
B &= \frac{2}{\mathbf{b}_T^4} \int d^2\mathbf{p}_T \, e^{i\mathbf{b}_T\cdot\mathbf{p}_T} \left[(\mathbf{p}_T \cdot \mathbf{b}_T)^2 - \frac{\mathbf{p}_T^2 \mathbf{b}_T^2}{2}\right] h_1^{\perp g}(x, \mathbf{p}_T^2) \\
&= -\frac{2\pi}{b_T^2} \int_0^\infty dp_T \, p_T^3 \, J_2(b_T \, p_T) \, h_1^{\perp g}(x, \mathbf{p}_T^2) \,.
\end{aligned}
\tag{4.23}
$$

So, the convolution becomes

$$
\begin{aligned}
\mathcal{C}[w h_1^{\perp g} \Delta_h^{[n]}](x, z, \mathbf{q}_T^2) &= -\frac{1}{2\pi} \frac{1}{2M_h^2 \mathbf{q}_T^2} \int d^2\mathbf{b}_T \, e^{-i\mathbf{b}_T\cdot\mathbf{q}_T} \\
\times \left[2(\mathbf{q}_T \cdot \mathbf{b}_T)^2 - \mathbf{q}_T^2 \mathbf{b}_T^2\right] &\int_0^\infty dp_T \, \frac{p_T^3}{b_T^2} \, h_1^{\perp g}(x, \mathbf{p}_T^2) \, J_2(b_T \, p_T) \, \hat{\Delta}_h^{[n]}(z, \mathbf{b}_T^2) \\
= \frac{1}{2M_h^2} \int_0^\infty db_T \, b_T^3 \, J_2(b_T \, q_T) &\int_0^\infty dp_T \, \frac{p_T^3}{b_T^2} \, h_1^{\perp g}(x, \mathbf{p}_T^2) \, J_2(b_T \, p_T) \, \hat{\Delta}_h^{[n]}(z, \mathbf{b}_T^2) \,,
\end{aligned}
\tag{4.24}
$$

where only the B term survived the contraction. Precisely the remaining integral over p_T can be related to the Fourier transform defined in Eq. 4.15

$$\hat{h}_1^{\perp g}(x, \mathbf{b}_T^2) = -\pi \int_0^\infty dp_T \, \frac{p_T^3}{M_h^2} \, J_2(b_T \, p_T) \, h_1^{\perp g}(x, \mathbf{p}_T^2) \,, \tag{4.25}$$

such that:

$$\mathcal{C}[w h_1^{\perp g} \Delta_h^{[n]}](x, z, \mathbf{q}_T^2) = -\int_0^\infty \frac{db_T}{2\pi} \, b_T \, J_2(b_T \, q_T) \, \hat{h}_1^{\perp g}(x, \mathbf{b}_T^2) \, \hat{\Delta}_h^{[n]}(z, \mathbf{b}_T^2) \,. \tag{4.26}$$

Similarly, the convolutions for proton-proton collisions are evaluated [92], i.e.

$$\mathcal{C}[w_2 h_1^{\perp g} h_1^{\perp g}](x_a, x_b, \mathbf{q}_T^2) = \int_0^\infty \frac{db_T}{2\pi} \, b_T \, J_0(b_T q_T) \, \hat{h}_1^{\perp g}(x_a, \mathbf{b}_T^2) \, \hat{h}_1^{\perp g}(x_b, \mathbf{b}_T^2) \,, \tag{4.27}$$

$$\mathcal{C}[w_3 f_1^g h_1^{\perp g}](x_a, x_b, \mathbf{q}_T^2) = \int_0^\infty \frac{db_T}{2\pi} \, b_T \, J_2(b_T q_T) \, \hat{f}_1^g(x_a, \mathbf{b}_T^2) \, \hat{h}_1^{\perp g}(x_b, \mathbf{b}_T^2) \,, \tag{4.28}$$

$$\mathcal{C}[w_4 h_1^{\perp g} \, h_1^{\perp g}](x_a, x_b, \mathbf{q}_T^2) = \int_0^\infty \frac{db_T}{2\pi} \, b_T \, J_4(b_T q_T) \, \hat{h}_1^{\perp g}(x_a, \mathbf{b}_T^2) \, \hat{h}_1^{\perp g}(x_b, \mathbf{b}_T^2) \,. \tag{4.29}$$

For more details of their derivation we refer to [121]. Indeed, the convolutions take a rather simple form in b_T space where the angular structure (determined by the weight) is incorporated by $J_n(b_T \, q_T)$. Our next step involves utilising the evolution equations to assess them at different scales.

As discussed above, the TMDs depend on two auxiliary parameters ζ and μ. To obtain useful predictions for experiments at different scales, equations are needed to relate these functions at different values of their auxiliary parameters. The Collins-Soper equation for the evolution of a Fourier transformed TMD $\hat{f}$ with respect to ζ is [3, 122]

$$\frac{\partial \ln \hat{f}(x, \mathbf{b}_T^2; \zeta, \mu)}{\partial \ln \sqrt{\zeta}} = \hat{K}(b_T, \mu) \,, \tag{4.30}$$

where $\hat{K}$ is the Collins-Soper kernel. This kernel is universal, i.e. it is flavour and spin independent, and does not depend on the momentum fraction x. It is different for quarks and gluons as it depends on the colour representation of the considered parton. The kernel has a renormalisation group equation

$$\frac{d \, \hat{K}(b_T, \mu)}{d \ln \mu} = -\gamma_K(\alpha_s(\mu)) \,, \tag{4.31}$$

like $\hat{f}$:

$$\frac{d \ln \hat{f}(x, \mathbf{b}_T^2; \zeta, \mu)}{d \ln \mu} = \gamma(\alpha_s(\mu), \zeta/\mu^2) \,. \tag{4.32}$$

Derivatives with respect to different variables commute, which gives:

$$\frac{\partial}{\partial \ln \sqrt{\zeta}} \gamma(\alpha_s(\mu), \zeta/\mu^2) = -\gamma_K(\alpha_s(\mu)) \,. \tag{4.33}$$

Therefore, the anomalous dimension can be written as

$$\gamma(\alpha_s(\mu), \zeta/\mu^2) = \gamma(\alpha_s(\mu), 1) - \frac{1}{2}\gamma_K(\alpha_s(\mu)) \ln\frac{\zeta}{\mu^2}\,, \tag{4.34}$$

such that the above differential equations relate $\hat{f}$ at different parameter values:

$$\ln\frac{\hat{f}(x, \mathbf{b}_T^2; \zeta, \mu)}{\hat{f}(x, \mathbf{b}_T^2; \zeta, \mu_0)} = \int_{\mu_0}^{\mu}\frac{d\mu'}{\mu'}\left(\gamma(\alpha_s(\mu'), 1) - \frac{1}{2}\gamma_K(\alpha_s(\mu'))\ln\frac{\zeta}{\mu'^2}\right), \tag{4.35}$$

$$\ln\frac{\hat{f}(x, \mathbf{b}_T^2; \zeta, \mu)}{\hat{f}(x, \mathbf{b}_T^2; \zeta_0, \mu)} = \frac{1}{2}\hat{K}(b_T, \mu)\ln\frac{\zeta}{\zeta_0}\,, \tag{4.36}$$

In particular, we can evolve the TMD from the scales $\{\zeta_0, \mu_0\}$ to the scales $\{\zeta, \mu\}$ by introducing a Sudakov factor S_P as follows

$$\hat{f}(x, \mathbf{b}_T^2; \zeta, \mu) = e^{-S_P(b_T;\zeta,\zeta_0,\mu,\mu_0)}\,\hat{f}(x, \mathbf{b}_T^2; \zeta_0, \mu_0)\,, \tag{4.37}$$

with:

$$\begin{aligned} S_P(b_T; \zeta, \zeta_0, \mu, \mu_0) = &-\frac{1}{2}\hat{K}(b_T, \mu_0)\ln\frac{\zeta}{\zeta_0} \\ &-\int_{\mu_0}^{\mu}\frac{d\mu'}{\mu'}\left(\gamma(\alpha_s(\mu'), 1) - \frac{1}{2}\gamma_K(\alpha_s(\mu'))\ln\frac{\zeta}{\mu'^2}\right). \end{aligned} \tag{4.38}$$

While the renormalisation scale μ in the hard factor should be set to $\mu \sim \mu_H$ to avoid large logarithms of μ/μ_H, the TMDs should be evaluated at a much lower scale in order to avoid large logarithms of μ/M_h or $\mu/\Lambda_{\mathrm{QCD}}$. Instead of selecting a fixed low, but still perturbative, scale for the TMDs, it is common to take $\sqrt{\zeta_0} \sim \mu_0 \sim \mu_b$, where

$$\mu_b \equiv \frac{b_0}{b_T} = \frac{2e^{-\gamma_E}}{b_T}\,, \tag{4.39}$$

and to make sure in the calculation that $\mu_b \leq \mu_H \sim \sqrt{\zeta} \sim \mu$, at which the scattering takes place. The Sudakov factor then expresses the resummation of logarithms in μ_b/μ_H:

$$\hat{f}(x, \mathbf{b}_T^2; \mu_H^2, \mu_H) = e^{-S_P(b_T;\mu_H,\mu_b)}\,\hat{f}(x, \mathbf{b}_T^2; \mu_b^2, \mu_b)\,. \tag{4.40}$$

The TMD scale μ_b should be much smaller than the hard scale μ_H, but it in the intermediate range where it is sufficiently larger than the nonperturbative scale Λ_{QCD}, TMD factorisation remains valid and the scale is still large enough to allow for a perturbative expansion of the Sudakov factor and the TMDs. For this purpose, we must restrict μ_b. On the one hand, the point where perturbation theory starts to fail is defined by $b_{T,\mathrm{max}} = 0.5 - 1.5\,\mathrm{GeV}^{-1}$, equivalent to $0.1 - 0.3\,\mathrm{fm}$, on which we elaborate later in this thesis. A usual method to ensure that $b_T \leq b_{T,\mathrm{max}}$ is the b_T^*-prescription [118], i.e.

$$b_T^* = \frac{b_T}{\sqrt{1 + \left(b_T/b_{T,\mathrm{max}}\right)^2}}\,. \tag{4.41}$$

On the other hand, because evolution should stop at the scale μ_H, we have that $b_{T,\min} = b_0/\mu_H \leq b_T$. This lower limit marks the point beyond which μ_b becomes larger than μ_H, such that it is assured that the perturbative Sudakov factor does not flip sign. This can be done by e.g. the b'_T-prescription [15], given by:

$$b'_T = \sqrt{b_T^2 + b_{T,\min}^2} \, . \tag{4.42}$$

The two expressions should be applied in the right order

$$\mu_b \to \tilde{\mu}'_b = \frac{b_0}{\sqrt{b_T^2 + b_0^2/\mu_H^2}} \to \tilde{\mu}'_{b^*} = \frac{b_0}{\sqrt{b_T^{*2} + b_0^2/\mu_H^2}} \, , \tag{4.43}$$

where we added a tilde on μ'_b to denote its difference with the μ'_b used in [65, 123] that uses a slightly different method to enforce $b_{T,\min} \leq b_T$:

$$\mu_b \to \mu'_{b^*} = \frac{b_0}{b_T^* + b_0/\mu_H} \, . \tag{4.44}$$

The latter prescription is also employed in this thesis, although there is in practice no preference for one or the other as discussed below. The replacement of the scale effectively boils down to a different resummation in the Sudakov factor, e.g. in logarithms of $\tilde{\mu}'_{b^*}/\mu_H$ rather than μ_b/μ_H. This scale is then also the one that should be used in the TMDs (and the TMDShFs).

In summary, the b_T-prescriptions, e.g. Eq. 4.41 and Eq. 4.42, ensure together that $b_{T,\min} \leq b_T \leq b_{T,\max}$. However, we note that $b_T^*(b_T = b_{T,\max}) < b_{T,\max}$, so, besides that the value of $b_{T,\max}$ is not known, b_T^* approaches it slowly and perturbative expressions as a function of $\tilde{\mu}'_{b^*}$ will continue to change when $b_T > b_{T,\max}$. Therefore, there is actually not a clean separation at $b_T = b_{T,\max}$ (after which nonperturbative physics comes into play, i.e. $b_T > b_{T,\max}$) and one does not know exactly what happens when $b_T \leq b_{T,\max}$ either. Similarly, we have that b'_T provides no clean separation at $b_T = b_{T,\min}$ and perturbative expressions as a function of $\tilde{\mu}'_{b^*}$ will continue to change for $b_T < b_{T,\min}$ too. These issues are further addressed in Sec. 6.2.

The perturbative expressions of the kernel and the anomalous dimensions are determined in [124, 125]. Particularly, we have that

$$\hat{K}(b_T, \mu) = -\alpha_s(\mu)\frac{C_A}{\pi}\ln\frac{\mu^2 b_T^2}{b_0^2} + O(\alpha_s^2) \, , \tag{4.45}$$

which equals zero in case $\mu = \mu_b$. Therefore, the perturbative Sudakov factor can be rewritten as

$$S_P(b_T; \mu_H, \mu_b) = \frac{1}{2}\int_{C_1^2\mu_b^2}^{C_2^2\mu_H^2} \frac{d\mu'^2}{\mu'^2}\left[A \ln\frac{C_2^2\,\mu_H^2}{\mu'^2} + B\right] , \tag{4.46}$$

similar to the quark case [120], where:

$$A = \sum_n^\infty A^{(n)}\left(\frac{\alpha_s(\mu)}{\pi}\right)^n , \quad B = \sum_n^\infty B^{(n)}\left(\frac{\alpha_s(\mu)}{\pi}\right)^n . \tag{4.47}$$

The LO expressions are given by

$$A^{(1)} = C_A \tag{4.48}$$

$$B^{(1)} = -C_A\left(\frac{\beta_0}{6} + 2\ln\frac{C_2}{C_1}\right), \tag{4.49}$$

with β_0 defined in Eq. A.16. Employing these we perform a leading-logarithmic (LL) resummation. For next-to-leading-logarithmic (NLL) accuracy, which is also applied in this thesis, we have to include $A^{(2)}$ according to [84], which is given by:

$$A^{(2)} = \frac{C_A}{2}\left[\left(\frac{67}{18} - \frac{\pi^2}{6}\right)N_c - \frac{10}{9}T_R n_f + \beta_0 \ln C_1\right]. \tag{4.50}$$

We note that S_P is spin independent, making it identical for all gluon TMDs, and in the proton-proton case this Sudakov factor is employed twice, once for each TMD, effectively multiplying the right-hand side of Eq. 4.46 by two. Besides, these expressions are also applicable for TMDFFs (see e.g. [122]).

The values C_1 and C_2 in the perturbative Sudakov factor should be of order one; they represent a prescription arbitrariness of the aforementioned differential equations. Typically, it is practical to set $C_1 = C_2 = 1$. However, they can be utilised when scale variation is considered. Specifically, in a complete non-truncated calculation at all orders, there should be no dependence on these (spurious) scales. Therefore, the dependence on these scales serves as an empirical measure of the quality of predictions at a specific order, i.e. varying these scales provides theoretical uncertainties of observables. Often they are varied between 1/2 and 2. The scale μ_b (that multiplies with C_1 in the perturbative Sudakov factor) also enters the TMD functions as can be seen in Eq. 4.40. Therefore, it is natural to define another value C_3 that multiplies with that scale in the TMD functions following [126]. We note that according to [118, 120] this value should actually equal C_1/C_2. In practice, we employ b_T-prescriptions, therefore we point out that C_2 enters via $b_{T,\min}$, e.g. Eq. 4.42, in the restricted version of μ_b as well. This procedure and its results are further discussed in Sec. 6.3.

Adopting the scale $\mu \sim \mu_H$ in the TMDShFs is also expected to lead to logarithms of μ_b/μ_H, which should be resummed. However, there are no rapidity divergences associated to the TMDShFs [70, 127]. So, for the electron-proton case, the natural choice would be $\zeta_A \approx \mu_H^2$, $\zeta_B \approx 1$ instead, similar as in [128] for open heavy-quark pair production in electron-proton collisions. Using again a renormalisation group equation, this leads to a contribution to the overall Sudakov factor at the single logarithm level (performing the integration in S_P by neglecting the μ dependence in α_s), i.e. in the B term of Eq. 4.46. The associated soft-gluon radiation in CO quarkonium production is therefore incorporated by changing S_A at LL accuracy into:

$$S_P(b_T;\mu_H,\mu_b) = \frac{1}{2}\frac{C_A}{\pi}\int_{\mu_b^2}^{\mu_H^2}\frac{d\mu'^2}{\mu'^2}\,\alpha_s(\mu')\left[\ln\frac{\mu_H^2}{\mu'^2} - \left(\frac{\beta_0}{6} + \mathrm{B_{CO}}\right)\right] + O(\alpha_s^2)\,. \tag{4.51}$$

Including the one loop running of α_s presented in Eq. A.17, one can perform the μ

integral explicitly:

$$S_P(b_T;\mu_H,\mu_b) = -\frac{1}{2}\frac{36}{33-2n_f}\left[\ln\frac{\mu_H^2}{\mu_b^2} + \ln\frac{\mu_H^2}{\Lambda_{\rm QCD}^2}\ln\left(1-\frac{\ln(\mu_H^2/\mu_b^2)}{\ln(\mu_H^2/\Lambda_{\rm QCD}^2)}\right)\right.$$
$$\left. + \left(\frac{\beta_0}{6} + \mathrm{B}_{\rm CO}\right)\ln\left(\frac{\ln(\mu_H^2/\Lambda_{\rm QCD}^2)}{\ln(\mu_b^2/\Lambda_{\rm QCD}^2)}\right)\right] + O(\alpha_s^2)\,. \tag{4.52}$$

The specific expression of $\mathrm{B}_{\rm CO}$ will be discussed below. Here we note that the LO MSHT20 PDF set employed is characterised by $\alpha_s(M_Z) = 0.130$. Therefore, by using the one loop running of α_s, $\Lambda_{\rm QCD}$ in our calculations is set by n_f. In particular, we have that $\Lambda_{\rm QCD} = 0.277\,\mathrm{GeV}$ for $n_f = 4$ and $\Lambda_{\rm QCD} = 0.168\,\mathrm{GeV}$ for $n_f = 5$. For simplicity we set $n_f = 4$ when $\mu_H < 2m_b \sim 10\,\mathrm{GeV}$, and $n_f = 5$ otherwise.

The TMDs themselves can be calculated within the collinear formalism as well (the terms that are not resummed in S_P), i.e. the large TM perturbative tails of the TMDs. For the two gluon TMDs considered the explicit expressions at LO are

$$\hat{f}_1^g(x,\mathbf{b}_T^2;\mu_b) = f_1^g(x;\mu_b) + O(\alpha_s) + O(b_T\Lambda_{\rm QCD})\,, \tag{4.53}$$

as we discuss in Sec. 5.2.2, and:

$$\hat{h}_1^{\perp g}(x,\mathbf{b}_T^2;\mu_b) = -\frac{\alpha_s(\mu_b)}{\pi}\int_x^1\frac{dx'}{x'}\left(\frac{x'}{x}-1\right)\left[C_A\, f_1^g(x';\mu_b) + C_F\sum_{i=q,\bar{q}} f_1^i(x';\mu_b)\right]$$
$$+ O(\alpha_s^2) + O(b_T\Lambda_{\rm QCD})\,. \tag{4.54}$$

The later expression is derived in [106]. They both are determined by collinear distributions f_1^a, but start at different orders in α_s since there is no collinear version of $h_1^{\perp g}$, i.e. it requires a helicity flip and therefore an additional gluon exchange. The last term denotes an additional error, which grows large when $b_T \gg \Lambda_{\rm QCD}^{-1}$.

The large TM perturbative tails of the TMDShFs for J/ψ electroproduction were first studied in [129] by a matching calculation with the collinear regime and were found to be the same for polarised quarkonium thereafter [130]. The logarithms that arise can then be resummed in S_P. However, these studies lead to a contradiction as it has been demonstrated for η_c production in proton-proton collisions [127] and for open heavy-quark pair production in electron-proton collisions [131] that there are no double logarithms associated to CO heavy-quark production (hence no rapidity divergences), i.e. they should contribute to $\mathrm{B}_{\rm CO}$ in Eq. 4.51. This mismatch and the correct calculation of $\mathrm{B}_{\rm CO}$ is explained in Ch. 5. Here we present simply the result [132]

$$\hat{\Delta}^{[n]}(z,\mathbf{b}_T^2;\mu_H,\mu_b) = \langle\mathcal{O}^{J/\psi}[n]\rangle\left(1+\frac{\alpha_s}{2\pi}C_A\,\mathrm{B}_{\rm CO}(\mu_H)\ln\frac{\mu_H^2}{\mu_b^2}\right)\delta(1-z)$$
$$+ O(\alpha_s^2) + O(b_T\Lambda_{\rm QCD})\,, \tag{4.55}$$

where:

$$\mathrm{B}_{\rm CO}(\mu_H) = 1 + \ln\frac{\mu_H^2 M_\mathcal{Q}^2}{(Q^2+M_\mathcal{Q}^2)^2}\,. \tag{4.56}$$

To determine the tail of $\hat{\Delta}_h^{[n]}$ requires a study at higher-order α_s study as we will see. We note that the Fourier transformed TMDShFs both start at order α_s^0, in contrast to the large TM perturbative tails of the TMDs discussed above. This order α_s^0 contribution stems from the small TM part, irrespective of whether they are simple expressions without smearing or more realistic versions of $\Delta_{(h)}^{[n]}(z, \mathbf{k}_T^2)$.

We point out that logically there should be an order α_s^0 contribution from $\hat{h}_1^{\perp g}$ as well. In particular, in a model prescription for the TMD, like a Gaussian, its contribution is in general non-zero, while by employing TMD evolution at $\alpha_s = 0$ it is, according to Eq. 4.54. Although in the complete evolution approach a model for the nonperturbative part needs to be taken into account, as discussed below, it leaves this discrepancy. Namely, to obtain a order α_s^0 contribution would imply that the proper nonperturbative contribution for $h_1^{\perp g}$ should be of order α_s^{-1}, while it is naturally of the order α_s^0. To incorporate both an intrinsically present nonperturbative $h_1^{\perp g}$ of order α_s^0 and a perturbative tail of order α_s, one could consider that the TMDs are approximately Gaussian for small TM, but have the proper power-law fall-off for large TM, following the Gaussian plus tail model presented in [65].

To recap, we note that Eqs. 4.46 (as well as 4.51 and 4.52), 4.53, 4.54 and 4.55 hold when μ_b is kept in the perturbative regime. Particularly, we take $\mu_b \to \tilde{\mu}'_{b^*}$ presented in Eq. 4.43 as an example, such that: $b_{T,\min} \leq b_T \leq b_{T,\max}$. While the equations freeze-out for $b_T < b_{T,\min}$ as the evolution stops at $b_T = b_{T,\min}$, when $b_T > b_{T,\max}$ one enters the nonperturbative regime that in principle can only be extracted from data. In addition, it depends on the prescriptions used to separate the perturbative and the nonperturbative components inside the convolutions, and could be very well different for different convolutions. Therefore, one can identify

$$\hat{W}(b_T, \mu_H) \equiv \hat{W}(b_T^*, \mu_H) e^{-S_{NP}(b_T;\mu_H,\mu_{NP})}\,, \tag{4.57}$$

such that $\hat{W}(b_T^*, \mu_H)$ contains the perturbative expressions which is multiplied with a correction factor, called the nonperturbative Sudakov factor S_{NP}, to make up for the difference to the real $\hat{W}(b_T, \mu_H)$. The explicit form of the correction factor is discussed below. Taking this factor into account, we summarise the TMD-evolution formalism by a general expression for the convolutions:

$$\begin{aligned} \mathcal{C}[w f_A f_B](q_T; \mu_H) = \int_0^\infty \frac{db_T}{2\pi}\, b_T\, J_m(b_T q_T)\, e^{-S_P(b_T^*;\mu_H,\tilde{\mu}'_{b^*})} e^{-S_{NP}(b_T;\mu_H,\mu_{NP})} \\ \times \hat{f}_A(b_T^*; \tilde{\mu}'_{b^*})\, \hat{f}_B(b_T^*; \tilde{\mu}'_{b^*})\,. \end{aligned} \tag{4.58}$$

We note that changes in the b_T^*-prescription, i.e. the value of $b_{T,\max}$, should not affect the physical cross section, but only the nonperturbative phenomena that are parametrised in S_{NP}.

In principle there are two convenient ways to study S_{NP}: one can either use a studied quark S_{NP} extracted from data and Casimir scale it, i.e. $C_F \to C_A$, or use a parametrisation. For the latter, it should be of the following form [118, 120]

$$S_{NP}(b_T; \mu_H, \mu_{NP}) = \ln\left(\frac{\mu_H}{\mu_{NP}}\right) g_K(b_T) + g_{f_A}(b_T) + g_{f_B}(b_T)\,, \tag{4.59}$$

where μ_{NP} is a parameter with the dimension of mass, that is chosen to be (near) the smallest scale at which perturbation theory is expected to be valid (see App. A). It is natural to identify $\mu_{NP} = b_0/b_{T,\max}$ in line with the formalism discussed in this section. g_K is related to $\hat{K}$ in S_P, and g_{f_A} and g_{f_B} are attributed to the two TMD functions. General constraints are that $\exp(-S_{NP})$ should be unity at $b_T = 0\,\mathrm{GeV}^{-1}$, and it should smoothly vanish at large b_T in order to exclude contributions from (far) outside the proton ($b_T \gtrsim 0.8\,\mathrm{fm}$). This also guarantees convergence of the convolutions. Therefore, it is logical to choose a simple Gaussian for the correction factor, e.g.

$$S_{NP}(b_T;\mu_H,\mu_{NP}) = A\ln\left(\frac{\mu_H}{\mu_{NP}}\right) b_T^2\,, \tag{4.60}$$

where A is the parameter of the model. In [92] a range of this parameter was employed, $A = 0.64 - 0.04\,\mathrm{GeV}^2$, to cover the maximal and minimal range of the nonperturbative regime for $b_{T,\max} = 1.5\,\mathrm{GeV}^{-1}$. This approach aimed to assess our lack of knowledge on nonperturbative physics by examining its effect on observables. Such a simple Gaussian ansatz works certainly in particular situations, however, it clearly has some limitations as well that are further investigated in Sec. 6.2.

We note that the perturbative Sudakov suppression of the convolutions presented in Eq. 4.58 can be calculated theoretically at $q_T = 0\,\mathrm{GeV}$. Namely, we can apply the saddle point approximation to the following expression [120, 133, 134]

$$\int_0^\infty db_T^2\, b_T^n\, e^{-S_P(b_T)} = \int \frac{d\ln(b_T^2\Lambda_{\mathrm{QCD}}^2)}{(\Lambda_{\mathrm{QCD}}^2)^{1+\frac{n}{2}}} \exp\Big\{\Big(1+\frac{n}{2}\Big)\ln(b_T^2\Lambda_{\mathrm{QCD}}^2) - S_P(b_T)\Big\}\,, \tag{4.61}$$

where we utilise the LO expression of Eq. 4.46 with the one loop expression of α_s, such that the perturbative Sudakov factor can be rewritten as:

$$S_P(b_T) = \int_{\mu_b^2}^{\mu_H^2} \frac{d\mu'^2}{\mu'^2}\frac{1}{\ln\left(\mu'^2/\Lambda_{\mathrm{QCD}}^2\right)}\left(a\ln\frac{\mu_H^2}{\mu'^2} + b\right) + O(\alpha_s^2)\,. \tag{4.62}$$

Employing the Leibniz rule, a saddle point of the integral is found at

$$b_{SP} = \frac{b_0}{\Lambda_{\mathrm{QCD}}}\left(\frac{\mu_H}{\Lambda_{\mathrm{QCD}}}\right)^{\gamma_n} \exp\left(\frac{b}{2a}\gamma_n\right)\,, \tag{4.63}$$

where we defined: $\gamma_n = -a/(a + (1+\frac{n}{2}))$. Therefore, the suppression that arises as function of the hard scale is found to be

$$\int_0^\infty db_T^2\, b_T^n\, e^{-S_P(b_T)} \overset{SP}{\propto} \left(\frac{\mu_H^2}{\Lambda_{\mathrm{QCD}}^2}\right)^{(1+\frac{n}{2})\gamma_n + a(1+\gamma_n+\ln(-\gamma_n))}\,, \tag{4.64}$$

where the μ_H dependence of b is neglected, that can arise from the TMDShFs (although suppressed). In particular, we obtain for $n = 0$ and $n_f = 4$, $(\mu_H^2)^{-0.76}$ in the proton-proton case, and $(\mu_H^2)^{-0.63}$ in the electron-proton case, where the distinction comes from a factor 2 in a. The case of 5 flavours makes only a small difference, i.e. it adds 0.01 in both cases. We note that the saddle point is not very pronounced at small scales. Besides, introducing the nonperturbative Sudakov factor and the b_T-prescriptions (specifically $b_{T,\max}$) will have an effect on the full Sudakov suppression. However, at large scales the majority of the suppression arises from the perturbative Sudakov. Consequently, the effect of the nonperturbative Sudakov can be neglected, such that an improved agreement is expected with the saddle point approximation for large μ_H (especially in the proton-proton case).

Although we have not yet examined specific process observables with the TMD-evolution approach, we have seen that it systematically allows for studies of TMD functions at different scales. Due to the discrimination between perturbative and nonperturbative contributions, it naturally involves model dependence through the nonperturbative Sudakov factor only, which is particularly important for small hard scales. Moreover, it enables the estimation of theoretical uncertainties through scale variation apart from the various nonperturbative uncertainties that can arise. These uncertainties are further investigated in the phenomenological studies presented in Ch. 6.

5

TMD shape functions

As discussed in Sec. 3.4, calculations within the TMD regime need to take into account the TMDShFs that describe final state smearing effects in quarkonium production. In particular, these functions are expected to be important for CO production due to the required soft-gluon radiation to become colourless [70]. On the other hand, it may be that for CS states no TMDShFs need to be taken into account, although we cannot exclude that any non-trivial TMDShFs apply to CS channels too, if one goes to next orders in perturbation theory, e.g. by considering two soft gluon emissions. In Sec. 4.2 it was shown that in the case of CO J/ψ photo- and electroproduction the TMDShFs give non-negligible modifications to the cross section. These were found by a matching procedure between the LTM and HTM region, in which the TMD and collinear differential cross sections are compared in the intermediate TM (ITM) region where both should be valid. The introduction of TMDShFs solves the mismatch between the collinear and TMD expressions by resumming q_T-divergences in the perturbative Sudakov factor [129, 130]. However, the term they found did not match the expectation from a study on hadronic collisions [127]. In this chapter we present the results of [132], where we investigate and solve this discrepancy. First, we calculate the differential cross section of J/ψ electroproduction within collinear factorisation in Sec. 5.1. Thereafter, we perform the naive matching with the cross section in the TMD formalism in Sec. 5.2. In particular, we explain how to evaluate the limiting cases: from the HTM to the ITM region in Sec. 5.2.1 and from the LTM to the ITM region in Sec. 5.2.2. Then the problem of the matching procedure is identified and the correct LO large TM perturbative tails of the TMDShFs are obtained in Sec. 5.3. In Sec. 5.4 we show that an eikonal approximation provides an additional verification of our findings. In Sec. 5.5 we discuss possible universality of the TMDShFs by a proposed factorisation that includes a process-dependent soft factor in analogy to what was done for open heavy-quark pair production in hadronic collisions [30].

5.1 Collinear J/ψ electroproduction

The difference between a collinear calculation and a TMD calculation lies in the master formula for the cross section, while at the amplitude level it proceeds along the same lines as presented in Sec. 3.2. As explained in Sec. 3.3, in the collinear case applicable in the HTM region, the cross section is not sensitive to the initial partonic TM. Specifically, for the process under investigation, the large TM of the quarkonium is produced by the recoil of another outgoing particle. In order to calculate this cross section, we first investigate the LO collinear squared amplitudes of J/ψ photoproduction to observe some simplifications in the gluon-induced hard scattering, which can be used for electroproduction as well. Thereafter, we investigate the difference at the cross section level to obtain the expressions that are necessary for the matching.

For convenience, we start by splitting up the amplitude $\mathcal{O}$ from Eq. 3.13 as follows

$$\mathcal{O}(p,q;k,p_g) = e e_c g_s^2\, \epsilon^{\mu}_{\lambda_a}(p)\epsilon^{\nu}_{\lambda_b}(q)\epsilon^{\rho*}_{\lambda_g}(p_g) \sum_{m=1}^{8} \mathcal{C}_m O_m(q,p;k,p_g)\,, \tag{5.1}$$

where the expressions of the individual gluon-induced Feynman diagrams, shown in Fig. 5.1, are given by:

$$O_1 = 4\,\gamma_\nu \frac{\slashed{P} + 2\slashed{k} - 2\slashed{q} + M_Q}{(P+2k-2q)^2 - M_Q^2}\gamma_\mu \frac{-\slashed{P} + 2\slashed{k} - 2\slashed{p}_g + M_Q}{(P-2k+2p_g)^2 - M_Q^2}\gamma_\rho\,, \tag{5.2}$$

$$O_2 = 4\,\gamma_\rho \frac{\slashed{P} + 2\slashed{k} + 2\slashed{p}_g + M_Q}{(P+2k+2p_g)^2 - M_Q^2}\gamma_\nu \frac{-\slashed{P} + 2\slashed{k} + 2\slashed{p} + M_Q}{(P-2k-2p)^2 - M_Q^2}\gamma_\mu\,, \tag{5.3}$$

$$O_3 = 4\,\gamma_\nu \frac{\slashed{P} + 2\slashed{k} - 2\slashed{q} + M_Q}{(P+2k-2q)^2 - M_Q^2}\gamma_\rho \frac{-\slashed{P} + 2\slashed{k} + 2\slashed{p} + M_Q}{(P-2k-2p)^2 - M_Q^2}\gamma_\mu\,, \tag{5.4}$$

$$O_4 = 2\,\gamma_\nu \frac{\slashed{P} + 2\slashed{k} - 2\slashed{q} + M_Q}{(P+2k-2q)^2 - M_Q^2}\gamma^\sigma \frac{1}{(p-p_g)^2}$$
$$\times \left[g_{\mu\rho}(p+p_g)_\sigma + g_{\rho\sigma}(p-2p_g)_\mu + g_{\sigma\mu}(p_g-2p)_\rho\right]. \tag{5.5}$$

The other expressions, O_5, O_6, O_7 and O_8, can be obtained by interchanging the particles Q and $\bar{Q}$ in the diagrams, i.e. by replacing $k \to -k$ and reversing the fermion flow (like in Fig. 3.2). $\mathcal{C}_m$ denotes the colour factor of each diagram and is given by:

$$\mathcal{C}_1 = \mathcal{C}_6 = \mathcal{C}_7 = \langle 3i, \bar{3}j | 8c\rangle\, (t^a t^b)_{ji}\,, \tag{5.6}$$

$$\mathcal{C}_2 = \mathcal{C}_3 = \mathcal{C}_5 = \langle 3i, \bar{3}j | 8c\rangle\, (t^b t^a)_{ji}\,, \tag{5.7}$$

$$\mathcal{C}_4 = \mathcal{C}_8 = \langle 3i, \bar{3}j | 8c\rangle\, i f^{abd} (t^d)_{ji}\,. \tag{5.8}$$

Using Eq. 3.44 and evaluating the colour traces (see App. A), we have the following colour factors for the production of the bound $Q\bar{Q}$ pair in a CS state

$$\mathcal{C}_1 = \mathcal{C}_2 = \mathcal{C}_3 = \mathcal{C}_5 = \mathcal{C}_6 = \mathcal{C}_7 = \frac{1}{2}\frac{\delta^{ab}}{\sqrt{N_c}}\,, \quad \mathcal{C}_4 = \mathcal{C}_8 = 0\,, \tag{5.9}$$

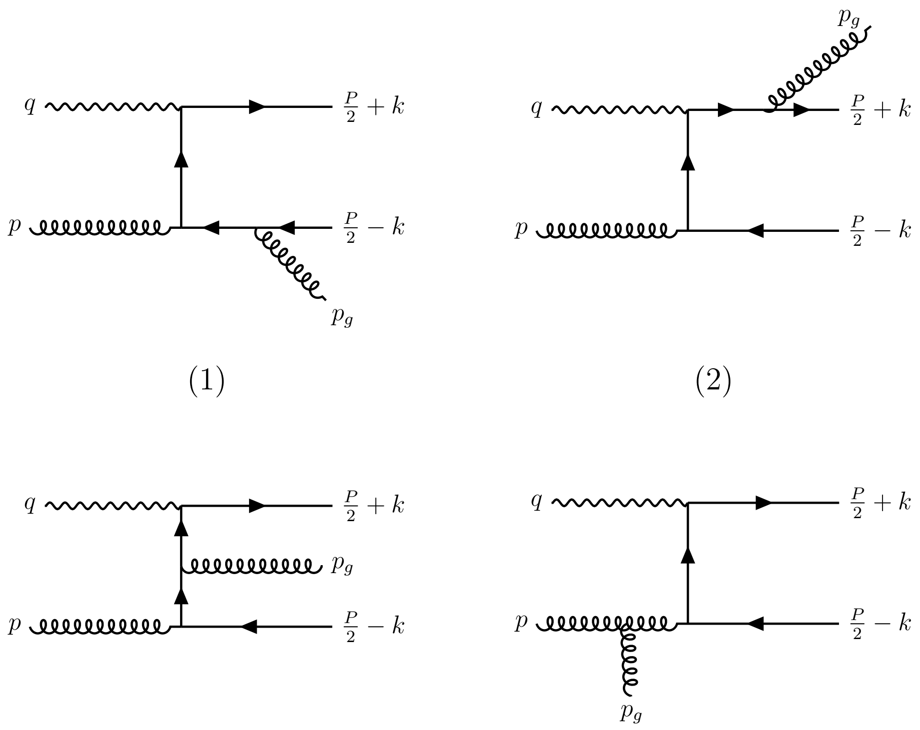

(1) (2)

(3) (4)

Figure 5.1: LO Feynman diagrams for $\gamma + g \to Q + \bar{Q} + g$. In total there are eight diagrams; the other four are obtained by interchanging the particles Q and $\bar{Q}$.

and the following factors for a CO state:

$$\mathcal{C}_1 = \mathcal{C}_6 = \mathcal{C}_7 = \frac{\sqrt{2}}{4}(d^{abc} + if^{abc})\,, \tag{5.10}$$

$$\mathcal{C}_2 = \mathcal{C}_3 = \mathcal{C}_5 = \frac{\sqrt{2}}{4}(d^{abc} - if^{abc})\,, \tag{5.11}$$

$$\mathcal{C}_4 = \mathcal{C}_8 = \frac{\sqrt{2}}{2} if^{abc}\,. \tag{5.12}$$

Employing these colour factors we can simplify the amount of diagrams that need to be evaluated. Taking $k = 0$, see Eq. 3.26 for S-wave amplitudes, we have the following symmetry relations for the ${}^3S_1$ state ($C = -1$)

$$\begin{aligned}
\mathrm{Tr}[O_1(0)\mathcal{P}_{1S_z}(0)] &= \mathrm{Tr}[O_5(0)\mathcal{P}_{1S_z}(0)]\,,\\
\mathrm{Tr}[O_2(0)\mathcal{P}_{1S_z}(0)] &= \mathrm{Tr}[O_6(0)\mathcal{P}_{1S_z}(0)]\,,\\
\mathrm{Tr}[O_3(0)\mathcal{P}_{1S_z}(0)] &= \mathrm{Tr}[O_7(0)\mathcal{P}_{1S_z}(0)]\,,\\
\mathrm{Tr}[O_4(0)\mathcal{P}_{1S_z}(0)] &= -\mathrm{Tr}[O_8(0)\mathcal{P}_{1S_z}(0)]\,,
\end{aligned} \tag{5.13}$$

with the CS factor

$$\mathcal{C}_1 + \mathcal{C}_5 = \mathcal{C}_2 + \mathcal{C}_6 = \mathcal{C}_3 + \mathcal{C}_7 = \frac{\delta^{ab}}{\sqrt{N_c}}\,, \tag{5.14}$$

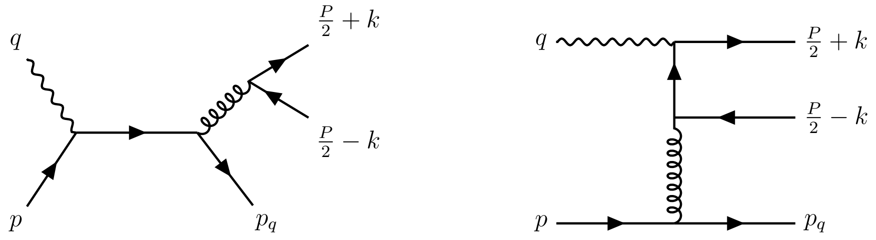

(1) (2)

Figure 5.2: LO Feynman diagrams for $\gamma + q(\bar{q}) \to Q + \bar{Q} + q(\bar{q})$. In total there are four diagrams; the other two are given by interchanging the particles Q and $\bar{Q}$.

or the CO factor:

$$\mathcal{C}_1 + \mathcal{C}_5 = \mathcal{C}_2 + \mathcal{C}_6 = \mathcal{C}_3 + \mathcal{C}_7 = \frac{\sqrt{2}}{2} d^{abc} \,. \tag{5.15}$$

We note that diagrams 4 and 8 do not contribute to the amplitude in this case. The amplitude expression in Eq. 5.1 for the ${}^3S_1$ state is therefore evaluated by only three diagrams, times the appropriate CS factor from Eq. 5.14 or CO factor from Eq. 5.15, which enters Eq. 3.34.

For the ${}^1S_0$ state ($C = +1$) the symmetry relations are given by

$$\begin{aligned}
\mathrm{Tr}[O_1(0)\mathcal{P}_{00}(0)] &= -\mathrm{Tr}[O_5(0)\mathcal{P}_{00}(0)] \,, \\
\mathrm{Tr}[O_2(0)\mathcal{P}_{00}(0)] &= -\mathrm{Tr}[O_6(0)\mathcal{P}_{00}(0)] \,, \\
\mathrm{Tr}[O_3(0)\mathcal{P}_{00}(0)] &= -\mathrm{Tr}[O_7(0)\mathcal{P}_{00}(0)] \,, \\
\mathrm{Tr}[O_4(0)\mathcal{P}_{00}(0)] &= \mathrm{Tr}[O_8(0)\mathcal{P}_{00}(0)] \,,
\end{aligned} \tag{5.16}$$

with the CO factors

$$\mathcal{C}_1 - \mathcal{C}_5 = -\mathcal{C}_2 + \mathcal{C}_6 = -\mathcal{C}_3 + \mathcal{C}_7 = \frac{\sqrt{2}}{2} i f^{abc} \,, \quad \mathcal{C}_4 + \mathcal{C}_8 = \sqrt{2} i f^{abc} \,, \tag{5.17}$$

such that Eq. 5.1 for the ${}^1S_0$ state requires only four diagrams to be evaluated, in order to compute Eq. 3.33 (note the factor of 2 difference in the colour factors when $m = 4$). The CS contribution is zero in this case.

Lastly, see Eq. 3.27 for P-wave amplitudes, the symmetry relations for ${}^3P_J$ states ($C = +1$) are given by:

$$\begin{aligned}
\mathrm{Tr}[\hat{O}_{1\alpha}(0)\mathcal{P}_{1S_z}(0) + O_1(0)\hat{\mathcal{P}}_{1S_z\alpha}(0)] &= -\mathrm{Tr}[\hat{O}_{5\alpha}(0)\mathcal{P}_{1S_z}(0) + O_5(0)\hat{\mathcal{P}}_{1S_z\alpha}(0)] \,, \\
\mathrm{Tr}[\hat{O}_{2\alpha}(0)\mathcal{P}_{1S_z}(0) + O_2(0)\hat{\mathcal{P}}_{1S_z\alpha}(0)] &= -\mathrm{Tr}[\hat{O}_{6\alpha}(0)\mathcal{P}_{1S_z}(0) + O_6(0)\hat{\mathcal{P}}_{1S_z\alpha}(0)] \,, \\
\mathrm{Tr}[\hat{O}_{3\alpha}(0)\mathcal{P}_{1S_z}(0) + O_3(0)\hat{\mathcal{P}}_{1S_z\alpha}(0)] &= -\mathrm{Tr}[\hat{O}_{7\alpha}(0)\mathcal{P}_{1S_z}(0) + O_7(0)\hat{\mathcal{P}}_{1S_z\alpha}(0)] \,, \\
\mathrm{Tr}[\hat{O}_{4\alpha}(0)\mathcal{P}_{1S_z}(0) + O_4(0)\hat{\mathcal{P}}_{1S_z\alpha}(0)] &= \mathrm{Tr}[\hat{O}_{8\alpha}(0)\mathcal{P}_{1S_z}(0) + O_8(0)\hat{\mathcal{P}}_{1S_z\alpha}(0)] \,.
\end{aligned} \tag{5.18}$$

Therefore, the ${}^3P_J$ amplitudes, Eqs. 3.41, 3.42 and 3.43, can be obtained using the same trick as for the ${}^1S_0$ amplitude, with no CS contributions. We note that the ${}^1P_1$ amplitude (presented in Eq. 3.35) is suppressed in v for J/ψ production (see Table 3.2) and therefore not considered.

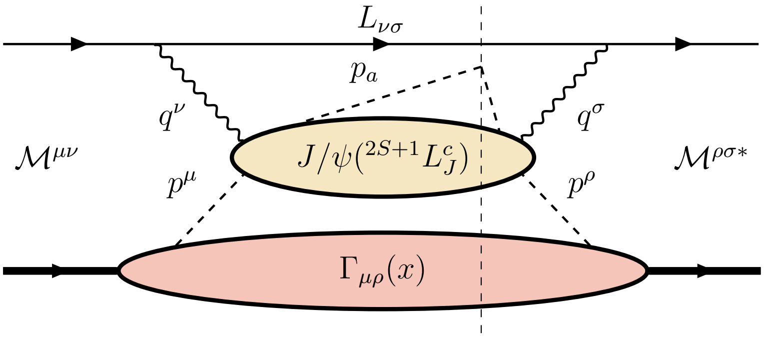

Figure 5.3: The LO inclusive cross section for $e+p \to e'+J/\psi+a+X$ within collinear factorisation and NRQCD.

For the quark contributions, shown in Fig. 5.2, equivalent simplifications are not explored because these diagrams are mathematically much easier to evaluate, i.e. they are more straightforward since they contain only one quark propagator. We note that, in this case, the quarkonium must be in a CO state to obtain non-zero amplitudes, as a three-flavour scheme is adopted. If (anti)charm contributions were included, four additional diagrams would need to be evaluated.

As usual in $2 \to 2$ processes we employ partonic Lorentz-invariant Mandelstam variables for the kinematics, which are defined for this process as follows:

$$\hat{s} = (q+p)^2\,, \quad \hat{t} = (q-P)^2\,, \quad \hat{u} = (p-P)^2\,, \quad \hat{s}+\hat{t}+\hat{u} = M_{\mathcal{Q}}^2\,. \tag{5.19}$$

The summation over the transverse polarisations of the photon, as well as the initial and final on-shell gluons, is performed using completeness relations, see Eq. A.24 with $n^\alpha = P^\alpha/M_{\mathcal{Q}}$. For the quark-induced diagrams, we need to sum over spinors instead, which are provided in Eqs. A.26 and A.27. Employing these relations, we confirm the squared amplitudes from previous photoproduction studies, gluon induced [135] as well as quark induced [136]. For the explicit expressions we refer to their appendices.

Besides the kinematic variables in Eq. 3.71, we introduce the partonic scaling variables:

$$\hat{x} = \frac{Q^2}{2p\cdot q}, \quad \hat{z} = \frac{p\cdot P}{p\cdot q}\,. \tag{5.20}$$

If we neglect the proton mass and any smearing effects, we can write

$$\hat{x} = \frac{x_B}{x}, \quad \hat{z} = z\,, \tag{5.21}$$

which implies that:

$$\hat{x}p = x_B P \quad \text{and} \quad \hat{x} \geq x_B\,. \tag{5.22}$$

In the collinear computation the proton is parametrised by PDFs via the collinear correlator derived in Eq. 2.30, therefore the inclusive cross section for quarkonium electroproduction with an unpolarised proton, shown in Fig. 5.3, can be written as:

$$\sum_{a=q,\bar{q},g} d\sigma(e+p \to e'+J/\psi+a+X) = \int_0^1 dx \sum_a f_1^a(x;\mu) \times d\sigma(e+a \to e'+J/\psi+a)\,. \tag{5.23}$$

Furthermore, according to the NRQCD factorisation formalism, i.e. Eq. 3.9, we write

$$d\sigma(e+a\to e'+J/\psi+a)=\sum_n d\hat{\sigma}\big(e+a\to e'+c\bar{c}(n)+a\big)\,\langle\mathcal{O}^{J/\psi}[n]\rangle\,, \tag{5.24}$$

which we again truncate at order v^4, i.e. $n={}^3S_1^1,\ {}^1S_0^8,\ {}^3S_1^8$ and ${}^3P_J^8$ with $J=0,1,2$. We note that the outgoing parton can fragment into a jet for example. Decomposing the partonic subprocess into a leptonic part, $e\to e'+\gamma^*$, L, and a hadronic one, $\gamma^*+a\to c\bar{c}(n)+a$, H, from which the virtual photon leg is amputated, we can write the partonic cross section as

$$d\hat{\sigma}\big(e+a\to e'+c\bar{c}(n)+a\big)=\frac{1}{2sx}\,\frac{1}{2}\,\frac{1}{Q^4}\,d\mathrm{PS}_3(p+q;l',P,p_a)\,L^{\mu\nu}\,H_{\mu\nu}^{a[n]}\,, \tag{5.25}$$

where the leptonic tensor L is given in Eq. 3.73 and the hadronic tensor H, the squared amplitude of the hadronic scattering subprocess, is calculated with Eq. 3.11 (from which the LDMEs are removed). The latter includes the average over the colour multiplicities ($N_g=d(G)$ and $N_q=N_{\bar{q}}=d(F)$, see App. A) and the summation over polarisations when $a=g$ or the summation over spinors when $a=q$. The first factor in Eq. 5.25 comes from the flux, the second is due to the average over the initial parton spin and the third factor arises from the squared photon propagator, like in the TMD cross section presented in Eq. 3.72. Moreover, we introduced the general Lorentz-invariant phase-space measure:

$$d\mathrm{PS}_n(p;p_1,\ldots,p_n)=(2\pi)^4\,\delta^4\Big(p-\sum_n p_n\Big)\prod_n\frac{d^3p_n}{(2\pi)^3 2p_n^0}\,. \tag{5.26}$$

The frame where the momenta P_h and q are collinear and lie on the $\hat{z}$ axis, is discussed in Sec. 3.4. In particular, the decomposition of the four-momenta in terms of light-like vectors n_+ and n_- is given in Eqs. 3.74, 3.75, 3.76, 3.77 (dismiss p_T) and 3.78. Employing these, the Mandelstam variables in Eq. 5.19 read:

$$\hat{s}=Q^2\left(\frac{1-\hat{x}}{\hat{x}}\right), \tag{5.27}$$

$$\hat{t}=-(1-\hat{z})Q^2-\frac{1}{\hat{z}}\mathbf{P}_\perp^2-\frac{1-\hat{z}}{\hat{z}}M_\mathcal{Q}^2\,, \tag{5.28}$$

$$\hat{u}=-\frac{\hat{z}}{\hat{x}}Q^2+M_\mathcal{Q}^2\,. \tag{5.29}$$

Another convenient reference frame is the one in which the hadron four-momenta P and P_h are collinear, where the light-like vectors (neglecting the proton mass again) can be expressed as:

$$k_+^\mu=P_h^\mu,\qquad k_-^\mu=\frac{1}{P_h\cdot P}\left(P^\mu-\frac{M_\mathcal{Q}^2}{2P_h\cdot P}P_h^\mu\right). \tag{5.30}$$

Hence, the four-momentum of the virtual photon is defined by

$$q^\mu=-x_B\left(1-\frac{q_T^2}{Q^2}\right)k_+^\mu+\frac{Q^2}{2x_B}k_-^\mu+q_T^\mu\,, \tag{5.31}$$

and the following relations between the light-like vectors of the two frames are found:

$$n_+^\mu = k_+^\mu \,, \qquad n_-^\mu = 2x_B^2 \frac{\mathbf{q}_T^2}{Q^4} k_+^\mu + k_-^\mu + \frac{2x_B}{Q^2} q_T^\mu \,. \tag{5.32}$$

In the frame where the four-momenta are expressed in terms of k_+ and k_-, the expression for $\hat{t}$ is different

$$\hat{t} = -(1-\hat{z})Q^2 - \hat{z}\mathbf{q}_T^2 - \frac{1-\hat{z}}{\hat{z}} M_{\mathcal{Q}}^2 \,, \tag{5.33}$$

hence, by comparing with Eq. 5.28, we obtain the relation between the TM of the photon with respect to the hadrons, and the TM of the quarkonium with respect to the photon and the proton:

$$\mathbf{q}_T^2 = \frac{\mathbf{P}_\perp^2}{\hat{z}^2} \,. \tag{5.34}$$

The quarkonium phase space and the lepton phase space are given in Eq. 3.81 and Eq. 3.82, respectively. The remaining phase space of the outgoing parton can be simplified together with the momentum conserving delta function, i.e. we relate the momentum of the outgoing particle to the Mandelstam variables

$$p_a^2 = (p+q-P)^2 = (p+q)^2 + P^2 - 2(p+q)\cdot P = \hat{s} + \hat{t} + \hat{u} - M_{\mathcal{Q}}^2 + Q^2 \,, \tag{5.35}$$

such that we can write

$$\begin{aligned} \int \frac{d^3 p_a}{(2\pi)^3 2p_a^0}\, \delta^4(q+p-P-p_a) &= (2\pi)^{-3} \int d^4 p_a\, \delta(p_a^2 - m_i^2)\Big|_{p_i^0>0}\, \delta^4(q+p-P-p_a) \\ &= (2\pi)^{-3}\, \delta(\hat{s} + \hat{t} + \hat{u} - M_{\mathcal{Q}}^2 + Q^2) \,, \end{aligned} \tag{5.36}$$

where we neglected the mass of the outgoing particle. Furthermore, we rewrite the momentum conserving delta function as

$$\delta(\hat{s} + \hat{t} + \hat{u} - M_{\mathcal{Q}}^2 + Q^2) = \frac{1}{\hat{z}Q^2}\, \delta(F(\hat{x},\hat{z})) \,, \tag{5.37}$$

where we have defined

$$F(\hat{x},\hat{z}) = \frac{\mathbf{q}_T^2}{Q^2} + \frac{1-\hat{z}}{\hat{z}^2}\frac{M_{\mathcal{Q}}^2}{Q^2} - \frac{(1-\hat{x})(1-\hat{z})}{\hat{x}\hat{z}} \,, \tag{5.38}$$

using Eqs. 5.27, 5.28, 5.29 and 5.34. The complete differential cross section for the process under investigation, i.e. Eq. 5.23, can therefore be rewritten as follows, by performing a change to the variable $\hat{x}$:

$$\begin{aligned} \frac{d\sigma(J/\psi)}{dx_B\, dy\, dz\, d\mathbf{q}_T^2\, d\phi_T} &= \frac{1}{64}\, \frac{1}{(2\pi)^4}\, yz \int_{x_B}^{\hat{x}_{\max}} \frac{d\hat{x}}{\hat{x}} \int_z^1 \frac{d\hat{z}}{\hat{z}}\, \delta\big(F(\hat{x},\hat{z})\big) \\ &\times \sum_a \sum_n \left[\frac{1}{Q^6}\, f_1^a\!\left(\frac{x_B}{\hat{x}};\mu\right) L^{\mu\nu}\, H_{\mu\nu}^{a[n]}\, \langle \mathcal{O}^{J/\psi}[n] \rangle \right] \delta(z-\hat{z}) \,. \end{aligned} \tag{5.39}$$

The kinematic constraint

$$\hat{x}_{\max} = \frac{Q^2}{Q^2 + M_{\mathcal{Q}}^2}\,, \tag{5.40}$$

for the integration over $\hat{x}$, follows from Eq. 3.80. Besides, we rewrite the leptonic tensor as [129]

$$\begin{aligned} L^{\mu\nu} = \frac{e^2 Q^2}{y^2}\Big\{ & \left[1 + (1-y)^2\right] \epsilon_T^{\mu\nu} + 4(1-y)\Big(\epsilon_L^{\mu\nu} + \epsilon_{\cos 2\phi_T}^{\mu\nu}\Big) \\ & + 2(2-y)\sqrt{1-y}\,\epsilon_{\cos\phi_T}^{\mu\nu}\Big\}\,, \end{aligned} \tag{5.41}$$

which can be found by substituting Eqs. 3.75 and 3.76 in Eq. 3.73, where we introduced the tensors

$$\begin{aligned} \epsilon_T^{\mu\nu} &= -g_T^{\mu\nu}\,, \qquad \epsilon_L^{\mu\nu} = \epsilon_L^{\mu}\epsilon_L^{\nu}\,, \\ \epsilon_{\cos\phi_T}^{\mu\nu} &= \Big(\epsilon_L^{\mu}\hat{l}_\perp^{\nu} + \epsilon_L^{\nu}\hat{l}_\perp^{\mu}\Big), \qquad \epsilon_{\cos 2\phi_T}^{\mu\nu} = \left(\hat{l}_\perp^{\mu}\hat{l}_\perp^{\nu} + \frac{1}{2}g_T^{\mu\nu}\right), \end{aligned} \tag{5.42}$$

and the longitudinal polarisation vector of the exchanged virtual photon

$$\epsilon_L^{\mu} = \frac{1}{Q}\left(q + \frac{Q^2}{P_h\cdot q}P_h\right)^{\mu}, \tag{5.43}$$

which fulfils the relations $\epsilon_L^2 = 1$ and $q_\mu \epsilon_L^{\mu} = 0$. Moreover, the transverse projector defined in Eq. 2.11 can be written as

$$g_T^{\mu\nu} = g^{\mu\nu} - \frac{1}{P_h\cdot q}\left(q^\mu P_h^\nu + P_h^\mu q^\nu\right) - \frac{Q^2}{(P_h\cdot q)^2}P_h^\mu P_h^\nu\,, \tag{5.44}$$

for which $\epsilon_T^2 = -2$ and $q_\mu \epsilon_T^{\mu\nu} = 0$. We note that the sum of these tensors, $\epsilon_T^{\mu\nu} - \epsilon_L^{\mu\nu}$, gives the polarisation tensor of an unpolarised spin-1 boson with mass q^2 following Eq. A.25. Moreover, the Ward identity, given in Eq. C.3, can be employed for further simplifications of the leptonic tensor in the cross section. This identity is generally not true for individual Feynman diagrams, i.e. one must sum over the diagrams at any given order. By taking Eq. 5.41 into account, the final result can be expressed as

$$\begin{aligned} \frac{d\sigma(J/\psi)}{dx_B\,dy\,dz\,d\mathbf{q}_T^2\,d\phi_T} = \frac{\alpha}{yQ^2}\Big\{ & \left[1 + (1-y)^2\right] \mathcal{F}_{UU,T} + 4(1-y)\,\mathcal{F}_{UU,L} \\ & + 2(2-y)\sqrt{1-y}\cos\phi_T\,\mathcal{F}_{UU}^{\cos\phi_T} + 4(1-y)\cos 2\phi_T\,\mathcal{F}_{UU}^{\cos 2\phi_T}\Big\}\,, \end{aligned} \tag{5.45}$$

where we have used a different font for the structure functions to denote their difference to the ones presented in Eq. 3.83 that are calculated within TMD factorisation. They are given by

$$\begin{aligned} \mathcal{F}_{UU,\mathcal{P}}^{\Phi} = & \frac{1}{4(4\pi)^3}\,z\int_{x_B}^{\hat{x}_{\max}}\frac{d\hat{x}}{\hat{x}}\int_z^1\frac{d\hat{z}}{\hat{z}}\,\delta\big(F(\hat{x},\hat{z})\big) \\ & \times \sum_a\sum_n\left[\frac{1}{Q^2}\,f_1^a\!\left(\frac{x_B}{\hat{x}};\mu\right)\epsilon_{\mathcal{P};\Phi}^{\mu\nu}\,H_{\mu\nu}^{a[n]}\,\langle\mathcal{O}^{J/\psi}[n]\rangle\right]\delta(z-\hat{z})\,, \end{aligned} \tag{5.46}$$

where we have introduced a shorthand notation in which $\mathcal{P}$ refers to the virtual photon polarisation and Φ to the azimuthal modulation when applicable.

We note that this process was studied in [137,138]. In particular, we have that our $F_{UU,T}$ and $F_{UU,L}$ are related to the explicit hard factors provided in the first reference:

$$\epsilon_T^{\mu\nu}\, H_{\mu\nu}^{a[n]} = 64\pi\, (\hat{s}+Q^2)^2\, F_a[n]\, T_a[n]\,, \tag{5.47}$$

$$\epsilon_L^{\mu\nu}\, H_{\mu\nu}^{a[n]} = -64\pi\, Q^2\, (\hat{s}+Q^2)^2\, F_a[n]\, L_a[n]\,. \tag{5.48}$$

This can be observed by rewriting Eq. 5.39 as follows

$$\frac{d\sigma(J/\psi)}{dx_B\, dy\, dz\, d\mathbf{P}_\perp^2\, d\phi_T} = \frac{\alpha}{yQ^2}\frac{1}{4(4\pi)^3}\sum_a\sum_n\int_{x_B}^{\hat{x}_{\max}} d\hat{x}\, f_1^a\!\left(\frac{x_B}{\hat{x}};\mu\right)\delta\big(D(\hat{x},z)\big)$$
$$\times\left\{[1+(1-y)^2]\,\epsilon_T^{\mu\nu}\, H_{\mu\nu}^{a[n]} + 4(1-y)\,\epsilon_L^{\mu\nu}\, H_{\mu\nu}^{a[n]}\right\}, \tag{5.49}$$

where we introduced:

$$D(\hat{x},z) = \hat{x}z^2Q^2\, F(\hat{x},z)\,. \tag{5.50}$$

Integrating over ϕ_T and changing the integration variable back to x gives

$$\frac{d\sigma(J/\psi)}{dy\, dx_B\, d\mathbf{P}_\perp^2\, dz} = \frac{\alpha}{yQ^2}\frac{1}{32(2\pi)^2}\sum_a\sum_n\int_{x_B/\hat{x}_{\max}}^{1} dx\, f_1^a(x;\mu)\,\frac{1}{x_B}\frac{Q^4}{(\hat{s}+Q^2)^2}\,\delta\big(D(\hat{x},z)\big)$$
$$\times\left\{[1+(1-y)^2]\,\epsilon_T^{\mu\nu}\, H_{\mu\nu}^{a[n]} + 4(1-y)\,\epsilon_L^{\mu\nu}\, H_{\mu\nu}^{a[n]}\right\}, \tag{5.51}$$

such that by subsequently changing $dx_B\, d\mathbf{P}_\perp^2 \to dQ^2\, d\hat{t}$ and integrating over z (employing the delta function) confirms [137]:

$$\frac{d\hat{\sigma}\big(c\bar{c}(n)+a\big)}{dy\, dQ^2\, d\hat{t}} = \frac{\alpha}{2\pi}\, F_a[n]\left\{\frac{1+(1-y)^2}{yQ^2}\, T_a[n] - \frac{4(1-y)}{y}\, L_a[n]\right\}. \tag{5.52}$$

5.2 Matching high and low TM

So far we have discussed that, depending on the value of q_T, two different TM regions are determined: the HTM region is given by the condition $q_T \gg \Lambda_{\mathrm{QCD}}$, while the LTM region corresponds to $q_T \ll \mu_H$. These regions denote the collinear and TMD regime, respectively. Adopting the proper factorisations in each regime enables one to separate the short-distance from the long-distance contributions in the differential cross sections and calculate them. In the ITM region, namely $\Lambda_{\mathrm{QCD}} \ll q_T \ll \mu_H$, we have that both prescriptions of the process are valid, such that the differential cross section within this overlap region should match, schematically shown in Fig. 5.4. The idea is as follows: the mismatch that occurs in the ITM is solved by introducing the TMDShFs in the LTM description. Particularly, we perform this computation at LO in order to find the large TM perturbative tails of the TMDShFs.

The differential cross section of the process was derived for the LTM region in Sec. 3.4 and for the HTM region in Sec. 5.1. Therefore, to perform the actual matching

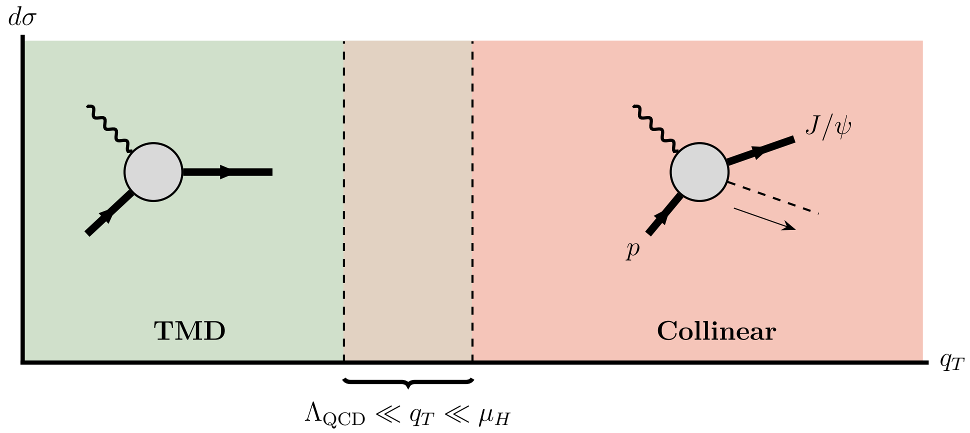

Figure 5.4: Schematical overview of matching the TMD and collinear differential cross section of the investigated process $e+p \to e'+J/\psi+X$: the mismatch of the differential cross section in the overlap region is solved by introducing the TMDShFs.

it remains to obtain the differential cross section in the ITM region from the HTM region and from the LTM region. The latter is done by utilising evolution, while the former can be achieved by replacing the momentum conserving Dirac delta function in the differential cross section by its expansion in the small-q_T limit [129, 139].

5.2.1 From HTM to ITM

Applying the expanded delta function in Eq. 5.46, derived in App. D, we obtain the leading power behaviour of the structure functions[1]

$$F_{UU,\mathcal{P}} = \sigma_{UU,\mathcal{P}} \frac{\alpha_s}{\mathbf{q}_T^2} \left[L(\mathbf{q}_T^2)\, f_1^g(x;\mu) + (P_{gg} \otimes f_1^g + P_{gi} \otimes f_1^i)(x;\mu) \right] , \tag{5.55}$$

$$F_{UU}^{\cos 2\phi_T} = \sigma_{UU}^{\cos 2\phi_T} \frac{\alpha_s}{\mathbf{q}_T^2} \left[(\delta P_{gg} \otimes f_1^g)(x;\mu) + (\delta P_{gi} \otimes f_1^i)(x;\mu) \right] , \tag{5.56}$$

where a sum over $i = q, \bar{q}$ is understood. Here we have defined the logarithmic function

$$L(\mathbf{q}_T^2) \equiv C_A \left\{ 2 \ln \left(\frac{Q^2 + M_Q^2}{\mathbf{q}_T^2} \right) - \frac{\beta_0}{6} \right\} , \tag{5.57}$$

and:

$$x \equiv x_B / \hat{x}_{\max} \, . \tag{5.58}$$

---

[1] To perform the $\hat{z} \to 1$ and $\hat{x}' \to 1$ limits that appear in Eq. D.21 one can use the following replacements from the delta function:

$$\frac{1}{1-\hat{z}} = \frac{1}{\mathbf{q}_T^2} \frac{Q^2(1-\hat{x}')\hat{z} + M_Q^2(\hat{z}-\hat{x}')}{\hat{x}'\hat{z}^2} , \tag{5.53}$$

$$\frac{1}{1-\hat{x}'} = \frac{\hat{z}(1-\hat{z})}{\hat{z}} \frac{Q^2 + M_Q^2}{\hat{z}^2\mathbf{q}_T^2 + (1-\hat{z})^2 M_Q^2} \, . \tag{5.54}$$

Up to corrections of $O(\Lambda_{\rm QCD}/q_T)$ and $O\big(q_T^2/(Q^2+M_{\mathcal{Q}}^2)\big)$ these structure functions are valid. Furthermore, $F_{UU}^{\cos\phi_T}$ is power-suppressed by a factor of $q_T/\sqrt{Q^2+M_{\mathcal{Q}}^2}$ compared to the others ones and is not considered for matching, since there exist no $\mathcal{F}_{UU}^{\cos\phi_T}$ at the order we consider. The symbol $\otimes$ denotes a convolution in the longitudinal momentum fractions, i.e.

$$(P\otimes f)(x;\mu) = \int_x^1 \frac{d\hat{x}'}{\hat{x}'}\, P(\hat{x}';\mu)\, f\left(\frac{x}{\hat{x}'};\mu\right), \tag{5.59}$$

where $\hat{x}'$ is defined in Eq. D.2. The well-known unpolarised splitting functions read [140]

$$P_{gg}(x) = 2C_A\left[\frac{x}{(1+x)_+} + \frac{1-x}{x} + x(1-x)\right] + \delta(1-x)\, C_A\frac{\beta_0}{6}, \tag{5.60}$$

$$P_{gq}(x) = P_{g\bar{q}}(x) = C_F\frac{1+(1-x)^2}{x}, \tag{5.61}$$

while the splitting functions of an unpolarised parton into a linearly polarised gluon are given by [106, 141]:

$$\delta P_{gg}(x) = C_A\frac{1-x}{x}, \tag{5.62}$$

$$\delta P_{gq}(x) = \delta P_{g\bar{q}}(x) = C_F\frac{1-x}{x}. \tag{5.63}$$

We note that the '+'-prescription on the singular parts of the splitting functions is given in Eq. D.11 and that the β_0 term in P_{gg} cancels with the second term of the logarithmic function L, given in Eq. 5.57, in $F_{UU,T}$ and $F_{UU,L}$.

The quantities $\sigma_{UU,\mathcal{P}}$ and $\sigma_{UU}^{\cos 2\phi_T}$, that are related to the partonic process $\gamma^* + g \to [Q\bar{Q}]$, can be written as

$$\begin{aligned}\sigma_{UU,T} = {}& \frac{\alpha\alpha_s e_c^2}{M_{\mathcal{Q}}(M_{\mathcal{Q}}^2+Q^2)}\Bigg[\langle\mathcal{O}^{J/\psi}[{}^1S_0^8]\rangle \\ & + 4\frac{(7M_{\mathcal{Q}}^4 + 2M_{\mathcal{Q}}^2Q^2 + 3Q^4)}{M_{\mathcal{Q}}^2(M_{\mathcal{Q}}^2+Q^2)^2}\langle\mathcal{O}^{J/\psi}[{}^3P_0^8]\rangle\Bigg]\,\delta(1-z),\end{aligned} \tag{5.64}$$

$$\sigma_{UU,L} = \frac{\alpha\alpha_s e_c^2}{M_{\mathcal{Q}}(M_{\mathcal{Q}}^2+Q^2)}\left[16\frac{Q^2}{(M_{\mathcal{Q}}^2+Q^2)^2}\langle\mathcal{O}^{J/\psi}[{}^3P_0^8]\rangle\right]\delta(1-z), \tag{5.65}$$

$$\begin{aligned}\sigma_{UU}^{\cos 2\phi_T} = {}& \frac{\alpha\alpha_s e_c^2}{M_{\mathcal{Q}}(M_{\mathcal{Q}}^2+Q^2)}\Bigg[-\langle\mathcal{O}^{J/\psi}[{}^1S_0^8]\rangle \\ & + 4\frac{3M_{\mathcal{Q}}^2 - Q^2}{M_{\mathcal{Q}}^2(M_{\mathcal{Q}}^2+Q^2)}\langle\mathcal{O}^{J/\psi}[{}^3P_0^8]\rangle\Bigg]\,\delta(1-z),\end{aligned} \tag{5.66}$$

by using the heavy-quark spin symmetry relations in Eq. 3.46. We note that the partonic subprocess contributing to the cross section in the LTM region are only the $n = {}^1S_0^8,\ {}^3P_J^8$ ones, which correspond to $\hat{t}$-channel Feynman diagrams: Fig. 5.1.4 and Fig. 5.2.2. The other subprocess depicted in these figures are suppressed, including the CS one that is only non-zero in the gluon-induced case. We point out that the structure function $F_{UU}^{\cos 2\phi_T}$ does not contain any large logarithm like $F_{UU,T}$ and $F_{UU,L}$ in the region $q_T^2 \ll Q^2 + M_{\mathcal{Q}}^2$, whereas the corresponding observable in SIDIS diverges logarithmically and is suppressed by an overall factor of q_T^2/Q^2 [142]. Moreover, the appearance of the logarithm $(Q^2+M_{\mathcal{Q}}^2)/\mathbf{q}_T^2$ in the expressions, instead of $\ln Q^2/\mathbf{q}_T^2$, suggest that $Q^2 + M_{\mathcal{Q}}^2$ is the natural choice for the factorisation scale μ^2 of the process.

5.2.2 From LTM to ITM

The same differential cross section in the TMD regime with the corresponding structure functions are given in Eq. 3.83 and Eqs. 3.84, 3.85 and 3.86, respectively. To conduct the matching at order α_s^2 we employ evolution following Sec. 4.2, with the appropriate scale choices. By Fourier transforming as done in Eq. 4.14, we first investigate the perturbative part of the gluon TMD f_1^g. In general, its expression valid in the limit $b_T \ll \Lambda_{\text{QCD}}^{-1}$ is given by [3, 529–530]

$$\hat{f}_1^g(x, \mathbf{b}_T^2; \mu = \mu_H) = \sum_a (C_{g/a} \otimes f_1^a)(x; \mu_b)\, e^{-S_P(b_T;\mu_H,\mu_b)}\,, \tag{5.67}$$

where we note that we fixed the hard scale to the factorisation scale of the collinear calculation, as from our analysis it will turn out that this choice is needed to allow for a smooth transition of the cross section from the LTM to the HTM region. The coefficient functions can be expanded in powers of α_s as follows

$$C_{g/a}(x, \mu_b) = \delta_{ga}\delta(1-x) + \sum_{k=1}^{\infty} C_{g/a}^{(k)}(x) \left(\frac{\alpha_s(\mu_b)}{\pi}\right)^k\,, \tag{5.68}$$

where the explicit expressions for $C_{g/a}^{(k)}$ are not relevant for this analysis (they can be found in e.g. [66]). Employing the perturbative Sudakov factor in Eq. 4.46 at LO

$$S_P(b_T; \mu_H, \mu_b) = \frac{1}{2}\frac{C_A}{\pi}\alpha_s \left(\frac{1}{2}\ln^2\frac{\mu_H^2}{\mu_b^2} - \frac{\beta_0}{6}\ln\frac{\mu_H^2}{\mu_b^2}\right)\,, \tag{5.69}$$

by neglecting the running of the coupling, and substituting Eq. 5.68 in Eq. 5.67, we find:

$$\begin{aligned}\hat{f}_1^g(x, \mathbf{b}_T^2; \mu_H) = f_1^g(x; \mu_b) - \frac{\alpha_s}{2\pi}\Bigg[C_A\left(\frac{1}{2}\ln^2\frac{\mu_H^2}{\mu_b^2} - \frac{\beta_0}{6}\ln\frac{\mu_H^2}{\mu_b^2}\right) f_1^g(x; \mu_b)\\ - 2\sum_a (C_{g/a}^{(1)} \otimes f_1^a)(x; \mu_b)\Bigg]\,.\end{aligned} \tag{5.70}$$

Using the well-known DGLAP equations we can evolve the PDF f_1^g, from the scale μ_H down to the scale μ_b:

$$f_1^g(x; \mu_b) = f_1^g(x; \mu_H) - \frac{\alpha_s}{2\pi}(P_{gg} \otimes f_1^g + P_{gi} \otimes f_1^i)(x; \mu_H)\ln\frac{\mu_H^2}{\mu_b^2} + O(\alpha_s^2)\,. \tag{5.71}$$

Substituting the above expression in Eq. 5.70 we obtain

$$\begin{aligned}\hat{f}_1^g(x, \mathbf{b}_T^2; \mu_H) = f_1^g(x; \mu_H) - \frac{\alpha_s}{2\pi}\Bigg[C_A\left(\frac{1}{2}\ln^2\frac{\mu_H^2}{\mu_b^2} - \frac{\beta_0}{6}\ln\frac{\mu_H^2}{\mu_b^2}\right) f_1^g(x; \mu_H)\\ + (P_{gg} \otimes f_1^g + P_{gi} \otimes f_1^i)(x; \mu_H)\ln\frac{\mu_H^2}{\mu_b^2} - 2\sum_a (C_{g/a}^{(1)} \otimes f_1^a)(x; \mu_H)\Bigg]\,,\end{aligned} \tag{5.72}$$

such that Eq. 4.53 is proven. Using the following integrals

$$\int d^2\mathbf{b}_T\, e^{-i\mathbf{b}_T\cdot\mathbf{q}_T}\ln^2\frac{\mu^2}{\mu_b^2} = -\frac{8\pi}{\mathbf{q}_T^2}\ln\frac{\mu^2}{\mathbf{q}_T^2}\,, \qquad \int d^2\mathbf{b}_T\, e^{-i\mathbf{b}_T\cdot\mathbf{q}_T}\ln\frac{\mu^2}{\mu_b^2} = -\frac{4\pi}{\mathbf{q}_T^2}\,, \tag{5.73}$$

we can transform the TMD back to momentum space:

$$
\begin{aligned}
f_1^g(x, \mathbf{p}_T^2; \mu_H) &= \frac{1}{(2\pi)^2} \int d^2\mathbf{b}_T \, e^{-i\mathbf{b}_T \cdot \mathbf{q}_T} \, \hat{f}_1^g(x, \mathbf{b}_T^2; \mu_H) \\
&= \frac{\alpha_s}{2\pi^2 \mathbf{p}_T^2} \left[C_A \left(\ln \frac{\mu_H^2}{\mathbf{p}_T^2} - \frac{\beta_0}{6} \right) f_1^g(x; \mu_H) + (P_{gg} \otimes f_1^g + P_{gi} \otimes f_1^i)(x; \mu_H) \right] . \qquad (5.74)
\end{aligned}
$$

We note that the term at the order α_s^0 and the coefficient $C_{g/a}^{(1)}$ do not appear because they are independent of b_T and hence give a contribution to f_1^g proportional to $\delta^2(\mathbf{p}_T^2)$. Since we require $p_T \gg \Lambda_{\text{QCD}}$, such terms are discarded. For the same reason, the PDFs in the HTM region do not depend on any nonperturbative TM model [142, 143].

By substituting Eq. 5.74 in Eqs. 3.84 and 3.85, evolved up to the scale $\mu_H^2 \equiv \widetilde{Q}^2 = Q^2 + M_{\mathcal{Q}}^2$, we find that the structure functions $\mathcal{F}_{UU,\mathcal{P}}$ do not match with the corresponding collinear expressions $F_{UU,\mathcal{P}}$ in Eq. 5.55 at $\mu^2 = \widetilde{Q}^2$. This mismatch can be solved by introducing the TMDShFs in the form of a convolution following Eqs. 3.87 and 3.88. Assuming the logarithmic function in Eq. 5.57 is correct, despite being incomplete due to the invalid expansion of the delta function for this process as explained in the next section, we proceed by taking

$$
\begin{aligned}
\hat{\Delta}^{[n]}(z, \mathbf{b}_T^2; \mu = \widetilde{Q}, \mu_b) = \langle \mathcal{O}^{J/\psi}[n] \rangle \left(1 - \frac{\alpha_s}{2\pi} \frac{C_A}{2} \ln^2 \frac{\widetilde{Q}^2}{\mu_b^2} \right) \delta(1-z) \\
+ O(\alpha_s^2) + O(b_T \, \Lambda_{\text{QCD}}) \, , \qquad (5.75)
\end{aligned}
$$

that in momentum space becomes

$$
\Delta^{[n]}(z, \mathbf{k}_T^2; \widetilde{Q}) = \frac{\alpha_s}{2\pi^2 \mathbf{k}_T^2} \, C_A \ln \frac{\widetilde{Q}^2}{\mathbf{k}_T^2} \, \langle \mathcal{O}^{J/\psi}[n] \rangle \, \delta(1-z) \, , \qquad (5.76)
$$

for $k_T \gg \Lambda_{\text{QCD}}$. The derivation of the convolution is then as follows

$$
\begin{aligned}
\mathcal{C}[f_1^g \Delta^{[n]}](x, z, \mathbf{q}_T^2; \widetilde{Q}) &= \frac{\langle \mathcal{O}^{J/\psi}[n] \rangle}{(2\pi)^2} \int d^2\mathbf{b}_T \, e^{-i\mathbf{b}_T \cdot \mathbf{q}_T} \Bigg\{ f_1^g(x; \widetilde{Q}) \\
&- \frac{\alpha_s}{2\pi} \left[C_A \left(\frac{1}{2} \ln^2 \frac{\widetilde{Q}^2}{\mu_b^2} - \frac{\beta_0}{6} \ln \frac{\widetilde{Q}^2}{\mu_b^2} \right) f_1^g(x; \widetilde{Q}) + (P_{gg} \otimes f_1^g + P_{gi} \otimes f_1^i)(x; \mu_H) \ln \frac{\widetilde{Q}^2}{\mu_b^2} \right. \\
&\left. - 2 \sum_a (C_{g/a}^{(1)} \otimes f_1^a)(x; \widetilde{Q}) \right] \Bigg\} \times \left(1 - \frac{\alpha_s}{2\pi} \frac{C_A}{2} \ln^2 \frac{\widetilde{Q}^2}{\mu_b^2} \right) \delta(1-z) \\
&= \frac{\langle \mathcal{O}^{J/\psi}[n] \rangle}{(2\pi)^2} \int d^2\mathbf{b}_T \, e^{-i\mathbf{b}_T \cdot \mathbf{q}_T} \Bigg\{ f_1^g(x; \widetilde{Q}) - \frac{\alpha_s}{2\pi} \left[C_A \left(\ln^2 \frac{\widetilde{Q}^2}{\mu_b^2} - \frac{\beta_0}{6} \ln \frac{\widetilde{Q}^2}{\mu_b^2} \right) f_1^g(x; \widetilde{Q}) \right. \\
&\left. + (P_{gg} \otimes f_1^g + P_{gi} \otimes f_1^i)(x; \widetilde{Q}) \ln \frac{\mu_H^2}{\mu_b^2} - 2 \sum_a (C_{g/a}^{(1)} \otimes f_1^a)(x; \widetilde{Q}) \right] \Bigg\} \delta(1-z) \\
&= \frac{\alpha_s}{2\pi^2 \mathbf{q}_T^2} \langle \mathcal{O}^{J/\psi}[n] \rangle \left[L(\mathbf{q}_T^2) \, f_1^g(x; \widetilde{Q}) + (P_{gg} \otimes f_1^g + P_{gi} \otimes f_1^i)(x; \widetilde{Q}) \right] \delta(1-z) \, , \quad (5.77)
\end{aligned}
$$

such that by multiplying with the corresponding hard factors matching is seemingly obtained for the cross section.

The large TM perturbative tail of the linearly polarised gluon distribution $h_1^{\perp g}$ in Eq. 4.54 can be derived along the same lines of f_1^g, where its expansion in powers of the coupling starts at order α_s as discussed in Sec. 4.2. According to [106], the tail in momentum space is given by:

$$\begin{aligned}\frac{\mathbf{q}_T^2}{2M_h^2}\, h_1^{\perp g}(x, \mathbf{q}_T^2; \mu) = {} & \frac{\alpha_s}{\pi^2}\frac{1}{\mathbf{q}_T^2}\int_x^1 \frac{dx'}{x'}\left(\frac{x'}{x} - 1\right) \\ & \times \Big\{ C_A\, f_1^g(x';\mu) + C_F\, f_1^i(x';\mu) \Big\} + O(\alpha_s^2)\,. \end{aligned} \tag{5.78}$$

Employing this gives direct matching between $\mathcal{F}_{UU}^{\cos 2\phi_T}$ in Eq. 3.86 and $F_{UU}^{\cos 2\phi_T}$ in Eq. 5.56. This is achieved without the need of any extra smearing contribution from the TMDShFs, i.e. $\Delta_h^{[n]}(z, \mathbf{k}_T^2) = \langle \mathcal{O}^{J/\psi}[n] \rangle\, \delta^2(\mathbf{k}_T)\, \delta(1 - z)$ in Eq. 3.89, because of the absence of a logarithmic term at the perturbative order we consider. Therefore, a higher-order α_s matching computation is needed to obtain their non-trivial perturbative tails. Having examined the technical aspects of the matching procedure, we now focus on addressing its underlying issue.

5.3 An effective delta function

Although the correct derivation of the LO large TM perturbative tails of the TMDShFs proceeds along the same lines as in Sec. 5.2, their expressions given in Eq. 5.75 and Eq. 5.76 are incorrect. The origin of the discrepancy with respect to the expectation that the TMDShFs should contribute to the single logarithm of the perturbative Sudakov factor, instead of to the double logarithm as explained in Sec. 4.2 (i.e. by resumming the term between brackets of Eq. 5.75), comes from the fact that the expansion of the delta function in Eq. D.21 was obtained by applying the full delta function to two continuous test functions. However, the structure functions in Eq. 5.45 actually contain infinite discontinuities that originate from the soft-gluon radiation associated with the CO final state. These contributions in the structure functions of Eq. 5.46 are explicitly exposed via a decomposition into poles through a Laurent expansion[2]

$$\begin{aligned}\frac{1}{4(4\pi)^3}\frac{1}{Q^2}\,\epsilon^{\mu\nu}_{\mathcal{P};\Phi}\, H^{a[n]}_{\mu\nu} &\equiv \mathcal{H}^{a[n]}_{\mathcal{P};\Phi}(\hat{x}', \hat{z}) \\ &= \mathcal{H}^{a[n];(0)}_{\mathcal{P};\Phi}(\hat{x}', \hat{z}) + \sum_{k=1}^{\infty}\left(\frac{1-\hat{z}}{1-\hat{x}'}\right)^{k} \mathcal{H}^{a[n];(k)}_{\mathcal{P};\Phi}(\hat{z})\,, \end{aligned} \tag{5.79}$$

where we changed to the variable $\hat{x}'$ as before. In this expression $\mathcal{H}^{a[n];(0)}_{\mathcal{P},\Phi}$ and $\mathcal{H}^{a[n];(k)}_{\mathcal{P},\Phi}$ are finite for all $\hat{x}'$ and $\hat{z}$, including their limits to 1. We have found that the poles are present only for the gluon initiated process with the expansion running up to $k = 2$. Instead, the quark initiated processes are fully described by the $k = 0$ finite term. Moreover, up to the precision considered in this work, the poles contribute only to the structure functions $F_{UU,\mathcal{P}}$ as expected. These poles are under control when the amplitude squared is evaluated at large q_T, as the TM forces the phase space to deviate

---

[2] Before performing the expansion we suggest applying Eq. 5.53 once.

from $\hat{z} = 1$ and $\hat{x}' = 1$. They have a significant impact solely when we consider the small-q_T limit.

Because of the poles the expanded delta function in Eq. D.21 is applicable only to the first term $\mathcal{H}^{a[n];(0)}_{\mathcal{P},\Phi}$, while all other terms require a different approach. In particular, we can split the differential cross section into three parts in the HTM region

$$\frac{d\sigma(J/\psi)}{dy\, dx_B\, dz\, d\mathbf{q}_T^2\, d\phi_T} \equiv d\sigma_A + d\sigma_B + d\sigma_C \,, \tag{5.80}$$

where

$$\begin{aligned} d\sigma_A = {} & \frac{\alpha}{yQ^2}\, z \sum_a \sum_n \int_0^1 d\hat{x}' \int_0^1 d\hat{z}\, \hat{z}\, f_1^a\!\left(\frac{x_B}{\hat{x}_{\max}\, \hat{x}'};\mu\right) \delta\big(G(\hat{x}',\hat{z})\big)\, \langle \mathcal{O}^{J/\psi}[n]\rangle\, \delta(z-\hat{z}) \\ & \times \Big\{ [1+(1-y)^2]\, \mathcal{H}_T^{a[n];(0)}(\hat{x}',\hat{z}) + 4(1-y)\, \mathcal{H}_L^{a[n];(0)}(\hat{x}',\hat{z}) \\ & + (2-y)\sqrt{1-y}\cos\phi_T\, \mathcal{H}^{a[n];(0)}_{\cos\phi_T}(\hat{x}',\hat{z}) + (1-y)\cos 2\phi_T\, \mathcal{H}^{a[n];(0)}_{\cos 2\phi_T}(\hat{x}',\hat{z}) \Big\} \,, \end{aligned} \tag{5.81}$$

and

$$\begin{aligned} d\sigma_B = {} & \frac{\alpha}{yQ^2}\, z \sum_n \int_0^1 d\hat{x}' \int_0^1 d\hat{z}\, \hat{z}\, f_1^g\!\left(\frac{x_B}{\hat{x}_{\max}\, \hat{x}'};\mu\right) \delta\big(G(\hat{x}',\hat{z})\big)\, \langle \mathcal{O}^{J/\psi}[n]\rangle\, \delta(z-\hat{z}) \\ & \times \left(\frac{1-\hat{z}}{1-\hat{x}'}\right) \Big\{ [1+(1-y)^2]\, \mathcal{H}_T^{g[n];(1)}(\hat{z}) + 4(1-y)\, \mathcal{H}_L^{g[n];(1)}(\hat{z}) \Big\} \,, \end{aligned} \tag{5.82}$$

$$\begin{aligned} d\sigma_C = {} & \frac{\alpha}{yQ^2}\, z \sum_n \int_0^1 d\hat{x}' \int_0^1 d\hat{z}\, \hat{z}\, f_1^g\!\left(\frac{x_B}{\hat{x}_{\max}\, \hat{x}'};\mu\right) \delta\big(G(\hat{x}',\hat{z})\big)\, \langle \mathcal{O}^{J/\psi}[n]\rangle\, \delta(z-\hat{z}) \\ & \times \left(\frac{1-\hat{z}}{1-\hat{x}'}\right)^2 \Big\{ [1+(1-y)^2]\, \mathcal{H}_T^{g[n];(2)}(\hat{z}) + 4(1-y)\, \mathcal{H}_L^{g[n];(2)}(\hat{z}) \Big\} \,, \end{aligned} \tag{5.83}$$

with $G(\hat{x}',\hat{z})$ defined in Eq. D.4. The difference in the lower integration limit for both $\hat{x}$ and $\hat{z}$ between the above equations and Eq. 5.46 has been introduced for the convenience of the calculation as before. This modification is possible since the added integration range does not contribute to the final result (see App. D).

As mentioned, the first integral $d\sigma_A$ involves only finite terms in the double limit $\hat{x}', \hat{z} \to 1$ and can therefore be calculated in the ITM region by using the naive expansion of the delta function. Instead, the expansions of $d\sigma_B$ and $d\sigma_C$ are obtained by considering the integral with respect to $d\hat{x}$ and $d\hat{z}$ of those terms that are truly indeterminate in the limit $q_T \to 0$, with the indeterminacy solved by the presence of the full delta function. In particular, in the double limit the indeterminate terms in $d\sigma_B$ and $d\sigma_C$ are given by poles, while the other quantities can be Taylor expanded around $\hat{z} = 1$ and $\hat{x}' = 1$, e.g. the quantities $\mathcal{H}^{a[n];(k)}_{\mathcal{P}}(\hat{z})$ are decomposed as:

$$\mathcal{H}^{a[n];(k)}_{\mathcal{P}}(\hat{z}) = \mathcal{H}^{a[n];(k)}_{\mathcal{P}}(1) + \sum_l (1-\hat{z})^l\, \frac{d^l \mathcal{H}^{a[n];(k)}_{\mathcal{P},\Phi}(\hat{z})}{d\hat{z}^l}\bigg|_{\hat{z}=1} \,. \tag{5.84}$$

After the first order, the presence of $(1-\hat{z})^l$ solves the indeterminacy, making the quantity $(1-\hat{z})^{k+l}/(1-\hat{x})$ null in the double limit. Hence, one can approximate $\hat{z} = 1$ and $\hat{x}' = 1$ whenever possible, and subsequently perform the analytic integral.

It turns out that the $\mathcal{H}^{g[n];(k)}_{\mathcal{P}}(\hat{z}) \to \mathcal{H}^{g[n];(k)}_{\mathcal{P}}(1)$ limit gives

$$\mathcal{H}^{g[n];(1)}_{\mathcal{P}}(1) = -2\frac{M_{\mathcal{Q}}^2}{Q^2+M_{\mathcal{Q}}^2}\mathcal{H}^{g[n];(0)}_{\mathcal{P}}(1,1)\,, \tag{5.85}$$

$$\mathcal{H}^{g[n];(2)}_{\mathcal{P}}(1) = \left(\frac{M_{\mathcal{Q}}^2}{Q^2+M_{\mathcal{Q}}^2}\right)^2\mathcal{H}^{g[n](0)}_{\mathcal{P}}(1,1)\,, \tag{5.86}$$

such that $d\sigma_B$ can be expanded as follows

$$\begin{aligned}
d\sigma_B \approx{}& \frac{\alpha}{yQ^2}\,f_1^g(x;\mu)\sum_n\left\{\left[1+(1-y)^2\right]\mathcal{H}^{g[n];(1)}_{T}(1)+4(1-y)\,\mathcal{H}^{g[n];(1)}_{L}(1)\right\}\\
&\times\int_0^1 d\hat{x}'\int_0^1 d\hat{z}\left(\frac{1-\hat{z}}{1-\hat{x}'}\right)\delta\big(G(\hat{x}',\hat{z})\big)\,\langle\mathcal{O}^{J/\psi}[n]\rangle\,\delta(1-z)\\
={}& \frac{\alpha}{yQ^2}\,f_1^g(x;\mu)\sum_n\left\{\left[1+(1-y)^2\right]\mathcal{H}^{g[n];(1)}_{T}(1)+4(1-y)\,\mathcal{H}^{g[n];(1)}_{L}(1)\right\}\\
&\times\,Q^2\int_0^1 d\hat{x}'\int_0^1 d\hat{z}\left(\frac{1-\hat{z}}{\hat{z}^2\mathbf{q}_T^2+(1-\hat{z})^2M_{\mathcal{Q}}^2}\right)\delta(\hat{x}'-\hat{x}_0')\,\langle\mathcal{O}^{J/\psi}[n]\rangle\,\delta(1-z)\\
={}& \frac{\alpha}{yQ^2}\,f_1^g(x;\mu)\sum_n\left\{\left[1+(1-y)^2\right]\mathcal{H}^{g[n];(1)}_{T}(1)+4(1-y)\,\mathcal{H}^{g[n];(1)}_{L}(1)\right\}\\
&\times\left(\frac{Q^2}{2M_{\mathcal{Q}}^2}\ln\frac{M_{\mathcal{Q}}^2}{\mathbf{q}_T^2}\right)\langle\mathcal{O}^{J/\psi}[n]\rangle\,\delta(1-z)\\
={}& \frac{\alpha}{yQ^2}\,f_1^g(x;\mu)\sum_n\left\{\left[1+(1-y)^2\right]\mathcal{H}^{g[n];(0)}_{T}(1,1)+4(1-y)\,\mathcal{H}^{g[n];(0)}_{L}(1,1)\right\}\\
&\times\left(-\,\hat{x}_{\max}\ln\frac{M_{\mathcal{Q}}^2}{\mathbf{q}_T^2}\right)\langle\mathcal{O}^{J/\psi}[n]\rangle\,\delta(1-z)\,,
\end{aligned} \tag{5.87}$$

and $d\sigma_C$ as

$$\begin{aligned}
d\sigma_C \approx{}& \frac{\alpha}{yQ^2}\,f_1^g(x;\mu)\sum_n\left\{\left[1+(1-y)^2\right]\mathcal{H}^{g[n];(2)}_{T}(1)+4(1-y)\,\mathcal{H}^{g[n];(2)}_{L}(1)\right\}\\
&\times\int_0^1 d\hat{x}'\int_0^1 d\hat{z}\left(\frac{1-\hat{z}}{1-\hat{x}'}\right)^2\delta\big(G(\hat{x}',\hat{z})\big)\,\langle\mathcal{O}^{J/\psi}[n]\rangle\,\delta(1-z)\\
={}& \frac{\alpha}{yQ^2}\,f_1^g(x;\mu)\sum_n\left\{\left[1+(1-y)^2\right]\mathcal{H}^{g[n];(2)}_{T}(1)+4(1-y)\,\mathcal{H}^{g[n];(2)}_{L}(1)\right\}\langle\mathcal{O}^{J/\psi}[n]\rangle\\
&\times\,Q^2\int_0^1 d\hat{x}'\int_0^1 d\hat{z}\,\frac{(1-\hat{z})^2[\hat{z}^2\mathbf{q}_T^2+(1-\hat{z})(\hat{z}Q^2+M_{\mathcal{Q}}^2)]}{[\hat{z}^2\mathbf{q}_T^2+(1-\hat{z})^2M_{\mathcal{Q}}^2]^2}\,\delta(\hat{x}'-\hat{x}_0')\,\delta(1-z)\\
\approx{}& \frac{\alpha}{yQ^2}\,f_1^g(x;\mu)\sum_n\left\{\left[1+(1-y)^2\right]\mathcal{H}^{g[n];(2)}_{T}(1)+4(1-y)\,\mathcal{H}^{g[n];(2)}_{L}(1)\right\}\langle\mathcal{O}^{J/\psi}[n]\rangle\\
&\times\,Q^2\int_0^1 d\hat{x}'\int_0^1 d\hat{z}\,\frac{(1-\hat{z})^3}{[\hat{z}^2\mathbf{q}_T^2+(1-\hat{z})^2M_{\mathcal{Q}}^2]^2}\,(Q^2+M_{\mathcal{Q}}^2)\,\delta(\hat{x}'-\hat{x}_0')\,\delta(1-z)\\
={}& \frac{\alpha}{yQ^2}\,f_1^g(x;\mu)\sum_n\left\{\left[1+(1-y)^2\right]\mathcal{H}^{g[n];(2)}_{T}(1)+4(1-y)\,\mathcal{H}^{g[n];(2)}_{L}(1)\right\}
\end{aligned}$$

$$\times \left[\frac{Q^2+M_{\mathcal{Q}}^2}{M_{\mathcal{Q}}^2}\frac{Q^2}{2M_{\mathcal{Q}}^2}\left(\ln\frac{M_{\mathcal{Q}}^2}{\mathbf{q}_T^2}-1\right)\right]\langle\mathcal{O}^{J/\psi}[n]\rangle\,\delta(1-z)$$

$$= \frac{\alpha}{yQ^2}\,f_1^g(x;\mu)\sum_n\left\{[1+(1-y)^2]\,\mathcal{H}_T^{g[n];(0)}(1,1)+4(1-y)\,\mathcal{H}_L^{g[n];(0)}(1,1)\right\}$$

$$\times\left[\frac{\hat{x}_{\max}}{2}\left(\ln\frac{M_{\mathcal{Q}}^2}{\mathbf{q}_T^2}-1\right)\right]\langle\mathcal{O}^{J/\psi}[n]\rangle\,\delta(1-z)\,, \tag{5.88}$$

where we recall that x is defined in Eq. 5.58. We note that in these derivations the solution of $\hat{x}'$ imposed by $\delta(G(\hat{x}',\hat{z}))$ is utilised, namely $\hat{x}_0'$ presented in Eq. D.7. Since the small-q_T limit of these additional cross sections is proportional to $\hat{H}_{\mathcal{P}}^{g[n];(0)}(1,1)$, we can effectively add these terms to the coefficient in front of the double delta of the naive expansion of the delta function given in Eq. D.21, i.e.

$$\mathcal{H}_{\mathcal{P}}^{g[n]}(\hat{x}',\hat{z})\,\delta\!\left(\frac{G(\hat{x}',\hat{z})}{\hat{x}'\hat{z}^2}\right)\sim\mathcal{H}_{\mathcal{P}}^{g[n](0)}(\hat{x}',\hat{z})\,\delta_{\text{eff}}(\hat{x},\hat{z})\,, \tag{5.89}$$

such that:

$$\delta_{\text{eff}}(\hat{x}',\hat{z}) = \hat{x}_{\max}\left\{\frac{1}{2}\left(\ln\frac{Q^2+M_{\mathcal{Q}}^2}{\mathbf{q}_T^2}-1-\ln\frac{M_{\mathcal{Q}}^2}{Q^2+M_{\mathcal{Q}}^2}\right)\delta(1-\hat{x}')\,\delta(1-\hat{z})\right.$$
$$\left.+\frac{\hat{x}'}{(1-\hat{x}')_+}\,\delta(1-\hat{z})+\frac{Q^2+M_{\mathcal{Q}}^2}{Q^2+M_{\mathcal{Q}}^2/\hat{z}}\frac{\hat{z}}{(1-\hat{z})_+}\,\delta(1-\hat{x}')\right\}. \tag{5.90}$$

Considering the contributions from the various terms in Eq. 5.90, we found that the small-q_T limit is dominated by the first two terms for the gluon channel (and similarly the first two terms of Eq. D.21 for the quark and antiquark channels). Instead, the contribution coming from the '+'-distribution of $\hat{z}$ is subdominant and can be neglected.

Taking this into account, the logarithmic function in Eq. 5.57 needs to be rewritten as follows

$$L(\mathbf{q}_T^2) = C_A\left\{\ln\frac{Q^2+M_{\mathcal{Q}}^2}{\mathbf{q}_T^2}-\mathrm{B}_{\mathrm{CO}}-\frac{\beta_0}{6}\right\}, \tag{5.91}$$

where:

$$\mathrm{B}_{\mathrm{CO}}(\widetilde{Q}) = 1+\ln\frac{M_{\mathcal{Q}}^2}{Q^2+M_{\mathcal{Q}}^2}\,. \tag{5.92}$$

Following the matching procedure in Sec. 5.2 it can be easily understood that the revised large TM perturbative tails of the TMDShFs are given by Eq. 4.55 (with $\mu_H=\widetilde{Q}$; the more general form will be discussed in Sec. 5.5), where the difference with respect to the incorrect expression in Eq. 5.75 arises from the new logarithmic function given in Eq. 5.91. This function contains only once the logarithm of $(Q^2+M_{\mathcal{Q}}^2)/\mathbf{q}_T^2$ such that the double logarithm from the perturbative Sudakov factor is directly matched. This is due to the factor of $1/2$ in Eq. 5.90 that originates from the presence of the poles. Indeed, it is through the inclusion of Eqs. 5.87 and 5.88 that in Eq. 5.91 one of the logarithms has been removed. The price to pay corresponds to the novel q_T-independent terms in Eq. 5.92 defined as B_{CO}. Now, we find that the tails of the TMDShFs deviate from a TMDFF one, having a less divergent behaviour compared to the latter: they contribute to the single logarithm in S_A and hence do not contain rapidity divergences. In the limit $k_T \gg \Lambda_{\rm QCD}$ the TMDShFs can be written in momentum space as follows:

$$\Delta^{[n]}(z, \mathbf{k}_T^2; \widetilde{Q}) = -\frac{\alpha_s}{2\pi^2 \mathbf{k}_T^2}\, C_A\, \mathrm{B}_{\rm CO}(\widetilde{Q})\, \langle \mathcal{O}^{J/\psi}[n] \rangle\, \delta(1-z) + O(\alpha_s^2)\,. \tag{5.93}$$

We note how the modification of Eq. 5.91 compared to Eq. 5.57 has a significant impact on the TMDShF expression. Indeed, the TMDShF perturbative tail in Eq. 5.93 does not contain any kind of logarithmic divergence in k_T, being tamed by the presence of the heavy mass. We emphasise that the absence of k_T-divergent terms associated to the quarkonium is in accordance with other works in the literature, e.g. [70, 71, 127, 131, 144].

We remark that our results on the TMDShF for observables involving f_1^g hold for every CO quarkonium state with the same quantum numbers as the J/ψ we considered, e.g. $\Upsilon(nS)$ and $\psi(2S)$. The magnitudes of TMDShFs are different though, determined by the LDMEs. This conclusion holds up to the precision considered, corresponding to the $\alpha\alpha_s^2$ and v^4 orders in the NRQCD double expansion. Moreover, the same considerations apply if we take into account the polarisation of the J/ψ, since the kinematics are the same. Namely, we have the same TMDShF tails for both the longitudinal and transverse J/ψ polarisation states. Besides, to check that the same form of the TMDShF applies for observables involving $h_1^{\perp g}$ it would require the computation of the cross section within NRQCD at higher-order α_s, both for polarised and unpolarised J/ψ productions. However, this calculation is currently still unavailable.

Recently, subsequent work on the TMDShFs for the same process was performed within the soft-collinear effective theory approach [145]. We point out that our results are in agreement with theirs for a specific choice of ζ_B. Besides, they included LDME mixing contributions by considering higher-order terms in the NRQCD v expansion (beyond the order v^4 considered here, see e.g. [146]), which are significantly suppressed in phenomenological analyses.

Although our work is based on J/ψ electroproduction, we expect that the presence of the poles, as in Eq. 5.79, at small q_T is an intrinsic feature of any inclusive quarkonium production, and they apply to different processes and observables too. Hence, the logarithmic dependence on TM in Eq. 5.91 (unlike when a TMDFF contribution is considered) is not an exclusive outcome of the specific process under consideration, but rather a general statement. Thus, the observed singularities in this process may be connected to other regularisation procedures associated with CO contributions to heavy quarkonium production. While it is worthwhile to further pursue these connections in the NRQCD factorisation, such a study is beyond the scope of the current research. However, to emphasise the importance of further investigation, we will briefly comment on the similarities of our findings with those obtained by adopting the FF description.

The same cross section in the HTM region can be expressed in terms of FFs, as shown in [53–55]. Hence, the TMDShFs may also be seen as a fragmentation-like function of a $c\bar{c}$ into a J/ψ evaluated at ITM. The evolution of the latter has been studied in [55], which includes real contributions having a component proportional to the $(1-\hat{z})_+$ distribution and another one to $\delta(1-\hat{z})$. Hence, our analysis is related to the latter term. Moreover, an important difference concerns the integration range of the outgoing gluon. The integration of the soft-gluon momentum in our case has a lower limit set by the J/ψ TM as is shown in Eq. 5.117 in the next section, whereas no lower limit is present in [55] causing infrared divergences. On the other hand, subdominant terms and higher-order corrections in the LTM region are also expected to contribute away from $z = 1$. In that case the description of the heavy-quark pair that hadronises into the heavy quarkonium state will be even more similar to a single-parton TMDFF description applied in light hadron production. See also [147] for a description involving both single-parton and parton-pair fragmentation processes. Therefore, the connection between our work and the FF description cannot be carried out further without the inclusion of next order (real and virtual) contributions and we leave this discussion to further studies.

5.4 The eikonal approximation

In this section we explain how to evaluate the soft-gluon radiation from the LO partonic subprocess by adopting the eikonal approximation that provides agreement with the logarithmic function presented in Eq. 5.91. The Born amplitude is depicted in Fig. 5.5.1 and the soft-gluon emission is obtained by attaching a (soft) gluon to the initial (hard) gluon, as in Fig. 5.5.2, or to the heavy-quark pair, as in Figs. 5.5.3 and 5.5.4. The eikonal gluon has a four-momentum p_g that is negligible compared to the other (hard) momenta in the process. Hence, its polarisation vector ϵ_{λ_g} fulfils the relation

$$\sum_{\lambda_g=\pm 1} \epsilon^{\mu}_{\lambda_g}(p_g)\epsilon^{\nu *}_{\lambda_g}(p_g) \to -g^{\mu\nu} \,, \tag{5.94}$$

which follows from Eq. A.24. The soft external gluon has colour index c and the initial gluon and the outgoing heavy-quark pair have colour index a and b, respectively.

The LO amplitude of Fig. 5.5.1 can be written as

$$\mathcal{M}^{(0)} = \delta_{ab}\, M^{(0)} \,, \tag{5.95}$$

where

$$M^{(0)} = \int \frac{d^4k}{(2\pi)^4}\, \mathcal{O}_{ij}(P,k)\Phi^{b}_{ji}(P,k) \,, \tag{5.96}$$

similar to Eq. 3.11. Here we included an explicit dependence on the colour configuration of the pair, i.e. $\Phi^{1}_{ji}(P,k) = N_c^{-1/2}\delta_{ij}\,\Phi(P,k)$ for CS states, while $\Phi^{8}_{ji}(P,k) = \sqrt{2}\,t^{b}_{ji}\,\Phi(P,k)$ for CO states. Specifically, we have taken the colour projection to be part of the projection operator, i.e. $\mathcal{P}^{b}_{SS_Z}(P,k)_{ji} = \langle 3i, \bar{3}j|1,8\rangle \mathcal{P}_{SS_Z}(P,k)$, to keep the colour structure evident in this derivation (instead it is usually part of $\mathcal{O}$).

The corresponding amplitudes for the Figs. 5.5.2-4 with the eikonal gluon insertion are given by $\mathcal{M}^{(1)}_{I}$, with $I = 2, 3, 4$. They can be obtained from the Born one in Fig. 5.5.1 through proper replacements in a light-cone gauge. In particular, for $\mathcal{M}^{(1)}_{2}$

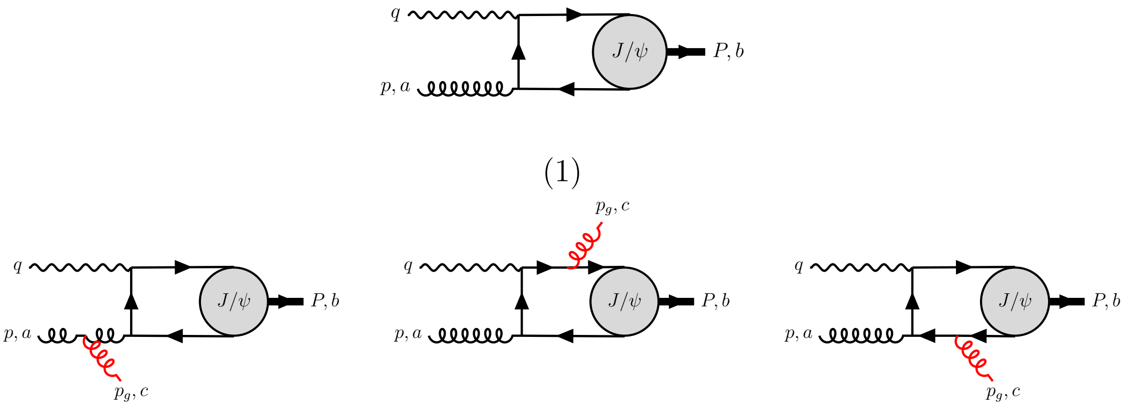

(1)

(2) (3) (4)

Figure 5.5: LO diagrams for the process $\gamma^* + g \to J/\psi$, with the inclusion of soft-gluon emission (in red) from the initial and final state.

we have the following replacement:

$$\begin{aligned}
\epsilon^{\mu}_{\lambda_g}(p) \to\ & \epsilon^{\nu}_{\lambda_a}(p)\, \epsilon^{\alpha *}_{\lambda_g}(p_g)\, (-g_s f_{adc})\, [(2p - p_g)_\alpha\, g_{\nu\beta} + (2p_g - p)_\nu\, g_{\beta\alpha} - (p + p_g)_\beta\, g_{\alpha\nu}] \\
& \times \frac{i}{(p - p_g)^2 + i\varepsilon} \left[- g^{\beta\mu} + \frac{p_g^\beta n^\mu + p_g^\mu n^\beta}{p_g \cdot n} \right] \\
\approx\ & \epsilon^{\nu}_{\lambda_a}(p)\, \epsilon^{\alpha *}_{\lambda_g}(p_g)\, (-g_s f_{adc})\, [2p_\alpha\, g_{\nu\beta} - p_\nu\, g_{\beta\alpha} - p_\beta\, g_{\alpha\nu}]\, \frac{i g^{\beta\mu}}{2p \cdot p_g - i\varepsilon} \\
=\ & \epsilon^{\mu}_{\lambda_a}(p)\, \epsilon^{\alpha *}_{\lambda_g}(p_g)\, (-i g_s f_{adc}) \left[\frac{p_\alpha}{p \cdot p_g - i\varepsilon} \right] .
\end{aligned} \tag{5.97}$$

For completeness, we retain the $i\varepsilon$ in the replacements presented here. According to the eikonal approximation we can neglect p_g^μ with respect to the hard momenta in the numerators, such as p^μ. Moreover, the last two terms in the second line do not contribute because of $\epsilon_{\lambda_a}(p) \cdot p = 0$ and the Ward identity (see Eq. C.3). Since this replacement does not depend on the internal momentum k we can apply it directly to Eq. 5.96, such that we obtain:

$$\mathcal{M}_2^{(1)} = \delta_{db}\, M_2^{(1)} = (-i g_s f_{abc})\, \epsilon^{\alpha *}_{\lambda_g}(p_g) \left[\frac{p_\alpha}{p \cdot p_g - i\varepsilon} \right] M^{(0)} . \tag{5.98}$$

Similarly, we can evaluate $\mathcal{M}_3^{(1)}$ and $\mathcal{M}_4^{(1)}$ via the replacement of the projection operator $\mathcal{P}_{SS_z}$ in the amplitudes: for S-waves we refer to Eq. 3.26, while for P-waves to Eq. 3.27. While both equations involve $\mathcal{P}_{SS_z}(P, 0)$, the P-waves require also the evaluation of $\partial \mathcal{P}_{SS_z}(P_\psi, k)/\partial k|_{k=0}$. Moreover, this replacement is slightly different between the quark and antiquark cases, given by Fig. 5.5.3 and 5.5.4, respectively. Considering first the common term, the substitution of the projector reads for $M_3^{(1)}$

$$\begin{aligned}
\mathcal{P}^b_{SS_z}(P, k)_{ji} \Big|_{k=0} & \to \mathcal{P}^b_{SS_z}(P, k)_{jl}\, (-i g_s\, \gamma_\alpha\, t^c_{li})\, \epsilon^{\alpha *}_{\lambda_g}(p_g)\, \frac{i(\not{P}/2 + \not{k} + \not{p}_g + m_c)}{(P/2 + k + p_g)^2 - m_c^2 + i\varepsilon} \Bigg|_{k=0} \\
& \approx g_s\, t^c_{li}\, \epsilon^{\alpha *}_{\lambda_g}(p_g) \left[\mathcal{P}^b_{SS_z}(P, k)_{jl}\, \frac{(-\not{P}/2 - \not{k} + m_c)\gamma_\alpha + (P + 2k)_\alpha}{P \cdot (k + p_g) + i\varepsilon} \right]_{k=0}
\end{aligned}$$

$$\begin{aligned} &= g_s\, t^c_{li}\, \epsilon^{\alpha *}_{\lambda_g}(p_g) \left[\mathcal{P}^b_{SS_z}(P,k)_{jl}\, \frac{(P+2k)_\alpha}{P\cdot(k+p_g)+i\varepsilon} \right]_{k=0} \\ &\approx g_s\, t^c_{li}\, \frac{P_\alpha}{P\cdot p_g + i\varepsilon}\, \epsilon^{\alpha *}_{\lambda_g}(p_g)\, \mathcal{P}^b_{SS_z}(P,0)_{jl}\,, \end{aligned} \tag{5.99}$$

where in the second line we neglected p_g whenever possible. Moreover, in the third line we made use of the Dirac equation for the heavy-quark spinor

$$\mathcal{P}_{SS_z}(P,k)\,(-\not{P} - 2\not{k} + M) \propto \bar{u}(P/2+k)\,\big((\not{P}/2+\not{k}) - m_c\big) = 0\,, \tag{5.100}$$

by Eq. 3.14. Analogously, for $M_4^{(1)}$ we have:

$$\begin{aligned} \mathcal{P}^b_{SS_z}(P,k)_{ji}\bigg|_{k=0} &\to \frac{i(\not{P}/2 - \not{k} - \not{p}_g - m_c)}{(P/2-k-p_g)^2 - m_c^2 + i\varepsilon}\, (-i g_s\, \gamma_\alpha\, t^c_{jl})\, \epsilon^{\alpha *}_{\lambda_g}(p_g)\, \mathcal{P}^b_{SS_z}(P,k)_{li}\bigg|_{k=0} \\ &\approx -g_s\, t^c_{jl}\, \frac{P_\alpha}{P\cdot p_g + i\varepsilon}\, \epsilon^{\alpha *}_{\lambda_g}(p_g)\, \mathcal{P}^b_{SS_z}(P,0)_{li}\,. \end{aligned} \tag{5.101}$$

Moving to the derivative of the projection operator, we have for $M_3^{(1)}$

$$\begin{aligned} \epsilon^{\rho *}_{L_z}(P)\, \frac{\partial \mathcal{P}^b_{SS_z}(P,k)_{ji}}{\partial k^\rho}\bigg|_{k=0} &\to g_s\, t^c_{li}\, \epsilon^{\alpha *}_{\lambda_g}(p_g)\, \epsilon^{\rho *}_{L_z}(P)\, \frac{\partial}{\partial k^\rho} \left[\mathcal{P}^b_{SS_z}(P,k)_{jl}\, \frac{(P+2k)_\alpha}{P\cdot(k+p_g)+i\varepsilon} \right]_{k=0} \\ &\approx g_s\, t^c_{li}\, \frac{P_\alpha}{P\cdot p_g + i\varepsilon}\, \epsilon^{\alpha *}_{\lambda_g}(p_g)\, \epsilon^{\rho *}_{L_z}(P)\, \frac{\partial \mathcal{P}^b_{SS_z}(P,k)_{jl}}{\partial k^\rho}\bigg|_{k=0} \\ &+ g_s\, t^c_{li}\, \frac{2\, g_{\alpha\rho}}{P\cdot p_g + i\varepsilon}\, \epsilon^{\alpha *}_{\lambda_g}(p_g)\, \epsilon^{\rho *}_{L_z}(P)\, \mathcal{P}^b_{SS_z}(P,0)_{jl}\,, \end{aligned} \tag{5.102}$$

where we again made use of the Dirac equation, neglected p_g whenever possible and in addition employed the identity of the J/ψ polarisation vector. The same derivation for $M_4^{(1)}$ reads:

$$\begin{aligned} \epsilon^{\rho *}_{L_z}(P)\, \frac{\partial \mathcal{P}^b_{SS_z}(P,k)_{ji}}{\partial k^\rho}\bigg|_{k=0} &\to -g_s\, t^c_{jl} \epsilon^{\alpha *}_{\lambda_g}(p_g)\, \epsilon^{\rho *}_{L_z}(P)\, \frac{\partial}{\partial k^\rho} \left[\mathcal{P}^b_{SS_z}(P,k)_{li}\, \frac{(P-2k)_\alpha}{P\cdot(k+p_g)+i\varepsilon} \right]_{k=0} \\ &\approx -g_s\, t^c_{jl}\, \frac{P_\alpha}{P\cdot p_g + i\varepsilon}\, \epsilon^{\alpha *}_{\lambda_g}(p_g)\, \epsilon^{\rho *}_{L_z}(P)\, \frac{\partial \mathcal{P}^b_{SS_z}(P,k)_{li}}{\partial k^\rho}\bigg|_{k=0} \\ &+ g_s\, t^c_{jl}\, \frac{2\, g_{\alpha\rho}}{P\cdot p_g + i\varepsilon}\, \epsilon^{\alpha *}_{\lambda_g}(p_g)\, \epsilon^{\rho *}_{L_z}(P)\, \mathcal{P}^b_{SS_z}(P,0)_{li}\,. \end{aligned} \tag{5.103}$$

Although the last lines of Eq. 5.102 and 5.103 are present at the amplitude level, when considering the squared amplitude, they vanish (i.e. the cross term is null due to the polarisation vector and the second term squared effectively becomes a ${}^3S_1$-state contribution, which is null too in the TMD regime). This was also found for the quarkonium decay into two gluons [50].

In the end the replacement rules for the projection operator and its derivative are the same, such that we can write:

$$\begin{aligned} M^{(1)}_{3+4} &= g_s\, \frac{P_\alpha}{P\cdot p_g}\, \epsilon^{\alpha *}_{\lambda_g}(p_g) \\ &\times \int \frac{d^4 k}{(2\pi)^4} \left[\mathcal{O}_{il}(P,k)\, \left(\mathcal{P}^b_{SS_z}(P,k)_{jl}\, t^c_{li} - t^c_{jl}\, \mathcal{P}^b_{SS_z}(P,k)_{li} \right) \right]. \end{aligned} \tag{5.104}$$

Due to the opposite signs of $M_3^{(1)}$ and $M_4^{(1)}$, the sum of their contributions is only non-zero for CO states. Independently of the wave type it is given by

$$\begin{aligned} M_{3+4}^{(1)} &= g_s \,\frac{P_\alpha}{P\cdot p_g}\,\epsilon^{\alpha *}_{\lambda_g}(p_g) \int \frac{d^4k}{(2\pi)^4}\sqrt{2}\Big[\mathcal{O}_{ij}(P,k)\,\big(t^b_{jl}\,t^c_{li} - t^c_{jl}\,t^b_{li}\big)\Phi(P,k)\Big] \\ &= (ig_s\, f_{bcd})\frac{P_\alpha}{P\cdot p_g}\,\epsilon^{\alpha *}_{\lambda_g}(p_g) \int \frac{d^4k}{(2\pi)^4}\Big[\mathcal{O}_{ij}(P,k)\,\Phi^d_{ji}(P,k)\Big]\,, \end{aligned} \tag{5.105}$$

such that:

$$\mathcal{M}_{3+4}^{(1)} = \delta_{ad}\, M_1^{(1)} = (ig_s f_{abc})\,\frac{P_\alpha}{P\cdot p_g}\,\epsilon^{\alpha *}_{\lambda_g}(p_g)\, M^{(0)}\,. \tag{5.106}$$

Finally, we can combine the contribution from the single diagrams to obtain the full amplitude:

$$\mathcal{M}^{(1)} = (ig_s f_{abc})\left[\frac{P_\alpha}{P\cdot p_g} - \frac{p_\alpha}{p\cdot p_g}\right]\epsilon^{\alpha *}_{\lambda_g}(p_g)\, M^{(0)}\,. \tag{5.107}$$

The squared amplitude is then found using Eq. 5.94

$$|\mathcal{M}^{(1)}|^2 = g_s^2\, C_A\Big[2S_g\big(p,P\big) - S_g\big(P,P\big)\Big]\,|M^{(0)}|^2\,, \tag{5.108}$$

where the soft functions dependent on the momenta v_i are defined as:

$$S_g(v_1,v_2) = \frac{v_1\cdot v_2}{(v_1\cdot p_g)(v_2\cdot p_g)} \tag{5.109}$$

Considering the frame where q and p are along the $\hat{z}$ axis, the momenta of the particles can be decomposed as follows

$$p^\mu = p^+ n_+^\mu = \frac{x_B}{\hat{x}_{\max}} n_+^\mu\,, \tag{5.110}$$

$$q^\mu = q^+ n_+^\mu - \frac{Q^2}{2q^+} n_-^\mu = -x_B n_+^\mu + \frac{Q^2}{2x_B} n_-^\mu\,, \tag{5.111}$$

$$p_g^\mu = p_g^+ n_+^\mu + p_g^- n_-^\mu + p_{gT}^\mu = \frac{\mathbf{p}_{gT}^2}{2p_g^-} n_+^\mu + p_g^- n_-^\mu + p_{gT}^\mu\,, \tag{5.112}$$

and the TM of the quarkonium satisfies the relation $\mathbf{P}_T = -\mathbf{p}_{gT}$. So, we have that

$$\hat{s} = -Q^2 + 2p^+q^- = M_\mathcal{Q}^2 \quad\Longrightarrow\quad 2p^+q^- = Q^2 + M_\mathcal{Q}^2\,, \tag{5.113}$$

and we define the following variable:

$$x_g \equiv \frac{p_g\cdot p}{q\cdot p} = \frac{p_g^-}{q^-} = \frac{2x_B}{Q^2} p_g^-\,. \tag{5.114}$$

In the TMD limit, we have that $p_{gT} \to 0$ and $q + p \approx P$. Hence, we have that $P^- \approx q^-$ and $P^+ \approx p^+ - Q^2/(2q^+)$. Furthermore, momentum conservation implies that:

$$p_g^- \leq q^- \quad \text{and} \quad p_g^+ \leq p^+ - \frac{Q^2}{2q^+} \leq p^+\,. \tag{5.115}$$

If we divide the first inequality by q^-, we obtain $x_g \leq 1$, while, taking into account that $p_g^+ = \mathbf{p}_{gT}^2/(2p_g^-)$, the second one implies:

$$p_g^- \geq \frac{\mathbf{p}_{gT}^2}{2p^+}\,. \tag{5.116}$$

Dividing the latter by q^-, we get $x_g \geq \mathbf{p}_{gT}^2/(Q^2+M_Q^2)$, such that an upper and lower bound are found:

$$\frac{\mathbf{p}_{gT}^2}{Q^2+M_Q^2} \leq x_g \leq 1\,. \tag{5.117}$$

Using that phase space of the emitted (on-shell) soft gluon can be written as follows

$$\frac{d^4p_g}{(2\pi)^4}\,\delta(p_g^2) = \frac{1}{(2\pi)^4}\,dp_g^+\,dp_g^-\,d^2\mathbf{p}_{gT}\,\delta(2p_g^+p_g^- - \mathbf{p}_{gT}^2) = \frac{1}{2(2\pi)^4}\,\frac{dp_g^-}{p_g^-}\,d^2\mathbf{P}_T\,, \tag{5.118}$$

the differential cross section can be calculated:

$$\begin{aligned} d\sigma^{(1)} &\propto \frac{g_s^2}{2(2\pi)^3}\,C_A \int_{\frac{\mathbf{p}_{gT}^2}{Q^2+M^2}}^{1} \frac{dx_g}{x_g}\left[2S_g(p,P) - S_g(P,P)\right]|M^{(0)}|^2 \\ &= \frac{g_s^2}{2(2\pi)^3}\,C_A\left[2I_1(p,P) - I_2(P,P)\right]|M^{(0)}|^2\,. \end{aligned} \tag{5.119}$$

The soft functions read explicitly

$$S_g(p,P) = \frac{2}{M_Q^2\,x_g^2 + \mathbf{p}_{gT}^2}\,, \tag{5.120}$$

and

$$S_g(P,P) = \frac{4\,M_Q^2\,x_g^2}{(M_Q^2\,x_g^2 + \mathbf{p}_{gT}^2)^2}\,, \tag{5.121}$$

such that we find

$$I_1 = \int_{\frac{\mathbf{p}_{gT}^2}{Q^2+M_Q^2}}^{1} \frac{dx_g}{x_g}\,\frac{2}{M_Q^2\,x_g^2 + \mathbf{p}_{gT}^2} \approx \frac{1}{\mathbf{p}_{gT}^2}\left[\ln\frac{Q^2+M_Q^2}{\mathbf{p}_{gT}^2} + \ln\frac{Q^2+M_Q^2}{M_Q^2}\right], \tag{5.122}$$

and:

$$I_2 = \int_{\frac{\mathbf{p}_{gT}^2}{Q^2+M_Q^2}}^{1} \frac{dx_g}{x_g}\,\frac{4\,M_Q^2\,x_g^2}{(M_Q^2\,x_g^2 + \mathbf{p}_{gT}^2)^2} \approx \frac{2}{\mathbf{p}_{gT}^2}\,. \tag{5.123}$$

Therefore, Eq. 5.119 becomes

$$d\sigma_{ep}^{(1)} \propto \frac{\alpha_s}{2\pi^2\mathbf{p}_{gT}^2}\,C_A\left[\ln\frac{Q^2+M_Q^2}{\mathbf{p}_{gT}^2} - 1 - \ln\frac{M_Q^2}{Q^2+M_Q^2}\right]|M^{(0)}|^2\,, \tag{5.124}$$

where the term in square brackets agrees with the first terms of Eq. 5.91 that belong to the large TM perturbative tails of the TMD and the revised TMDShF.

Similarly, for single CO quarkonium photoproduction and hadroproduction[3]

$$d\sigma_{\gamma p}^{(1)} \propto \frac{\alpha_s}{2\pi^2\mathbf{p}_{gT}^2}\, C_A\left[\ln\frac{M_\mathcal{Q}^2}{\mathbf{p}_{gT}^2} - 1\right]|M^{(0)}|^2\,, \tag{5.125}$$

$$d\sigma_{pp}^{(1)} \propto \frac{\alpha_s}{2\pi^2\mathbf{p}_{gT}^2}\, C_A\left[2\ln\frac{M_\mathcal{Q}^2}{\mathbf{p}_{gT}^2} - 1\right]|M^{(0)}|^2\,, \tag{5.126}$$

where the factor 2 in front of the logarithm in the proton-proton case is related to the fact that this process contains two TMDs.

On a different note, we point out that recent calculations using soft-gluon radiation have demonstrated that azimuthal correlations between a J/ψ and a jet in photoproduction at EIC provide a unique probe of the quarkonium production mechanism [148]: a significant $\cos(\phi)$-asymmetry is found for the CS channel, whereas it vanishes or has an opposite sign for CO production, depending on the TM of the jet.

5.5 Universality and factorisation

We have seen that the LO TMDShF tails from the matching procedure absorb all the q_T-divergent terms coming from the collinear limit. However, they have been obtained at the particular scale $\widetilde{Q}$, whereas for more general application they need to be considered at a general scale μ_H. This can be obtained by tracing back the μ_H dependence in Eq. 5.91, which is related to the full Sudakov for J/ψ electroproduction in terms of this general scale up to order α_s. Namely, evaluating Eq. 4.51 gives

$$S_P^{ep}(b_T;\mu_H,\mu_b) = \frac{1}{2}\frac{C_A}{\pi}\alpha_s\left[\frac{1}{2}\ln^2\frac{\mu_H^2}{\mu_b^2} - \left(\frac{\beta_0}{6} + \mathrm{B_{CO}}(\mu_H)\right)\ln\frac{\mu_H^2}{\mu_b^2}\right], \tag{5.127}$$

where the scale dependent $\mathrm{B_{CO}}$ term is defined in Eq. 4.56. This agrees with the Sudakov factor obtained in heavy-quark pair production in electron-proton collisions [131]. Specifically, they have instead of $\mathrm{B_{CO}}(\mu_H)$

$$\mathrm{B_{final}}(\mu_H) = -\frac{1}{2N_c^2}\frac{1+\beta^2}{\beta}\ln\frac{1-\beta}{1+\beta} + 2\frac{C_F}{N_c} - \ln\frac{t_1u_1}{\mu_H^2m_c^2}\,, \tag{5.128}$$

for which the kinematic variables are defined as follows:

$$\beta = \sqrt{1-4m_c^2/M_\mathcal{Q}^2}\,, \tag{5.129}$$

$$t_1 = (k_1 - xP_h)^2 - m_c^2\,, \tag{5.130}$$

$$u_1 = (k_2 - xP_h)^2 - m_c^2\,. \tag{5.131}$$

When the heavy-quark pair binds we obtain $\beta \to 0$ and $u_1 = t_1$, because $k_1 = k_2 = P/2$. This gives in the small-q_T limit:

$$u_1 = t_1 = P\cdot p = \frac{Q^2+M_\mathcal{Q}^2}{2}\,. \tag{5.132}$$

---

[3] It should be mentioned that vector quarkonia produced from gluon-gluon fusion are necessarily in the CO state due to the Landau-Yang theorem. Moreover, in case of a CO final state in proton-proton collisions the gluon TMD will involve a different gauge link structure than in electroproduction and TMD factorisation may not even hold. As there is much unclear about this, we will ignore this complicating matter in this thesis.

The limit of the first two terms in $\mathrm{B}_{\text{final}}$ give rise to a constant term

$$-\lim_{\beta\to 0}\frac{1}{2N_c^2}\frac{1+\beta^2}{\beta}\ln\frac{1-\beta}{1+\beta}-2\frac{C_F}{N_c}=1\,, \tag{5.133}$$

while the last term can be rewritten as:

$$\ln\frac{\mu_H^2 M_{\mathcal{Q}}^2}{(Q^2+M_{\mathcal{Q}}^2)^2}\,. \tag{5.134}$$

However, it is not natural to fully include Eq. 4.56 into something that we identify as the TMDShF, as done in Eq. 4.55 (although it might be convenient for numerical calculations). Indeed, being a quarkonium-related object, its complete dependence is given by $\Delta^{[n]}_{\text{ShF}}(z,\mathbf{k}_T^2;M_{\mathcal{Q}},\mu=\mu_H)$, while it may depend on the process-related hard-quantity Q only via the μ_H choice. Thus, the Q^2 dependence deriving from Eq. 4.56 must stem from a process-dependent part, which can be incorporated into an extra process-dependent factor $S(\mathbf{b}_T^2;M_{\mathcal{Q}},Q,\mu=\mu_H)$. Therefore, we split the full $\Delta^{[n]}_{ep}$ into these two terms:

$$\Delta^{[n]}_{ep}(\mu_H)=\Delta^{[n]}_{\text{ShF}}(\mu_H)\times S_{ep}(\mu_H)\,. \tag{5.135}$$

The $\Delta^{[n]}_{\text{ShF}}$ is what we truly identify as the TMDShF and is expected to be universal because it solely depend on $M_{\mathcal{Q}}$. Instead, the S_{ep} is an extra soft factor which incorporates the specific process dependence and it can be removed by a proper choice of the factorisation scale $\mu=\mu_H$. This implies that at that scale the full $\Delta^{[n]}_{ep}$ is equivalent to the TMDShF. At this level, the simplest way to perform the splitting in b_T space is to take:

$$\hat{\Delta}^{[n]}_{\text{ShF}}(z,\mathbf{b}_T^2;\mu_H,\mu_b)=\langle\mathcal{O}^{\mathcal{Q}}[n]\rangle\left(1+\frac{\alpha_s}{2\pi}C_A\left[1+\ln\frac{M_{\mathcal{Q}}^2}{\mu_H^2}\right]\ln\frac{\mu_H^2}{\mu_b^2}\right)\delta(1-z)\,, \tag{5.136}$$

$$S_{ep}(\mathbf{b}_T^2;\mu_H,\mu_b)=1+\frac{\alpha_s}{2\pi}C_A\left[2\ln\frac{\mu_H^2}{Q^2+M_{\mathcal{Q}}^2}\right]\ln\frac{\mu_H^2}{\mu_b^2}\,. \tag{5.137}$$

Then, by taking $\mu_H=\widetilde{Q}$, the full $\Delta^{[n]}_{ep}$ reduces to the TMDShF, implying that the latter is given by Eq. 5.93 with Eq. 5.92.

To test the proposed factorisation, one can take another process and check if it is possible to identify the same TMDShF in Eq. 5.136. We consider J/ψ hadroproduction, for which the small-q_T behaviour of the cross section evaluated in the HTM region has been calculated in [127]. The corresponding Sudakov factor for the channels $g+g\to[Q\bar{Q}]({}^1S_0^c,\,{}^3P_J^c)$ can be written as

$$S_P^{pp}(b_T;\mu_H,\mu_b)=\frac{C_A}{\pi}\alpha_s\left(\frac{1}{2}\ln^2\frac{\mu_H^2}{\mu_b^2}-\left(\frac{\beta_0}{6}+\frac{1}{2}\mathrm{B}^{pp}_{\text{CO}}(\mu_H)\right)\ln\frac{\mu_H^2}{\mu_b^2}\right)\,, \tag{5.138}$$

where

$$\mathrm{B}^{pp}_{\text{CO}}(\mu_H)=1+2\ln\frac{\mu_H^2}{M_{\mathcal{Q}}^2}\,, \tag{5.139}$$

in which the first term is directly related to the δ_{8c} term in [127]. Also in this case we checked that previous equations agree in the kinematic limit corresponding to a bound pair with the open heavy-quark pair production Sudakov factor, which can be found in the literature (see e.g. [144]). Moreover, we find that in proton-proton collisions, our perturbative tail applies exclusively to CO states as well. Despite this, we cannot exclude that any non-trivial TMDShF perturbative tail applies to the CS channel at higher-order α_s.

Even if the full $\Delta_{pp}^{[n]}$ is different from $\Delta_{ep}^{[n]}$, we can still identify the same $\Delta_{\mathrm{ShF}}^{[n]}$, which is now combined with a different (extra) soft factor S_{pp}, namely

$$\Delta_{pp}^{[n]}(\mu_H) = \Delta_{\mathrm{ShF}}^{[n]}(\mu_H) \times S_{pp}(\mu_H)\,, \tag{5.140}$$

with:

$$S_{pp}(\mathbf{b}_T^2; \mu_H, \mu_b) = 1 + \frac{\alpha_s}{2\pi} C_A \left[3 \ln \frac{\mu_H^2}{M_\mathcal{Q}^2}\right] \ln \frac{\mu_H^2}{\mu_b^2}\,. \tag{5.141}$$

Interestingly, for S_{pp} the coefficient in front of the logarithm is 3, whereas the same coefficient for S_{ep} is 2, which corresponds to the number of TMD quantities (PDFs and ShFs) involved. Hence, even if process dependent, these terms are the same apart from the number of TMDs involved. This may allow one to guess the required term for other processes, such as for quarkonium-pair hadroproduction (if this process factorises at all for CO-CO production).

The factor S_{pp} reduces to unity when $\mu_H = M_\mathcal{Q}$, such that $\Delta_{pp}^{[n]}(M_\mathcal{Q}) = \Delta_{\mathrm{ShF}}^{[n]}(M_\mathcal{Q})$, which agrees with our result in the eikonal approximation presented in Eq. 5.126. For this scale choice, $\Delta_{\mathrm{ShF}}^{[n]}(M_\mathcal{Q})$ is compatible with the corresponding one presented in [71] for χ_c decay into light-quarks, where the NLO TMDShF up to corrections of $O(k_T^{-1})$ is given by a constant too.

According to our findings, in principle one may obtain the value of $\Delta_{ep}^{[n]}(\widetilde{Q})$ from the experimentally determined $\Delta_{pp}^{[n]}(M_\mathcal{Q}^2) = \Delta_{\mathrm{ShF}}^{[n]}(M_\mathcal{Q}) \big(\neq \Delta_{ep}^{[n]}(M_\mathcal{Q})\big)$, by evolving $\Delta_{\mathrm{ShF}}^{[n]}(M_\mathcal{Q})$ to $\Delta_{\mathrm{ShF}}^{[n]}(\widetilde{Q})$. Hence, we propose a strategy for the extraction of the TMDShF from different processes, relying on their factorisability. For processes where we have a dominant hard scale it is reasonable to expect that by setting μ_H equivalent to it we reduce our uncertainties in the extraction of the TMDShF. This applies to both proton-proton collisions, where we have only $M_\mathcal{Q}$, and electron-proton collisions, if $Q \gg M_\mathcal{Q}$ or $Q \ll M_\mathcal{Q}$ (including photoproduction). Then, this term can be re-used for every process involving a CO J/ψ by evolving $\Delta_{\mathrm{ShF}}^{[n]}$ to the scale μ_H' and combining it with the proper process-dependent extra soft factor $S(\mu_H')$.

For completeness, we mention that the soft factor derived for the open heavy-quark pair production also involves an additional process-dependent factor [30, 149, 150] (which is sometimes denoted by Δ, but should not to be confused with ours). This additional factor stems from soft radiation in the $Q\bar{Q}$ production and can in principle even depend on the angle of $\mathbf{q}_T$. Hence, it is natural to expect an additional process-dependent soft term in the quarkonium case too. In that sense we expect that our extra soft term S will acquire azimuthal and rapidity dependencies if one goes beyond the order and approximation we have considered, as they are present in the Δ quantity of [30, 150].

“Master your instrument, master the music,
and then forget all that stuff and just play.”

- Charlie Parker

6

Predictions of TM spectra and azimuthal modulations

In this chapter we present numerical predictions for observables that have been discussed in this thesis by employing TMD evolution. We assess multiple approaches for the nonperturbative Sudakov factor. First, we improve on predictions of the convolutions and the $\cos 2\phi$ azimuthal asymmetry in quarkonium electroproduction by including the TMDShF contributions in Sec. 6.1. To do so we use an extracted nonperturbative Sudakov factor from quark induced processes and vary it to estimate the nonperturbative uncertainty. Thereafter, we investigate the nonperturbative Sudakov factor in greater detail in Sec. 6.2. Specifically, we examine the problems associated with using a simple Gaussian ansatz for it and revise the b_T-prescriptions to address the issues mentioned in Sec. 4.2, leading to the construction of a novel nonperturbative Sudakov factor. In Sec. 6.3 this correction factor is employed for $\mathcal{C}[f_1^g f_1^g]$ and quarkonium-pair production observables. The particular focus on this convolution arises from the observation that it is a general quantity that determines the differential cross section for any unpolarised proton-proton collisions that are dominated by gluon-gluon fusion, such as quarkonium production [24], Higgs production [104, 106], quarkonium-dilepton production [97] and quarkonium-pair production [92]. Moreover, it is important in processes next to quark-antiquark and quark-gluon contributions, like in photon-pair production [151], Higgs plus jet production [152], dijet production [153] and open heavy-quark pair production [12, 80, 94]. In this section we also examine the theoretical and nonperturbative uncertainties in more depth. Besides, we compare our results with data on J/ψ-pair production, which shows good agreement. Lastly, we present examples of numerical matching between the collinear and TMD regimes for J/ψ electroproduction in Sec. 6.4, as a first step towards a complete theoretical TM spectrum for gluon-induced quarkonium production.

6.1 TMD-evolution results for J/ψ production at EIC

In this section we update on the results presented in [123] since this work was carried out prior to the study of the corrected LO TMDShF tails discussed in Ch. 5. In particular, we utilise the TMD-evolution formalism presented in Sec. 4.2 with $\mu_H = Q$ and apply μ'_{b^*} in Eq. 4.44 to constrain the perturbative expressions (we note that the difference in μ_b does not alter the matching procedure to obtain the TMDShF tails). Moreover, we employ the perturbative Sudakov factor given in Eq. 4.52, and use the tails of the TMDs presented in Eqs. 4.53 and 4.54. Since the tail of $\Delta_h^{[n]}(z, \mathbf{k}_T^2)$ is currently unknown we take it equal to the tail of $\Delta^{[n]}(z, \mathbf{k}_T^2)$, i.e. absence of smearing is considered (they are simply equal to $\delta^2(\mathbf{k}_T)$ times the LDMEs). This is what we adopt, but only after including effects from TMD evolution, i.e. their large TM perturbative part is resummed in S_P by the $\mathrm{B_{CO}}$ term defined in Eq. 4.56. We note that this choice is supported by the eikonal approximation presented in Sec. 5.4 since it is spin independent.

Following Eq. 4.58 the only missing ingredient to evaluate $\mathcal{C}[f_1^g \Delta^{[n]}]$ and $\mathcal{C}[w h_1^{\perp g} \Delta_h^{[n]}]$ is the nonperturbative Sudakov factor. A parametrisation for S_{NP} for quarks was obtained from fits to low energy SIDIS data as well as higher energy DY and Z-boson production data [122]

$$S_{NP}(b_T; Q, \mu_{NP}) = \left[g_1 \ln\frac{Q}{2\mu_{NP}} + g_2\left(1 + 2g_3 \ln\frac{10 x x_0}{x_0 + x}\right)\right] b_T^2\,, \tag{6.1}$$

with $g_1 = 0.184\,\mathrm{GeV}^2$, $g_2 = 0.201\,\mathrm{GeV}^2$, $g_3 = -0.129$, $x_0 = 0.009$, $\mu_{NP} = 1.6\,\mathrm{GeV}$ and $b_{T,\max} = 1.5\,\mathrm{GeV}^{-1}$. We take this expression for two fixed small-x values as our starting point and Casimir scale it in order to apply to gluons:

$$S_{NP}(b_T; Q, \mu_{NP}) = \left[A \ln\frac{Q}{\mu_{NP}} + B(x)\right] b_T^2\,, \quad \text{with} \quad A = \frac{C_A}{C_F}\, g_1 = 0.414\,\mathrm{GeV}^2\,. \tag{6.2}$$

The B term can be thought of as related to the intrinsic TM of the TMD (in case there is no nonperturbative contribution from the TMDShF), which generally is x dependent. By Fourier transforming a simple Gaussian dependence for $f_1^g(x, \mathbf{p}_T^2) \propto \exp[-\mathbf{p}_T^2/\langle p_T^2\rangle]$, we obtain $B \approx \langle p_T^2\rangle/4$ (at $Q = \mu_{NP}$). Of course, the B term is not necessarily the same for the convolution containing $h_1^{\perp g}(x, \mathbf{p}_T^2)$, but for simplicity we do not distinguish between these cases. Matching Eq. 6.1 and 6.2 for the x values that we will consider yields the specific B values shown in Table 6.1.

To perform an error estimate and to assess the importance of S_{NP} for the size of the convolutions and asymmetry, we will vary A within the extreme limits following [92] (where the difference with respect to their A values, presented below Eq. 4.60, comes from their choice of $\mu_{NP} = 1\,\mathrm{GeV}$), instead of taking the one quoted in Eq. 6.2. The idea is that one expects the $\exp(-S_{NP})$ term to be non-negligible (arbitrary defined as being larger than 10^{-3}) anywhere between $b_{T,\max}$ and the charge radius of the proton. If $\exp(-S_{NP})$ becomes negligible around $b_{T,\max}$ already, then there will be hardly any nonperturbative contribution outside the perturbative regime, which is not intuitive. On the other hand, one does not expect significant contributions to the convolutions beyond the charge radius of the proton, offering an upper bound. To implement this range, we define a value $b_{T,\lim}$ such that for large Q, where the A term is dominant and

Table 6.1: Values of the parameters A and B used in the Gaussian S_{NP}. Left the A values are shown along with the corresponding $b_{T,\mathrm{lim}}$ and r determined at $Q = 12\,\mathrm{GeV}$. Right the B values are shown determined by x.

$b_{T,\mathrm{lim}}$ (GeV^{-1})	$r\,(\mathrm{fm} \sim 1/0.2\,\mathrm{GeV}^{-1})$	$A\,(\mathrm{GeV}^2)$
2	0.2	0.80
4	0.4	0.20
8	0.8	0.05

x	$B\,(\mathrm{GeV}^2)$
10^{-1}	0.456
10^{-2}	0.521
10^{-3}	0.715

the B term can be neglected, $\exp(-S_{NP})$ becomes negligible, i.e. $\sim 10^{-3}$. Considering $b_{T,\mathrm{lim}}$ as the diameter, since it is conjugate to q_T, r is defined as the characteristic radius $r = b_{T,\mathrm{lim}}/2$, that can be thought of as the range over which the interactions occur from the centre of the proton. For three values of $b_{T,\mathrm{lim}}$ or r we determined the A values at $Q = 12$ GeV, which are shown in Table 6.1. We note that $A = 0.414\,\mathrm{GeV}^2$ from Eq. 6.2 lies roughly in the middle of this range.

We will include the B term in S_{NP} as it is needed for smaller Q values and large-$b_{T,\mathrm{lim}}$ values. This is illustrated in Fig. 6.1: the product $\exp(-S_P)\exp(-S_{NP})$ for $Q = 3\,\mathrm{GeV}$ receives large contributions from S_P all the way up to or even beyond the proton radius. This results in an upward bump at small q_T in the convolutions, in particular for $\mathcal{C}[wh_1^{\perp g}\Delta_h^{[n]}]$. Moreover, for small Q the limit of $B \to 0$ can result in a violation of the positivity bound for the convolutions: $\mathcal{C}[wh_1^{\perp g}\Delta_h^{[n]}] \leq \mathcal{C}[f_1^g\Delta^{[n]}]$. These issues will be discussed in greater detail in the following section. For larger Q values, the curves with and without B term lie increasingly closer to each other, as expected.

To illustrate the typical features of the TMD evolution of the convolutions $\mathcal{C}[f_1^{\perp g}\Delta^{[n]}]$ and $\mathcal{C}[wh_1^{\perp g}\Delta_h^{[n]}]$, and their ratio R (see Eq. 3.96), we present in Fig. 6.2 results for a specific LDME, namely $\langle\mathcal{O}^{J/\psi}[{}^1S_0^8]\rangle$ from CMSWZ (that only contributes to the magnitude of the convolutions). The results are shown for a range of Q values of relevance to the EIC, $Q = 3$, 6, 12, 20 and 30 GeV, and for three different values of x: 10^{-3}, 10^{-2}, and 10^{-1}. Although $x = 10^{-1}$ lies outside the gluon dominated region and we do not include the contribution from quark TMDs, we include this case for illustration purposes in order to see the results for larger Q values. For the two smaller values of x, the contribution from the collinear quark PDF to the tail of $h_1^{\perp g}$ is non-negligible, therefore it is included. We note that in this figure, as well as in the remaining figures of this section, the dashed line represents that $b_{T,\mathrm{lim}} = 2\,\mathrm{GeV}^{-1}$ is employed for the nonperturbative part of the computation, while the solid line indicates that $b_{T,\mathrm{lim}} = 8\,\mathrm{GeV}^{-1}$ is used. Moreover, in this chapter all curves are shown up to $q_{T,\mathrm{max}}$ to remain within the TMD regime as is commonly done, i.e. $Q/2$ in this particular section.

We identify that the TM spectrum broadens and the estimated uncertainty band from the unknown nonperturbative contributions becomes smaller with increasing Q, as one would expect. Generally the maxima of the convolutions increase towards smaller Q, for which the $Q = 3\,\mathrm{GeV}$ cases with small x are an exception. For $q_T\,\mathcal{C}[f_1^g\Delta]$ this can be understood from the significant relative decrease in magnitude of the perturbative f_1^g tail for smaller Q values in combination with the Sudakov factors,

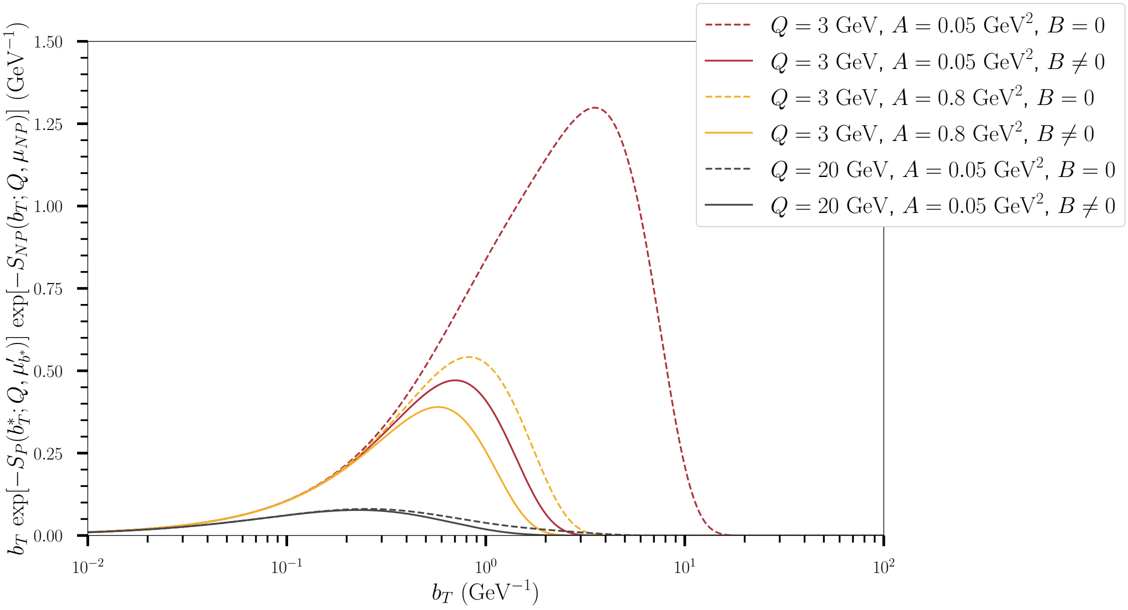

Figure 6.1: b_T times the product of the Sudakov factors as a function of b_T for $Q = 3\,\text{GeV}$ and $Q = 20\,\text{GeV}$, which shows the importance of the extra B term in S_{NP} at small Q and large $b_{T,\text{lim}}$, suppressing the unwanted contributions at large b_T. Here $b_{T,\text{max}} = 1.5\,\text{GeV}^{-1}$ and B at $x = 10^{-3}$ is used.

where the B term is then of large influence. The decrease of $q_T\,\mathcal{C}[w h_1^{\perp g} \Delta_h]$ is, on the other hand, predominantly due to the Sudakov factors as the perturbative $h_1^{\perp g}$ tail with these x values stays approximately constant when varying Q.

The differences in behaviour of the two convolutions depends on various factors: the differences between the tails of the TMDs, the type of Bessel function and the Sudakov factors. It can be seen in Fig. 6.2 that the presence of $h_1^{\perp g}$ in a convolution contributes to reducing the magnitude of the integrand. This is because its tail is naturally suppressed by order α_s in comparison to f_1^g. We note that $\alpha_s(\mu'_{b_*})$ increases as a function of b_T, up to its upper value $\sim \alpha_s(b_0/b_{T,\text{max}})$, such that the $h_1^{\perp g}$ tail can become larger in comparison to the f_1^g tail at large b_T. This effect becomes more pronounced for smaller x. Besides, while the product of the tail with the Sudakov factors approaches zero at large b_T, the $h_1^{\perp g}$ tail typically exhibits a more gradual slope compared to f_1^g. As a result, its presence contributes to b_T-broadening.

It is observed that all convolutions begin to decrease as a function of q_T beyond a certain point. This specific behaviour depends on the type of Bessel function and the width of the integrands in b_T space. In particular, the consequence of the b_T-broadening is that more damped oscillations of the J_0 Bessel function in $\mathcal{C}[f_1^g \Delta]$ occur before the integrand becomes zero. Each additional oscillation in the integrand brings the convolution closer to zero and more oscillations fit in a given b_T range when q_T increases. Therefore, $\mathcal{C}[f_1^g \Delta]$ with smaller Q decreases faster, taking into account the b_T-broadening of the Sudakov factors. It is important to note that the peaks of these convolutions in Fig. 6.2 arise from their multiplication with q_T. The situation is different for $\mathcal{C}[w h_1^{\perp g} \Delta_h]$ that contains the J_2 Bessel function. This function starts its damped oscillation at zero, instead of one, and goes up, instead of down. The consequence is that the b_T integrals benefit from unsuppressed intermediate b_T values.

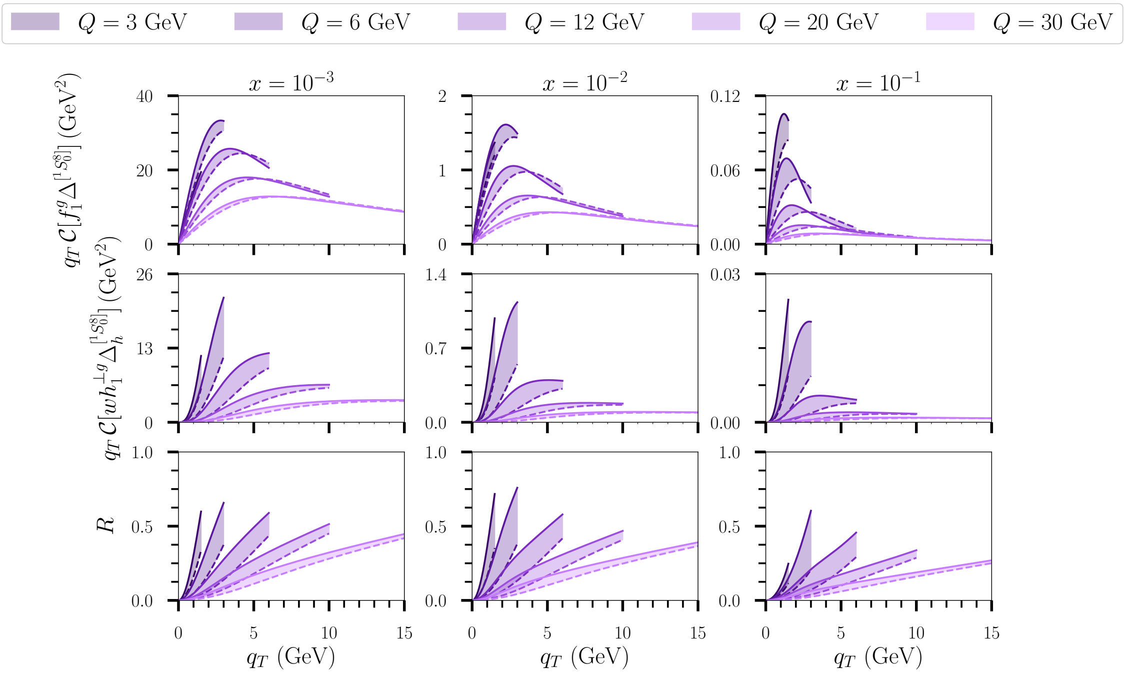

Figure 6.2: The convolutions times q_T and the ratio of the convolutions, R, as a function of q_T for various values of Q, with $x = 10^{-3}$ (left), $x = 10^{-2}$ (middle) and $x = 10^{-1}$ (right), using $b_{T,\lim} = [2 : 8]\,\text{GeV}^{-1}$. Here we are using the central value of $\langle \mathcal{O}^{J/\psi}[^1S_0^8] \rangle$ from CMSWZ as an example (see Table 3.3).

This results in a peak maximum before large-b_T oscillations will bring the convolution down towards zero in a similar way as for $\mathcal{C}[f_1^g \Delta]$, i.e. the peaks in these convolutions are generated by themselves. As can be seen, these maxima naturally occur at smaller q_T for smaller Q. Another crucial difference is that the envelope of J_2 tends slower towards zero than the J_0 one with increasing b_T. The consequence is that $\mathcal{C}[w h_1^{\perp g} \Delta_h]$ falls slower than $\mathcal{C}[f_1^g \Delta]$, although $h_1^{\perp g}$ generally gives rise to more broad integrands. Hence, R and the azimuthal asymmetry, always grow with q_T, but more slowly for larger Q. In addition, as the large-b_T values in $\mathcal{C}[w h_1^{\perp g} \Delta_h]$ are less suppressed than in $\mathcal{C}[f_1^g \Delta]$, the azimuthal asymmetry and $\mathcal{C}[w h_1^{\perp g} \Delta_h]$ are more sensitive to the changes in S_{NP}.

Varying x in the computations changes the convolutions. First, we notice that the overall magnitude of the convolutions decreases for larger x, as the collinear gluon PDF is less prominent at larger x. Additionally, except for the smallest Q computations, the magnitude of R becomes smaller for large Q. Second, the shape of the perturbative TMD tails is different, in particular the f_1^g tail is broader in b_T for larger x. Moreover, the B term in S_{NP} is smaller, as can be seen in Table 6.1. Together, the broader b_T integrands make these convolutions go faster to zero for larger x. This explains the behaviour of the magnitude of R and that the azimuthal asymmetry increases slower with q_T for larger x, especially visible for larger Q. For the small-Q values, the magnitude of R as a function of x is found to be dictated by a delicate balance between both convolutions.

After these general qualitative observations, we present predictions for the azimuthal asymmetry at the EIC by employing Eq. 3.95. These are shown in Figs. 6.3

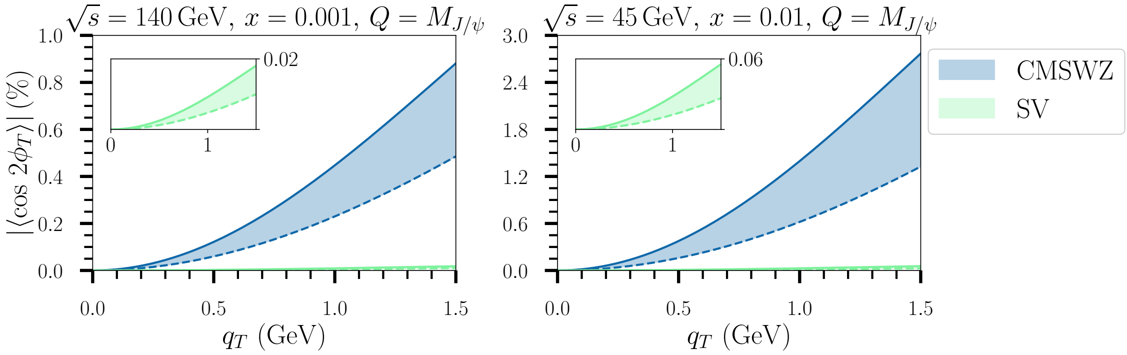

Figure 6.3: The azimuthal asymmetry as a function of q_T for $Q = M_{J/\psi}$ with the CMSWZ and SV LDMEs. Left is for $\sqrt{s} = 140\,\mathrm{GeV}$ and $x = 10^{-3}$. Right is for $\sqrt{s} = 45\,\mathrm{GeV}$ and $x = 10^{-2}$.

to 6.6, using the LDMEs from Table 3.3 and $s = Q^2/(x_B y)$ for two $\sqrt{s}$ values, 45 GeV and 140 GeV, commonly considered for the EIC. Specifically, we use the CMSWZ and SV sets here, and in the rest of this thesis, because the BCKL set gives similar results as the CMSWZ set for this process, and the BK set is not favourable to use as discussed in Sec. 3.4. We recall that the CMSWZ set is based on a NLO analyses, while the SV set is based on a LO calculation. In general, the asymmetry is (much) larger when using the CMSWZ set compared to the SV set, especially for small Q. TMD evolution predicts the azimuthal asymmetry to grow with q_T as discussed previously, and we see that the choice of LDMEs is of large influence in the predictions. This results in an uncertainty in the predictions that is larger than that due to S_{NP}, in some cases even an order of magnitude. Given this, going to the next order in α_s in the TMD-evolution calculation will not lead to much more precise predictions at the current stage. Besides, in the plots we restrict to the central values of the LDME fits, but of course, taking into account the uncertainties in these values would broaden the bands further, such that the bands for CMSWZ and SV start to overlap more, giving rise to a large range of possible asymmetry values at EIC. Depending on the kinematics measurably large asymmetries may thus be expected at the EIC, especially for the larger centre-of-mass energy of 140 GeV. Improved constraints on the CO LDMEs, and more generally on the TMDShFs, can very likely be obtained in this way.

In contrast to a LO Gaussian TMD model prediction [89], like the one presented in Fig. 4.3, we find that the azimuthal asymmetry grows monotonically in the TMD regime, more in line with the predictions from the generalised parton model approach with additional gluon radiation [93], except that the magnitude can be much larger by as much as an order of magnitude depending on the LDME set considered. Of course, the asymmetry cannot keep continuously growing, therefore the expectation is that a maximum will be reached outside the TMD regime. Larger and monotonically rising asymmetries have also been obtained in [26] for the McLerran-Venugopalan model including non-linear evolution x, showing decreasing asymmetries with decreasing x values. In our results the x dependence of the asymmetries is less systematic in the EIC kinematic range, as it depends on the considered Q value and on the LDMEs. Especially predictions with the SV set for $Q = M_{J/\psi}$ do not follow the observed trends and are exceptionally small due to a cancellation of the S- and P-wave LDMEs

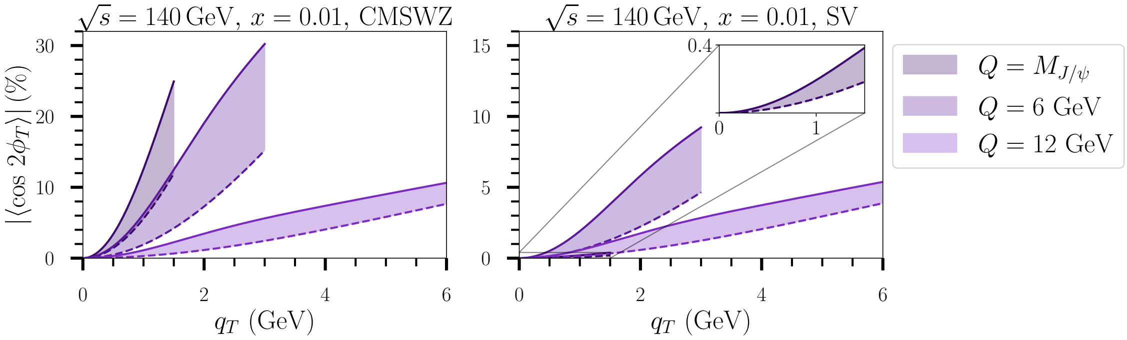

Figure 6.4: The azimuthal asymmetry as a function of q_T for $x = 10^{-2}$ using the CMSWZ (left) and SV (right) LDMEs, for various Q values that are kinematically allowed.

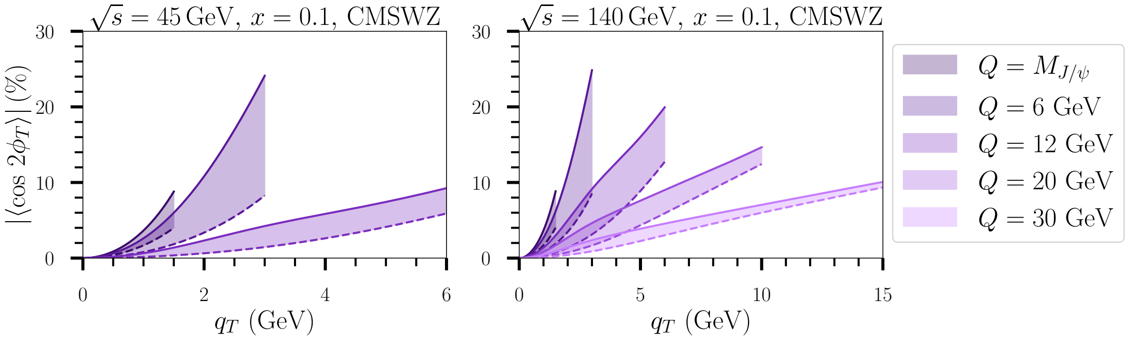

Figure 6.5: The azimuthal asymmetry as a function of q_T for $x = 10^{-1}$ using the CMSWZ LDMEs.

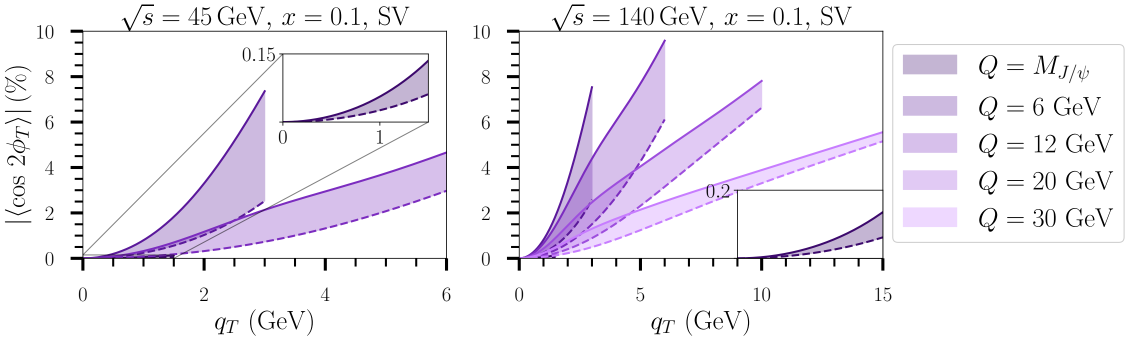

Figure 6.6: The azimuthal asymmetry as a function of q_T for $x = 10^{-1}$ using the SV LDMEs.

at Q^2 near $M_{\mathcal{Q}}^2$ in the numerator of the azimuthal hard factor (see Eq. 3.86). As Q increases, the P-wave LDME increasingly dominates the azimuthal hard factor, leading the predictions with different LDME sets to become similar, i.e. differing only in their magnitude.

In comparison to the previous results presented in [123], we point out that our educated guess was to take the TMDShFs universal, i.e. we chose $\mathrm{B_{CO}} = 1$ as for J/ψ hadroproduction in [127]. The additional Q dependence in this factor, see Eq. 4.56, makes a significant difference for the TMD evolved predictions, especially for large Q. In retrospect, this explains why we had to reduce the usual validity range in q_T of the TMD regime to ensure that $R \leq 1$, i.e. the process was actually not completely factorised.

6.2 A novel nonperturbative Sudakov factor

Before we continue with our discussion on the nonperturbative Sudakov factor we point out that we make a couple of different choices for the TMD evolution. First, we take $\tilde{\mu}'_{b^*}$, given in Eq. 4.43, instead of μ'_{b^*}, such that the perturbative expressions as a function b_T in both limiting cases of the b_T-regime, i.e. $b_{T,\min}$ and $b_{T,\max}$, converge to particular values with the same power (we elaborate more on this below). Moreover, here we use NLL resummation for the perturbative Sudakov (defined below Eq. 4.46) and consider the case of hadroproduction as an example, i.e. two TMDs are employed (instead of a TMD and a TMDShF as for electroproduction).

Because we can identify that $b_{T,\max} = b_0/\mu_{NP}$, we have that $\mu_{NP} \sim 750\,\mathrm{MeV}$ when $b_{T,\max} = 1.5\,\mathrm{GeV}^{-1}$. This can be considered doubtfully small since most of the evolution will be determined by perturbative physics as the integrand of the convolutions will already be quite small at large $b_{T,\max}$. On the other hand, a much smaller value of $b_{T,\max}$, such as $0.5\,\mathrm{GeV}^{-1}$, results in $\mu_{NP} \sim 2.25\,\mathrm{GeV}$, which can be considered conservative as the integrand of the convolutions will be still large at $b_{T,\max}$ such that the nonperturbative Sudakov factor is very relevant. Whatever the value of $b_{T,\max}$, a change in μ_{NP}, that alters the correction factor S_{NP}, should compensate the corresponding change in $\hat{W}(b_T^*, \mu_H)$ to leave the physical cross section unchanged, i.e.

$$\hat{W}(b_T, \mu_H) \approxeq \hat{W}(b_T^* \to b_T^{*\prime}, \mu_H) e^{-S_{NP}(b_T;\mu_H,\mu_{NP}\to\mu'_{NP})}\,, \tag{6.3}$$

for which the left-hand side should remain unchanged (see Eq. 4.57). For example, take the Gaussian ansatz

$$S_{NP}(b_T; \mu_H, \mu_{NP}) = A \ln\left(\frac{\mu_H}{\mu_{NP}}\right) b_T^2\,, \tag{6.4}$$

as recalled from Eq. 4.60. When $b_{T,\max}$ is altered, an additional change must come from A in order to obtain a $b_{T,\max}$-invariant $\hat{W}(b_T, \mu_H)$. Although there is for the particular Gaussian ansatz an educated guess to determine the A values for different hard scales, it is not $b_{T,\max}$ dependent and thus will not provide adequate compensation. In other words, if one wants a $b_{T,\max}$-invariant $\hat{W}(b_T, \mu_H)$, then one needs to allow for the most general form of Eq. 4.59, in particular with $g_K(b_T)$ more general than $\propto b_T^2$. Besides, we note that the Gaussian ansatz is TMD independent: it does not contain

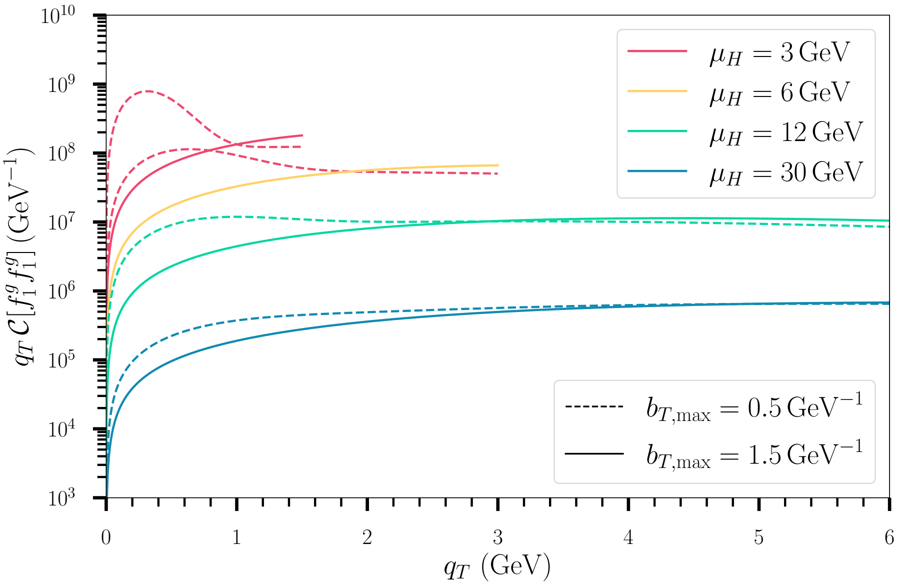

Figure 6.7: $q_T\,\mathcal{C}[f_1^g f_1^g]$ as a function of q_T by employing Eq. 6.4 with $A = 0.16\,\mathrm{GeV}^2$ as an example, for various μ_H and $b_{T,\max}$ values, with $y = 0$ and $\sqrt{s} = 13\,\mathrm{TeV}$.

x dependence and it is taken to be the same for every convolution although different TMDs may enter the convolution.

As mentioned before, for small hard scales the integrand of the convolutions can have large contributions at large values of b_T, all the way up to or even beyond the proton radius, depending on the value of $b_{T,\max}$ and the value of A in the Gaussian ansatz (in the examples of this section we simply adopt the various A values presented below Eq. 4.60 without taking into account the variation of μ_{NP}). These large-b_T nonperturbative contributions lead to an upward bump at small q_T in the convolutions as shown for $\mathcal{C}[f_1^g f_1^g]$ in Fig. 6.7. Since these upward bumps can violate the positivity bounds of the convolutions, a solution was implemented to avoid this in the previous section: an extra x-dependent B term in S_{NP} based on data. We note that contrary to the electroproduction case, no such term is necessary to satisfy the positivity bounds of the convolutions for hadroproduction when $b_{T,\max}$ is chosen to be $1.5\,\mathrm{GeV}^{-1}$. This is because of the extra perturbative Sudakov suppression and that NLL instead of LL accuracy is employed. However, we do observe the strange upward bump behaviour too when taking smaller values of $b_{T,\max}$ instead, for $\mu_H = 3\,\mathrm{GeV}$ as well as for larger values. It disappears again at some point due to suppression by S_P, when one continues to increase the hard scale. On the contrary, we can observe oscillations for the convolutions within the TMD regime by decreasing A from $0.16\,\mathrm{GeV}^2$ to $0.04\,\mathrm{GeV}^2$ (the smallest value of A; that gives the largest nonperturbative contributions), especially for small μ_H and small $b_{T,\max}$. This originates from unsuppressed oscillations of the Bessel function in the convolutions at large b_T too. Indeed, the upward bump at small q_T is merely the initial indication of it. Since the f_1^g TMD cannot be negative, such large-b_T contributions that lead to unphysical oscillations should be suppressed. However, whether the upward bump is real in the end, while not violating the positivity bound, depends on the extent of nonperturbative physics, which can only be determined by experimental data. We note that, unlike in q_T space, there is no positivity bound in b_T space.

If one investigates the perturbative expressions of the computation (the perturbative Sudakov factor, the TMD tails and α_s) as a function of b_T via $\tilde{\mu}'_{b*}$, one observes that these will deviate from those as a function of μ_b when b_T is around $b_{T,\min}$ and $b_{T,\max}$. This is simply due to the definitions of b_T^* and b_T' in Eq. 4.41 and Eq. 4.42, respectively, as was mentioned in Sec. 4.2. Moreover, when $b_{T,\min}$ and $b_{T,\max}$ are close together there is almost no agreement between the perturbative expressions as a function of $\tilde{\mu}'_{b*}$ and μ_b. Quarkonium production is very sensitive to this effect as one can have very small hard scales, i.e. less evolution from μ_H to $\tilde{\mu}'_{b*}$, much smaller than e.g. Higgs production [65]. Nevertheless, this is considered acceptable because the freeze-outs at both limits are satisfied, the same b_T-prescriptions are applied for all perturbative expressions and the perturbative expressions are smooth. Moreover, one still needs to multiply with S_{NP} which is unknown and alters the computation anyway.

Although it is expected that in reality there exists a region where nonperturbative physics takes over, we have chosen to enforce a clear separation between the perturbative and nonperturbative regimes. This allows us to fully rely on the perturbative expressions as a function of $\tilde{\mu}'_{b*}$ and, more specifically, to conduct a more careful study of S_{NP}. In particular, to make the perturbative expressions within $b_{T,\min} \leq b_T \leq b_{T,\max}$ more equal to the ones as a function of μ_b, we increase the power of the two restriction methods [1]

$$b_T^* = \frac{b_T}{\left(1 + (b_T/b_{T,\max})^n\right)^{1/n}} \,, \qquad b_T' = \left(b_T^n + b_{T,\min}^n\right)^{1/n} \,, \tag{6.5}$$

where n is an arbitrary integer and when $n = 2$ we retrieve Eqs. 4.41 and 4.42. We note that the same order n in both b_T^* and b_T' motivates our choice for $\tilde{\mu}'_{b*}$ presented in Eq. 4.43. The larger the value of n the closer the trend of the perturbative expressions as a function of μ_b is followed by the perturbative expressions as a function of $\tilde{\mu}'_{b*}$. We found that $n = 20$ is sufficient for our purposes as increasing n to larger values only continues to make the curves even closer together at the limiting points $b_{T,\min}$ and $b_{T,\max}$. Henceforth, we adopt $n = 20$ as the representative value for large n.

Naturally, it follows that the nonperturbative physics should only contribute when $b_T \gtrsim b_{T,\max}$ with the same order n. Therefore, we define

$$b_T^{\dagger\,2} = \left(b_T^n + b_{T,\max}^n\right)^{2/n} - b_{T,\max}^2 \,, \tag{6.6}$$

such that

$$S_{NP}(b_T^\dagger) = g\, b_T^{\dagger\,2} \,, \tag{6.7}$$

where g is the parameter of our Gaussian-like nonperturbative Sudakov factor. Although one can determine the exact asymptotic behaviour of S_{NP} as $b_T \to 0$ using perturbation theory, i.e. $S_{NP} \propto b_T^2$, we note that any power-law behaviour in this limit is considered acceptable [118]. Besides, when $n = 2$, i.e. $b_T^\dagger = b_T$, we retrieve Eq. 6.4 by considering $g = A \ln(\mu_H/\mu_{NP})$.

---

[1] We note that we are not the first to explore alternatives to the standard b_T^*-prescription given the limited understanding of nonperturbative physics, see e.g. [154–157]; however these studies adopt approaches that differ from the one presented here.

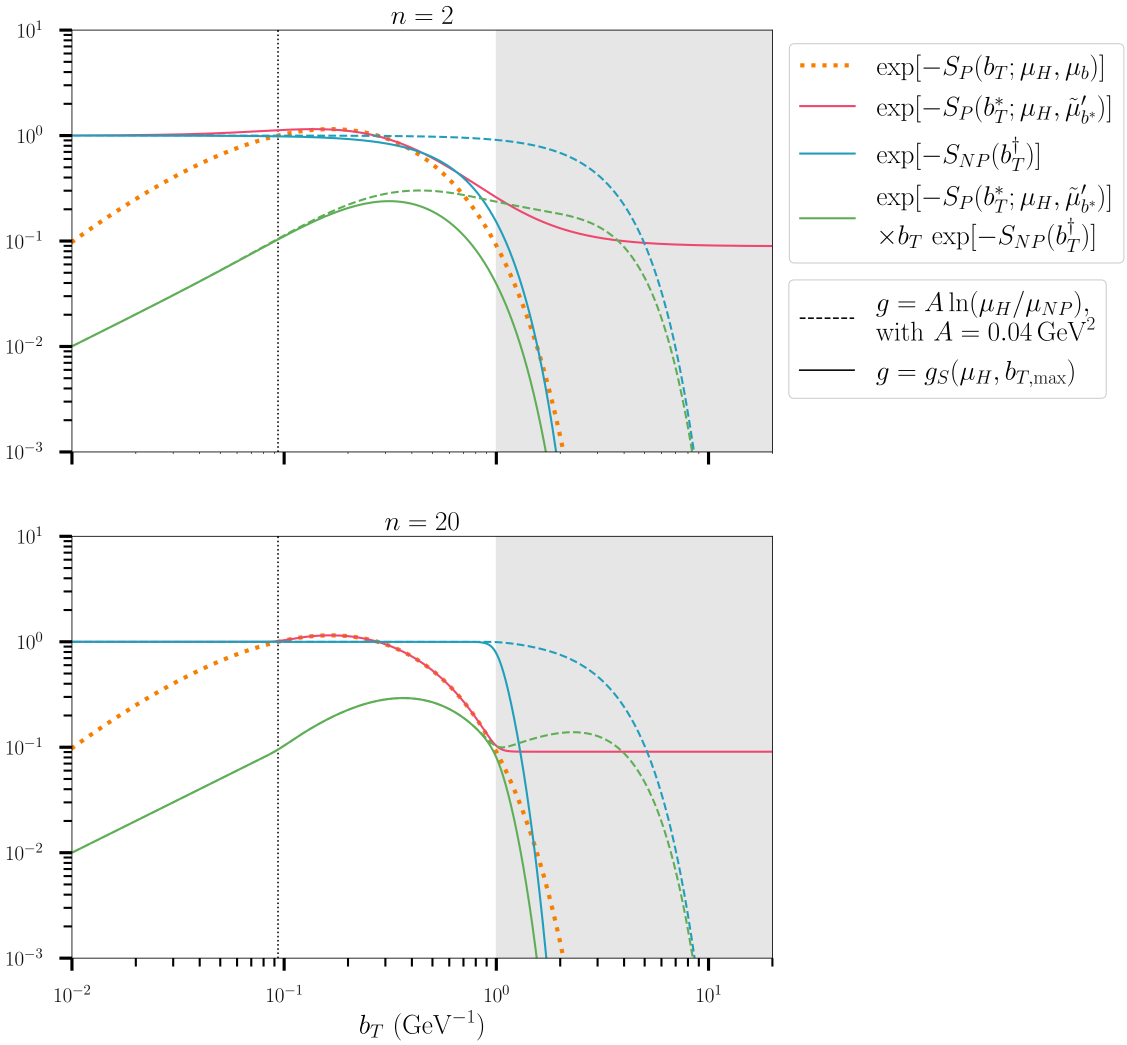

Figure 6.8: An example of the interplay between S_{NP} and S_P for $n=2$ (above) and $n=20$ (below) as a function of b_T, with $b_{T,\max} = 1\,\mathrm{GeV}^{-1}$ and $\mu_H = 12\,\mathrm{GeV}$. The dark grey area is not taken into account for actual computations (i.e. this region is not part of the TMD evolution since $b_T \leq b_{T,\min}$), the white area is the perturbative regime and the light grey area is the nonperturbative regime ($b_T \geq b_{T,\max}$). We note that the dotted orange line is better followed by the solid red line when $n=20$. The dashed blue line is produced with the Gaussian ansatz for S_{NP}, where $g = 0.09\,\mathrm{GeV}^2$, while the solid blue line is produced by our novel S_{NP} presented in Eq. 6.7, where $g_S = 1.89\,\mathrm{GeV}^2$ for $n=2$ and $g_S = 3.52\,\mathrm{GeV}^2$ for $n=20$ following Eq. 6.8. The green lines are the multiplication of $\exp(-S_P)$ with the corresponding $\exp(-S_{NP})$, both dashed and solid.

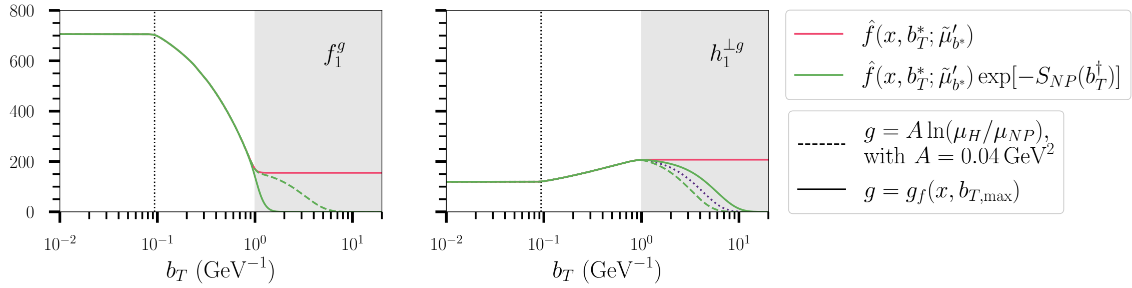

Figure 6.9: An example of the interplay between S_{NP} and the perturbative tails f_1^g (left) and $h_1^{\perp g}$ (right) as a function of b_T for $n = 20$, with $b_{T,\max} = 1\,\mathrm{GeV}^{-1}$, $\mu_H = 12\,\mathrm{GeV}$ and $x = 10^{-2}$, similar to Fig. 6.8. The dashed green line is produced with the Gaussian ansatz, where $g = 0.09\,\mathrm{GeV}^2$, while the solid green line is produced by our novel S_{NP} presented in Eq. 6.7, where $g_{f_1^g} = 2.76\,\mathrm{GeV}^2$ following Eq. 6.9 and $g_{h_1^{\perp g}} = \Lambda_{\mathrm{QCD}}^2 = 0.03\,\mathrm{GeV}^2$ due to the exception. For comparison, the dotted line, obtained by using $g = g_{h_1^{\perp g}} = 0.06\,\mathrm{GeV}^2$, is also shown.

With these new b_T-prescriptions we first investigate the interplay between S_{NP} and S_P. In Fig. 6.8 we show these Sudakov factors and their product for $n = 2$ and $n = 20$, with $b_{T,\max} = 1\,\mathrm{GeV}^{-1}$ and $\mu_H = 12\,\mathrm{GeV}$ as an example. We note that due to the increase of n we obtain two peaks from their product, one in the perturbative regime and one in the nonperturbative regime, while for $n = 2$ one obtains a more smeared-out curve such that only one peak is observed. So, as this local minimum between the two peaks introduces an inflection point in the convolutions, although they quickly revert to their original curvature (thus, it actually gives rise to two inflection points), we have actually worsened the computation by increasing n. On the other hand, we have gained that the two regimes are separated from each other and (almost) do not interfere. To remove the local minimum in the large-n case we notice that S_{NP} is dependent on perturbative physics by inverting Eq. 6.3. i.e. we find that we can remove the second peak (at large b_T) through g in Eq. 6.7 by matching the derivative of S_{NP} and S_P at $b_T = b_{T,\max}$

$$g_S(\mu_H, b_{T,\max}) = \frac{\left| \frac{\partial}{\partial b_T} S_P(b_T; \mu_H, \mu_b)\Big|_{b_T = b_{T,\max}} \right|}{2^{2/n}\, b_{T,\max}}, \tag{6.8}$$

where we added a subscript S to denote its relation to S_P. Its relation to g_K in Eq. 4.59 is discussed below. The value of g_S makes the product of the Sudakov factors double peak free for large n. In principle, the value of g_S serves as a lower bound, i.e. it can be taken larger than the value in Eq. 6.8 to further suppress nonperturbative physics. By continuing to larger values, one will reach almost a vertical cut-off at some point. However, g_S cannot be smaller than the found numerical value in Eq. 6.8 because then one will generate the second peak in b_T space like we have seen in the example and, hence the local minimum. We note that the absolute value of the numerator is taken because the derivative of S_P can switch sign in exceptional cases (depending on the value of μ_H, as shown in Fig. 6.10 and discussed below), which is not allowed as the correction factor should give a suppression.

After employing g_S for S_{NP} one will still observe similar inflection points in the full convolutions when n is taken large since $\tilde{\mu}'_{b^*}$ also enters the TMD tails. To remove these again, we employ the same method as before, namely

$$g_f(x, b_{T,\max}) = \frac{\left| \frac{\partial}{\partial b_T} \ln \hat{f}(x, b_T; \mu_b) \big|_{b_T = b_{T,\max}} \right|}{2^{2/n}\, b_{T,\max}}\,, \tag{6.9}$$

where we added a subscript f to denote its relation to the TMD f. We note that $g_f(x, b_{T,\max})$ is independent of μ_H for large n. In Fig. 6.9 we show an example of the interplay between S_{NP} and the perturbative tails for $b_{T,\max} = 1\,\mathrm{GeV}^{-1}$, $\mu_H = 12\,\mathrm{GeV}$ and $x = 0.01$. Again, one can choose a larger numerical value for g_f than to the one from Eq. 6.9, but not a smaller one, and we take the absolute value of the derivative to avoid a sign flip of g_f. However, since the latter occurs quite often for g_f (depending on the value of x, as shown in Fig. 6.11 and discussed below), it is unnatural to use the flipped derivative of the perturbative tail at $b_{T,\max}$ for its large-b_T suppression coefficient. Therefore, we introduce an exception: when $g_f \leq \Lambda^2_{\mathrm{QCD}}$ we take $g_f = \Lambda^2_{\mathrm{QCD}}$ instead of the value found by Eq. 6.9. We note that a similar exception could be employed for g_S; however, in practical applications we will use values for μ_H and $b_{T,\max}$ for which this is unnecessary.

Putting everything together our complete novel nonperturbative Sudakov factor that includes TMD and x dependence reads

$$S_{NP}(b_T; x, \mu_H, b_{T,\max}) = \big(g_S(\mu_H, b_{T,\max}) + g_{f_A}(x_a, b_{T,\max}) + g_{f_B}(x_b, b_{T,\max})\big)\, b_T^{\dagger\,2}\,, \tag{6.10}$$

which removes the local minima in the computations that arise due to the large-n b_T^*-prescription we employ in the TMD evolution. We note that this form is consistent with predictions from QCD, see [158, p. 7] and [159], like the general expression in Eq. 4.59; we elaborate below that our S_{NP} expression has a similar form. The indirect consequence of our correction factor is that large-b_T contributions of the perturbative Sudakov factor and the TMD tails are likely suppressed. Therefore, upward bumps at small q_T (or oscillations in an extreme case), which originate from large-b_T contributions to the integrand of the convolutions, are then removed. An example of this is shown in Fig. 6.12, in which the same convolutions of Fig. 6.7 are presented by employing Eq. 6.10. Furthermore, we observe that all computations with $b_{T,\max} = 0.5\,\mathrm{GeV}^{-1}$ lie consistently below those with $b_{T,\max} = 1.5\,\mathrm{GeV}^{-1}$. This is due to the fact that our novel nonperturbative Sudakov factor consistently forces the peak of the integrand in b_T space into the perturbative regime, a point we will elaborate on below. Other types of convolutions and their ratios will be discussed in the following sections. It should be understood that the upward bump is not removed in general, i.e. there could be cases in which $g = g_S + g_{f_A} + g_{f_B}$ is still too small. However, it turns out that this is actually rare for hadroproduction, as we will elaborate. On the other hand, in electroproduction this is not the case due to the different shape of S_P and the fact that only one TMD is involved as we will see in Sec. 6.4. Besides, it can be seen in Fig. 6.12 (especially for small μ_H) that $b_{T,\max}$ invariance is not fully achieved with our robust novel nonperturbative Sudakov factor, as was anticipated. Nevertheless, Eq. 6.10 does now take $b_{T,\max}$ systematically into account. Therefore, $b_{T,\max}$-variation, as well as increasing the value of g, can actually serve as an estimate for the nonperturbative uncertainties.

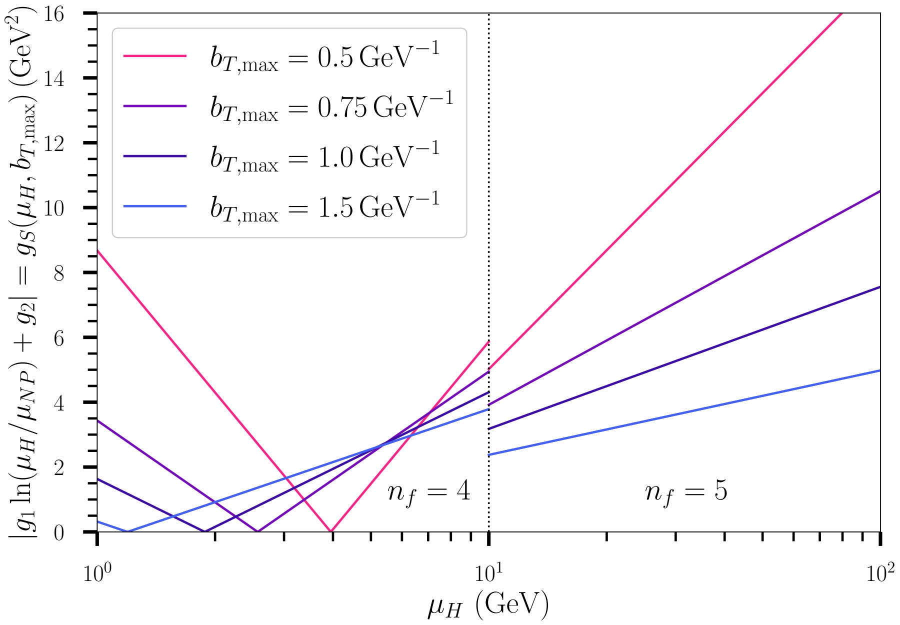

Figure 6.10: g_S as a function of μ_H for various $b_{T,\max}$ values with $n = 20$.

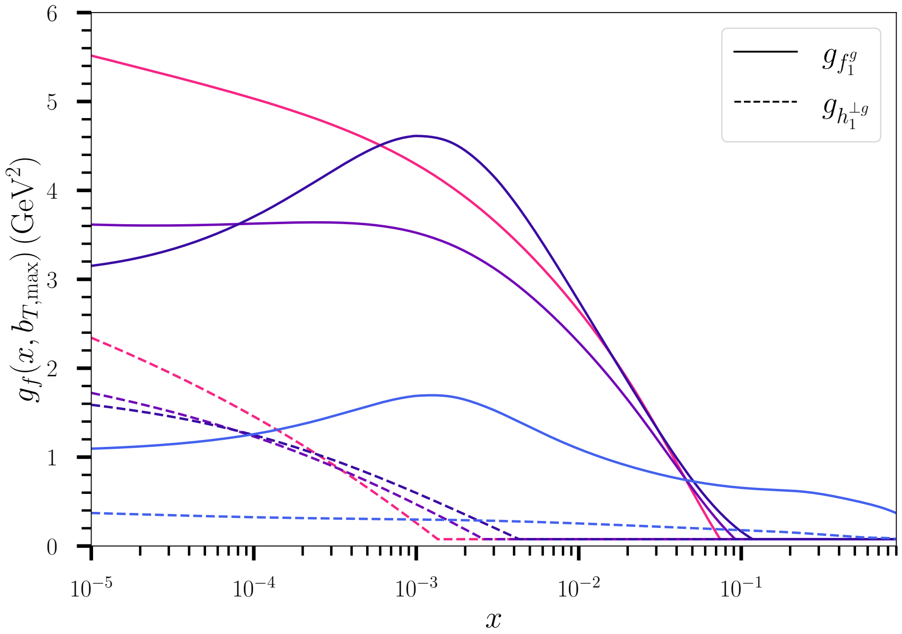

Figure 6.11: g_f as a function of x for various $b_{T,\max}$ values with $n = 20$.

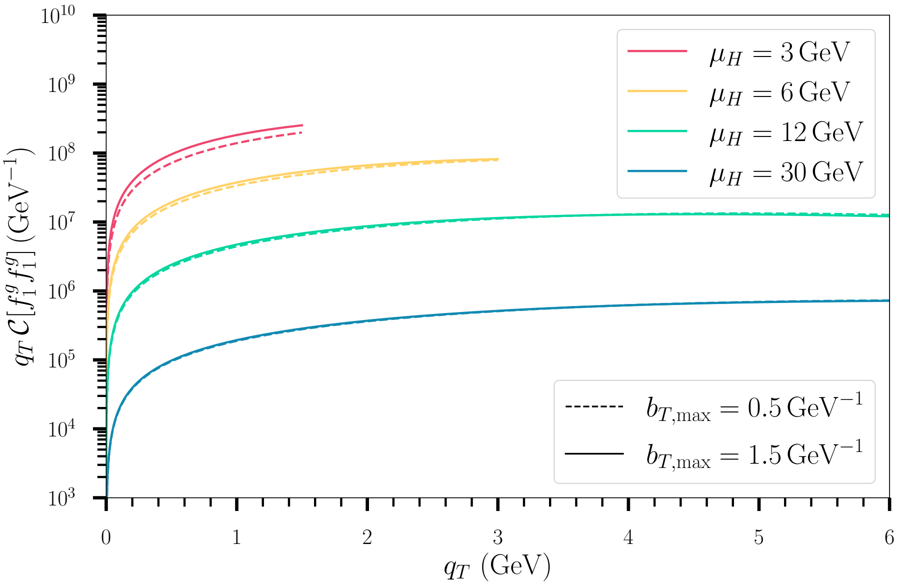

Figure 6.12: $q_T\,\mathcal{C}[f_1^g f_1^g]$ as a function of q_T by employing Eq. 6.10 with $n = 20$ for various μ_H and $b_{T,\max}$ values, similar to Fig. 6.7.

We can relate Eq. 6.10 to Eq. 4.59 which gives the following relations: $g_f(b_T) = g_f(x, b_{T,\max})\, b_T^{\dagger\,2}$ and $\ln(\mu_H/\mu_{NP})\, g_K(b_T) = g_S(\mu_H, b_{T,\max})\, b_T^{\dagger\,2}$. Especially, the latter relation is of interest because of the logarithmic μ_H dependence predicted by QCD that we mentioned. In particular, we found that we can fit g_S with the parametrisation $|g_1 \ln(\mu_H/\mu_{NP}) + g_2|$ as shown in Fig. 6.10, for which the values are given in Table 6.2. That is, we find the expected logarithmic behaviour, but we need an additional term g_2 in order to obtain good fits. This extra term is in line with parametrisations of correction factors from various studies of DY data summarised in [3, pp. 564–568]. In general, we observe larger values, which is expected due to the large-n b_T^*-prescription that is employed in our formalism. We observe that g_S increases more rapidly as a function of μ_H when one decreases $b_{T,\max}$. Moreover, the reason for the absolute value in Eq. 6.8 becomes evident: for small μ_H the derivative of S_P is taken before its minimum. In particular, $\exp[-S_P(b_T; \mu_H, \mu_b)]$ grows from zero to a maximum after which it decreases back towards zero, and this peak shifts for smaller μ_H to larger b_T. Therefore, the point where g_S touches the horizontal axis in Fig. 6.10 is for larger $b_{T,\max}$ is at smaller μ_H. Hence, around the minimum of g_S, one still obtains large contributions from S_P for large b_T.

Similarly, the behaviour of g_f as a function of x is shown in Fig. 6.11. Here we observe that the behaviour is less systematic as compared to g_S because the PDFs in the perturbative tails are obtained from fitting data rather than S_P, which is derived from theory. We observe that for large x, g_f reaches the point where it becomes equal to Λ^2_{QCD}, since this is where the tails start to increase instead of decrease at $b_{T,\max}$. For $h_1^{\perp g}$ this is observed at smaller x because the valence quark PDFs start to contribute significantly in its perturbative tail. For smaller $b_{T,\max}$, these observations occur at smaller x. Hence, at large x one still obtains large contributions from the TMD perturbative tails for large b_T. However, in large-y hadroproduction, when one value of x is large, the other becomes small, as can be seen from Eq. 3.98. It is the cumulative

Table 6.2: Values obtained from fitting the parametrisation of g_S that are shown in Fig. 6.10. For various values of $b_{T,\max}$ they are presented for $n_f = 4$ (left) and $n_f = 5$ (right).

$b_{T,\max}$ (GeV^{-1})	g_1 (GeV^2)	g_2 (GeV^2)
0.5	-6.317	7.945
0.75	-3.638	3.013
1.0	-2.580	1.333
1.5	-1.783	0.111

$b_{T,\max}$ (GeV^{-1})	g_1 (GeV^2)	g_2 (GeV^2)
0.5	-5.289	6.545
0.75	-2.863	2.340
1.0	-1.902	0.982
1.5	-1.131	0.097

contributions to g that determine whether large-b_T contritions to the integrand of the convolutions are sufficiently suppressed; consequently, instances where this is not the case in hadroproduction are rare. We note that it is difficult to compare g_f with other values from literature because they are differently parametrised; it is however possible to find values of similar magnitude, depending on x and the kind of TMD tail.

In Fig. 6.13 and Fig. 6.14 we show the behaviour of g_S and g_f (with $x = 10^{-3}$ as an example) as a function $b_{T,\max}$. One expects that both functions smoothly vary as a function of $b_{T,\max}$. In principle, g_S does so, except for small $b_{T,\max}$ when too small μ_H values are considered. On the other hand, g_f shows peculiar behaviour that does not originate from our formalism, i.e. it comes from the MSHT20lo_as130 PDF set [1] that is employed; for an unknown reason the derivative of the PDFs at a scale of 1.4 GeV is not smooth. Since this not our main interest here, we simply accept this observation. Besides, we note that the extrapolation of the PDFs to even smaller scales than $\mu_{NP} = 1$ GeV is questionable. In conclusion, we recommend avoiding too large values for $b_{T,\max}$ to prevent unpredictable behaviour, while also advising against too small values to avoid the critical point in g_S for the nonperturbative Sudakov factor discussed in this section.

While our developed nonperturbative Sudakov factor adheres to theoretical expectations, it has the downside of consistently shifting the peak of the integrand into the perturbative regime (with the exception if no decrease has occurred within the perturbative regime), leaving little room for nonperturbative physics. Specifically, we expect the integrand of the convolutions, see Eq. 4.58 (excluding the Bessel function from the angular integral), to first rise in b_T space and then fall to zero, without some kind of intermediate behaviour. However, this does not imply that this single smooth peak must occur in the perturbative regime. We can distinguish two extreme scenarios for the convolution integrand by comparing the use of the novel nonperturbative Sudakov factor and a Gaussian ansatz for the nonperturbative Sudakov factor, as illustrated in Fig. 6.15. On one hand, when $b_{T,\max}$ is small, a Gaussian ansatz would predict a peak at a larger b_T, in the nonperturbative regime, resulting in more nonperturbative contributions. On the other hand, when $b_{T,\max}$ is large, both nonperturbative Sudakov factors would roughly predict agreement on the position and magnitude of the peak in the perturbative regime, but the Gaussian ansatz would still predict more nonperturbative contributions. Since we expect that there could be more nonperturbative contributions in the integrand than with our novel nonperturbative Sudakov factor (especially for convolutions involving f_1^g that have generally a large g in S_{NP}), the actual smooth curve might lie somewhere between these two curves, having the same

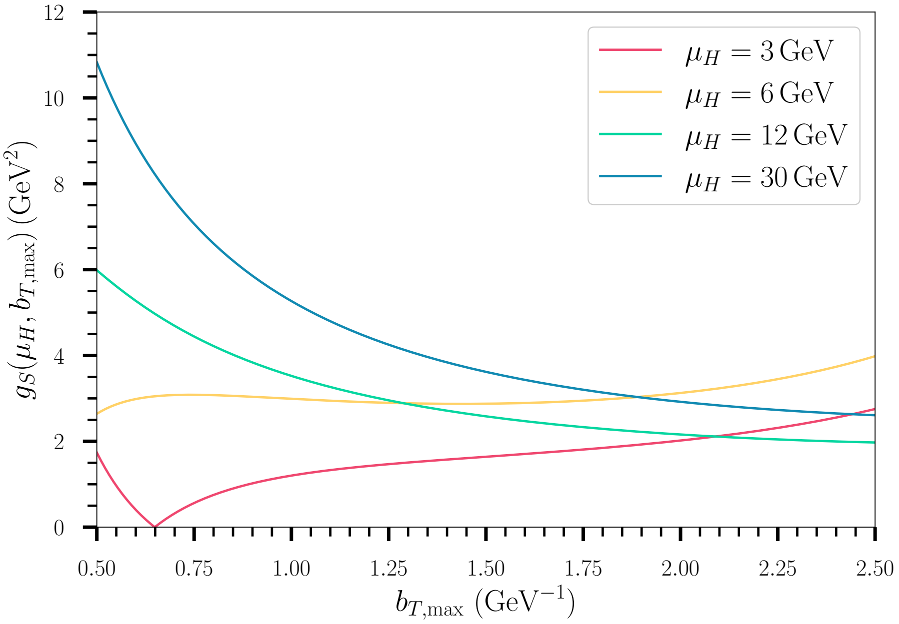

Figure 6.13: g_S as a function of $b_{T,\text{max}}$ for various values of μ_H with $n = 20$.

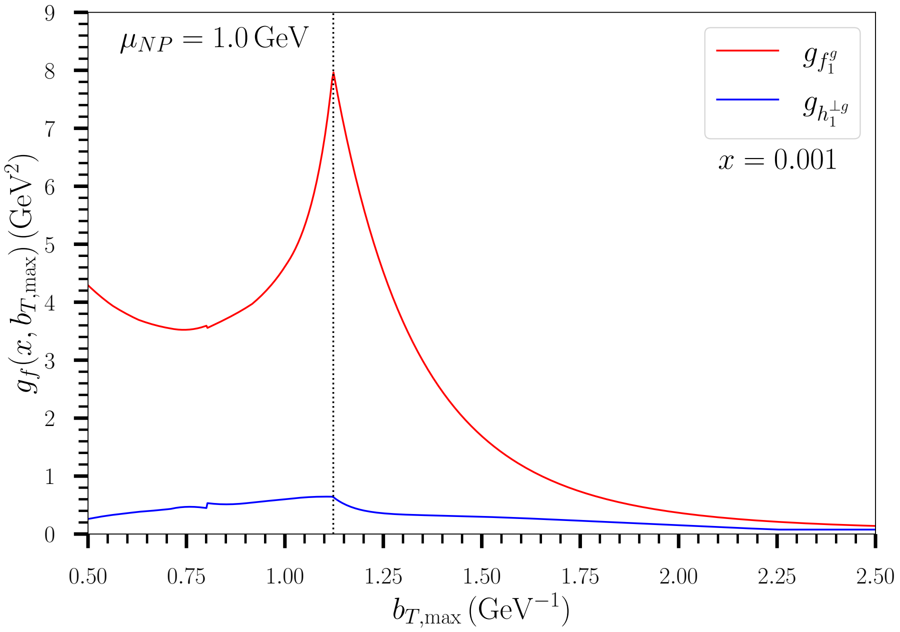

Figure 6.14: An example of g_f as a function of $b_{T,\text{max}}$ for $x = 10^{-3}$ with $n = 20$.

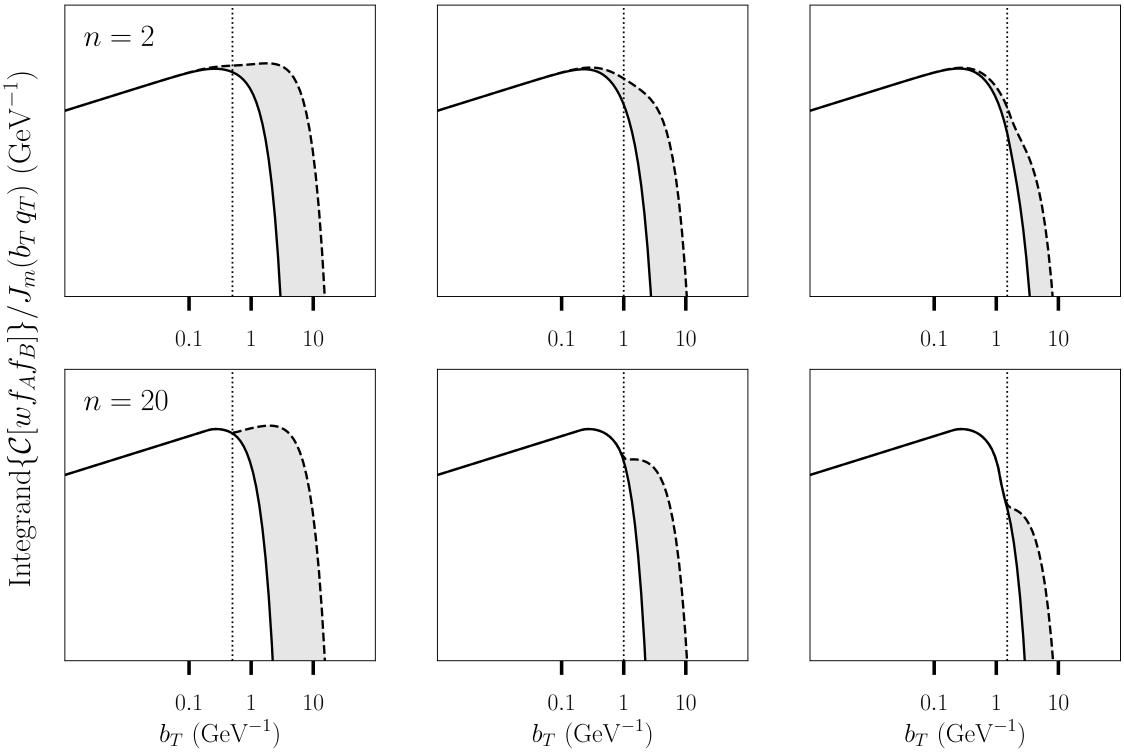

Figure 6.15: Schematic illustration on a log-log scale depicting the effect of the novel nonperturbative Sudakov factor (solid line) compared to a Gaussian ansatz for the nonperturbative Sudakov factor (dashed line) in the convolution integrand for unpolarised hadroproduction as a function of b_T, for $b_{T,\text{max}} = 0.5\,\text{GeV}^{-1}$ (left), $b_{T,\text{max}} = 1.0\,\text{GeV}^{-1}$ (middle) and $b_{T,\text{max}} = 1.5\,\text{GeV}^{-1}$ (right), and $n = 2$, 20.

kind of shape as with our novel nonperturbative Sudakov factor (whatever the value of n), but its peak at slightly larger b_T. Because a Gaussian(-like) function for the nonperturbative Sudakov factor cannot provide this in general, this suggests that the true correction factor cannot have such shape, i.e. alternative forms for it should be considered in future TMD-evolution studies, such as the one presented in [158, p. 7].

We note that the need for an alternative nonperturbative Sudakov factor, depending on the b_T^*-prescription and choice of $b_{T,\text{max}}$, is supported by the violation of positivity bounds observed with our novel nonperturbative Sudakov factor at small hard scales in both hadroproduction, and even more significantly in electroproduction, that are discussed in the following sections. That is, this issue could potentially be resolved by increasing nonperturbative contributions for convolutions involving f_1^g by employing a different nonperturbative Sudakov, or by decreasing nonperturbative contributions in the current formalism for convolutions involving $h_1^{\perp g}$, i.e. increasing $g_{h_1^{\perp g}}$. The latter is allowed since we can always increase g in our formalism, as explained above. All in all, the uncertainty regarding the form of S_{NP} introduces an additional layer of uncertainty in the predictions, highlighting the need for data to establish restrictions on it. Furthermore, the uncertainty associated with our novel S_{NP}, as discussed in the next section, should be regarded as an approximation rather than an accurate representation of the nonperturbative uncertainty.

6.3 $\mathcal{C}[f_1^g f_1^g]$ and quarkonium (-pair) production at LHC

Having established our novel nonperturbative Sudakov factor (with large n), we apply it in this section to the TMD-evolution formalism to study TM spectra and modulations in hadroproduction. In particular, we investigate $\mathcal{C}[f_1^g f_1^g]$, which provides theoretically the most important contribution to the differential cross section of gluon-induced unpolarised proton-proton collisions within the TMD regime. The only difference for this observable between single and quarkonium-pair production investigated in this thesis is the hard scale at which it occurs. Therefore, we first consider a general range of hard scales. Thereafter, we will move to the particular example of J/ψ-pair production for which we can compare our theoretical predictions with experimental data.

$\mathcal{C}[f_1^g f_1^g]$, and in general all the convolutions, are subjected to uncertainties from various factors. Specifically, we distinguish two cases: nonperturbative and perturbative uncertainties. As mentioned in the previous section, there are two nonperturbative uncertainties identified from our S_{NP}. Namely, the variation of $b_{T,\max}$ and the possible extra suppression of nonperturbative contributions by increasing g. Besides, we have uncertainties arising from the PDFs that originate from their extraction from data, i.e. the propagation of experimental uncertainties, as well as model and parametrisation uncertainties. Especially, since x is small, the gluon PDFs that enter the TMD tails,

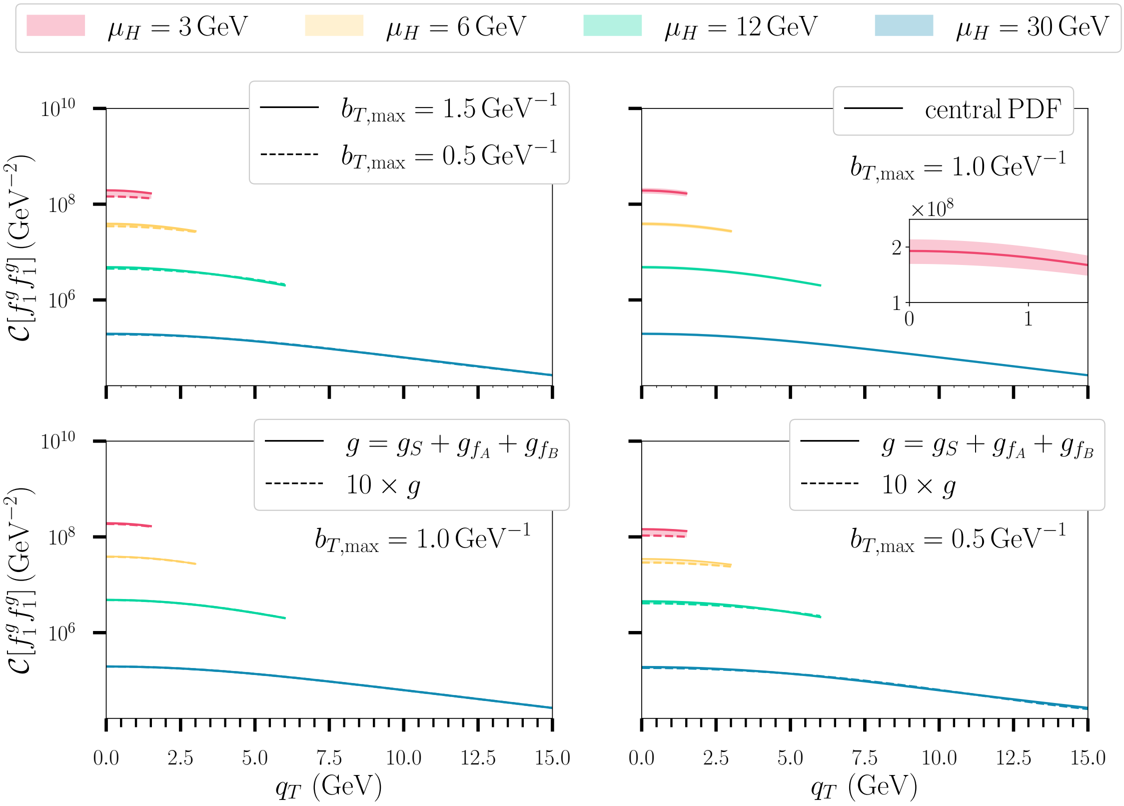

Figure 6.16: $\mathcal{C}[f_1^g f_1^g]$ as a function of q_T for various μ_H, with $y = 0$ and $\sqrt{s} = 13\,\text{TeV}$ that determine x_a and x_b (see Eq. 3.98). Various nonperturbative uncertainties are investigated: from $b_{T,\max}$ (upper left), from the PDFs (upper right), from g for $b_{T,\max} = 1.0\,\text{GeV}^{-1}$ (down left) and $b_{T,\max} = 0.5\,\text{GeV}^{-1}$ (down right).

given in Eqs. 4.53 and 4.54, are known to have quite large uncertainties depending on the scale: while the absolute uncertainty increases with scale, the relative uncertainty becomes much larger at smaller scales. The corresponding uncertainty in observables can be determined by calculating the observable using both the central PDFs and the eigenvector PDFs, following the Hessian method (e.g. see [1]). In Fig. 6.16 examples of these three nonperturbative uncertainties are shown. We note that although the use of $b_{T,\text{max}} = 0.5\,\text{GeV}^{-1}$ and $b_{T,\text{max}} = 1.5\,\text{GeV}^{-1}$ are not recommended for the developed S_{NP}, we have employed these values here to estimate the uncertainty from $b_{T,\text{max}}$-variation since these two extreme values provide the largest difference between the computations. Moreover, it can be seen that increasing g to for example $10g$ as an uncertainty estimate does not alter the results much because we already have a lot of suppression from our developed S_{NP}, especially when $b_{T,\text{max}} = 1.5\,\text{GeV}^{-1}$. In general, we observe significant uncertainties that are larger for small hard scales, but all appear small due to our use of logarithmic scale. This choice however facilitates a convenient comparison with the perturbative uncertainties that are discussed hereafter.

As explained in Sec. 4.2, scale variation is typically employed to estimate the perturbative uncertainty of the computations. Because of our S_{NP}, we point out that C_1 (that multiplies with $\tilde{\mu}'_{b^*}$) and C_2 (that multiplies with μ_H) affect g_S, and C_3 (that multiplies with the scale of the TMD tails $\tilde{\mu}'_{b^*}$) affect g_f (besides that C_2 enters $\tilde{\mu}'_{b^*}$). In particular, we can express the convolutions in this section, including scale variation, as

$$\begin{aligned}
\mathcal{C}[w f_A f_B](x_a, x_b, q_T; \mu_H) &= \int_0^\infty \frac{db_T}{2\pi}\, b_T\, J_m(b_T\, q_T) \\
&\times \exp\left(- \int_{C_1^2 \tilde{\mu}'_{b^*}(C_2)}^{C_2^2 \mu_H^2} \frac{d\mu'^2}{\mu'^2} \left[A(C_1) \ln \frac{C_2^2\, \mu_H^2}{\mu'^2} + B(C_1, C_2) \right] \right) \\
&\times \exp\left(- \left[g_S(C_1, C_2, \mu_H, b_{T,\text{max}}) + g_{f_A}(C_3, x_a, b_{T,\text{max}}) + g_{f_B}(C_3, x_b, b_{T,\text{max}}) \right] b_T^{\dagger\,2} \right) \\
&\times \hat{f}_A\big(x_a, b_T^*; C_3\, \tilde{\mu}'_{b^*}(C_2)\big)\, \hat{f}_B\big(x_b, b_T^*; C_3\, \tilde{\mu}'_{b^*}(C_2)\big)\,, \qquad (6.11)
\end{aligned}$$

following Eq. 4.58. In Fig. 6.17 we show their separate impact on $\mathcal{C}[f_1^g f_1^g]$, as well as the case in which $C_1 = C_3$ is varied since both multiply the same scale in principle. We observe that the variation of C_1 and C_2 have an opposite effect on the magnitude, and they alter the shape of the convolutions in slightly different ways. Indeed, they change the integration limits of S_P in opposite ways and the behaviour of S_{NP} as a function of its scales is non-linear. C_3 variation provides the largest uncertainty. The shape and as well as the magnitude variation due to C_3 variation are determined by the PDFs, e.g. if the gluon PDF increases as a function of its scale, a larger magnitude for the convolution with $C_3 = 2$ is observed as can be seen in Fig. 6.17 (this does not necessarily have to be the case, e.g. for large x the PDF decreases instead when the scale is increased). Besides, since C_1 and C_3 variation have opposite results on the convolutions, but C_3 variation has more impact (especially for small q_T), their combined variation is similar to the effect of C_3 variation giving a smaller uncertainty. Since the perturbative uncertainties are much larger than the nonperturbative ones, we will from now on only consider scale variation as uncertainty in our predictions. Moreover, to avoid $b_{T,\text{max}}$ being either too large or too small, and given that the nonperturbative uncertainty can be neglected, we simply choose it to be $1.0\,\text{GeV}$.

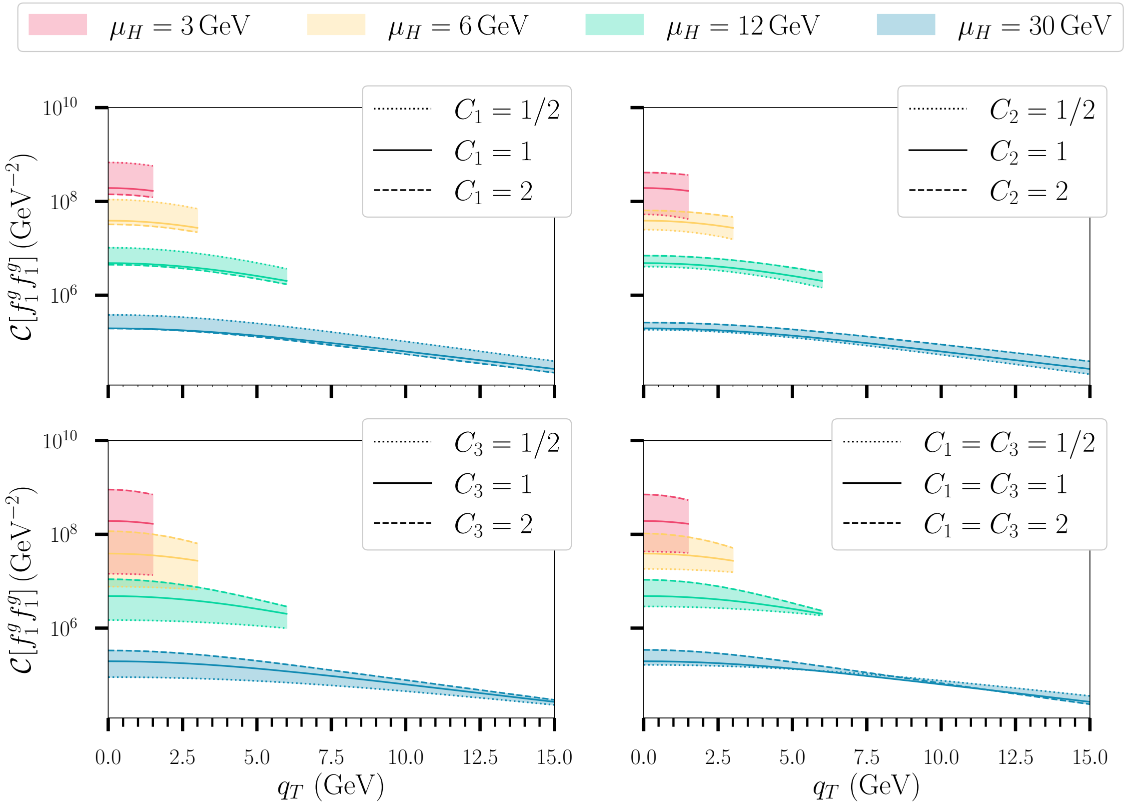

Figure 6.17: $\mathcal{C}[f_1^g f_1^g]$ as a function of q_T for various μ_H, similar to Fig. 6.16. Various perturbative uncertainties from scale variation are investigated: from C_1 (upper left), from C_2 (upper right), from C_3 (down left) and from $C_1 = C_3$ (down right).

Similar figures for the other convolutions in proton-proton collisions are shown in App. E: see Figs. E.2, E.3, and E.4, along with $\mathcal{C}[f_1^g f_1^g]$ in Fig. E.1, all having the same axis for comparison. In these examples the various scale variations have a similar effect on the convolutions as for $\mathcal{C}[f_1^g f_1^g]$, except that C_3 variation provides a smaller uncertainty than C_1 variation for $\mathcal{C}[w_2 h_1^{\perp g} h_1^{\perp g}]$ and that these variations have similar impact for $\mathcal{C}[w_4 h_1^{\perp g} h_1^{\perp g}]$. Hence, we have that $C_1 = C_3$ variation follows C_1 variation for $\mathcal{C}[w_2 h_1^{\perp g} h_1^{\perp g}]$, while a more complicated behaviour for this scale variation is found for $\mathcal{C}[w_4 h_1^{\perp g} h_1^{\perp g}]$. This makes sense since the quark PDFs contribute to the tail of $h_1^{\perp g}$ as well, making its scale variation less volatile. We note that we observe a small upward bump at small q_T in $\mathcal{C}[w_4 h_1^{\perp g} h_1^{\perp g}]$, which is absent in $\mathcal{C}[w_2 h_1^{\perp g} h_1^{\perp g}]$. This points out that the specific Bessel function in the convolution integrand logically affects the extent of large-b_T contributions as well. In the azimuthal modulations discussed below, this upward bump is no longer observed, due to the smallness of the associated hard factor of this convolution.

Before we continue our discussion on $\mathcal{C}[f_1^g f_1^g]$ and scale variation, we explain the different features of the various TMD evolved convolutions. In general, for smaller μ_H larger magnitudes are obtained for all the convolutions, and $\mathcal{C}[f_1^g f_1^g]$ and $\mathcal{C}[w_2 h_1^{\perp g} h_1^{\perp g}]$ exhibit the largest magnitudes, followed by $\mathcal{C}[w_3 f_1^g h_1^{\perp g}]$ (and $\mathcal{C}[w_3' h_1^{\perp g} f_1^g]$). The smallest magnitude is observed for $\mathcal{C}[w_4 h_1^{\perp g} h_1^{\perp g}]$. Besides, there is a clear difference in behaviour: while $\mathcal{C}[f_1^g f_1^g]$ and $\mathcal{C}[w_2 h_1^{\perp g} h_1^{\perp g}]$ decrease as function of q_T, $\mathcal{C}[w_3 f_1^g h_1^{\perp g}]$ and $\mathcal{C}[w_4 h_1^{\perp g} h_1^{\perp g}]$ increase instead (within $q_T \leq q_{T,\max}$). The difference in the magnitudes of the convolutions is due to the α_s suppression of $h_1^{\perp g}$ with respect to f_1^g and their shape, while the difference in shape is due to the specific Bessel function and the b_T-broadening of the integrand by $h_1^{\perp g}$, like for the electroproduction case discussed in Sec. 6.1. We note that the b_T-broadening is now clear from the fact that $g_{h_1^{\perp g}} < g_{f_1^g}$ in Fig. 6.11 (when choosing a specific $b_{T,\max}$). Indeed, $\mathcal{C}[w_2 h_1^{\perp g} h_1^{\perp g}]$ decreases faster than $\mathcal{C}[f_1^g f_1^g]$ as a function of q_T (both containing J_0), making their ratio fall with q_T. The integrand of the convolutions with J_2 or J_4 start their damped oscillation at zero and go up (instead of starting at one and going down), therefore $\mathcal{C}[w_3 f_1^g h_1^{\perp g}]$ and $\mathcal{C}[w_4 h_1^{\perp g} h_1^{\perp g}]$, reach a maximum before they decrease like the convolutions containing J_0. We note that in our example figures this decrease is not visible due to the cut at $q_{T,\max}$. Besides, since the envelopes of J_2 and J_4 decrease more gradually towards zero compared to J_0, $\mathcal{C}[w_3 f_1^g h_1^{\perp g}]$ and $\mathcal{C}[w_4 h_1^{\perp g} h_1^{\perp g}]$ decrease more slowly than the convolutions containing J_0. Hence, the modulations presented in Eqs. 3.101 and 3.102 will always increase with q_T, also after the peak maximum of $\mathcal{C}[w_3 f_1^g h_1^{\perp g}]$ and $\mathcal{C}[w_4 h_1^{\perp g} h_1^{\perp g}]$ (again equivalent to the electroproduction case). However, J_4 tends even slower towards zero than J_2 with increasing b_T, such that the increase of $\mathcal{C}[w_4 h_1^{\perp g} h_1^{\perp g}]$ to its peak maximum takes longer as a function of q_T. Therefore, one will observe a more rapid increase in the convolution and the corresponding $\cos(4\phi_{CS})$-modulation, although it has a smaller magnitude.

We now combine the scale variation, i.e. we calculate the full perturbative uncertainty estimation for observables by considering all the combinations of $[C_1, C_2, C_3]$. Since according to studies of Collins et al. [118, 120] $C_3 = C_1/C_2$, we distinguish two cases: Case 1 in which the observable is calculated 27 times and Case 2 in which the observable is calculated 7 times. We note that logically Case 2 always provides an uncertainty band within the uncertainty band given by Case 1. To denote their difference we present in the remainder of this section uncertainties from Case 1 by light areas and from Case 2 by darker areas.

Fig. E.5 displays the ratios of the convolutions calculated for the general hard scales using both scale variation cases. For ratios of observables, the same scale is applied to both the numerator and the denominator. These figures are shown up to unity, since from the positivity bounds it follows that these ratios cannot become larger than that (see Eq. 3.103). It should be noted that for small hard scales we observe violation of the positivity bounds within the uncertainty band, or even with the central value for $\mathcal{C}[w_2 h_1^{\perp g} h_1^{\perp g}]/\mathcal{C}[f_1^g f_1^g]$. However, this may not a problem as long as the entire range of perturbative uncertainties does not lie above 1, i.e. somewhere within the band we expect the occurrence of the true curve that does not disobey the positivity bounds, like the dashed lines which present the particular scale variation that agrees best with the experimental data of J/ψ-pair production as discussed below. Besides, the perturbative tails of the TMDs in the TMD-evolution formalism, which determine the magnitudes of the convolutions, do not know about the positivity bounds, i.e. they only enter via the weight factors in the Bessel functions that determine the shape. As mentioned before, a simple solution within the current formalism might be to decrease the amount of nonperturbative contributions further by increasing $g_{h_1^{\perp g}}$. On the other hand, it might be that higher-order perturbative corrections for the evolution formalism, as well as for higher-order nonperturbative PDFs, solve the issue as well by shrinking the estimated uncertainty band of the convolutions and their ratios. We

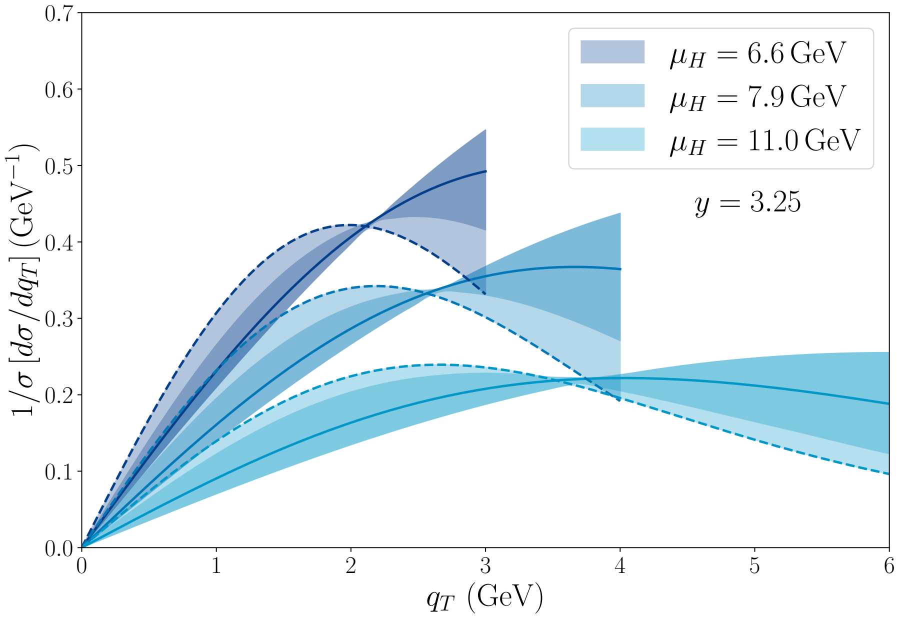

Figure 6.18: The normalised differential cross section as a function of q_T for various μ_H, with $y = 3.25$ and $\sqrt{s} = 13\,\mathrm{TeV}$. The solid lines done central values and the dashed line is the particular scale variation that agrees best with data from J/ψ-pair production.

note that since the violation of the positivity bound occurs only at small μ_H, we choose to disregard this issue here and leave it for future investigations.

Using the TMD-evolution formalism, a first comparison to J/ψ-pair production data from the LHCb collaboration in 2017 was conducted in [92], using a simple Gaussian ansatz for the nonperturbative Sudakov factor. This comparison to the theoretical normalised differential cross section was later updated in [160]. Here, we present another update by comparing to the new LHCb data for this process from 2023 [78]. On the theoretical side, we employ our developed nonperturbative Sudakov factor and take scale variation into account for the uncertainty. The normalised differential cross section is a promising observable because it suppresses the uncertainties in the TMD evolution. Additionally, this observable is unaffected by the LDME uncertainties, as these cancel out when adopting the naive TMDShFs. In particular, since $d\sigma/dq_T \propto q_T\,\mathcal{C}[f_1^g f_1^g]$, it is given by:

$$\frac{1}{\sigma}\left(\frac{d\sigma}{dq_T}\right) = \frac{d\sigma/dq_T}{\int_0^{q_{T,\max}} dq_T\,(d\sigma/dq_T)} \approx \frac{q_T\,\mathcal{C}[f_1^g f_1^g]}{\int_0^{q_{T,\max}} dq_T\,(q_T\,\mathcal{C}[f_1^g f_1^g])}\,. \tag{6.12}$$

As mentioned in Sec. 2.3, it is expected that DPS contributes significantly to this process. Therefore, one needs to subtract a part from the data in order to compare to our theoretical SPS description. The LHCb collaboration has accomplished this in the following manner. Since it is expected that the distributions as a function of $y_{J/\psi\,J/\psi}$ exhibit distinct shapes for SPS and DPS processes, it allows for the extraction of the DPS contribution using a data-driven template for the DPS process. Namely,

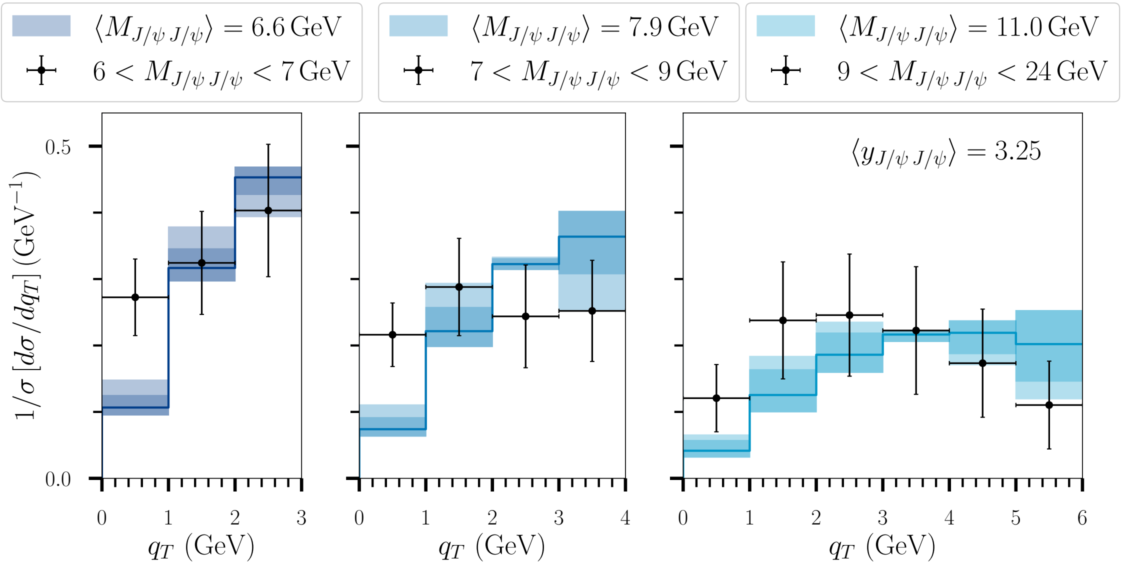

Figure 6.19: The normalised differential cross section in bins as a function of q_T together with the LHCb data for various $\langle M_{J/\psi\, J/\psi}\rangle$, with $\langle y_{J/\psi\, J/\psi}\rangle = 3.25$ and $\sqrt{s} = 13\,\text{TeV}$.

the shape of the DPS component is derived by employing the widely used ‘pocket formula’

$$\sigma_{\text{DPS}}(J/\psi + J/\psi) = \frac{1}{2}\frac{\sigma^2(J/\psi)}{\sigma_{\text{eff}}}\,, \tag{6.13}$$

which follows from the conjecture is that the distribution follows the measured production cross section of single prompt J/ψ (with the assumption that they are uniformly distributed over the azimuthal angle). Then, by assuming that the SPS contributions to J/ψ-pair production are negligible in the $1.8 < y_{J/\psi\, J/\psi} < 2.5$ region according to predictions within the NRQCD framework [161–164], they determine the normalisation of the DPS contribution σ_{eff} within this range. Subsequently, the DPS contributions can be subtracted to the data, assuming that the remainder is attributed to SPS.

Our results following the invariant masses $M_{J/\psi\, J/\psi}$ of the LHCb measurements are given in Fig. 6.18 and compared to their data in Fig. 6.19. We note that we have renormalised the LHCb data and the associated uncertainties in the TMD regime, as they normalised their data over the whole measured q_T region. Multiplying $\mathcal{C}[f_1^g f_1^g]$ with q_T naturally results in a peak for the normalised differential cross sections, after which they decrease. Besides, the magnitudes are smaller for larger μ_H, similar to the behaviour of $\mathcal{C}[f_1^g f_1^g]$ itself. Both cases of scale variation provide good description with the data. However, we observe that the data is in favour of having the peak of the distribution at small q_T. Therefore, we have investigated the average of q_T for the different scale variations as shown in Fig. 6.20. We note that the scale variations are sorted according to the values they produce for $\langle q_T\rangle$. Hence, the sequence of scale variations from left to right slightly differs for the various hard scale cases, although a general trend is observed. Besides, the impact on $\langle q_T\rangle$ from the different variations increases for larger μ_H. We find that the scale variation [1, 2, 2] gives the smallest

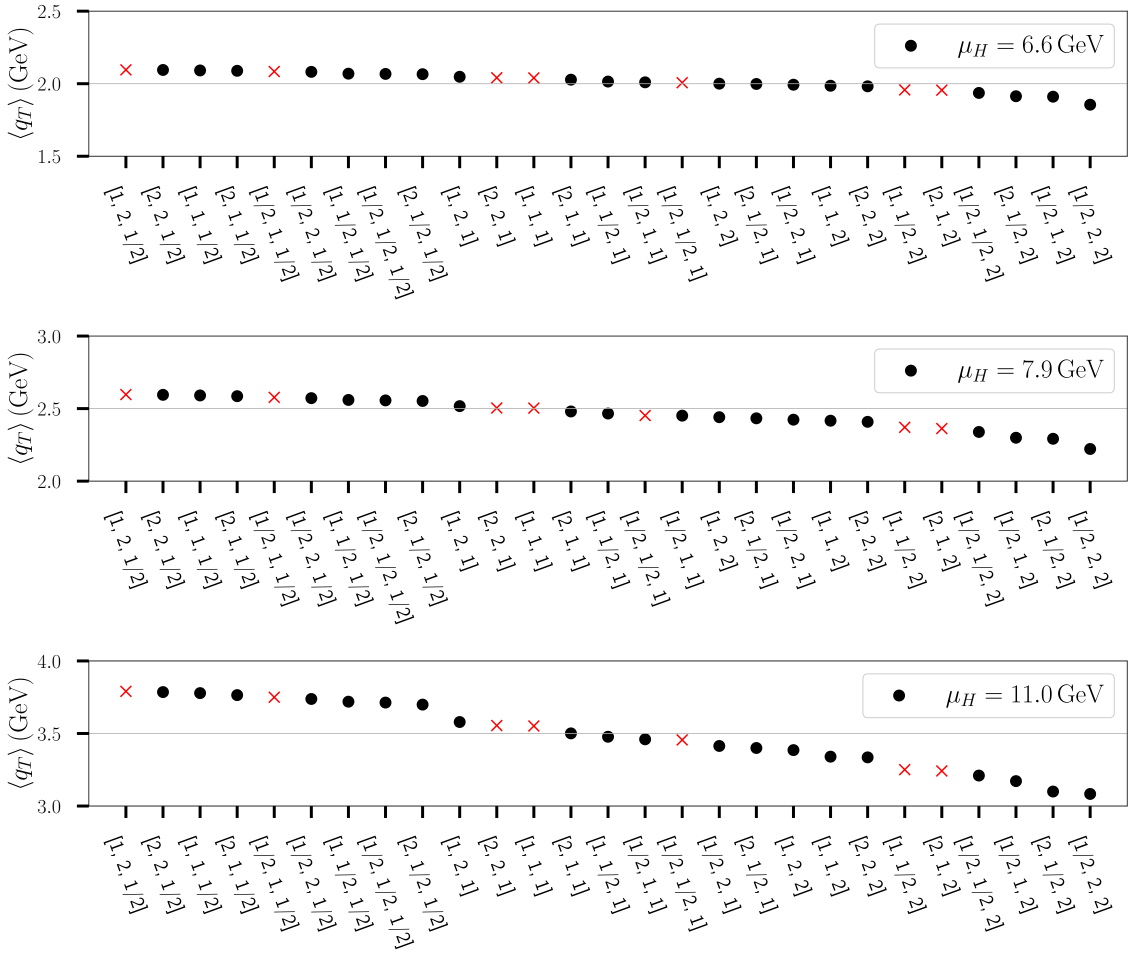

Figure 6.20: Average of q_T as a function of sorted variations of the scales via: $[C_1, C_2, C_3]$. The red crosses denote the combinations of Case 2 scale variation.

$\langle q_T \rangle$. Indeed, it is this variation, which is not part of Case 2 variation, that gives the best agreement with data, i.e. we have a good indication to allow for $C_3 \neq C_1/C_2$. In Fig. 6.21 we compare to different rapidity data instead, for which we again find good agreement and preference for the Case 1 scale variation. Moreover, as predicted by theory, there is (almost) no difference for the various investigated rapidities. We note that a recent study demonstrated that a CS high-energy factorisation approach can also successfully describe the data [165].

Despite these motivating observations of agreement between experiment and theory, we note that the smallest-q_T bin data does not overlap with our predictions at all. The theoretical multiplication of q_T with $\mathcal{C}[f_1^g f_1^g]$ forces the normalised differential cross section to approach zero at $q_T = 0\,\text{GeV}$, consequently the average value in the first bin is not necessarily required to be small, but it generally tends to be. We expect that this discrepancy with respect to the data might be due to flaws in the experimental detection or in the method used to subtract the DPS contributions. Given the substantial uncertainties, both theoretical and experimental, efforts should be made to achieve improvements on both fronts in the future.

We finish our discussion on the comparison with J/ψ-pair data by noting that the LHCb collaboration fitted the theoretical differential cross section given in Eq. 3.97

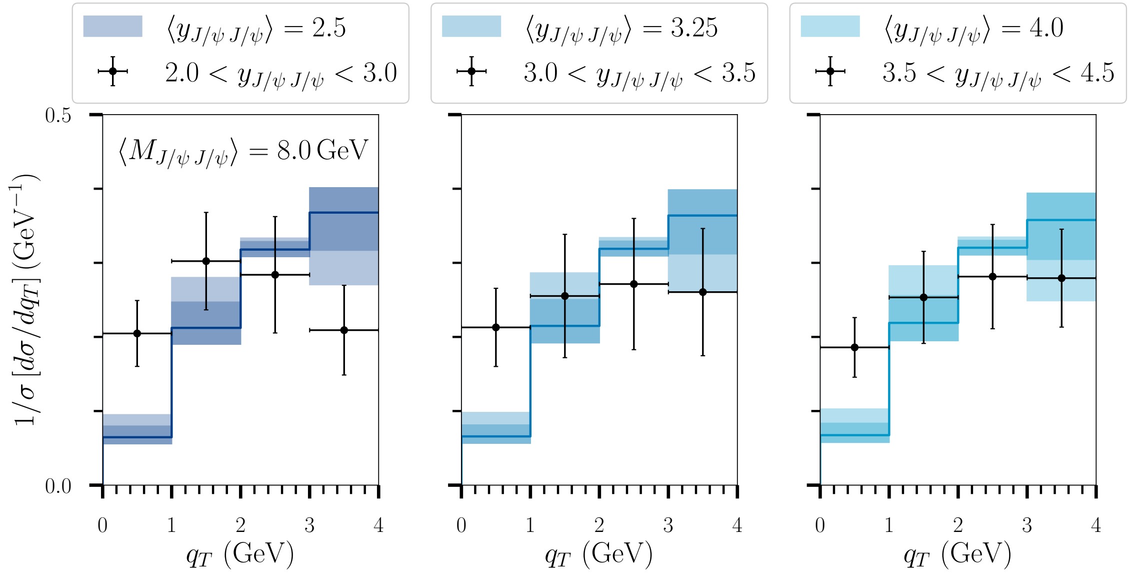

Figure 6.21: The normalised differential cross section in bins as a function of q_T together with the LHCb data for various $\langle y_{J/\psi\, J/\psi} \rangle$, with $\langle M_{J/\psi\, J/\psi} \rangle = 8.0\,\mathrm{GeV}$ and $\sqrt{s} = 13\,\mathrm{TeV}$.

in order to determine the azimuthal modulations [78]:

$$\langle \cos 2\phi_{CS} \rangle = -0.029 \pm 0.050\,(\mathrm{stat.}) \pm 0.009\,(\mathrm{syst.})\,, \tag{6.14}$$

$$\langle \cos 4\phi_{CS} \rangle = -0.087 \pm 0.052\,(\mathrm{stat.}) \pm 0.013\,(\mathrm{syst.})\,. \tag{6.15}$$

Unfortunately, their statistical (stat.) and systematic (syst.) uncertainties were too large to determine the sign of $h_1^{\perp g}$ via the $\cos(2\phi_{CS})$-modulation (see Eq. 3.101), although there is a hint of linearly polarised gluons in the proton, i.e. $|\langle \cos 4\phi_{CS} \rangle| > 0$ (see Eq. 3.102). Moreover, due to the lack of statistics they were unable to study the q_T dependence of the modulations, hence the extraction of the $h_1^{\perp g}$ TMD is currently impossible.

Regardless of these observations, we present in Fig. 6.22 the corresponding $\cos(2\phi_{CS})$- and $\cos(4\phi_{CS})$-modulations for the measured unpolarised J/ψ-pair. We employ again the two different θ_{CS}-bins, as for the Gaussian models presented in Fig. 4.4. In contrast, now the modulations are dependent on y, hence x. We observe that the evolution predictions have indeed a different shape, i.e. they constantly increase as a function for q_T. The Case 1 scale variation allows for larger modulations than the Case 2 variation. Moreover, we point out that the specific variation that agrees best with data predicts that the modulations are relatively large. Although the increase as a function of q_T within the considered TMD regime gives rise to similar magnitudes for the $\cos(2\phi_{CS})$-modulations, smaller magnitudes are obtained for the $\cos(4\phi_{CS})$-modulations. This is due to the additional α_s suppression in case there are two $h_1^{\perp g}$ tails in the numerator of the modulations. Similar to the Gaussian TMD case, we observe that the $M_{J/\psi\, J/\psi} = 6.6\,\mathrm{GeV}$ predictions are almost zero for the $\cos(4\phi_{CS})$-modulation. Moreover, the sign flip is naturally observed for the $\cos(4\phi_{CS})$-modulation due to the positive fixed sign of the $h_1^{\perp g}$ tail and the hard factor $\mathcal{F}_4$. However, taking into account the magnitude of the modulations according to TMD evolution, we expect that the

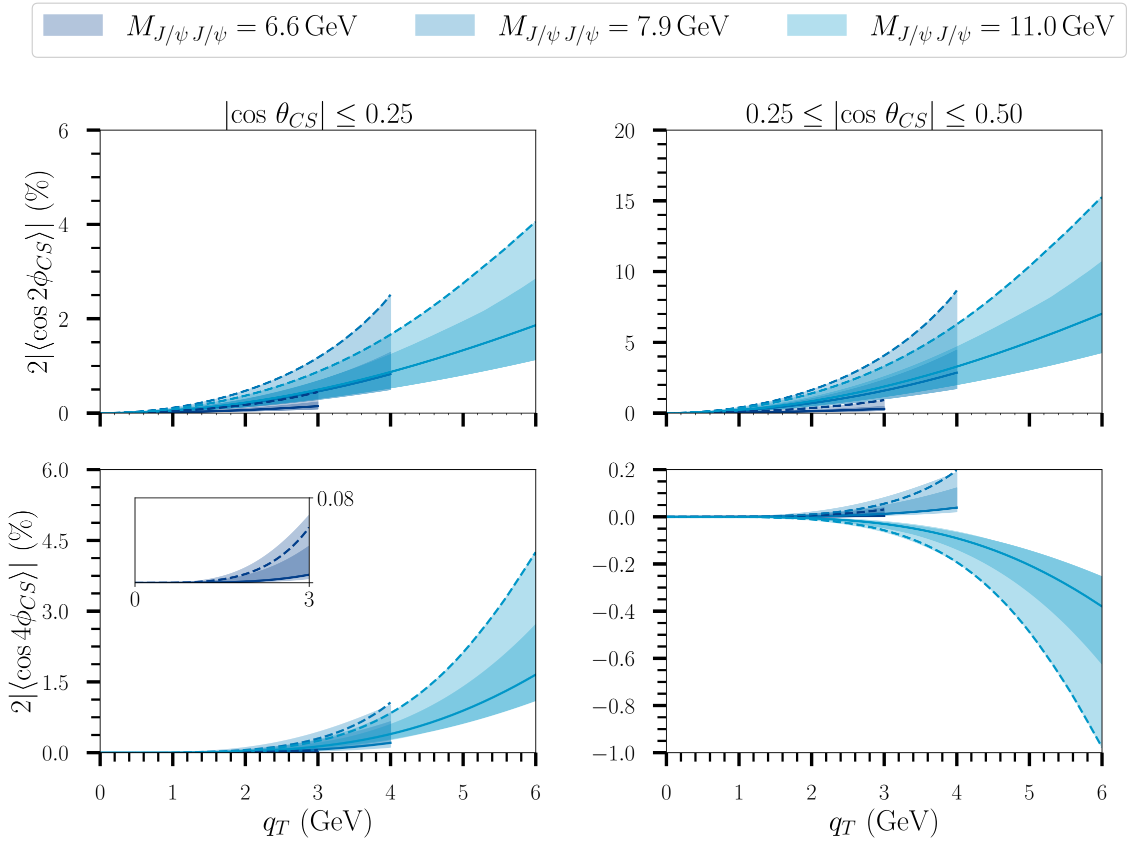

Figure 6.22: The $\cos(2\phi_{CS})$- and $\cos(4\phi_{CS})$-modulations in unpolarised J/ψ-pair hadroproduction as a function of q_T, similar to Fig. 4.4. Here the TMD-evolution formalism is employed instead with $y_{QQ} = 3.25$, $\sqrt{s} = 13\,\mathrm{TeV}$. The solid lines denote the central values, while the dashed lines show the specific scale variation that agrees best with the data from J/ψ-pair production.

sign flip is only measurable in the current kinematical configuration when very high precision is reached in the future. The evolution formalism predicts that the asymmetry will be measurably large, depending on the value of $M_{J/\psi J/\psi}$, i.e. larger $M_{J/\psi\,J/\psi}$ are more favourable for the modulations since they allow for larger $q_{T,\mathrm{max}}$.

For completeness, we show in Figs. E.6, E.7, E.8 and E.9 example modulations, in line with the hard scales employed in Fig 3.10, with separate scale variations. We find that C_1 variation allows for an increase of the modulations, while C_2 and C_3 variation provide both larger and smaller modulations, depending on the value of $M_{J/\psi\,J/\psi}$ and the modulation. C_2 variation allows for more larger than smaller modulations, while C_3 variation shows the opposite. $C_1 = C_3$ variation gives again a more complicated behaviour, i.e. for the small hard scale larger and smaller modulation can arise, while for the large hard scale only larger modulations are expected.

With regards to the fixed-target program at the LHCb [166], we provide an example of what can be expected for J/ψ-pair production. Our predictions for the normalised differential cross section and the modulations are shown Fig. 6.23 and Fig. 6.24, respectively, considering similar invariant masses of the pair as in the collider mode discussed above. The difference in the computations is due to the expected centre-of-mass energy of $\sqrt{s} = 115\,\mathrm{GeV}$ and the rapidity shift of y_{QQ}, chosen to be -1 chosen in

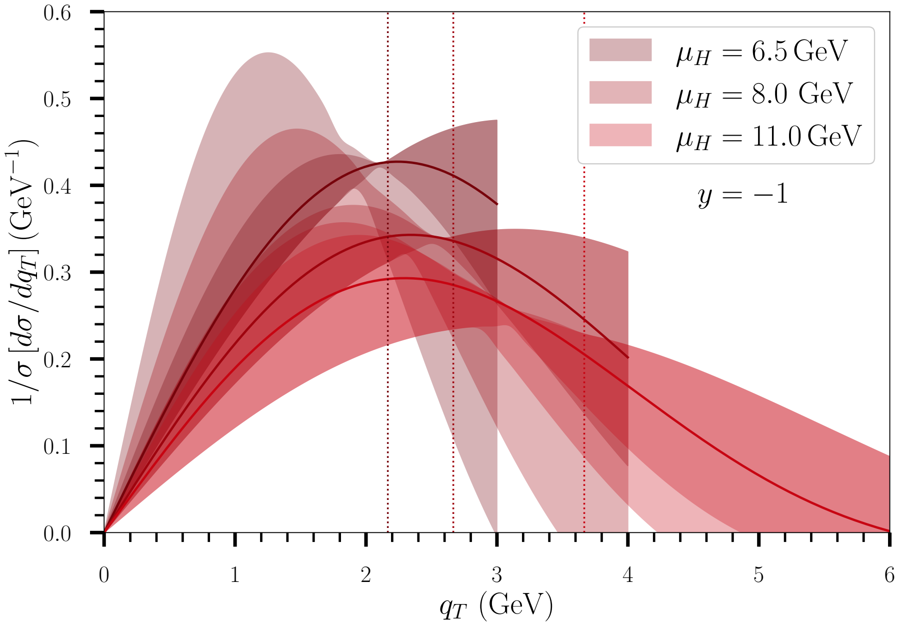

Figure 6.23: An example of the normalised differential cross sections for J/ψ-pair production in fixed-target mode ($\sqrt{s} = 115\,\mathrm{GeV}$) as a function of q_T for various μ_H with $y = -1$. The estimated TMD regime, $q_{T,\max} = M_{QQ}/3$, is denoted with the dotted lines.

our example. This leads to much larger x values following Eq. 3.98, outside the gluon dominated region, resulting in smaller magnitudes for the convolutions and causing them to approach zero more quickly, as explained in Sec. 6.1. Since we have that $\mathcal{C}[f_1^g f_1^g]$ including scale variation becomes negative within the usual considered TMD regime, we have to restrict the computations, i.e. we have chosen $q_{T,\max} = M_{QQ}/3$ to avoid this. We observe that the normalised differential cross section peaks at smaller q_T and has larger magnitudes in fixed-target mode compared to collider mode. The modulation increases much more rapidly, but due to the smaller $q_{T,\max}$, the $\cos(2\phi_{CS})$-modulations do not exceed the magnitudes observed in the collider mode. On the other hand, it results in very small magnitudes for the $\cos(4\phi_{CS})$-modulations. Taking these observations into account, we conclude that this process is interesting for testing the theoretical framework at large x, where corrections to it are likely necessary.

Another process of interest for future measurements would be Υ-pair production in collider mode, that is almost identical to the discussed J/ψ-pair production. The main difference is the mass of the heavy quarks and the corresponding quarkonia, here taken to be: $M_\Upsilon = 9.5\,\mathrm{GeV}$. Therefore, the evolution at generally larger scales is probed, making it possible to observe more of its behaviour. The value of the LDME also varies, but this difference cancels in observables like the normalised differential cross section and the modulations, as we use the simple LDME description for the quarkonium formation instead of the TMDShFs. In Fig. 6.25 and Fig. 6.26 example predictions of these observables are shown, i.e. we take a rapidity for the pair similar to the J/ψ-pair case, but consider larger invariant masses. Due to the increase of M_{QQ} one obtains larger TMD regimes favourable for observing the peaks of the convolutions and the normalised differential cross section, while their magnitudes are as expected

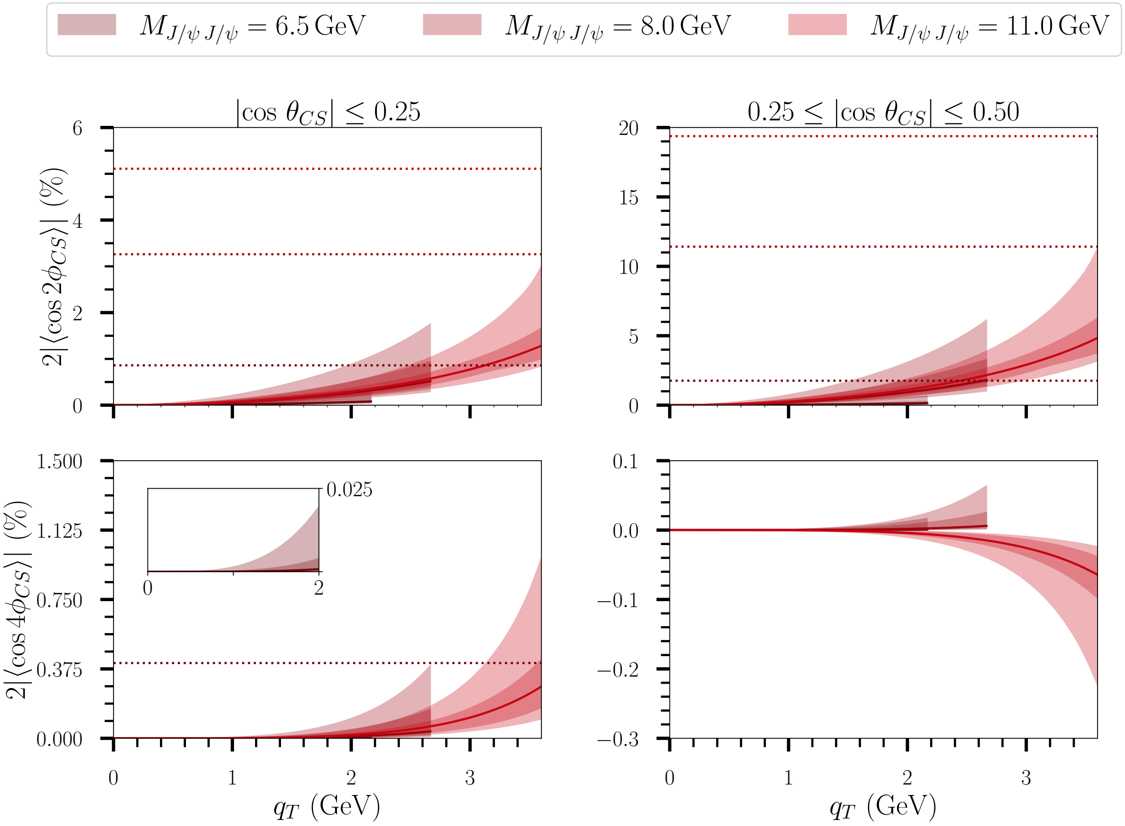

Figure 6.24: An example of the modulations in J/ψ-pair production in fixed-target mode as a function of q_T for different values of $M_{J/\psi\, J/\psi}$, similar to Fig. 6.22, with kinematics following Fig. 6.23. Since the $\cos(2\phi_{CS})$-modulations are large, we also present their corresponding upper bounds.

smaller. Besides, we note that these computations are less sensitive to nonperturbative physics. We observe that the modulations increase less quickly with q_T, but reach similar magnitudes as J/ψ-pair production in the collider mode. The latter can be explained as follows. The hard factors for Υ-pair production are much smaller in magnitude, but their ratios, and therefore their upper bounds, are equivalent to the ones for J/ψ-pair production when the following scaling is employed: if $M_\Upsilon = \nu M_{J/\psi}$ then $M_{\Upsilon\Upsilon} = \nu M_{J/\psi J/\psi}$. For example, since $\nu \sim 3$, the modulations for $M_{\Upsilon\Upsilon} = 30\,\mathrm{GeV}$ and $M_{J/\psi J/\psi} = 11\,\mathrm{GeV}$ should have approximately the same magnitude, hence small deviations from this come from the convolutions.

We end this section by investigating the hard scale dependences of observables, since this provides a way to study TMD evolution as well. In this regard we need to select a specific q_T to conduct our analysis. $\mathcal{C}[f_1^g f_1^g]$ has its maximum at $q_T = 0\,\mathrm{GeV}$, which is therefore a natural choice. Its behaviour as a function of μ_H is shown in Fig. E.10 for two different rapidities. We observe the expected decrease, which is faster for larger rapidity. By fitting, its proportionality to μ_H is obtained, which can be compared to the theoretical asymptotic behaviour of the perturbative Sudakov suppression as discussed in Sec. 4.2. Of course, we find much larger powers for μ_H due to the suppression by the nonperturbative Sudakov factor and the TMD tails. The same analysis holds for $\mathcal{C}[w_2 h_1^{\perp g} h_1^{\perp g}]$ that is shown in Fig. E.11, for which the

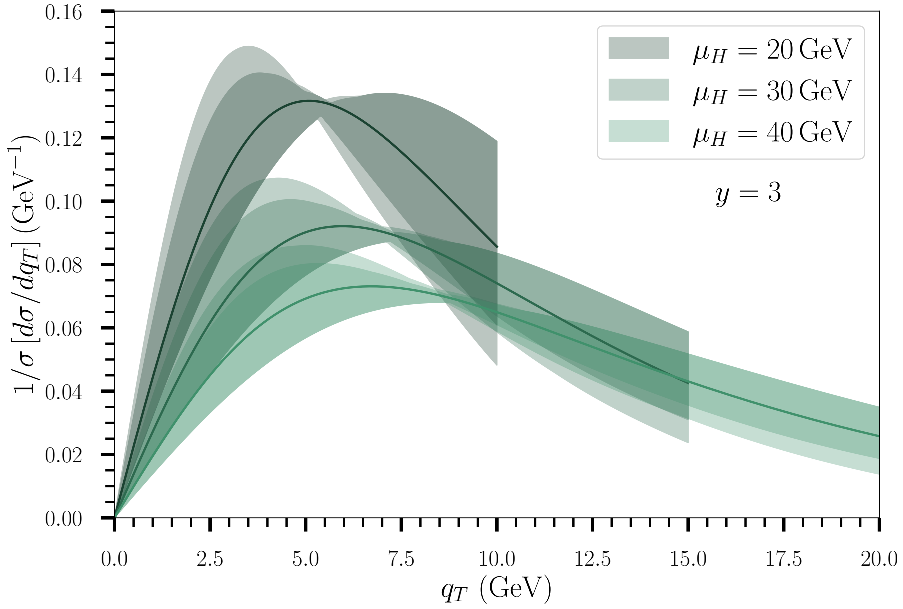

Figure 6.25: An example of the normalised differential cross sections for Υ-pair production in collider mode ($\sqrt{s} = 13\,\mathrm{TeV}$) as a function of q_T for various μ_H with $y = 3$.

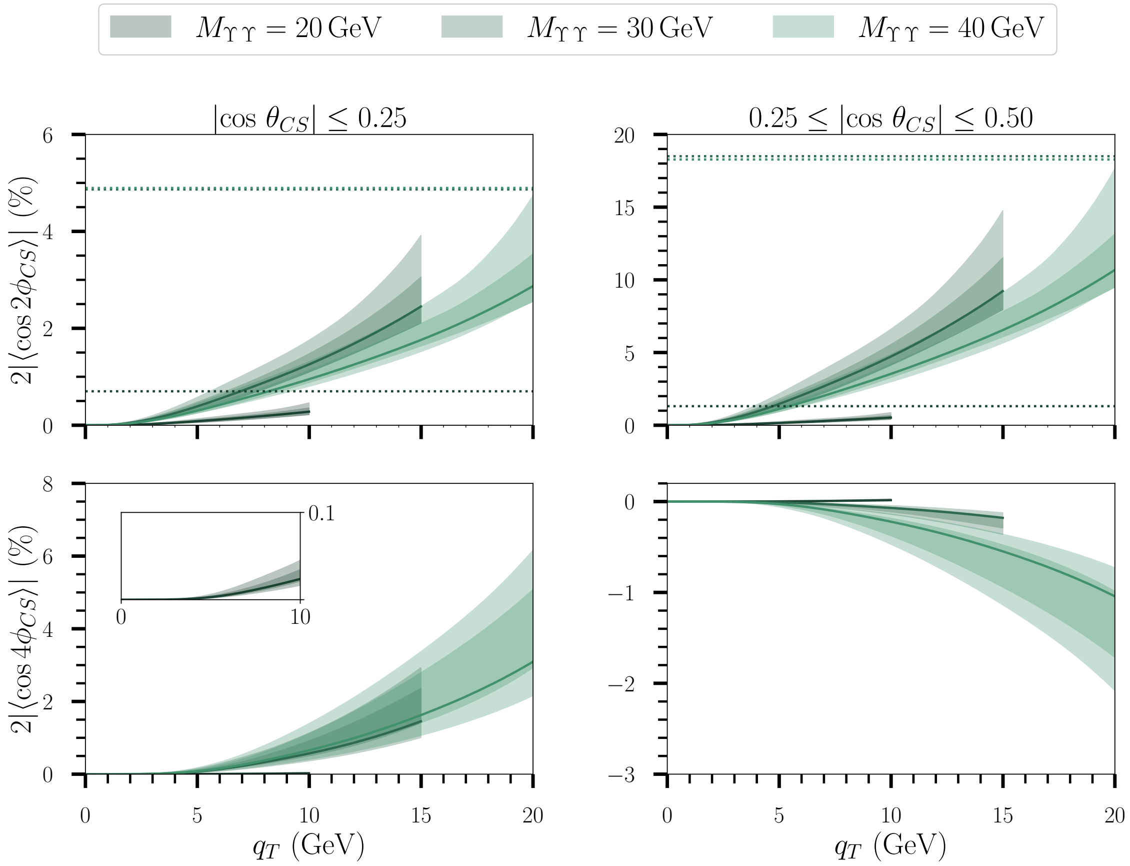

Figure 6.26: An example of the modulations in Υ-pair production in collider mode as a function of q_T for different values of $M_{\Upsilon\Upsilon}$, similar to Fig. 6.22, with kinematics following Fig. 6.25. Since the $\cos(2\phi_{CS})$-modulations are large, we also present their corresponding upper bounds.

power behaviour of μ_H is even larger. We note that the scale dependence of the differential cross section can be approximated by $d\sigma \propto M_{QQ}^{-3}\mathcal{C}[f_1^g f_1^g](q_T = 0\,\text{GeV})$, where $\mathcal{C}[f_1^g f_1^g](q_T = 0\,\text{GeV}) \propto M_{QQ}^{\alpha}$, with α depending on the rapidity as can be seen in the figures. Or course, another value for q_T may be chosen as well, but then a different power law will be expected in general.

The normalised differential cross section and the modulations are zero at $q_T = 0\,\text{GeV}$, therefore $q_{T,\text{max}}$ is chosen as the point at which their μ_H dependence is investigated. The results are shown in Fig. E.12 and Fig. E.13, respectively. For the normalised differential cross section similar behaviour as for $\mathcal{C}[f_1^g f_1^g]$ is found, where the normalisation suppresses naturally the power behaviour with respect to the non-normalised case. Similarly, its fitted power-law behaviour is displayed in the figure, once again showing dependence on rapidity, although this dependence is reduced. We observe that while the $\cos(2\phi_{CS})$-modulations increase in magnitude by increasing the rapidity, the $\cos(4\phi_{CS})$-modulations decrease. This opposite behaviour is found since all the convolutions decrease in magnitude when increasing y, while $\mathcal{C}[w_3 f_1^g h_1^{\perp g}]$ and $\mathcal{C}[w_3' h_1^{\perp g} f_1^g]$ decrease significantly less. We note that the $\cos(2\phi_{CS})$-modulations consistently exceed the upper bounds for large $M_{J/\psi J/\psi}$, regardless of both Case 1 and Case 2 scale variation and the rapidity (note that the upper bounds are independent of y). Even the central value surpasses the upper bounds at a certain point. Since this is likely not due to the choice of nonperturbative Sudakov factor, we suspect that other contributions become significant at such large scales or that higher-order corrections might solve this issue.

6

6.4 Towards a complete TM spectrum

We now return to the process of J/ψ electroproduction as an example since we have both the LO TMD and collinear differential cross section at our disposal, aiming to obtain a spectrum over the full q_T-range. This ongoing research is being conducted in collaboration with D. Boer and L. Maxia. Here we employ again our novel nonperturbative Sudakov factor developed in Sec. 6.2 together with scale variation to estimate the perturbative uncertainty. Indeed, this will alter our TMD predictions presented in Sec. 6.1, therefore we first investigate how the predictions are altered before we continue with discussing the numerical matching procedure.

With respect to hadroproduction, there are two differences taken into account. First, for consistency with the other predictions of this process we employ LL resummation for the perturbative Sudakov (defined below Eq. 4.46), which has an effect on the accuracy as we will see. Second, instead of a second TMD, we have a TMDShF, for which we note the following: since the LDMEs are scale- and therefore b_T-independent within the TMD-evolution formalism, we cannot determine a nonperturbative coefficient $g_{\Delta_{(h)}}$ for the nonperturbative Sudakov factor given in Eq. 6.10 as for the TMDs following Eq. 6.9. However, neglecting the TMDShF contribution in S_{NP} is not an issue, since our formalism guarantees a smooth continuation in b_T space of the perturbative Sudakov factor (incorporating the LO large TM TMDShF tail by resummation) and the LO large TM perturbative TMD tails within the integrand of the convolution through the nonperturbative Sudakov factor.

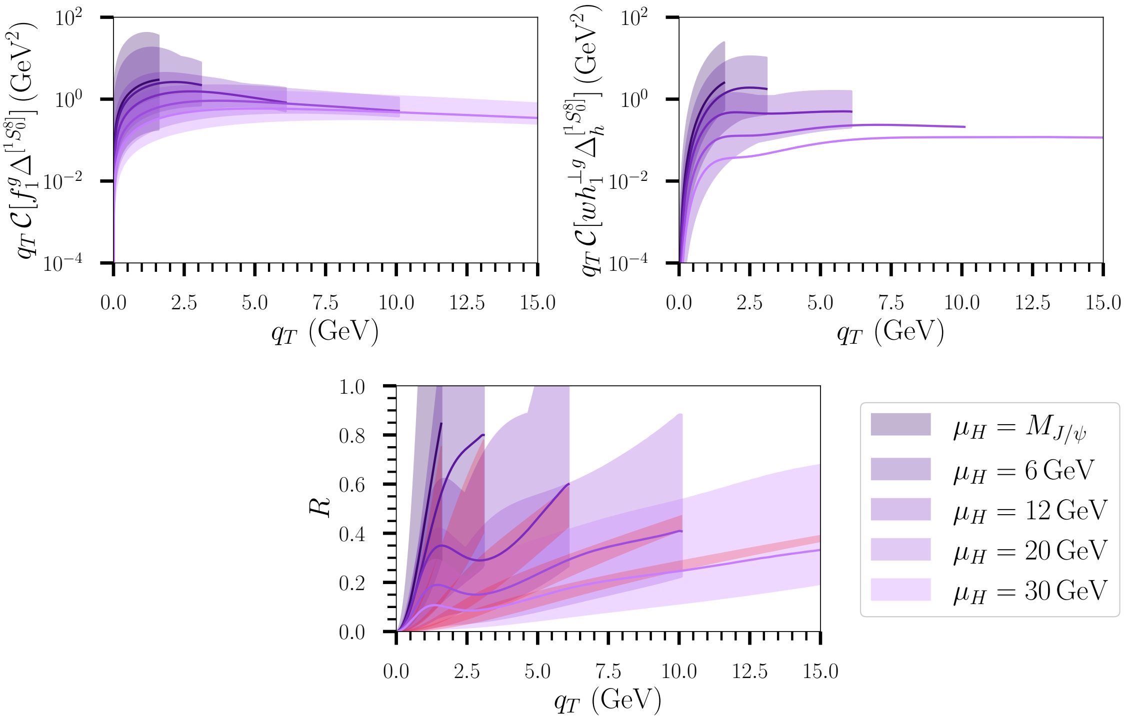

Figure 6.27: Example predictions for the convolutions and their ratio R for J/ψ electroproduction at $z = 1$ as a function of q_T by employing our novel nonperturbative Sudakov factor and Case 1 scale variation, for various values of Q, with $x = 10^{-2}$ and $b_{T,\max} = 1.0\,\mathrm{GeV}^{-1}$, similar to Fig. 6.2. We note that for R the previous predictions with a Gaussian ansatz are given in red for comparison.

In particular, we recompute the $x = 10^{-2}$ convolutions and their ratios from Sec. 6.2 that are shown in Fig. 6.27 in order to obtain a general understanding on how our new results compare to the previous ones. Here we have employed large n and $b_{T,\max} = 1.0\,\mathrm{GeV}^{-1}$ in line with the discussions presented in the previous sections. Indeed, we observe the upward bumps in $\mathcal{C}[w h_1^{\perp g} \Delta_h]$ as discussed in Sec. 6.2, which presence is enlarged in the observable R. Additionally, significantly larger uncertainties are observed. Since the R predictions only need to be multiplied by the corresponding azimuthal hard factors to obtain the azimuthal modulations, it is evident that these new calculations allow for a much larger range of possible asymmetries at the EIC. Additionally, the uncertainties are so significant that the variation in scale contributes as much to the overall uncertainty as the choice of LDME set. Our predictive power improves for larger Q like before, however such values lead to larger x values due to the kinematical constraints of this process where the gluon TMDs are unlikely to be probed.

However, the R predictions show that the positivity bound is largely violated for the three lowest values of μ_H. To address this issue, we point out that in the current implementation only less nonperturbative contributions could be assumed for $\mathcal{C}[w h_1^{\perp g} \Delta_h]$, to decrease its magnitude. With our novel S_{NP} there are two ways to do so. One way is to assume a smaller nonperturbative TMD part for $h_1^{\perp g}$, i.e. one can choose a larger value for $g_{h_1^{\perp g}}$. The other way is to change the point where nonperturbative physics takes over by altering $b_{T,\max}$, i.e. one can choose a larger $b_{T,\max}$

for which a larger g is found in general. Nevertheless, we expect that there are also nonperturbative TMD contributions from the TMDShFs, but we lack understanding of their values. Taking into account the assumption that the TMDShFs are the same for both convolutions, on top of our current state of our knowledge as summarised above, we conclude that more research is required and our formalism is currently unable to provide adequate predictions for the azimuthal modulations.

In the matching discussed below, we have chosen to proceed with our novel nonperturbative Sudakov factor for the TMD computations as only isotropic contributions are investigated, i.e. we solely focus on the angle-independent terms involving $\mathcal{C}[f_1^g \Delta]$. For the complete picture, non-isotropic contributions, those with $\mathcal{C}[w h_1^{\perp g} \Delta_h]$, should be taken into account too, but before that can be done the violation of the positivity bound discussed above should be settled first.

Keeping the correction terms general, we can re-express the differential cross section in the LTM region as

$$d\sigma\Big|_{q_T \ll \mu_H} = W(q_T, \mu_H) + \left[O\left(\frac{q_T}{\mu_H}\right)^a + O\left(\frac{m}{\mu_H}\right)^{a'}\right] d\sigma\,, \tag{6.16}$$

where W is the TMD approximation of the differential cross section $d\sigma$. The correction of order q_T/μ_H comes from the HTM region, identified as the Y term in Eq. 3.45, while the correction of order m/μ_H comes from corrections to the hadronic correlator, i.e. the scale $m = M_h$ is the hadronic mass scale of the order of 1 GeV. As q_T increases, the accuracy of the TMD approximation decreases and the power corrections are increasingly relevant until the expansion breaks down as q_T approaches μ_H. On the other hand, the differential cross section in the HTM region can be written as

$$d\sigma\Big|_{q_T \sim \mu_H \gg m \gg \Lambda_{\mathrm{QCD}}} = Z(q_T, \mu_H) + O\left(\frac{m}{q_T}\right)^b d\sigma\,, \tag{6.17}$$

where Z is the collinear approximation of the differential cross section $d\sigma$, also called the fixed-order (FO) differential cross section. For $q_T \sim \mu_H \gg m \gg \Lambda_{\mathrm{QCD}}$, Z is a good approximation of the full cross section, but as q_T decreases the accuracy of the collinear approximation diminishes, which breaks down as q_T approaches m.

The values of the exponents a and b are given by the strength of the power corrections and depend on the details of the process and its factorisation. In the case of an unpolarised processes, the smallest values allowed by Lorentz symmetry are $a = a' = 2$ and $b = 2$, since q_T is the only transverse vector that explicitly appears in the factorisation theorems. We therefore use these values in the numerical implementations presented below. We note that for cross sections involving spin (e.g. see App. B), a more conservative matching scheme can be employed with $a = b = 1$.

With both these factorisation theorems, the full numerical TM spectrum can be constructed through a matching scheme. Such a scheme must make sure that the result agrees with W in the LTM region and with Z in the HTM region, and that there is a smooth transition in the intermediate region. Instead of employing the commonly used theoretical CSS method, in which the complete cross section is given by $\overline{d\sigma} = W + Y = W + Z - A$, where A is the asymptotic term that is divergent for $q_T \to 0$ (i.e. the FO small-q_T expansion of Z), we employ the phenomenological inverse-error weighting (InEW) method from [167]. In this scheme the power corrections to the factorisation theorems are used to quantify the trustworthiness associated to the respective contributions, i.e. they are employed to build a weighted average. The resulting differential cross section over the full range in q_T is then given by

$$\overline{d\sigma} = \omega_1 \, W(q_T, \mu_H) + \omega_2 \, Z(q_T, \mu_H) \,, \tag{6.18}$$

where the normalised weights for each of the two terms are

$$\omega_1 = \frac{\Delta W^{-2}}{\Delta W^{-2} + \Delta Z^{-2}} \,, \tag{6.19}$$

$$\omega_2 = \frac{\Delta Z^{-2}}{\Delta W^{-2} + \Delta Z^{-2}} \,, \tag{6.20}$$

with ΔW and ΔZ being the uncertainties of both factorisation theorems generated by their power corrections. In particular, $\Delta W = \Delta_W \, d\sigma$ and $\Delta Z = \Delta_Z \, d\sigma$ are given by:

$$\Delta_W = \left(\frac{q_T}{\mu_H}\right)^2 + \left(\frac{m}{\mu_H}\right)^2 , \tag{6.21}$$

$$\Delta_Z = \left(\frac{m}{q_T}\right)^2 \left(1 + \ln \frac{\mu_H}{M_\mathcal{Q}} + \ln \frac{\sqrt{\mu_H^2 + q_T^2}}{q_T^2}\right) . \tag{6.22}$$

We elaborate on the additional term introduced in Δ_Z below. The uncertainty in Eq. 6.18 simply follows from the propagation of these (uncorrelated) theory uncertainties:

$$\Delta\overline{d\sigma} = \frac{1}{\sqrt{\Delta W^{-2} + \Delta Z^{-2}}} \approx \frac{\Delta_W \, \Delta_Z}{\sqrt{\Delta_W^2 + \Delta_Z^2}} \, \overline{d\sigma} \,. \tag{6.23}$$

In general, once the matched cross section is obtained, one can include other important sources of uncertainty, i.e. we will combine the uncertainty of the matching with those from scale variations and LDME extractions.

In the region where q_T becomes smaller than μ_H, large logarithms will reduce the accuracy of the power counting of the collinear cross section. Therefore, the additional term of Δ_Z is introduced as it improves the reliability of the scheme for all q_T, i.e. when $q_T \ll \mu_H$ it corresponds to the leading logarithms of the FO calculation. Unlike [167], we modified this term by exchanging one of the q_T-logarithms for another one over the hard scale, inspired by the divergent behaviour found for J/ψ electroproduction (see Eqs. 5.91 and 5.92). In particular, we take here: $\mu_H^2 = Q^2 + M_\mathcal{Q}^2$. This additional logarithm is negligible for small-Q values, whereas it contributes to reducing the applicability of the collinear factorisation at small q_T for large-Q values.

Before we continue to present results of the InEW method, we make two more remarks. First, for the FO calculation of order $\alpha\alpha_s^2$ performed with Eq. 5.39, $\hat{x}_{\max}$ was shown as independent of q_T, see Eq. 5.40, since we were primarily interested in the kinematical region where $q_T \ll M_\mathcal{Q}, Q$ (i.e. giving the asymptotic term). However, the following equation is needed to properly evaluate it when $q_T \gtrsim M_\mathcal{Q}, Q$:

$$\hat{x}_{\max}(\mathbf{q}_T) = \frac{Q^2}{Q^2 + M_\mathcal{Q}^2 + 2M_\mathcal{Q}|\mathbf{q}_T|} \,. \tag{6.24}$$

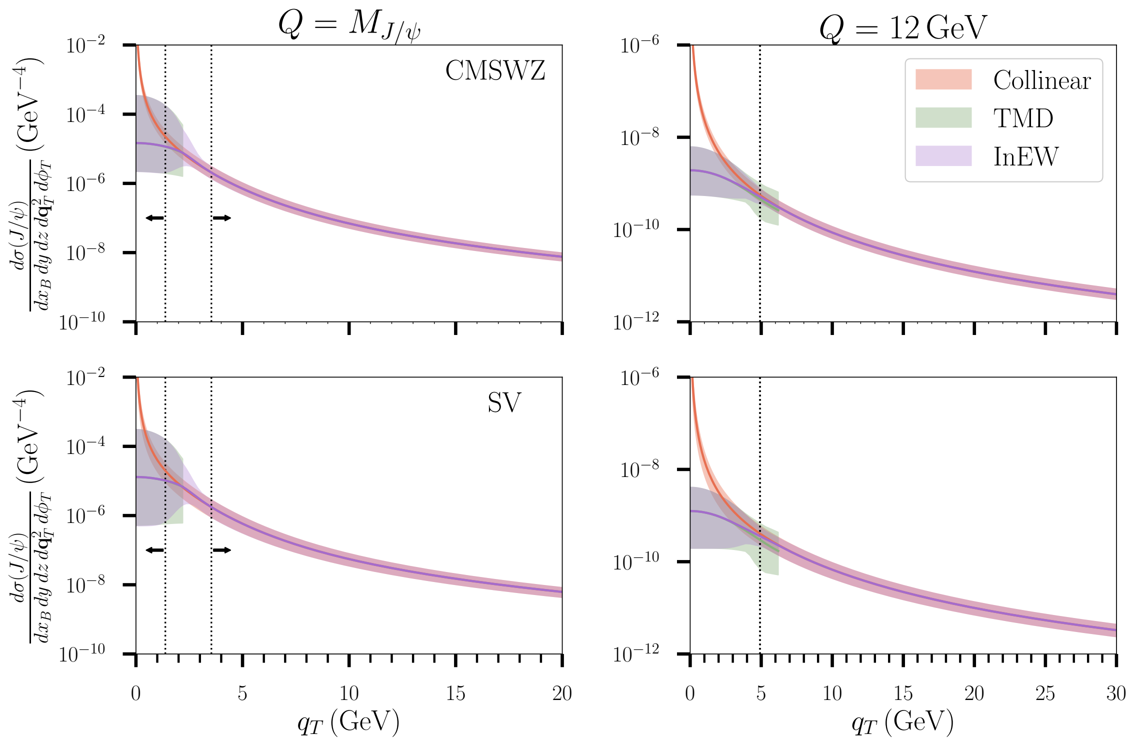

Figure 6.28: Examples of the J/ψ electroproduction differential cross section matched via the InEW method as a function of q_T for two values of Q and two LDME sets, with $x = 10^{-2}$ and $\sqrt{s} = 140\,\text{GeV}$. For the uncertainty bands we combine the uncertainties from (Case 1) scale variation, the LMDE set and the matching procedure. The dotted lines denote the regions for which Δ_W, $\Delta_Z < 0.15$; we note that in the right graphs they lie approximately on top of each other.

Second, unlike studies on the production of light hadrons in SIDIS (see e.g. [168, 169]), we have no flexibility in the choice of z for performing the matching in J/ψ (or generally quarkonium) production, with $z = 1$ being the only possibility. This constraint arises from approximating the invariant mass of the $c\bar{c}$ pair to the J/ψ mass in its rest frame. As q_T decreases, the energy fraction of the $c\bar{c}$ pair saturates, leading to $\hat{z} \to 1$, as shown in [129, 132] and in Ch. 5, which directly corresponds to the energy fraction of the J/ψ (z). However, we expect this approximation to break down with a more refined z dependence in the TMDShFs, allowing for slight deviations between z and $\hat{z}$, as suggested in [170, 171]. In particular, a complete TM spectra with $z \neq 1$ would allow for a comparison with Hadron–Electron Ring Accelerator (HERA) data [172] that could possibly set constraints on the TMDs and the TMDShFs. Nonetheless, given our primary focus on the Q dependence of the TMD observables, we continue using this approximation and leave a detailed study of the z dependence in the TMDShFs for future investigations.

In Fig. 6.28, we present the FO and TMD cross sections along with the matched curves obtained using the InEW method. Specifically, we show examples with $x = 10^{-2}$ and $\sqrt{s} = 140\,\text{GeV}$, identified in Sec. 6.1 as the optimal centre-of-mass energy for the TMD cross section at the EIC. Two different values for Q are considered, $M_{J/\psi}$ and $12\,\text{GeV}$, representing extreme kinematically allowed cases under these conditions. Like before, we also employ the CMSWZ and SV sets for the LDMEs (see Table 3.3) to illustrate the differences between them, i.e. the SV predictions lie slightly lower as expected. The uncertainty bands for each curve are obtained by propagation of independent errors. Specifically, for the TMD and FO cross sections we combined the LDMEs uncertainties with the scale variation, namely the factorisation scale for the latter and C_1, C_2 and C_3 variations for the former. For the matched curve, we combine these bands with the uncertainty given in Eq. 6.23.

We note that the uncertainty in Eq. 6.23 identifies two scenarios. On the one hand, we expect that for a sufficiently large μ_H matching occurs in an ITM region where both frameworks are reliable, i.e. the associated Δ_W and Δ_Z are small. On the other, if μ_H is smaller, the matching happens in a region where both factorisations lose there reliability. Which scenario occurs is decided by a certain threshold on $\Delta\overline{d\sigma}$, for which we have chosen $\Delta\overline{d\sigma}/\overline{d\sigma} = 0.15/\sqrt{2} \approx 10\%$. With this choice an ITM region is found for $Q > 12\,\text{GeV}$, which becomes larger when Q is further increased. Especially for smaller values of Q the identification of this matching region is relevant, i.e. to have greater control over the TMD cross section when $\Delta_W > 0.15$, we exclude its negative values. Indeed, within the TMD uncertainty band, the predictions lose at some point their physical meaning by allowing negative values for the cross sections, e.g. for $Q = M_{J/\psi}$ negative values are found for $q_T \gtrsim 2.5\,\text{GeV}$. On the contrary, when matching happens below this uncertainty threshold, this behaviour of the TMD cross section is suppressed by the smallness of the associated weight. We anticipate that this artificial solution is required due to the magnitude of the TMD uncertainties since we can choose the threshold to be larger. Hence, by improving the precision of both the TMD and FO descriptions, the uncertainty in the matched curve is expected to be dominated by $\Delta\overline{d\sigma}$.

The fact that the TMD curve tends to lie above the FO one, as can be clearly seen by comparing the central values within the two factorisations, is an important feature as this indicates smooth matching between the two regimes is possible. In particular, the TMD differential cross sections evaluated at the origin lie above the collinear cross sections evaluated at $q_{T,\max}$, the point at which the TMD calculation is expected to break down and where therefore approximately the matching occurs. To investigate this in greater detail we show in Fig. 6.29 these specific points as a function of Q. We observe that both the TMD and collinear curves decrease with q_T, but at different rates; in particular, the FO one will drop much faster. Indeed, it is found that the TMD curve lies above the collinear one in both the ${}^1S_0^8$ and ${}^3P_J^8$ channels, i.e. matching the cross section of those channels will have no surprising features.

However, when we take all contributions into account we observe that for large Q the FO computation becomes larger than the TMD one, for the CMSWZ set at smaller Q than for the SV set. Since this is not due to the ${}^1S_0^8$ and ${}^3P_J^8$ channels, this observation must come from the ${}^3S_1$ channel. Therefore, we also show the FO calculations without these contributions, for quark and gluons separately. In particular, the gluon contribution to the ${}^3S_1$ channel is proportional to $\langle\mathcal{O}^{J/\psi}[{}^3S_1^c]\rangle = \langle\mathcal{O}^{J/\psi}[{}^3S_1^1]\rangle + \frac{15}{8}\langle\mathcal{O}^{J/\psi}[{}^3S_1^8]\rangle \approx \langle\mathcal{O}^{J/\psi}[{}^3S_1^1]\rangle$ (where the factor of 15/8 comes from the relative colour projectors and the LDME normalisations), i.e. of order unity, while the quark contribution to this channel is proportional to $\langle\mathcal{O}^{J/\psi}[{}^3S_1^8]\rangle$, i.e. suppressed by order v^4 (see Table 3.2). Hence, as Q increases, the hard factor associated with the quark ${}^3S_1$-wave in the FO calculation grows, becoming more important than the other

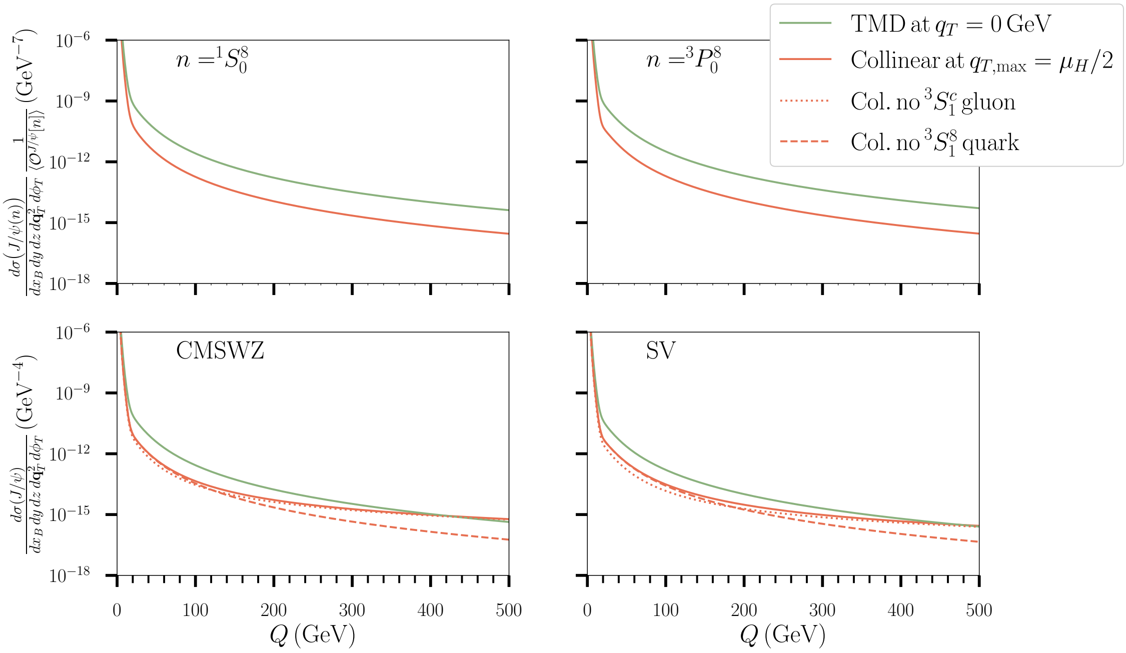

Figure 6.29: The central values of the TMD differential cross section at $q_T = 0$ GeV and the collinear differential cross section at $q_{T,\max}$ for J/ψ electroproduction as a function of Q, with $x = 10^{-2}$ and $\sqrt{s} = 140$ GeV. In the upper graphs we show the ${}^1S_0$ and ${}^3P_0$ CO cross sections independently, while in the lower graphs we show the complete cross sections with the CMSWZ and the SV set. In the latter we also present the FO cross section without ${}^3S_1$ contributions, from gluons, as well as from quarks, to explain the observed behaviour at large Q.

contributions. The corresponding expected outcome is a distinctive bump in the ITM region of the matched curve for large Q.

Nevertheless, one can question whether such large-Q values will ever be relevant, and once these values are reached it is likely that additional contributions must be incorporated such as QED corrections [173] and fragmentation contributions [53, 147]. However, it is currently unclear how these connect to their TMD counterparts. The QED corrections should correspond to a TMD photon distribution of the proton or are affiliated with the electron, while the FFs require an understanding of how the TMDShFs relate to the TMDFFs. We note that a transition region in Q likely exists between our predictions and these additional contributions. As a result, a more complex behaviour could already be expected at smaller-Q values compared to those shown in Fig. 6.29.

In addition to investigating non-isotropic contributions, other kinematic regimes at the EIC should also be explored as was done previously. Moreover, the uncertainty from CO LDME values remains a significant challenge, so a broader range of LDME sets should be investigated as well. Furthermore, a next step would be to explore the matching in J/ψ photoproduction, since there is data available from HERA and indirectly from ultra-peripheral collisions (UPCs) at the LHC. For an overview of these experiments and how proton-lead UPCs, in which a quasi-real photon emitted by a fully stripped lead ion breaks a proton, can be used to study inclusive vector-quarkonium production we refer to [174].

7

Discussion and conclusions

Quarkonium production is considered as a main tool for probing the unknown gluon TMDs at the current LHC but also at the upcoming EIC. Therefore, we analysed the differential cross sections of quarkonium (-pair) production in proton-proton collisions, as well as quarkonium production in electron-proton collision, for which TMD factorisation is expected to hold. Specifically, by treating all incoming particles as unpolarised, we were able to study both the unpolarised and linearly polarised gluon TMDs. Moreover, we investigated these TMDs by examining the azimuthal modulations that can arise in these processes due to the presence of linearly polarised gluons within unpolarised protons. In particular, we studied the convolutions of TMD functions in these reactions by employing the TMD-evolution formalism, as opposed to relying on models. This is because their large transverse momentum perturbative tails are related to known functions, namely the nonperturbative PDFs from collinear factorisation and the nonperturbative LDMEs from NRQCD factorisation for quarkonium production. As a result, only the unknown nonperturbative TMD contributions, incorporated in the nonperturbative Sudakov factor, needed to be parametrised. In order to study TMD evolution, we concentrated on processes with a variable hard scale, i.e. quarkonium-pair hadroproduction and quarkonium electroproduction. In particular, we consider mainly J/ψ production, as this quarkonium is relatively straightforward to detect in collider experiments.

The TMD shape functions (TMDShFs), which generalise the LDMEs within TMD factorisation, are important in the phenomenological description of quarkonium production as they account for final state smearing effects. So far the LO expression for the TMDShF in terms of LDMEs has proven to be sufficient for CS quarkonium production. However, we have shown that their contribution to the evolution of CO J/ψ electroproduction at LO is essential due to the unavoidable soft-gluon radiation required for the quarkonium to become colourless. Particularly, we showed that the large transverse momentum perturbative tails of the TMDShFs can be found by matching the TMD and collinear cross sections of a process in the region where both factorisations are applicable, provided that collinear singularities in the hard factors, that were not noticed before, are properly taken into account when performing the small transverse momentum limit. We expect that the presence of these poles from the gluon channel are an intrinsic feature of any inclusive quarkonium production process. Specifically, at LO the large transverse momentum perturbative tails of the TMDShFs that convolute with the unpolarised gluon TMD have been determined, while for the TMDShFs that convolute with the linearly polarised gluon TMD, a higher-order α_s matching is required. The functional form of the TMDShFs is supported by an eikonal approximation, which does not discriminate which gluon TMD is employed, hinting that they might be the same. Moreover, we found that the TMDShFs provide a unique contribution to the process, different from a FF description. Given that the TMDShFs should solely depend on the quarkonium mass and the hard scale of the process, we proposed that the TMDShFs are universal. This implies that a process-dependent soft factor must be considered, which can be removed by a proper scale choice. Hence, we proposed a strategy for determining the TMDShFs experimentally from different processes: extract them from one process and validate them in another by evolving to the relevant hard scale and including the appropriate soft factor.

By incorporating the large transverse momentum tails of the TMDShFs (assuming them to be the same for both convolutions), we predicted significantly large azimuthal asymmetries for J/ψ electroproduction at the future EIC, depending on the specific kinematics and the poorly determined CO LDMEs. The asymmetries were found to increase monotonically as a function of transverse momentum in the TMD regime, with the expectation that their peak will occur outside of it. Generally, smaller hard scales (sufficiently larger than the quarkonium mass) and the larger centre-of-mass energy of 140 GeV will result in larger asymmetries, while the dependence on the collinear momentum fraction is less systematic within the EIC kinematic range. Due to the uncertainty in the LDMEs, going to higher-order calculations in the TMD evolution at this stage is unlikely to yield significantly more precise predictions. These predictions were made using a Gaussian ansatz for the nonperturbative Sudakov factor, with its coefficient varied to estimate the nonperturbative uncertainty. The EIC experiment is crucial for reducing these uncertainties, such that our understanding of gluon TMDs and TMDShFs, and with them the LMDEs, can be improved.

Given the limitations associated with a general Gaussian ansatz for the nonperturbative Sudakov factor, we developed a novel nonperturbative Sudakov factor for the TMD-evolution formalism. In particular, since real measurements are independent of the theoretical separation between perturbative and nonperturbative physics by $b_{T,\max}$, the nonperturbative Sudakov factor should provide $b_{T,\max}$ invariance of observables (at a specific perturbative order). Additionally, it should account for the specific TMD functions employed. Our novel Gaussian-like nonperturbative Sudakov factor is based on a stricter separation between perturbative and nonperturbative physics, ensuring a smooth transition of known contributions into the nonperturbative regime. Specifically, we expected that the integrand of the convolutions (without the Bessel function) would increase in b_T space, followed by a decrease towards zero, resulting in a single smooth peak. By matching the derivatives of the TMD functions in the convolutions at $b_{T,\max}$, we identified the minimal value of the coefficient in our nonperturbative Sudakov factor necessary to achieve this behaviour. Consequently, the peak in b_T space consistently occurs within the perturbative regime, with the extent of nonperturbative physics determined by perturbative physics. Approximate $b_{T,\max}$ invariance for the observables followed from this formalism as well. Besides, we note that in general an upward bump at small transverse momentum can arise in the convolutions, driven by large-b_T contributions. It was found that our novel nonperturbative Sudakov factor generally does not allow for such a bump in proton-proton collisions, whereas it does permit such a bump in electron-proton collisions, due to the different perturbative Sudakov factor and the different combinations of TMD functions involved in the convolutions. Although our nonperturbative Sudakov factor provides an innovative approach to exploring TMD evolution by utilising the interplay between perturbative and nonperturbative physics, it may not be the definitive solution as some concerns have been raised in particular situations; it remains a process-dependent factor that requires validation through experimental data.

When applying the novel nonperturbative Sudakov factor in the TMD-evolution formalism for quarkonium (-pair) hadroproduction at LHC kinematics, we found that the nonperturbative uncertainties in the convolutions are negligible compared to the perturbative uncertainties. That is, we observed that the uncertainties arising from $b_{T,\max}$-variation, extra suppression by increasing the coefficient of the nonperturbative Sudakov factor and the PDF set, are much smaller than those from scale variation. In particular, we took two distinct approaches to scale variation: one more conservative than the other, which restricts the scale entering the large transverse momentum perturbative tails of the TMDs. In general, we found good agreement to recent normalised differential cross section data of J/ψ-pair production from LHCb, but the best fit was achieved by relaxing this additional scale-variation restriction, especially when different hard scales are employed. Continuing with only scale variation as the source of uncertainty, we generated predictions for the azimuthal modulations in J/ψ-pair production, which exhibited a similar behaviour to the modulation observed in J/ψ electroproduction as a function of transverse momentum. In contrast, in this process larger asymmetries within the TMD regime are expected when the hard scale is increased. Generally, the magnitudes of the $\cos(2\phi_{CS})$-modulations are found to be larger than those of the $\cos(4\phi_{CS})$-modulations and our results indicate how to optimise the binning in θ_{CS}. Future measurements at the LHCb of J/ψ-pair production in fixed-target mode or Υ-pair production in collider mode could offer valuable complementary information by probing the gluon TMDs under different kinematic conditions, at larger collinear momentum fractions or at larger hard scales, respectively. Moreover, further improved measurements of the J/ψ-pair differential cross section in the current collider mode (with optimised binning), along with an analysis of the azimuthal modulations in specific θ_{CS}-bins, would help to better constrain the gluon TMDs too. Besides, it might be suitable to test the TMD-evolution formalism as well by analysing the power-law behaviour of observables with respect to the hard scale of the process, e.g. the normalised cross section at a specific transverse momentum.

We finished our analysis by presenting some examples of the complete J/ψ electroproduction cross section by numerically matching its collinear and TMD regimes. We demonstrated that when our novel nonperturbative Sudakov factor is applied to this process at EIC kinematics, along with scale variation, similar results are observed to those obtained using a Gaussian ansatz, but with significantly larger uncertainties in the observables. Given that our findings show a significant violation of the positivity bound for this process and that other uncertainties, such as the lack of knowledge about nonperturbative TMD contributions from the TMDShFs, need to be addressed, we focused solely on matching isotropic cross sections, i.e. terms involving the unpolarised gluon TMD. We demonstrated the potential of the inverse-error weighting method for matching, for which we introduced an alternative collinear weight function to account for the distinct divergent behaviour caused by the TMDShFs in this process. This forms a preliminary step towards developing a complete theoretical transverse momentum spectrum for gluon-induced quarkonium production. Moreover, for the total uncertainty of the matched curve we combined the perturbative uncertainties from scale variation with the uncertainties from the LDME sets and the matching procedure itself. Additionally, we examined the hard scale dependence in both regimes. Although the TMD and collinear cross sections follow significantly different power laws in the kinematic regime to be probed by the EIC, we find that smooth matching is expected in general since the TMD cross sections lie above the collinear ones in the regime where matching occurs.

A

QCD in a nutshell

In this appendix we summarise some important results and identities from QFT, in particular QCD, that are used throughout this thesis. For details we refer to standard textbooks such as [175, 176].

Conventions

- We work in natural units: $\hbar = c = 1$.
- We adopt the following Minkowski metric: $g^{00} = -g^{11} = -g^{22} = -g^{33} = 1$.

Colour Algebra

QCD is a non-abelian gauge theory with a local $SU(N_c)$ symmetry, where $N_c = 3$ denotes the number of colours. The invariance of the fermionic quark fields under these local transformations gives rise to eight massless gauge boson fields: the gluons. The special unitary symmetry group $SU(N_c)$ consists of all $N_c \times N_c$ unitary matrices V with determinant 1:

$$V^\dagger = V^{-1}\,, \quad \det V = 1\,. \tag{A.1}$$

Therefore, the group elements of the local symmetry can be represented by

$$V(\xi) = e^{i\omega_a(\xi)t^a}\,, \tag{A.2}$$

where t^a are the traceless Hermitian generators spanning the Lie algebra $su(N_c)$ of the Lie group $SU(N_c)$ and $\omega_a(\xi)$ are the (arbitrary) transformation parameters. The index a runs from 1 to $d(G)$, where $d(G) = N_c^2 - 1$ is the dimension of the group.

In particular, the generators of QCD in the fundamental representation are the eight Gell-Mann matrices λ^a, with $t^a = \lambda^a/2$. The traces of the generators, also referred to as colour matrices, are normalised according to

$$\mathrm{Tr}[t^a t^b] = t^a_{ij} t^b_{ji} = \frac{1}{2}\delta^{ab}\,, \tag{A.3}$$

where the index i and j run from 1 to N_c. They obey the commutation and anticommutation relations

$$[t^a, t^b] = i f^{abc}\, t^c\,, \tag{A.4}$$

$$\{t^a, t^b\} = \frac{1}{N_c}\delta^{ab} + d^{abc}\, t^c\,, \tag{A.5}$$

where:

$$f^{abc} = -2i\,\mathrm{Tr}(t^a[t^b, t^c])\,, \tag{A.6}$$

$$d^{abc} = 2\,\mathrm{Tr}(t^a\{t^b, t^c\})\,. \tag{A.7}$$

The brackets denote the standard commutator, $[a,b] = ab - ba$, and anticommutator, $\{a,b\} = ab + ba$. The structure constants f are antisymmetric in all indices, and the structure constants d are symmetric in all indices. From these equations one can derive:

$$\mathrm{Tr}[t^a t^b t^c] = \frac{1}{4}(d^{abc} + i f^{abc})\,. \tag{A.8}$$

In general, one can write for a representation R

$$\mathrm{Tr}_R[t^a t^b] = T(R)\delta^{ab}\,, \quad \mathrm{Tr}_R[I] = d(R)\,, \tag{A.9}$$

where $T(R)$ and $d(R)$ are the index and dimension, respectively, and I the identity matrix. Besides the fundamental representation (F), there are two other important representations: the trivial representation with dimension one, in which the generators are zero, so, every group element 1, and the adjoint representation (A) with dimension $d(G)$, in which the generators are: $(t^a_A)^{bc} = -i f^{abc}$. The invariant quadratic Casimir is found by

$$C_R = \frac{\mathrm{Tr}_R[t^a t^a]}{d(R)} = \frac{T(R)d(G)}{d(R)}\,, \tag{A.10}$$

where $d(F) = N_c$, $d(A) = d(G)$, $T(F) = 1/2$ and $T(A) = N_c$, i.e. for the fundamental and adjoint representations we obtain:

$$C_F = \frac{N_c^2 - 1}{2N_c}\,, \quad C_A = N_c\,. \tag{A.11}$$

In QCD quarks transform under the fundamental representation (triplet, **3**), antiquarks under the antifundamental representation ($\bar{\mathbf{3}}$) and gluons under the adjoint representation (octet, **8**) of the colour gauge symmetry. The trivial representation is colourless (singlet, **1**).

The Lagrangian

A QFT is described by a Lagrangian, for QCD given by

$$\mathcal{L}_{\text{QCD}} = -\frac{1}{4}F_{\mu\nu}F^{\mu\nu} + \sum_{q}^{n_f} \bar{\psi}_q(i\not{D} - m_q)\psi_q \,, \tag{A.12}$$

where the Dirac field ψ_q with mass m_q represents a quark with a flavour q and n_f denotes the number of flavours. Here the Feynman slash notation $\not{D} = \gamma^\mu D_\mu$ is employed, where γ_μ are the Dirac matrices. Besides, $\bar{\psi} = \psi^\dagger\gamma^0$ is the Dirac adjoint. The covariant derivative is given by

$$D_\mu = \partial_\mu - ig_s A_\mu \,, \tag{A.13}$$

where g_s is the strong coupling constant, also called colour charge, and A the four-vector field representing a gluon, in particular, $A_\mu = A_\mu^a t^a$. The gluon field strength tensor, $F_{\mu\nu} \equiv (i/g_s)[D_\mu, D_\nu]$, is expressed as:

$$F_{\mu\nu}^a = \partial_\mu A_\nu^a - \partial_\nu A_\mu^a + g_s f^{abc} A_\mu^b A_\nu^c \,. \tag{A.14}$$

We note that Eq. A.12 is by construction invariant under local $SU(3)$ transformations given in Eqs. 2.3 and 2.6. From the Lagrangian one can derive the Feynman rules for perturbative calculations of scattering amplitudes. In particular, one can expand the action in correlators, that are vacuum expectation values of time-ordered products of field operators, when the coupling constant is small. The Feynman rules that are used in this thesis are summarised below.

The last term of Eq. A.14 gives rise to gluonic self interactions, which is absent in an abelian theory like QED. In the latter, the gauge symmetry group is $U(1)$, where the generator is identity. $\mathcal{L}_{\text{QED}}$ is similar to Eq. A.12: one can just replace g_s with e, where e is the elementary electric charge. In case the fermionic field describes a quark instead of a charged lepton, the coupling constant must be multiplied by the fractional electric charge e_q. In this theory, the invariance under local $U(1)$ transformations gives rise to the massless four-vector photon fields.

Confinement and asymptotic freedom

Opposite charges are drawn to each other via the electromagnetic force of QED, which diminishes quickly as the distance between them increases. This enables the separation of oppositely charged particles over long distances. In contrast, the strong force of QCD involves self-interacting gluons forming a flux tube between two quarks. As the quarks approach each other, the interaction weakens. On the other hand, as the distance between quarks increases, the interaction intensifies. At a sufficiently large distance, it becomes energetically more favourable to generate quark-antiquark pairs than to isolate the quarks as free particles. Consequently, isolating colour charged particles is impossible, and only colour singlet composite particles, known as hadrons, are observed. This property is referred to as *confinement*.

In QED, a single electron is surrounded by a cloud of e^+e^- pairs. The fluctuating pairs arrange themselves in such a way that the e^+ particles are closer to the electron, thereby screening its charge. This results in a reduced effective charge for the electron, causing the QED coupling constant $\alpha = e^2/4\pi$ to decrease as the distance increases. At lower energies, α is approximately 1/137, whereas at large scales, e.g. the mass of the Z-boson (around 90 GeV), α measures around 1/128. As energy increases, α continues to increase, eventually leading to a strong coupling.

Conversely, in QCD, a quark with a colour charge is surrounded not only by $q\bar{q}$ pairs contributing to a similar screening effect but also by gluons due to their self-interactions, giving an antiscreening effect. Ultimately, the antiscreening effect from gluons outweighs the screening effect, causing the running of the strong coupling $\alpha_s = g_s^2/4\pi$ to be smaller at higher energies instead. This allows quarks to be treated as free particles at high energies, a phenomenon known as *asymptotic freedom*. This property permits the application of perturbation theory in high-energy collisions. However, in the strong coupling region, one enters the nonperturbative regime. Perturbation theory relies on the small coupling, and the first order expansion in α_s is referred to as the leading order (LO), followed by the next-to-leading order (NLO), etc. Higher-order terms in the expansion provide smaller contributions due to the larger powers of α_s.

In high-energy collisions single quarks and gluons with some colour charge can be created. Then, in order to obey confinement, other coloured objects will be created to form colourless hadrons. The ensemble of these particles tend to travel in the same direction and is called a jet; a narrow cone of hadrons and other particles produced by the hadronisation of quarks and gluons.

In practice, the running of the coupling is derived from the renormalisation group equations, which follow from the requirement that observables associated with the Lagrangian, such as the coupling, should not depend on an arbitrary renormalisation scale μ. Namely, a renormalisation scheme is needed to absorb the infinities that arise in perturbative calculations beyond LO. Quantitatively, the running of α_s is encoded in the β-function

$$\beta(a_s) \equiv \frac{d\,a_s(\mu)}{d\ln\mu^2} = -\sum_{i\geq 0} \beta_i\, a_s^{i+2}(\mu)\,, \tag{A.15}$$

where $a_s \equiv \alpha_s(\mu)/4\pi$. In this thesis we solely utilise the LO (one loop) coefficient, that is given by

$$\beta_0 = \frac{11}{3}C_A - \frac{4}{3}T(F)n_f \overset{\text{QCD}}{=} 11 - \frac{2}{3}n_f\,, \tag{A.16}$$

where the first term comes from gluon loops and the second term from quark loops. Hence, in the standard model $n_f = 6$, the β-function is negative (while for QED it is positive). Higher-order terms up to five loops can be found in [177]. Using the first order differential equation, α_s at any scale μ can be related to a particular reference scale. For this reference scale one usually takes the Landau pole Λ_{QCD}, also referred to as the QCD scale, which is the energy scale at which the coupling constant becomes infinite. So, at the LO one obtains:

$$\alpha_s(\mu) = \frac{4\pi}{\beta_0 \ln\frac{\mu^2}{\Lambda_{\text{QCD}}^2}}\,. \tag{A.17}$$

Typically, $\Lambda_{\text{QCD}} \sim 0.2\,\text{GeV}$, however it is not uniquely determined: besides a dependence on n_f and the perturbative accuracy, it also depends on the renormalisation scheme (which starts at three loops). The strong coupling behaviour around Λ_{QCD} and the rapid decrease of α_s at larger values of μ have led to the commonly accepted practice of applying a scale of $\mu \gtrsim \mu_{NP} = 1\,\text{GeV}$ in order to employ perturbation theory ($\alpha_s \lesssim 0.4$). So, μ_{NP} can be thought of as the energy scale that determines the separation between the perturbative and nonperturbative regime of QCD.

Feynman rules of QED and QCD

- **Vertices**

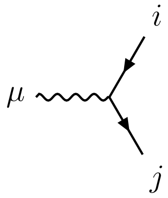

$$= -iee_q\gamma^\mu\delta_{ij}$$

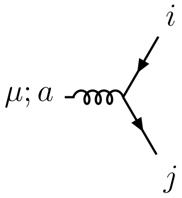

$$= ig_s\gamma^\mu t^a_{ij} \tag{A.18}$$

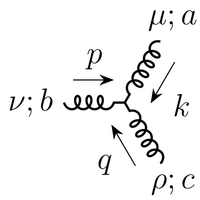

$$= g_s f^{abc} C^{\mu\nu\rho}(k,p,q)$$

$$\text{with } C^{\mu\nu\rho}(k,p,q) = g^{\mu\nu}(k-p)^\rho + g^{\nu\rho}(p-q)^\mu + g^{\rho\mu}(q-k)^\nu \tag{A.19}$$

- **Propagators**

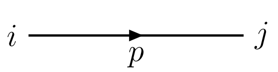

$$= \frac{i\delta_{ij}}{\not{p} - m + i\varepsilon} = i\frac{\not{p} + m}{p^2 - m^2}\delta_{ij} \tag{A.20}$$

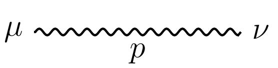

$$= i\frac{-g^{\mu\nu} + (1-\xi)\frac{p^\mu p^\nu}{p^2}}{p^2 + i\varepsilon} \tag{A.21}$$

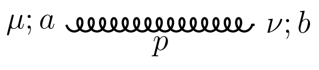

$$\begin{aligned} &= i\frac{-g^{\mu\nu} + (1-\xi)\frac{p^\mu p^\nu}{p^2}}{p^2 + i\varepsilon}\delta^{ab} \\ &= -i\frac{g^{\mu\nu}}{p^2}\delta^{ab} \text{ when } \xi = 1 \text{ (Feynman gauge)} \end{aligned} \tag{A.22}$$

- **External lines**

$= \epsilon_\mu(p)$ (incoming)

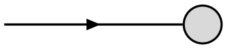

$= u_s(p)$

$= \epsilon^*_\mu(p)$ (outgoing)

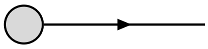

$= \bar{u}_s(p)$

$= \epsilon_\mu(p)$

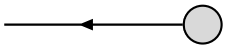

$= \bar{v}_s(p)$

$= \epsilon^*_\mu(p)$

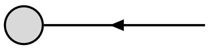

$= v_s(p)$ (A.23)

Completeness relations

- **Polarisation sum massless vector boson**

$$\sum_{\lambda=\pm 1} \epsilon^{\mu}_{\lambda}(p)\epsilon^{\nu *}_{\lambda}(p) = -g^{\mu\nu} + \frac{p^{\mu}n^{\nu} + p^{\nu}n^{\mu}}{p\cdot n} - \frac{n^2\, p^{\mu}p^{\nu}}{(p\cdot n)^2} \tag{A.24}$$

  in the axial gauge, where n is an auxiliary vector such that $p\cdot n \neq 0$

- **Polarisation sum massive vector boson**

$$\sum_{\lambda=-1,0,1} \epsilon^{\mu}_{\lambda}(p)\epsilon^{\nu *}_{\lambda}(p) = -g^{\mu\nu} + \frac{p^{\mu}p^{\nu}}{p^2} \equiv \mathcal{Z}^{\mu\nu} \tag{A.25}$$

- **Spin sum Dirac spinors**

$$\sum_{s=\pm 1/2} u_s(p)\bar{u}_s(p) = \not{p} + m \tag{A.26}$$

$$\sum_{s=\pm 1/2} v_s(p)\bar{v}_s(p) = \not{p} - m \tag{A.27}$$

Identities Dirac matrices

$$\{\gamma^{\mu},\gamma^{\nu}\} = 2g^{\mu\nu} I \tag{A.28}$$

$$\gamma^5 \equiv i\gamma^0\gamma^1\gamma^2\gamma^3 \tag{A.29}$$

$$(\gamma^{\mu})^{\dagger} = \gamma^0\gamma^{\mu}\gamma^0 \tag{A.30}$$

$$\gamma^{\mu}\gamma_{\mu} = 4I \tag{A.31}$$

$$\gamma^{\mu}\gamma^{\nu}\gamma_{\mu} = -2\gamma^{\nu} \tag{A.32}$$

$$\gamma^{\mu}\gamma^{\nu}\gamma^{\rho}\gamma_{\mu} = 4g^{\nu\rho} I \tag{A.33}$$

$$\gamma^{\mu}\gamma^{\nu}\gamma^{\rho}\gamma^{\sigma}\gamma_{\mu} = -2\gamma^{\sigma}\gamma^{\rho}\gamma^{\nu} \tag{A.34}$$

$$\mathrm{Tr}(\gamma^{\mu}) = \mathrm{Tr}(\gamma^5) = 0 \tag{A.35}$$

trace of any product of an odd number of γ^{μ} is zero (A.36)

trace of γ^5 times a product of an odd number of γ^{μ} is zero (A.37)

$$\mathrm{Tr}(\gamma^{\mu}\gamma^{\nu}) = 2g^{\mu\nu} \tag{A.38}$$

$$\mathrm{Tr}(\gamma^{\mu}\gamma^{\nu}\gamma^{\rho}\gamma^{\sigma}) = 4(g^{\mu\nu}g^{\rho\sigma} - g^{\mu\rho}g^{\nu\sigma} + g^{\mu\sigma}g^{\nu\rho}) \tag{A.39}$$

$$\mathrm{Tr}(\gamma^{\mu}\gamma^{\nu}\gamma^{\rho}\gamma^{\sigma}\gamma^5) = -4i\epsilon^{\mu\nu\rho\sigma} \tag{A.40}$$

Note that Eq. A.28 and the Schouten identity, $g^{\mu[\nu}e^{\rho\sigma\alpha\beta]} = 0$, can be used to evaluate traces with an even larger number of Dirac matrices.

B

Polarised interactions

Using polarised initial state particles gives access to other azimuthal asymmetries and other TMDs than the one studied in this thesis. Besides, by a small adaptation in the calculation of the amplitudes, also the hard factors for polarised final state quarkonium can be calculated. In this appendix we show how these calculations are performed and what it gives in the case of single J/ψ electroproduction as an example, extending Sec. 3.4. Concerning the illustrative purpose here, final state smearing is neglected for this process.

Proton and electron polarisation

If the proton in the calculation is taken to be polarised it will carry a spin and this will introduce a new angle ϕ_S in the system as shown in Fig. B.1. This spin vector is defined in Eq. 2.10. We also consider a polarised electron beam for the interaction. In particular, the longitudinally polarised antisymmetric leptonic tensor is given by $L^{\mu\nu} = 2ie^2\epsilon^{\mu\nu l l'}$, while the unpolarised leptonic tensor presented in Eq. 3.73 is symmetric. Together with the gluon correlators for a longitudinally and transversely polarised proton that are parametrised in Eq. 2.26 and Eq. 2.27, respectively, additional contributions of the differential cross section are found [26, 178]

$$\frac{d\sigma(J/\psi)}{dx_B\, dy\, d^2\mathbf{q}_T} \equiv \sum_{\mathcal{P}_e,\mathcal{P}_p} d\sigma^{\mathcal{P}_e,\mathcal{P}_p}(\phi_T, \phi_S)\,, \tag{B.1}$$

where the superscripts denote the polarisation of the electron and the proton. The unpolarised cross section is of course the same as presented in Eq. 3.83, however here

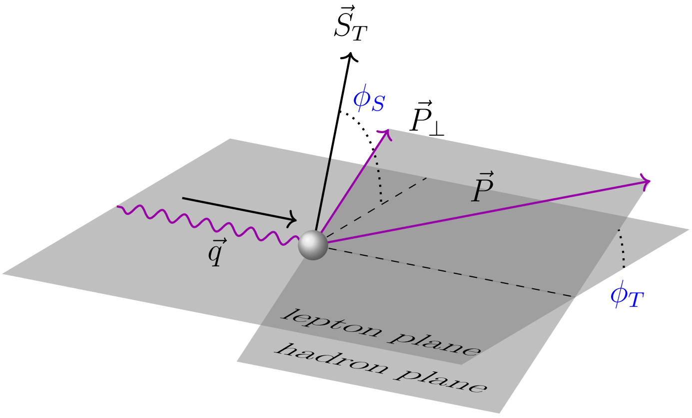

Figure B.1: Visualisation of the azimuthal angles ϕ_T and ϕ_S in quarkonium electroproduction with a polarised proton, similar to Fig. 3.4.

a different notation is adopted:

$$d\sigma^{UU} = \mathcal{N}\left[\mathrm{A}^U\, f_1^g(x,\mathbf{q}_T^2) + \frac{\mathbf{q}_T^2}{M_h^2}\,\mathrm{B}^U\, h_1^{\perp g}(x,\mathbf{q}_T^2)\cos 2\phi_T\right]. \tag{B.2}$$

The other contributions are found to be:

$$\begin{aligned} d\sigma^{UT} &= \mathcal{N}\,|\mathbf{S}_T|\,\frac{|\mathbf{q}_T|}{M_h}\Bigg[\mathrm{A}^T\, f_{1T}^{\perp g}(x,\mathbf{q}_T^2)\sin\left(\phi_S-\phi_T\right) \\ &\quad + \mathrm{B}^T\left\{h_1^g(x,\mathbf{q}_T^2)\sin\left(\phi_S+\phi_T\right) - \frac{\mathbf{q}_T^2}{2M_h}h_{1T}^{\perp g}(x,\mathbf{q}_T^2)\sin\left(\phi_S-3\phi_T\right)\right\}\Bigg], \qquad \text{(B.3)} \\ d\sigma^{UL} &= \mathcal{N}\,S_L\,\frac{\mathbf{q}_T^2}{M_h^2}\,\mathrm{B}^L\,h_{1L}^{\perp g}(x,\mathbf{q}_T^2)\sin 2\phi_T\,, \qquad \text{(B.4)} \\ d\sigma^{LU} &= 0\,, \qquad \text{(B.5)} \\ d\sigma^{LT} &= 0\,, \qquad \text{(B.6)} \\ d\sigma^{LL} &= \mathcal{N}\,S_L\,\mathrm{C}^L\,g_{1L}^g(x,\mathbf{q}_T^2)\,. \qquad \text{(B.7)} \end{aligned}$$

The normalisation factor is given by

$$\mathcal{N} = (2\pi)^2\frac{\alpha^2\alpha_s e_c^2}{yQ^2M_{\mathcal{Q}}(M_{\mathcal{Q}}^2+Q^2)}\,, \tag{B.8}$$

and the factors are

$$\begin{aligned} \mathrm{A}^U &= \mathrm{A}^T = \left[(1-y)^2+1\right]\mathcal{A}_1^{\gamma^* g\to J/\psi} - y^2\,\mathcal{A}_2^{\gamma^* g\to J/\psi}\,, \qquad \text{(B.9)} \\ \mathrm{B}^U &= \mathrm{B}^T = \mathrm{B}^L = (1-y)\,\mathcal{B}^{\gamma^* g\to J/\psi}\,, \qquad \text{(B.10)} \\ \mathrm{C}^L &= \left[(1-y)^2-1\right]\mathcal{C}^{\gamma^* g\to J/\psi}\,, \qquad \text{(B.11)} \end{aligned}$$

where:

$$\begin{aligned} \mathcal{A}_1^{\gamma^* g\to J/\psi} &= \langle\mathcal{O}^{J/\psi}[{}^1S_0^8]\rangle + \frac{1}{3}\frac{4}{M_{\mathcal{Q}}^2(M_{\mathcal{Q}}^2+Q^2)^2}\Big[(3M_{\mathcal{Q}}^2+Q^2)^2\langle\mathcal{O}^{J/\psi}[{}^3P_0^8]\rangle \\ &\quad + 2Q^2(2M_{\mathcal{Q}}^2+Q^2)\langle\mathcal{O}^{J/\psi}[{}^3P_1^8]\rangle \end{aligned}$$

$$+ \frac{2}{5}(6M_\mathcal{Q}^4 + 6M_\mathcal{Q}^2 Q^2 + Q^4)\langle \mathcal{O}^{J/\psi}[^3P_2^8]\rangle \Bigg] , \tag{B.12}$$

$$\mathcal{A}_2^{\gamma^* g\to J/\psi} = \frac{16}{3}\frac{Q^2}{(M_\mathcal{Q}^2+Q^2)^2}\left[\langle \mathcal{O}^{J/\psi}[^3P_1^8]\rangle + \frac{3}{5}\langle \mathcal{O}^{J/\psi}[^3P_2^8]\rangle\right] , \tag{B.13}$$

$$\begin{aligned}\mathcal{B}^{\gamma^* g\to J/\psi} &= -\langle \mathcal{O}^{J/\psi}[^1S_0^8]\rangle + \frac{1}{3}\frac{4}{M_\mathcal{Q}^2(M_\mathcal{Q}^2+Q^2)^2}\Bigg[(3M_\mathcal{Q}^2+Q^2)^2\langle \mathcal{O}^{J/\psi}[^3P_0^8]\rangle \\ &\quad - 2Q^4\langle \mathcal{O}^{J/\psi}[^3P_1^8]\rangle + \frac{2}{5}Q^4\langle \mathcal{O}^{J/\psi}[^3P_2^8]\rangle\Bigg] , \end{aligned} \tag{B.14}$$

$$\begin{aligned}\mathcal{C}^{\gamma^* g\to J/\psi} &= \langle \mathcal{O}^{J/\psi}[^1S_0^8]\rangle + \frac{1}{3}\frac{4}{M_\mathcal{Q}^2(M_\mathcal{Q}^2+Q^2)^2}\Bigg[(3M_\mathcal{Q}^2+Q^2)^2\langle \mathcal{O}^{J/\psi}[^3P_0^8]\rangle \\ &\quad + 2Q^4\langle \mathcal{O}^{J/\psi}[^3P_1^8]\rangle + \frac{2}{5}(-6M_\mathcal{Q}^4+Q^4)\langle \mathcal{O}^{J/\psi}[^3P_2^8]\rangle\Bigg] . \end{aligned} \tag{B.15}$$

The explicit expressions for $\mathcal{A}$, $\mathcal{B}$ and $\mathcal{C}$ can be further simplified by the heavy-quark spin relations presented in Eq. 3.46:

$$\mathcal{A}_1^{\gamma^* g\to J/\psi} = \langle \mathcal{O}^{J/\psi}[^1S_0^8]\rangle + 4\frac{7M_\mathcal{Q}^2+3Q^2}{M_\mathcal{Q}^2(M_\mathcal{Q}^2+Q^2)}\langle \mathcal{O}^{J/\psi}[^3P_0^8]\rangle , \tag{B.16}$$

$$\mathcal{A}_2^{\gamma^* g\to J/\psi} = 32\frac{Q^2}{(M_\mathcal{Q}^2+Q^2)^2}\langle \mathcal{O}^{J/\psi}[^3P_0^8]\rangle , \tag{B.17}$$

$$\mathcal{B}^{\gamma^* g\to J/\psi} = -\langle \mathcal{O}^{J/\psi}[^1S_0^8]\rangle + 4\frac{3M_\mathcal{Q}^2-Q^2}{M_\mathcal{Q}^2(M_\mathcal{Q}^2+Q^2)}\langle \mathcal{O}^{J/\psi}[^3P_0^8]\rangle , \tag{B.18}$$

$$\mathcal{C}^{\gamma^* g\to J/\psi} = \langle \mathcal{O}^{J/\psi}[^1S_0^8]\rangle + 4\frac{3Q^2-M_\mathcal{Q}^2}{M_\mathcal{Q}^2(M_\mathcal{Q}^2+Q^2)}\langle \mathcal{O}^{J/\psi}[^3P_0^8]\rangle . \tag{B.19}$$

We note that each independent azimuthal modulation in the cross section probes a different gluon TMD. These modulations are the same for open heavy-quark pair production in electron-proton collisions after integration over the azimuthal angle $\phi_\perp$ [179]. Moreover, such angular structures along with the corresponding quark TMDs are found in SIDIS as well [180].

Additional azimuthal asymmetries

In order to single out the different azimuthal modulations of the differential cross section we define the following azimuthal moments

$$A^{W(\phi_T,\phi_S)} \equiv 2\frac{\int d\phi_T\, d\phi_S\, W(\phi_T,\phi_S)\, d\sigma(\phi_T,\phi_S)}{\int d\phi_T\, d\phi_S\, d\sigma^{U\mathcal{P}_p}(\phi_T,\phi_S)} , \tag{B.20}$$

where the denominator reads:

$$\int d\phi_T\, d\phi_S\, d\sigma^{U\mathcal{P}_p}(\phi_T,\phi_S) = \int d\phi_T\, d\phi_S\, \frac{d\sigma^{U\mathcal{P}_p}}{dx_B\, dy\, d^2\mathbf{q}_T} = (2\pi)^2\mathcal{N}\mathrm{A}^U\, f_1^g(x,\mathbf{q}_T^2) . \tag{B.21}$$

By taking $W = \cos 2\phi_T$ we obtain

$$\begin{aligned}\langle \cos 2\phi_T\rangle &= \frac{1}{2}A^{\cos 2\phi_T} \\ &= \frac{(1-y)\,\mathcal{B}^{\gamma^* g\to J/\psi}}{[(1-y)^2+1]\,\mathcal{A}_1^{\gamma^* g\to J/\psi} - y^2\,\mathcal{A}_2^{\gamma^* g\to J/\psi}}\frac{\mathbf{q}_T^2}{2M_h^2}\frac{h_1^{\perp g}(x,\mathbf{q}_T^2)}{f_1^g(x,\mathbf{q}_T^2)} , \end{aligned} \tag{B.22}$$

which is equivalent to Eq. 3.95. Assuming that $S_L = 1$ or $|\mathbf{S}_T| = 1$, the other moments can be written as:

$$A^{\sin(\phi_S-\phi_T)} = \frac{|\mathbf{q}_T|}{M_h}\,\frac{f_{1T}^{\perp g}(x,\mathbf{q}_T^2)}{f_1^g(x,\mathbf{q}_T^2)}\,, \tag{B.23}$$

$$A^{\sin(\phi_S+\phi_T)} = \frac{(1-y)\,\mathcal{B}^{\gamma^* g\to J/\psi}}{[(1-y)^2+1]\,\mathcal{A}_1^{\gamma^* g\to J/\psi} - y^2\,\mathcal{A}_2^{\gamma^* g\to J/\psi}}\,\frac{|\mathbf{q}_T|}{M_h}\,\frac{h_1^g(x,\mathbf{q}_T^2)}{f_1^g(x,\mathbf{q}_T^2)}\,, \tag{B.24}$$

$$A^{\sin(\phi_S-3\phi_T)} = -\frac{(1-y)\,\mathcal{B}^{\gamma^* g\to J/\psi}}{[(1-y)^2+1]\,\mathcal{A}_1^{\gamma^* g\to J/\psi} - y^2\,\mathcal{A}_2^{\gamma^* g\to J/\psi}}\,\frac{|\mathbf{q}_T|^3}{2M_h^3}\,\frac{h_{1T}^{\perp g}(x,\mathbf{q}_T^2)}{f_1^g(x,\mathbf{q}_T^2)}\,, \tag{B.25}$$

$$A^{\sin 2\phi_T} = \frac{(1-y)\,\mathcal{B}^{\gamma^* g\to J/\psi}}{[(1-y)^2+1]\,\mathcal{A}_1^{\gamma^* g\to J/\psi} - y^2\,\mathcal{A}_2^{\gamma^* g\to J/\psi}}\,\frac{\mathbf{q}_T^2}{M_h^2}\,\frac{h_{1L}^{\perp g}(x,\mathbf{q}_T^2)}{f_1^g(x,\mathbf{q}_T^2)}\,. \tag{B.26}$$

We note that only the unpolarised TMD f_1^g appears in the denominators by its definition, because the contributions related to the other TMDs are angular dependent and therefore vanish upon integration over ϕ_T and ϕ_S. The azimuthal moments in Eqs. B.22, B.24, B.25 and B.26 vanish in the limit $y \to 1$ when the virtual photon is longitudinally polarised. Moreover, we point out that a measurement of their ratios would directly probe the relative magnitude of the different gluon TMDs, without any dependence on the CO LDMEs

$$\frac{A^{\cos 2\phi_T}}{A^{\sin(\phi_S+\phi_T)}} = \frac{|\mathbf{q}_T|}{M_h}\,\frac{h_1^{\perp g}(x,\mathbf{q}_T^2)}{h_1^g(x,\mathbf{q}_T^2)}\,, \tag{B.27}$$

$$\frac{A^{\sin(\phi_S-3\phi_T)}}{A^{\cos 2\phi_T}} = -\frac{|\mathbf{q}_T|}{2M_h}\,\frac{h_{1T}^{\perp g}(x,\mathbf{q}_T^2)}{h_1^{\perp g}(x,\mathbf{q}_T^2)}\,, \tag{B.28}$$

$$\frac{A^{\sin(\phi_S-3\phi_T)}}{A^{\sin(\phi_S+\phi_T)}} = -\frac{\mathbf{q}_T^2}{2M_h^2}\,\frac{h_{1T}^{\perp g}(x,\mathbf{q}_T^2)}{h_1^g(x,\mathbf{q}_T^2)}\,, \tag{B.29}$$

$$\frac{A^{\sin 2\phi_T}}{A^{\cos 2\phi_T}} = \frac{h_{1L}^{\perp g}(x,\mathbf{q}_T^2)}{h_1^{\perp g}(x,\mathbf{q}_T^2)}\,, \tag{B.30}$$

where Eq. B.30 can be used to define two additional rations from Eqs. B.27 and B.28. In contrast, since the contribution to the g_{1L}^g TMD (like f_1^g) to the cross section is angle independent, it can only be isolated by defining another azimuthal moment:

$$A^{LL} \equiv \frac{\int d\phi_T\, d\sigma^{LL}}{\int d\phi_T\, d\sigma^{UU}} = \frac{[(1-y)^2-1]\,\mathcal{C}^{\gamma^* g\to J/\psi}}{[(1-y)^2+1]\,\mathcal{A}_1^{\gamma^* g\to J/\psi} - y^2\,\mathcal{A}_2^{\gamma^* g\to J/\psi}}\,\frac{g_{1L}^g(x,\mathbf{q}_T^2)}{f_1^g(x,\mathbf{q}_T^2)}\,. \tag{B.31}$$

Quarkonium polarisation

In this example the spin-1 quarkonium in the final state can be longitudinally or transversely polarised. If the bound $Q\bar{Q}$ pair is produced in a ${}^1S_0$ state, namely with $L = S = 0$, the final quarkonium will be unpolarised. Therefore, in a ${}^1S_0$ configuration each helicity state will contribute 1/3 to the differential cross section. This results in a relative multiplicative factor of 1/3 when the quarkonium is longitudinally polarised and a factor of 2/3 when transversely polarised. For the P-wave states, with $L = S = 1$, the method consisting of the projection of the hard-scattering amplitudes onto states of definite quantum numbers J and J_z is not useful when the final quarkonium is polarised. Instead, one can project the amplitudes onto states of definite L_z and $\lambda \equiv S_z$ in Eq. 3.36, square them and sum over L_z and λ. The results for the longitudinal and transversely polarised quarkonium are then obtained by using, respectively, the following relations for the λ polarisation vectors [181]

$$\epsilon_0^\mu(P)\epsilon_0^{\nu *}(P) = \frac{P^\mu P^\nu}{M_\mathcal{Q}^2} - \frac{P^\mu n^\nu + P^\nu n^\mu}{P\cdot n} + \frac{M_\mathcal{Q}^2\, n^\mu n^\nu}{(P\cdot n)^2}\,, \tag{B.32}$$

$$\sum_{\lambda=\pm 1} \epsilon_\lambda^\mu(P)\epsilon_\lambda^{\nu *}(P) = -g^{\mu\nu} + \frac{P^\mu n^\nu + P^\nu n^\mu}{P\cdot n} - \frac{M_\mathcal{Q}^2\, n^\mu n^\nu}{(P\cdot n)^2}\,, \tag{B.33}$$

where n is a vector which obeys $n^2 = 0$ and $P\cdot n \neq 0$. By summing these equations we obtain the usual completeness relation of a massive vector boson presented in Eq. A.25, and we note that Eq. B.33 is similar to Eq. A.24.

With respect to the previous calculations only the factors $\mathcal{A}$, $\mathcal{B}$ and $\mathcal{C}$ change, while naturally the sum of the differential cross sections for polarised quarkonium gives back the unpolarised quarkonium one. The explicit expressions for longitudinally polarised quarkonium are as follows

$$\mathcal{A}_1^{\gamma^* g\to J/\psi_L} = \frac{1}{3}\langle\mathcal{O}^{J/\psi}[{}^1S_0^8]\rangle + 4\frac{M_\mathcal{Q}^4 + 10M_\mathcal{Q}^2Q^2 + Q^4}{M_\mathcal{Q}^2(M_\mathcal{Q}^2+Q^2)^2}\langle\mathcal{O}^{J/\psi}[{}^3P_0^8]\rangle\,, \tag{B.34}$$

$$\mathcal{A}_2^{\gamma^* g\to J/\psi_L} = \mathcal{A}_2^{\gamma^* g\to J/\psi} = 32\frac{Q^2}{(M_\mathcal{Q}^2+Q^2)^2}\langle\mathcal{O}^{J/\psi}[{}^3P_0^8]\rangle\,, \tag{B.35}$$

$$\mathcal{B}^{\gamma^* g\to J/\psi_L} = -\frac{1}{3}\langle\mathcal{O}^{J/\psi}[{}^1S_0^8]\rangle + \frac{4}{M_\mathcal{Q}^2}\langle\mathcal{O}^{J/\psi}[{}^3P_0^8]\rangle\,, \tag{B.36}$$

$$\mathcal{C}^{\gamma^* g\to J/\psi_L} = \frac{1}{3}\langle\mathcal{O}^{J/\psi}[{}^1S_0^8]\rangle + \frac{4}{M_\mathcal{Q}^2}\langle\mathcal{O}^{J/\psi}[{}^3P_0^8]\rangle\,, \tag{B.37}$$

and for transversely polarised quarkonium given by:

$$\mathcal{A}_1^{\gamma^* g\to J/\psi_T} = \frac{2}{3}\langle\mathcal{O}^{J/\psi}[{}^1S_0^8]\rangle + 8\frac{3M_\mathcal{Q}^4 + Q^4}{M_\mathcal{Q}^2(M_\mathcal{Q}^2+Q^2)^2}\langle\mathcal{O}^{J/\psi}[{}^3P_0^8]\rangle\,, \tag{B.38}$$

$$\mathcal{A}_2^{\gamma^* g\to J/\psi_T} = 0\,, \tag{B.39}$$

$$\mathcal{B}^{\gamma^* g\to J/\psi_T} = -\frac{2}{3}\langle\mathcal{O}^{J/\psi}[{}^1S_0^8]\rangle + \frac{8}{M_\mathcal{Q}^2}\frac{M_\mathcal{Q}^2 - Q^2}{M_\mathcal{Q}^2 + Q^2}\langle 0|\mathcal{O}^{J/\psi}[{}^3P_0^8]\rangle\,, \tag{B.40}$$

$$\mathcal{C}^{\gamma^* g\to J/\psi_T} = \frac{2}{3}\,\langle\mathcal{O}^{J/\psi}[{}^1S_0^8]\rangle - \frac{8}{M_\mathcal{Q}^2}\frac{M_\mathcal{Q}^2 - Q^2}{M_\mathcal{Q}^2 + Q^2}\langle 0|\mathcal{O}^{J/\psi}[{}^3P_0^8]\rangle\,. \tag{B.41}$$

We note that for polarised quarkonium production it is possible to define azimuthal moments exactly as before, as well as their ratios. In particular, it turns out that such ratios of asymmetries depend neither on the LDMEs, nor on the polarisation state of the detected quarkonium.

C

The helicity formalism

The helicity formalism involves constructing each hard factor by contracting amplitudes with particular helicities of the incoming particles with their complex conjugates, in which their helicities can be different. In a collinear factorisation approach, polarised gluons are generated perturbatively, while in the framework of TMD factorisation polarised gluons are already present at tree level through the nonperturbative TMDs, e.g. $h_1^{\perp g}$ corresponds to an interference between +1 and -1 helicity gluon states that would be suppressed without TM dependence. This appendix demonstrates the construction of helicity amplitudes and helicity correlators from standard computations, and it is explained how the specific differential cross section of the subsequent example emerges from this formalism.

Gluon-induced unpolarised proton-proton collisions

In general, a proton-proton cross section can be written as follows:

$$d\sigma \propto \int d^2\mathbf{p}_{aT}\, d^2\mathbf{p}_{bT}\, \delta^2(\mathbf{p}_{aT} + \mathbf{p}_{bT} - \mathbf{q}_T)\, \Gamma_{\nu\sigma}(x_a, \mathbf{p}_{aT})\, \Gamma_{\mu\rho}(x_b, \mathbf{p}_{bT})\, \mathcal{M}^{\mu\nu}\, \mathcal{M}^{\rho\sigma *}\,. \tag{C.1}$$

To rewrite this expression in terms of helicity amplitudes and helicity correlators we insert gluon polarisation sums given in Eq. A.24, which become

$$\sum_{\lambda=\pm 1} \epsilon^{\mu}_{\lambda}(p)\epsilon^{\nu *}_{\lambda}(p) = -g^{\mu\nu}\,, \tag{C.2}$$

by virtue of the Ward identity:

$$p_\mu \mathcal{M}^\mu(p) = 0\,. \tag{C.3}$$

Therefore, we obtain for gluon-induced production

$$d\sigma \propto \int d^2\mathbf{p}_{aT}\, d^2\mathbf{p}_{bT}\, \delta^2(\mathbf{p}_{aT}+\mathbf{p}_{bT}-\mathbf{q}_T)\, \Gamma_{\lambda_1\bar{\lambda}_1}\,\Gamma_{\lambda_2\bar{\lambda}_2}\,\mathcal{M}^{\lambda_1\lambda_2}\,\mathcal{M}^{\bar{\lambda}_1\bar{\lambda}_2 *}\,, \tag{C.4}$$

where the helicity correlators are defined by

$$\Gamma_{\lambda_1\bar{\lambda}_1} = \Gamma_{\nu\sigma}\,\epsilon^{\nu *}_{\lambda_1}(p_a)\epsilon^{\sigma}_{\bar{\lambda}_1}(p_a)\,, \tag{C.5}$$

$$\Gamma_{\lambda_2\bar{\lambda}_2} = \Gamma_{\mu\rho}\,\epsilon^{\mu *}_{\lambda_2}(p_b)\epsilon^{\rho}_{\bar{\lambda}_2}(p_b)\,, \tag{C.6}$$

and the helicity amplitudes as:

$$\mathcal{M}^{\lambda_1\lambda_2} = \mathcal{M}^{\mu\nu}\,\epsilon^{\lambda_1}_{\nu}(p_a)\epsilon^{\lambda_2}_{\mu}(p_b)\,, \tag{C.7}$$

$$\mathcal{M}^{\bar{\lambda}_1\bar{\lambda}_2 *} = \mathcal{M}^{\rho\sigma *}\,\epsilon^{\bar{\lambda}_1 *}_{\sigma}(p_a)\epsilon^{\bar{\lambda}_2 *}_{\rho}(p_b)\,. \tag{C.8}$$

To calculate the helicity correlators we can use an explicit representation of the polarisation vectors in the lab frame (by adding a phase):

$$\epsilon^{\mu *}_{\lambda}(p_a) = \epsilon^{\mu}_{\lambda}(p_b) = (0,-\lambda,i,0)e^{-i\lambda(\phi+\phi_{\mathbf{q}_T})}/\sqrt{2}\,. \tag{C.9}$$

Contracting the polarisation vectors with the leading-twist gluon correlator for an unpolarised hadron in Eq. 2.25, the helicity correlators for an unpolarised hadron can be written as

$$\Gamma_{\lambda_1\bar{\lambda}_1}(x_a,\mathbf{p}_{aT}) = \frac{x}{2}\begin{cases} f_1^g(x_a,\mathbf{p}_{aT}^2) & ++,\,-- \\ w^*(\mathbf{p}_{aT})\,h_1^{\perp}(x_a,\mathbf{p}_{aT}^2) & +- \\ w(\mathbf{p}_{aT})\,h_1^{\perp}(x_a,\mathbf{p}_{aT}^2) & -+ \end{cases}\,, \tag{C.10}$$

and

$$\Gamma_{\lambda_2\bar{\lambda}_2}(x_b,\mathbf{p}_{bT}) = \frac{x}{2}\begin{cases} f_1^g(x_b,\mathbf{p}_{bT}^2) & ++,\,-- \\ w(\mathbf{p}_{bT})\,h_1^{\perp}(x_b,\mathbf{p}_{bT}^2) & +- \\ w^*(\mathbf{p}_{bT})\,h_1^{\perp}(x_b,\mathbf{p}_{bT}^2) & -+ \end{cases}\,, \tag{C.11}$$

where we have defined

$$w(\mathbf{p}_T) \equiv \frac{\mathbf{p}_T^2}{2M_h^2}e^{i2(\phi_{\mathbf{p}_T}-\phi_{\mathbf{q}_T}-\phi)}\,, \tag{C.12}$$

that includes an extra phase from the partonic gluon. We note that:

$$\Gamma_{\lambda_2\bar{\lambda}_2}(x_a,\mathbf{p}_{aT}) = \Gamma^*_{\lambda_2\bar{\lambda}_2}(x_b,\mathbf{p}_{bT})\,, \tag{C.13}$$

and that it is evident from the helicity correlator that f_1^g conserves the gluon helicity at the nonperturbative level, while the the distribution of linearly polarised gluons $h_1^{\perp g}$ flips it.

Taking the different helicity combinations into account the cross section can be split up with different hard factors:

$$\mathcal{F}_1 = \sum_{\lambda_1,\lambda_2}\mathcal{M}^{\lambda_1\lambda_2}\,\mathcal{M}^{\lambda_1\lambda_2 *}\,, \tag{C.14}$$

$$\mathcal{F}_2 = \sum_{\lambda_1,\lambda_2} \mathcal{M}^{\lambda_1\lambda_2}\,\mathcal{M}^{-\lambda_1-\lambda_2*}\,, \tag{C.15}$$

$$\mathcal{F}_3 = \sum_{\lambda_1,\lambda_2} \mathcal{M}^{\lambda_1\lambda_2}\,\mathcal{M}^{-\lambda_1\lambda_2*}\,, \tag{C.16}$$

$$\mathcal{F}_3' = \sum_{\lambda_1,\lambda_2} \mathcal{M}^{\lambda_1\lambda_2}\,\mathcal{M}^{\lambda_1-\lambda_2*}\,, \tag{C.17}$$

$$\mathcal{F}_4 = \sum_{\lambda_1,\lambda_2} \mathcal{M}^{\lambda_1-\lambda_2}\,\mathcal{M}^{-\lambda_1\lambda_2*}\,. \tag{C.18}$$

We note that $\mathcal{F}_2$ corresponds to a double helicity flip, where the two gluons within one amplitude possess identical helicities, while $\mathcal{F}_4$ corresponds to the double-flip scenario with initial state gluons having opposite helicities. From the general property of the helicity amplitudes

$$\mathcal{M}^{\lambda_1\lambda_2} = \mathcal{M}^{-\lambda_1-\lambda_2}\,, \tag{C.19}$$

which is a consequence of parity conservation, it follows that the imaginary parts of $\mathcal{F}_i$ are zero. Therefore, the differential cross section can be rewritten as

$$\begin{aligned} d\sigma \propto\ & \mathcal{F}_1\,\mathcal{C}[f_1^g f_1^g] \\ & + \mathcal{F}_2\,\mathcal{C}[\mathfrak{Re}\{w(\mathbf{p}_{aT})w^*(\mathbf{p}_{bT})\}h_1^{\perp g}h_1^{\perp g}] \\ & + \mathcal{F}_3\,\mathcal{C}[\mathfrak{Re}\{w(\mathbf{p}_{aT})\}h_1^{\perp g}f_1^g] + \mathcal{F}_3'\,\mathcal{C}[\mathfrak{Re}\{w(\mathbf{p}_{bT})\}f_1^g h_1^{\perp g}] \\ & + \mathcal{F}_4\,\mathcal{C}[\mathfrak{Re}\{w(\mathbf{p}_{aT})w(\mathbf{p}_{bT})\}h_1^{\perp g}h_1^{\perp g}]\,, \end{aligned} \tag{C.20}$$

where the TM weights in the convolutions containing two momenta are symmetric when the momenta are swapped. In particular, they can be rewritten as

$$\mathfrak{Re}\{w(\mathbf{p}_{aT})w(\mathbf{p}_{bT})^*\} = \frac{\mathbf{p}_{aT}^2\mathbf{p}_{bT}^2}{4M_h^4}\cos 2(\phi_{\mathbf{p}_{aT}} - \phi_{\mathbf{p}_{bT}}) = \frac{2(\mathbf{p}_{aT}\cdot\mathbf{p}_{bT})^2 - \mathbf{p}_{aT}^2\mathbf{p}_{bT}^2}{4M_h^4}\,, \tag{C.21}$$

$$\mathfrak{Re}\{w(\mathbf{p}_T)\} = \frac{\mathbf{p}_T^2}{2M_h^2}\cos 2(\phi_{\mathbf{p}_T} - \phi_{\mathbf{q}_T} - \phi) = \frac{2(\mathbf{p}_T\cdot\mathbf{q}_T)^2 - \mathbf{p}_T^2\mathbf{q}_T^2}{2M_h^2\mathbf{q}_T^2}\cos(2\phi)\,, \tag{C.22}$$

$$\begin{aligned} \mathfrak{Re}\{w(\mathbf{p}_{aT})w(\mathbf{p}_{bT})\} &= \frac{\mathbf{p}_{aT}^2\mathbf{p}_{bT}^2}{4M_h^4}\cos 2(\phi_{\mathbf{p}_{aT}} + \phi_{\mathbf{p}_{bT}} - 2\phi_{\mathbf{q}_T} - 2\phi) \\ &= \left[2\left(\frac{\mathbf{p}_{aT}\cdot\mathbf{p}_{bT}}{2M_h^2} - \frac{(\mathbf{p}_{aT}\cdot\mathbf{q}_T)(\mathbf{p}_{bT}\cdot\mathbf{q}_T)}{M_h^2\mathbf{q}_T^2}\right)^2 - \frac{\mathbf{p}_{aT}^2\mathbf{p}_{bT}^2}{4M_h^4}\right]\cos(4\phi)\,, \end{aligned} \tag{C.23}$$

such that the differential cross section can be written as Eq. 3.97 including the redefinition of the weights following Eqs. 3.62, 3.99 and 3.100, where ϕ is identified with the Collins-Soper angle. We note that $\mathcal{F}_3$ and $\mathcal{F}_3'$ have picked up a minus sign along this way.

The results in this appendix are valid for an arbitrary production induced by the interaction of two initial state partonic gluons. In particular, from symmetry consideration it follows that $\mathcal{F}_3 = \mathcal{F}_3' = \mathcal{F}_4 = 0$ for single quarkonium production in proton-proton collisions presented in Sec. 3.3, namely $\phi_T = 0$. The fact that $\mathcal{F}_2 = 0$ for single χ_{Q2} production as well, see Eq. 3.59, simply arises from the actual computation of the amplitude itself. The latter would instead require a four-unit helicity flip, which is heavily suppressed. Additionally, we note that the sign of $\mathcal{F}_2$ is dictated by the parity of the quarkonium (see Table 3.1), hence opposite for η_Q and χ_{Q0} as shown in Eqs. 3.57 and 3.58, respectively.

Moreover, one can easily alter the derivation above for electron-proton collisions, i.e. one of the two initial state helicities can just be identified as the helicity of the photon instead. The weight functions that accompany $\mathcal{F}_2$, $\mathcal{F}_4$ and e.g. $\mathcal{F}_3'$ are then zero, such that only $\mathcal{F}_1$ and $\mathcal{F}_3$ are of relevance. Indeed, the remaining structure of the general differential cross section in terms of helicity hard factors corresponds to the one of single quarkonium production in electron-proton collisions presented in Sec. 3.4.

D

Expanding the delta function

In order to obtain the differential cross section in the ITM region from the collinear computation in the HTM region, one can replace the momentum conserving Dirac delta function by its expansion in the small-q_T limit. In this appendix the derivation of this expansion is shown for the delta function that occurs in the process $e + p \to e' + J/\psi + X$, originally presented in [129]. It is important to note that here it is (naively) assumed that the differential cross section is a continuous function of its kinematic variables.

Rewriting the differential cross section

Consider the following integral

$$I = \int_0^1 d\hat{z}\, g(\hat{z}) \int_0^{\hat{x}_{\max}} d\hat{x}\, f(\hat{x})\, \delta\big(F(\hat{x},\hat{z})\big)\,, \tag{D.1}$$

which corresponds to the differential cross section of the process given in Eq. 5.39. Here f and g are two generic continuous test functions, and $F(\hat{x},\hat{z})$ is defined in Eq. 5.38. By introducing the variable

$$\hat{x}' \equiv \frac{\hat{x}}{\hat{x}_{\max}} \quad \text{with} \quad 0 \leq \hat{x}' \leq 1\,, \tag{D.2}$$

the integral becomes

$$I = \hat{x}_{\max} \int_0^1 d\hat{z}\, \hat{z}^2\, g(\hat{z}) \int_0^1 d\hat{x}'\, \hat{x}'\, f(\hat{x}')\, \delta\big(G(\hat{x}',\hat{z})\big)\,, \tag{D.3}$$

where:

$$G(\hat{x}', \hat{z}) = \frac{\mathbf{q}_T^2}{Q^2}\hat{x}'\hat{z}^2 + \frac{M_\mathcal{Q}^2}{Q^2}(1-\hat{z})(\hat{x}'-\hat{z}) - \hat{z}(1-\hat{z})(1-\hat{x}')\,. \tag{D.4}$$

Performing the integral over $\hat{x}'$ one obtains

$$I = \hat{x}_{\max}\int_0^1 d\hat{z}\frac{\tilde{g}(\hat{z})\,\tilde{f}(\hat{x}_0')}{(1-\hat{z})\big[1+M_\mathcal{Q}^2/(\hat{z}Q^2)+\mathbf{q}_T^2\hat{z}/\big(Q^2(1-\hat{z})\big)\big]}\left(1+\frac{M_\mathcal{Q}^2}{\hat{z}Q^2}\right), \tag{D.5}$$

with

$$\tilde{g}(\hat{z}) = \hat{z}\left(1+\frac{M_\mathcal{Q}^2}{\hat{z}Q^2}\right)^{-1} g(\hat{z})\,, \quad \tilde{f}(\hat{x}') = \hat{x}'\,f(\hat{x}')\,, \tag{D.6}$$

and

$$\hat{x}_0'(\hat{z}) = \left(1+\frac{M_\mathcal{Q}^2}{Q^2}\right)\left[1+\frac{M_\mathcal{Q}^2}{\hat{z}Q^2}+\frac{\mathbf{q}_T^2}{Q^2}\frac{\hat{z}}{1-\hat{z}}\right]^{-1}, \tag{D.7}$$

where it is used that the delta function can be rewritten as: $\delta\big(G(\hat{x}')\big) = \delta(\hat{x}'-\hat{x}_0')/|G'(\hat{x}_0')|$. By employing

$$\tilde{g}(\hat{z})\tilde{f}(\hat{x}_0') = \big(\tilde{g}(\hat{z})-\tilde{g}(1)\big)\,\tilde{f}(1) + \tilde{g}(1)\,\tilde{f}(1) + \tilde{g}(\hat{z})\,\big(\tilde{f}(\hat{x}_0')-\tilde{f}(1)\big)\,, \tag{D.8}$$

one can split the integral into three parts respectively:

$$I = \hat{x}_{\max}\,(I_1+I_2+I_3)\,. \tag{D.9}$$

The small-q_T limit

In the integral I_1 one can directly take the limit $q_T \to 0$

$$\begin{aligned} I_1 &= \int_0^1 d\hat{z}\,\frac{\tilde{g}(\hat{z})-\tilde{g}(1)}{1-\hat{z}}\,\tilde{f}(1) \\ &= \int_0^1 d\hat{z}\,\tilde{g}(\hat{z})\,\tilde{f}(1)\,\frac{1}{(1-\hat{z})_+} \\ &= \int_0^1 d\hat{z}\int_0^1 d\hat{x}'\,\tilde{g}(\hat{z})\,\tilde{f}(\hat{x}')\,\frac{1}{(1-\hat{z})_+}\,\delta(1-\hat{x}') \\ &= \int_0^1 d\hat{z}\int_0^1 d\hat{x}'\,g(\hat{z})\,f(\hat{x}')\left(1+\frac{M_\mathcal{Q}^2}{\hat{z}Q^2}\right)^{-1}\frac{\hat{z}}{(1-\hat{z})_+}\,\delta(1-\hat{x}') \\ &= \hat{x}_{\max}^{-1}\int_0^1 d\hat{z}\int_0^{\hat{x}_{\max}} d\hat{x}\,g(\hat{z})\,f(\hat{x})\left(1+\frac{M_\mathcal{Q}^2}{\hat{z}Q^2}\right)^{-1}\frac{\hat{z}}{(1-\hat{z})_+}\,\delta(1-\hat{x}/\hat{x}_{\max})\,, \end{aligned} \tag{D.10}$$

where in the second line the '+'-prescription is introduced; the integral of a sufficiently smooth distribution f is given by

$$\int_a^1 dx\frac{f(x)}{(1-x)_+} = \int_a^1 dx\,\frac{f(x)-f(1)}{1-x} - f(1)\ln\left(\frac{1}{1-a}\right), \tag{D.11}$$

and:

$$\frac{1}{(1-x)_+} = \frac{1}{1-x} \quad \text{for} \quad 0 \le x < 1\,. \tag{D.12}$$

The integral I_2 can be performed exactly. Subsequently, the leading terms are kept in the expansion:

$$\begin{aligned}
I_2 &= \tilde{g}(1) \int_0^1 d\hat{z}\, \frac{1}{(1-\hat{z})\big[1 + M_{\mathcal{Q}}^2/(\hat{z}Q^2) + \mathbf{q}_T^2 \hat{z}/\big(Q^2(1-\hat{z})\big)\big]} \left(1 + \frac{M_{\mathcal{Q}}^2}{\hat{z}Q^2}\right) \tilde{f}(1) \\
&= \tilde{g}(1)\, \tilde{f}(1) \ln\left(\frac{Q^2 + M_{\mathcal{Q}}^2}{\mathbf{q}_T^2}\right) + O\left(\frac{\mathbf{q}_T^2}{Q^2 + M_{\mathcal{Q}}^2}\right) \\
&= \int_0^1 d\hat{z} \int_0^1 d\hat{x}'\, \tilde{g}(\hat{z})\, \tilde{f}(\hat{x}') \ln\left(\frac{Q^2 + M_{\mathcal{Q}}^2}{\mathbf{q}_T^2}\right) \delta(1-\hat{x}')\, \delta(1-\hat{z}) \\
&= \int_0^1 d\hat{z} \int_0^1 d\hat{x}'\, g(\hat{z})\, f(\hat{x}') \left(1 + \frac{M_{\mathcal{Q}}^2}{Q^2}\right)^{-1} \ln\left(\frac{Q^2 + M_{\mathcal{Q}}^2}{\mathbf{q}_T^2}\right) \delta(1-\hat{x}')\, \delta(1-\hat{z}) \\
&= \int_0^1 d\hat{z} \int_0^{\hat{x}_{\max}} d\hat{x}\, g(\hat{z})\, f(\hat{x}) \ln\left(\frac{Q^2 + M_{\mathcal{Q}}^2}{\mathbf{q}_T^2}\right) \delta(1-\hat{x}/\hat{x}_{\max})\, \delta(1-\hat{z})\,.
\end{aligned} \tag{D.13}$$

Lastly, the integral I_3 needs to be evaluated:

$$\begin{aligned}
I_3 &= \int_0^1 d\hat{z}\, \tilde{g}(\hat{z})\, \frac{\tilde{f}(\hat{x}'_0) - \hat{f}(1)}{(1-\hat{z})\big[1 + M_{\mathcal{Q}}^2/(\hat{z}Q^2) + \mathbf{q}_T^2 \hat{z}/\big(Q^2(1-\hat{z})\big)\big]} \left(1 + \frac{M_{\mathcal{Q}}^2}{\hat{z}Q^2}\right) \\
&= \int_0^1 d\hat{z}\, g(\hat{z})\, \frac{\hat{z}}{(1-\hat{z})}\, \frac{\tilde{f}(\hat{x}'_0) - \hat{f}(1)}{\big[1 + M_{\mathcal{Q}}^2/(\hat{z}Q^2) + \mathbf{q}_T^2 \hat{z}/\big(Q^2(1-\hat{z})\big)\big]}\,.
\end{aligned} \tag{D.14}$$

Trading the integration variable $\hat{z}$ with $\hat{x}'$ by inverting the relation $\hat{x}' = \hat{x}'_0(\hat{z})$ gives two solutions:

$$\begin{aligned}
\hat{z}_- = \frac{M_{\mathcal{Q}}^2}{Q^2}\, \frac{\hat{x}'}{M_{\mathcal{Q}}^2/Q^2 + 1 - \hat{x}'} \Bigg[1 &+ \frac{\mathbf{q}_T^2}{Q^2} \frac{M_{\mathcal{Q}}^2}{Q^2} \left(1 + \frac{M_{\mathcal{Q}}^2}{Q^2}\right)^{-1} \\
&\times \frac{\hat{x}'^2}{(M_{\mathcal{Q}}^2/Q^2 + 1 - \hat{x}')(1-\hat{x}')} \Bigg] + O\left(\frac{\mathbf{q}_T^4}{(Q^2 + M_{\mathcal{Q}}^2)^2}\right),
\end{aligned} \tag{D.15}$$

$$\hat{z}_+ = 1 - \frac{\mathbf{q}_T^2}{Q^2} \left(1 + \frac{M_{\mathcal{Q}}^2}{Q^2}\right)^{-1} \frac{\hat{x}'}{1-\hat{x}'} + O\left(\frac{\mathbf{q}_T^4}{(Q^2 + M_{\mathcal{Q}}^2)^2}\right). \tag{D.16}$$

The first solution is not physical since momentum conservation implies that $q_T = 0$ when $\hat{z} = 1$ and $0 < \hat{x}' < 1$. Therefore, we take $\hat{z} = \hat{z}_+$, which is the only solution that survives the massless limit. Neglecting terms of order $\mathbf{q}_T^4/(Q^2 + M_{\mathcal{Q}}^2)^2$, one finds that $\hat{x}' \le 1 - \mathbf{q}_T^2/(Q^2 + M_{\mathcal{Q}}^2)$ since $\hat{z} \ge 0$. Moreover, it can be shown that

$$d\hat{z} = \frac{\mathbf{q}_T^2}{Q^2} \left(1 + \frac{M_{\mathcal{Q}}^2}{Q^2}\right)^{-1} \frac{d\hat{x}}{(1-\hat{x}')^2}\,, \tag{D.17}$$

and:

$$\frac{\hat{z}}{(1-\hat{z})\big[1 + M_{\mathcal{Q}}^2/(\hat{z}Q^2) + \mathbf{q}_T^2 \hat{z}/\big(Q^2(1-\hat{z})\big)\big]} = \frac{Q^2}{\mathbf{q}_T^2}(1-\hat{x}')\,. \tag{D.18}$$

Substituting these equations into Eq. D.14 and tanking into account that $g(\hat{z}) \to g(1)$ as $q_T \to 0$ gives:

$$\begin{aligned} I_3 &= \left(1+\frac{M_Q^2}{Q^2}\right)^{-1} g(1) \int_0^1 d\hat{x}' \, \frac{\tilde{f}(\hat{x}')-\tilde{f}(1)}{1-\hat{x}'} \\ &= \left(1+\frac{M_Q^2}{Q^2}\right)^{-1} g(1) \int_0^1 d\hat{x}' \, \frac{\tilde{f}(\hat{x}')}{(1-\hat{x}')_+} \\ &= \int_0^1 d\hat{z}\, g(\hat{z}) \int_0^1 d\hat{x}' \, \tilde{f}(\hat{x}') \left(1+\frac{M_Q^2}{Q^2}\right)^{-1} \frac{\hat{x}'}{(1-\hat{x}')_+}\, \delta(1-\hat{z}) \\ &= \int_0^1 d\hat{z}\, g(\hat{z}) \int_0^{\hat{x}_{\max}} d\hat{x} \, \tilde{f}(\hat{x})\, \frac{\hat{x}/\hat{x}_{\max}}{(1-\hat{x}/\hat{x}_{\max})_+}\, \delta(1-\hat{z})\,. \end{aligned} \tag{D.19}$$

Combining the integrals, the integral in Eq. D.1 reads

$$\begin{aligned} I = \hat{x}_{\max} & \int_0^1 d\hat{z}\, g(\hat{z}) \int_0^{\hat{x}_{\max}} d\hat{x}\, f(\hat{x}) \\ & \times \left\{ \frac{\hat{x}/\hat{x}_{\max}}{(1-\hat{x}/\hat{x}_{\max})_+}\, \delta(1-\hat{z}) + \frac{Q^2+M_Q^2}{Q^2+M_Q^2/\hat{z}} \frac{\hat{z}}{(1-\hat{z})_+}\, \delta(1-\hat{x}/\hat{x}_{\max}) \right. \\ & \left. + \,\delta(1-\hat{x}/\hat{x}_{\max})\, \delta(1-\hat{z}) \ln\left(\frac{Q^2+M_Q^2}{\mathbf{q}_T^2}\right) \right\}, \end{aligned} \tag{D.20}$$

when $q_T^2 \ll Q^2 + M_Q^2$. Therefore, the final result becomes:

$$\begin{aligned} \delta\big(F(\hat{x},\hat{z})\big) = \hat{x}_{\max} & \left\{ \ln\left(\frac{Q^2+M_Q^2}{\mathbf{q}_T^2}\right) \delta(1-\hat{x}')\, \delta(1-\hat{z}) \right. \\ & \left. + \frac{\hat{x}'}{(1-\hat{x}')_+}\, \delta(1-\hat{z}) + \frac{Q^2+M_Q^2}{Q^2+M_Q^2/\hat{z}} \frac{\hat{z}}{(1-\hat{z})_+}\, \delta(1-\hat{x}') \right\}. \end{aligned} \tag{D.21}$$

In the limit $M_Q \to 0$ one recovers the relation

$$\begin{aligned} \delta\left(\frac{\mathbf{q}_T^2}{Q^2} - \frac{(1-\hat{x})(1-\hat{z})}{\hat{x}\hat{z}}\right) &= \frac{\hat{x}}{(1-\hat{x})_+}\, \delta(1-\hat{z}) + \frac{\hat{z}}{(1-\hat{z})_+}\, \delta(1-\hat{x}) \\ & \quad + \delta(1-\hat{x})\, \delta(1-\hat{z}) \ln\frac{Q^2}{\mathbf{q}_T^2}\,, \end{aligned} \tag{D.22}$$

in accordance with the one for SIDIS [139]. We note that in Eq. 5.39 the integration ranges do not start at zero, but from a minimal value. However, it follows from the definition in Eq. D.11 that one can just apply $f(x) \to \bar{f}(x) = f(x)\,\theta(x-a)$ in Eq. D.20, where θ denotes the Heaviside step function (even though $\bar{f}$ is not a smooth function). Therefore, the lower limits of the integration over the kinematical variables in the differential cross section do not affect the result of Eq. D.21.

E

Additional figures

In this appendix we present additional figures related to Sec. 6.3 obtained within the TMD-evolution formalism. Figs. E.1, E.2, E.3, and E.4 show examples of the convolutions $\mathcal{C}[f_1^g f_1^g]$, $\mathcal{C}[w_2 h_1^{\perp g} h_1^{\perp g}]$, $\mathcal{C}[w_3 f_1^g h_1^{\perp g}]$ and $\mathcal{C}[w_4 h_1^{\perp g} h_1^{\perp g}]$, respectively, as function of q_T for various scale variations. Using the full scale variation, we present in Fig. E.5 the relevant ratios of these convolutions. Furthermore, in Figs. E.6, E.7, E.8, and E.9, we show examples of modulations with separate scale variations.

In Fig. E.10, we present $\mathcal{C}[f_1^g f_1^g]$ at $q_T = 0\,\mathrm{GeV}$ as a function of μ_H, similarly for $\mathcal{C}[w_2 h_1^{\perp g} h_1^{\perp g}]$ in Fig. E.11. The other observables are zero at $q_T = 0\,\mathrm{GeV}$, therefore we show the normalised differential cross section as a function of μ_H at $q_{T,\max} = \mu_H/2$ in Fig. E.12. Finally, we display in Fig. E.13 examples of modulations as function of q_T at $q_{T,\max} = M_{J/\psi J/\psi}/2$ as well.

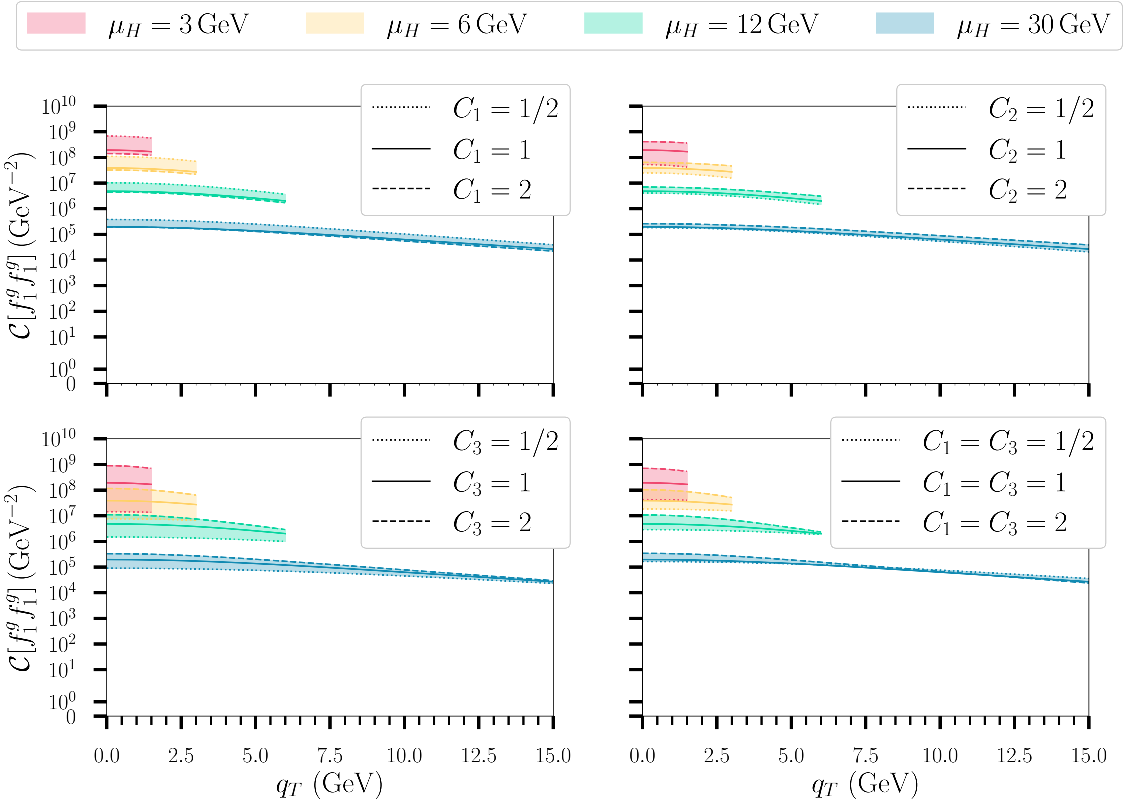

Figure E.1: $\mathcal{C}[f_1^g f_1^g]$ as a function of q_T for various μ_H, with $b_{T,\text{max}} = 1.0\,\text{GeV}^{-1}$, $y = 0$ and $\sqrt{s} = 13\,\text{TeV}$. Different perturbative uncertainties from scale variation are shown: from C_1 (upper left), from C_2 (upper right), from C_3 (down left) and from $C_1 = C_3$ (down right).

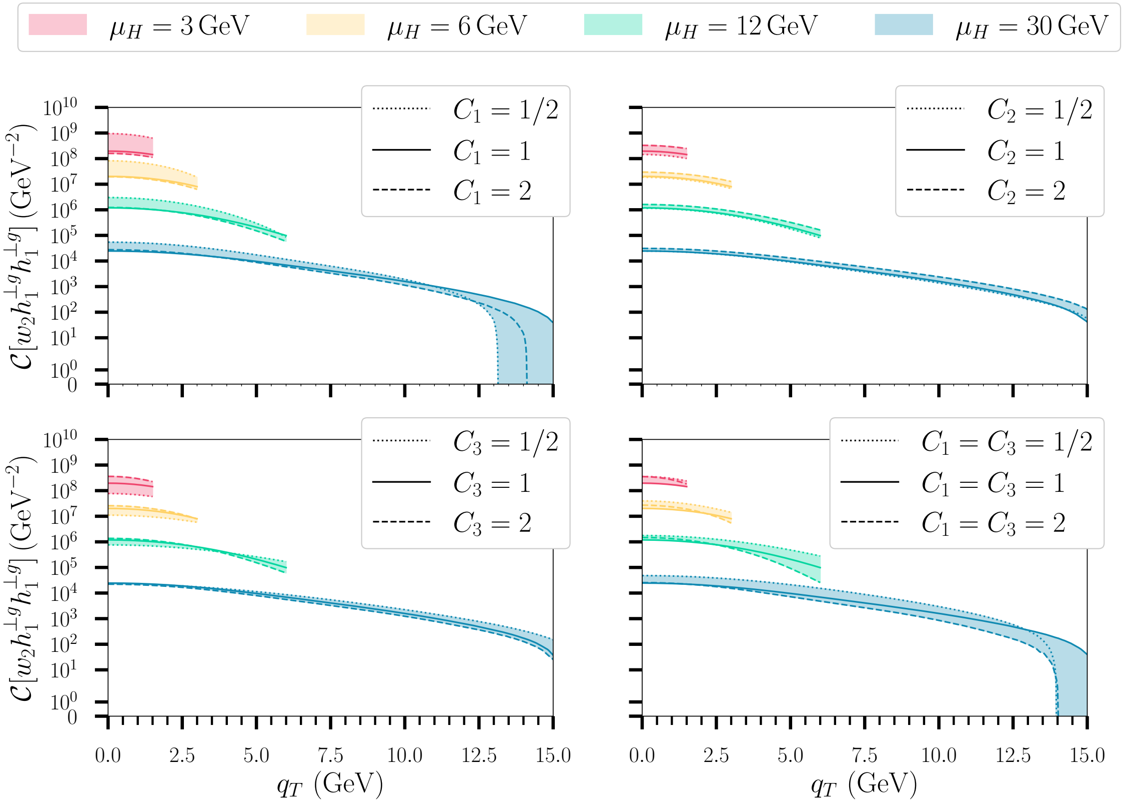

Figure E.2: The same analysis as in Fig. E.1 is presented here for $\mathcal{C}[w_2 h_1^{\perp g} h_1^{\perp g}]$.

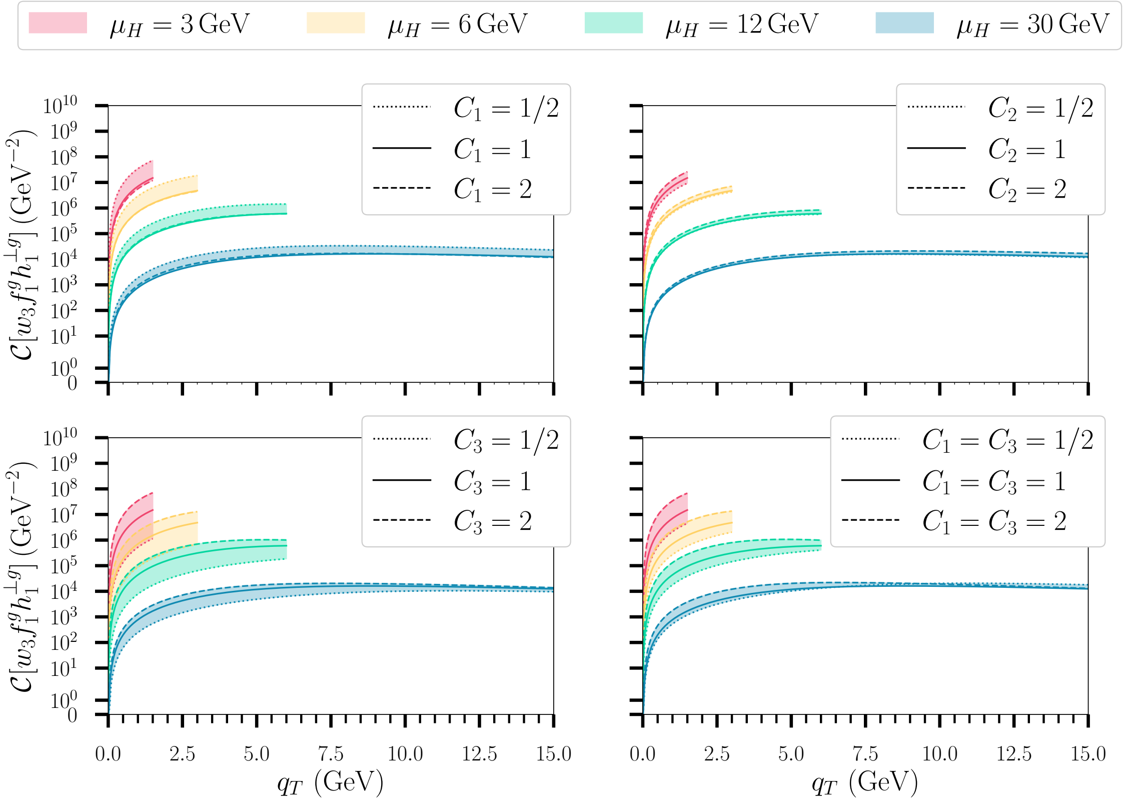

Figure E.3: The same analysis as in Fig. E.1 is presented here for $\mathcal{C}[w_3 f_1^g h_1^{\perp g}]$. We note that since $y = 0$ this figure is equivalent to the one for $\mathcal{C}[w_3' h_1^{\perp g} f_1^g]$.

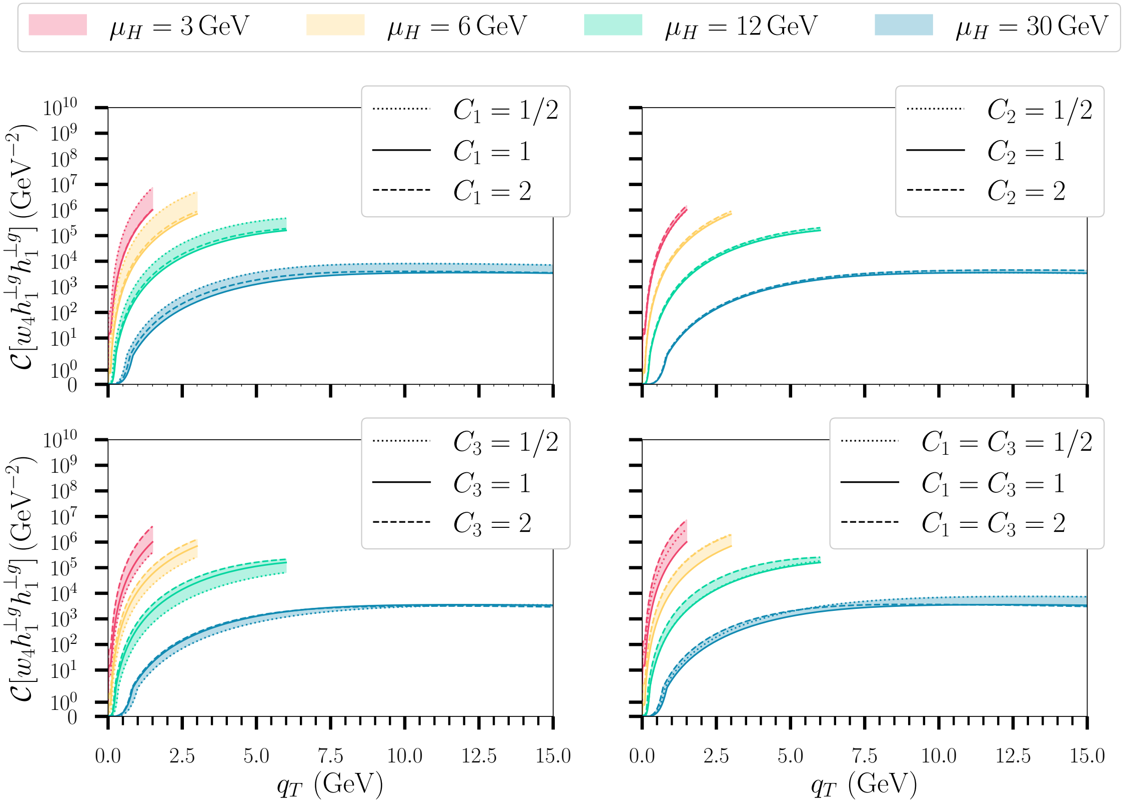

Figure E.4: The same analysis as in Fig. E.1 is presented here for $\mathcal{C}[w_4 h_1^{\perp g} h_1^{\perp g}]$. We note that at small q_T we observe small upward bumps appearing as kinks in this figure.

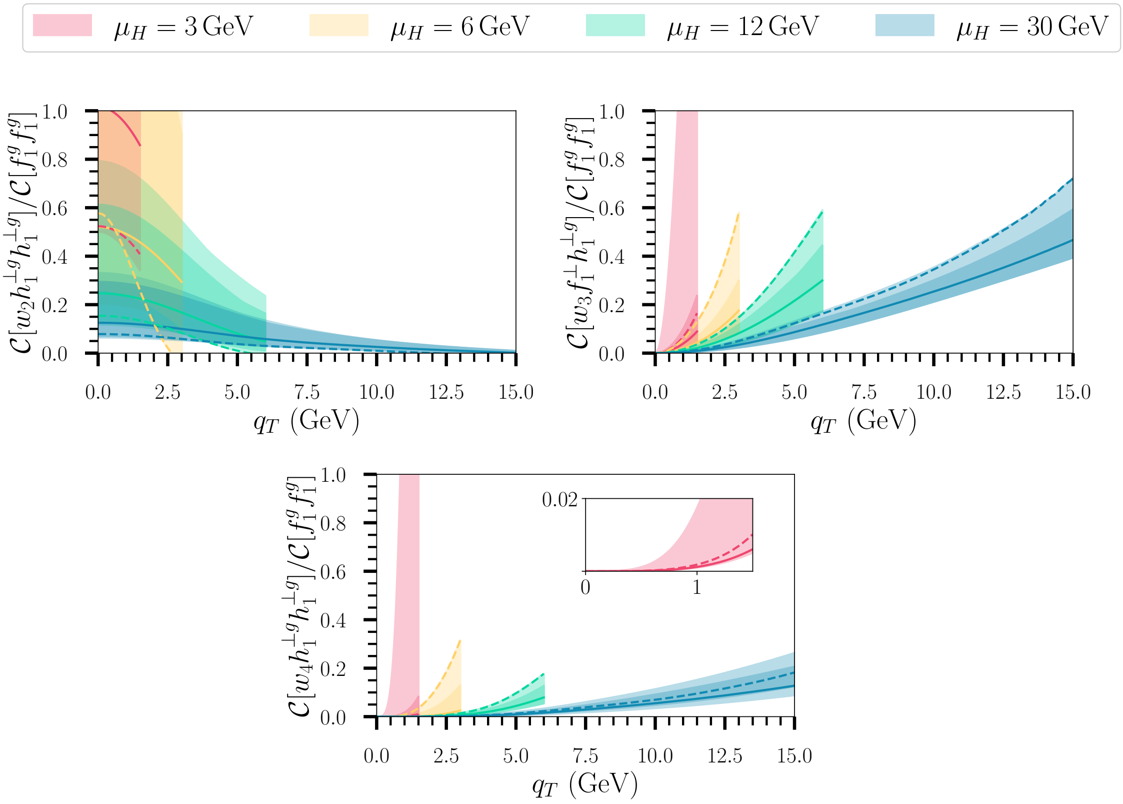

Figure E.5: Ratios of convolutions as a function of q_T for various μ_H, with $y = 0$ and $\sqrt{s} = 13\,\mathrm{TeV}$. The solid lines denote the central values, while the dashed lines show the specific scale variation that agrees best with the data from J/ψ-pair production. The uncertainties are found by employing scale variation: the light areas correspond to Case 1 scale variation, while the dark areas come from Case 2 scale variation.

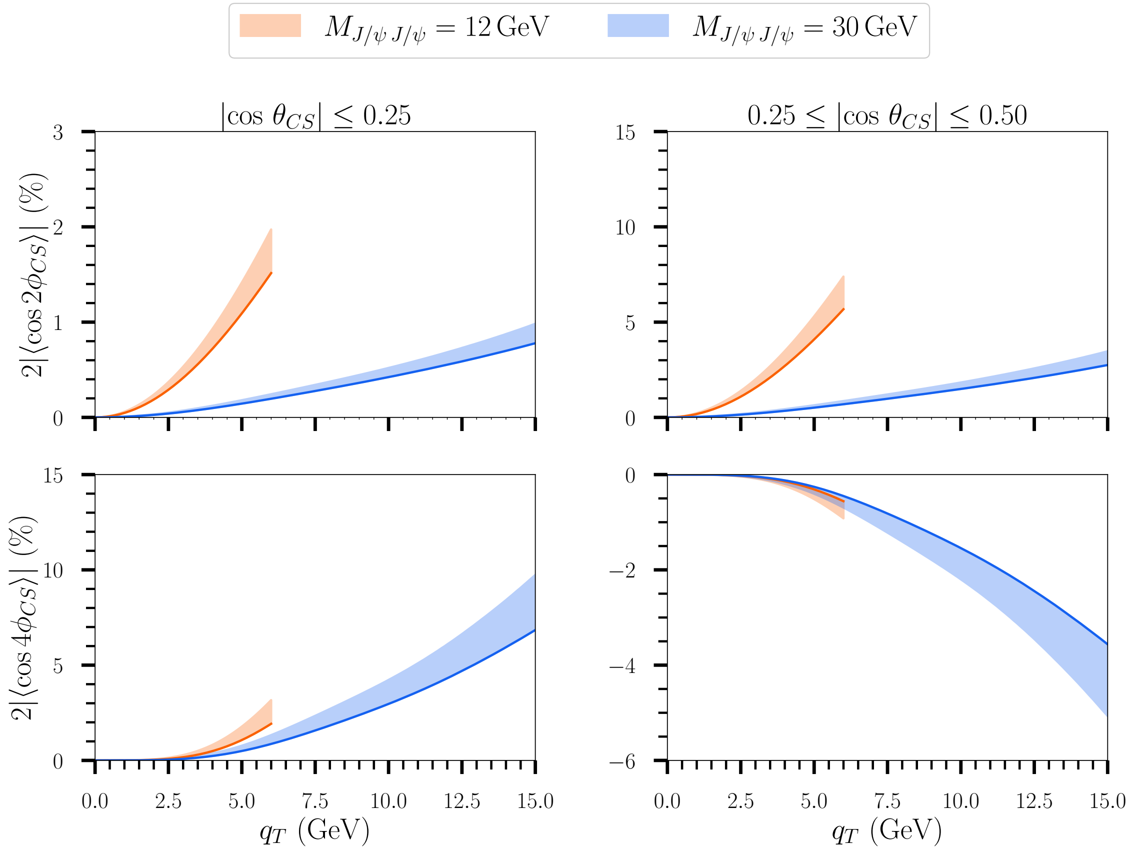

Figure E.6: The effect of C_1 scale variation on the $\cos(2\phi_{CS})$- and $\cos(4\phi_{CS})$-modulations in unpolarised J/ψ-pair hadroproduction as a function of q_T in two different θ_{CS}-bins, $|\cos\theta_{CS}| \leq 0.25$ (left column) and $0.25 \leq |\cos\theta_{CS}| \leq 0.25$ (right column), for two different values of $M_{J/\psi\, J/\psi}$ as an example, with $y = 0$ and $\sqrt{s} = 13\,\mathrm{TeV}$. The solid lines denote the central values of the predictions.

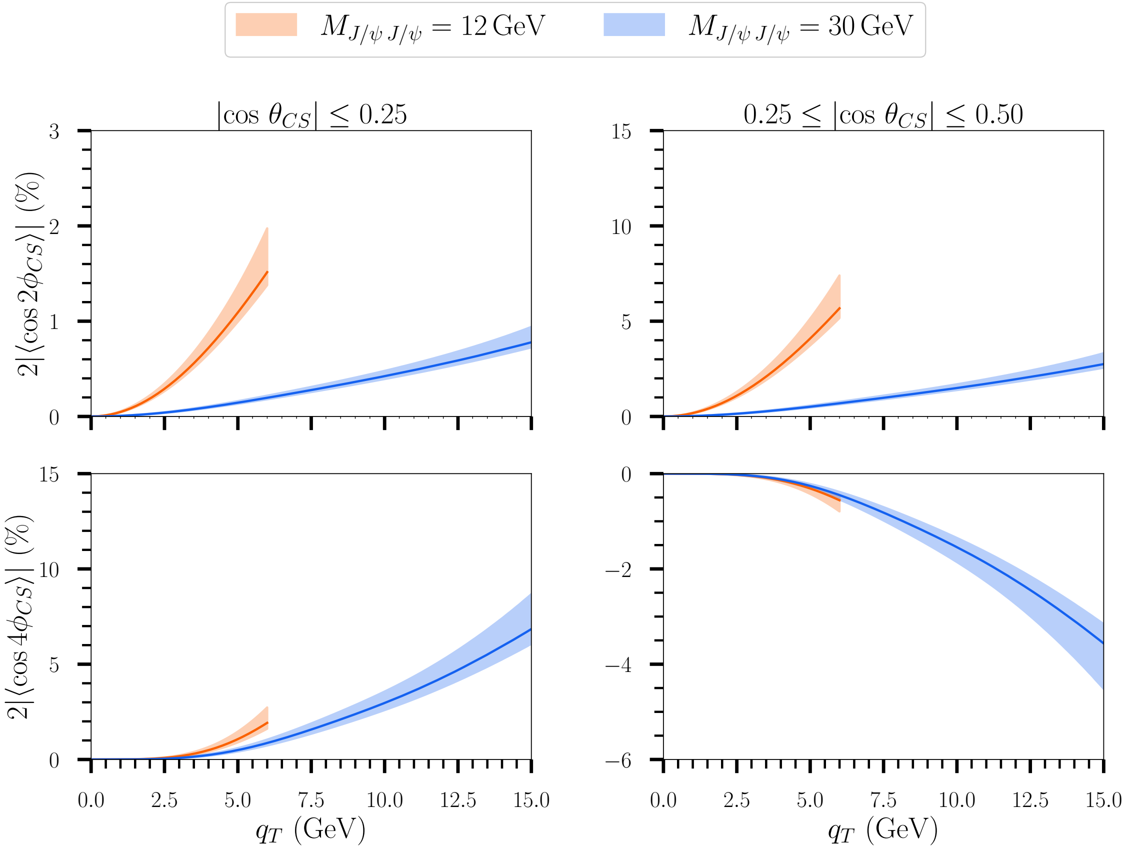

Figure E.7: The same analysis as in Fig. E.6 is presented here with C_2 scale variation.

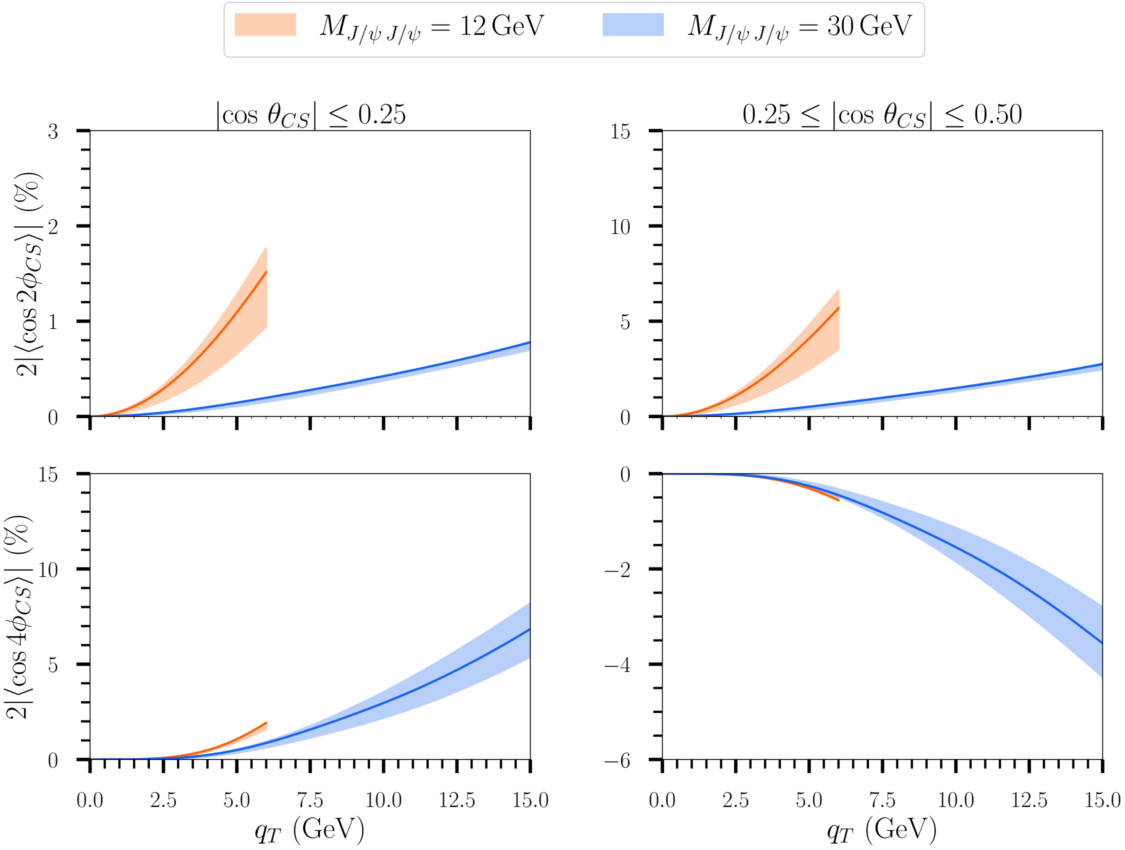

Figure E.8: The same analysis as in Fig. E.6 is presented here with C_3 scale variation.

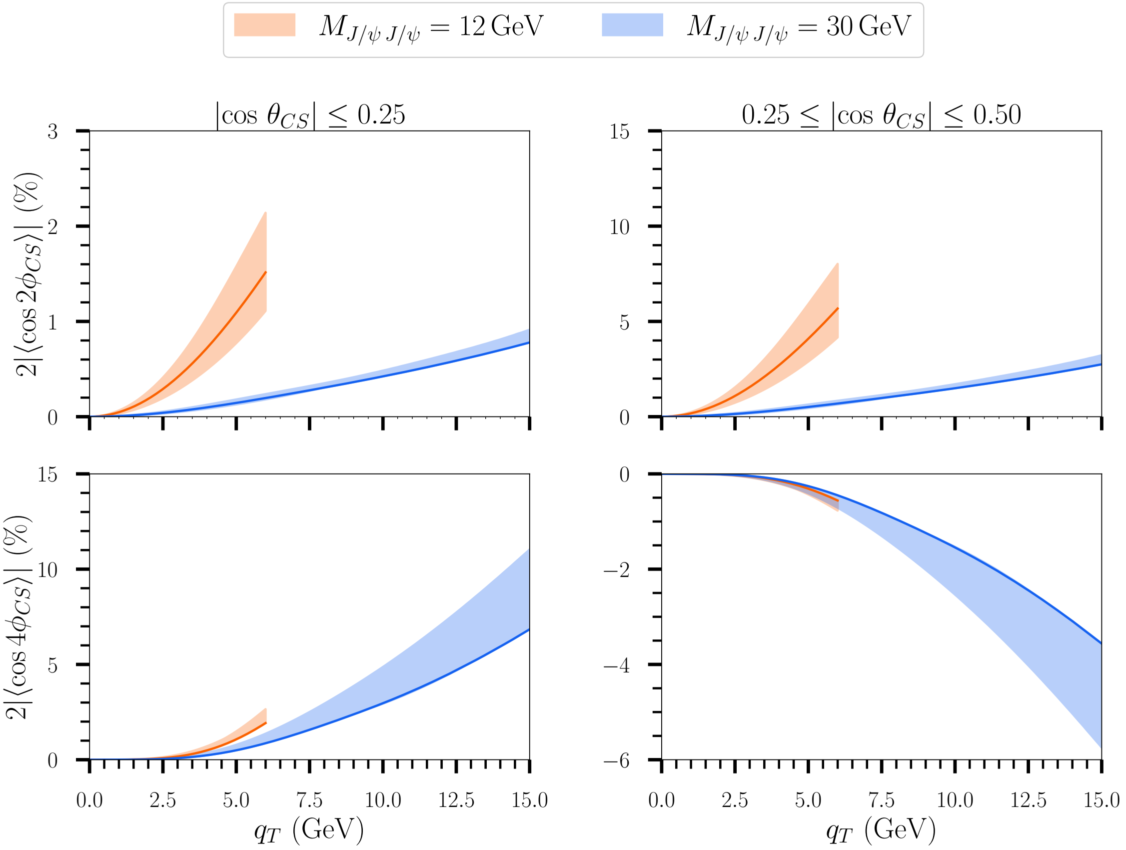

Figure E.9: The same analysis as in Fig. E.6 is presented here with $C_1 = C_2$ scale variation.

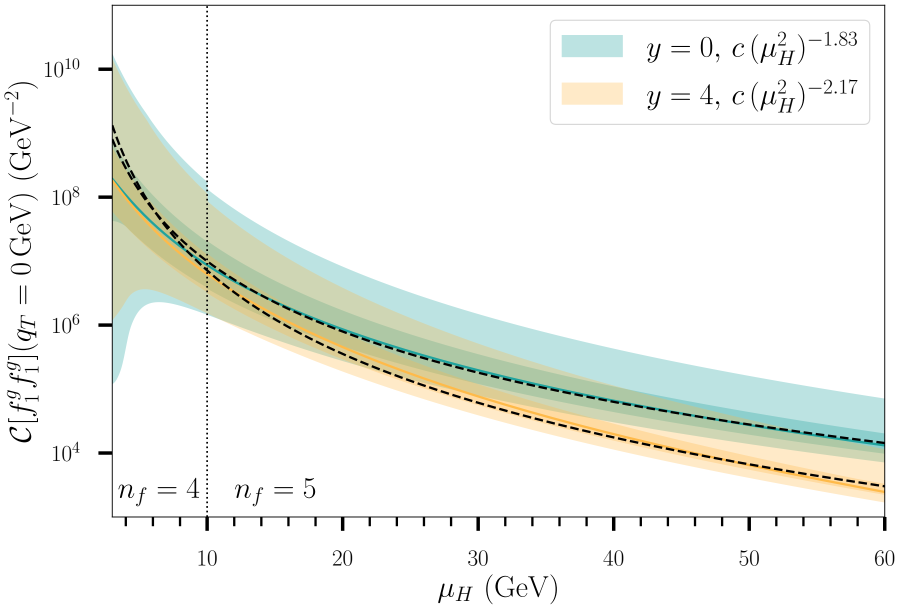

Figure E.10: $\mathcal{C}[f_1^g f_1^g]$ at $q_T = 0\,\mathrm{GeV}$ as a function of μ_H for $y = 0$ and $y = 4$ with $\sqrt{s} = 13\,\mathrm{TeV}$. The solid lines denote the central values of the predictions and the dashed lines show the best fits to the predictions. The uncertainties are found by employing scale variation: the light areas correspond to Case 1 scale variation, while the dark areas come from Case 2 scale variation.

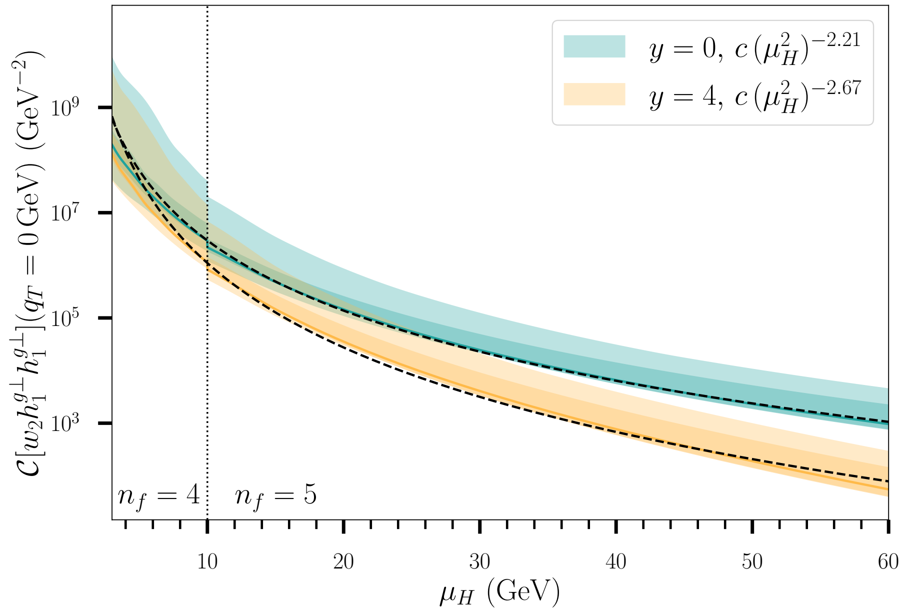

Figure E.11: The same analysis as in Fig. E.10 is presented here for $\mathcal{C}[w_2 h_1^{\perp g} h_1^{\perp g}]$.

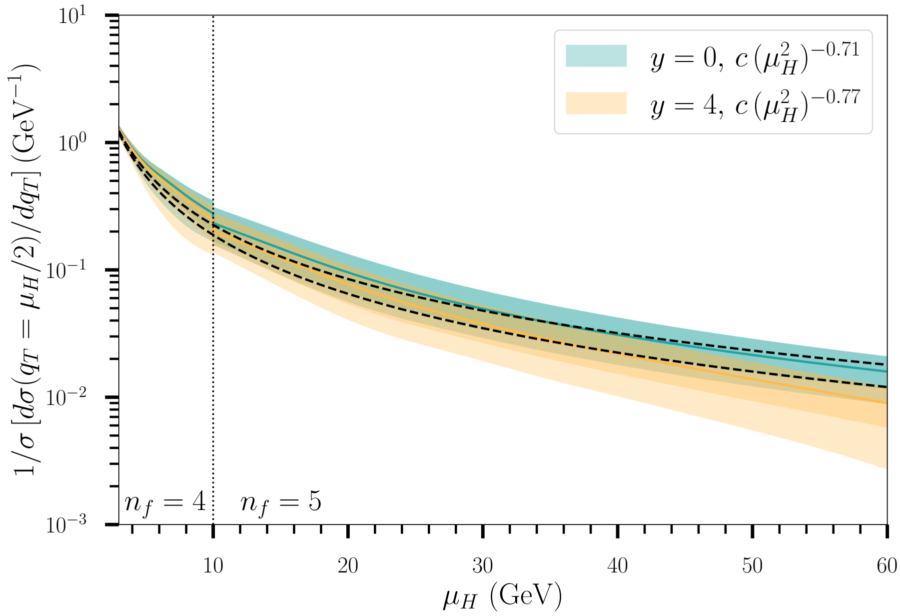

Figure E.12: The normalised differential cross section at $q_T = \mu_H/2$ as a function of μ_H for $y = 0$ and $y = 4$ with $\sqrt{s} = 13\,\mathrm{TeV}$, similar to Fig. E.10.

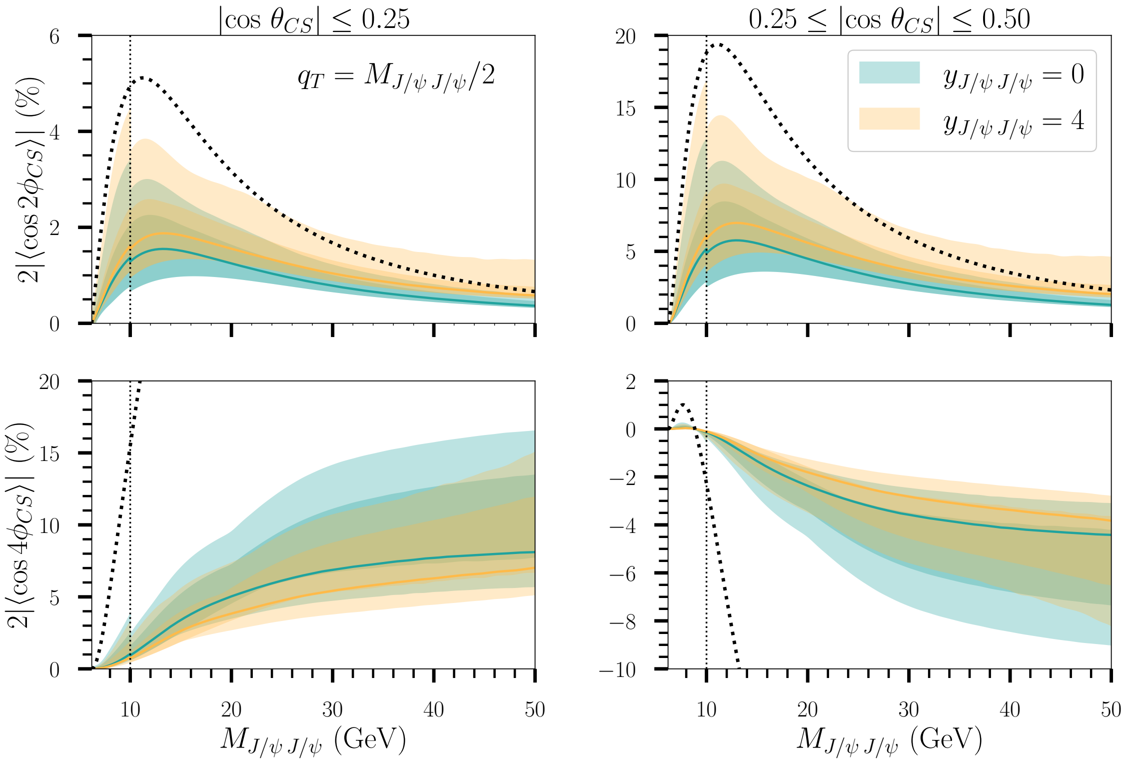

Figure E.13: The modulations at $q_T = M_{J/\psi\,J/\psi}/2$ as a function of $M_{J/\psi\,J/\psi}$ for $y = 0$ and $y = 4$ with $\sqrt{s} = 13\,\mathrm{TeV}$. The solid lines denote the central values of the predictions and their upper bounds are shown with dotted lines. The uncertainties are found by employing scale variation: the light areas correspond to Case 1 scale variation, while the dark areas come from Case 2 scale variation.

'Cause we're all just
Protons, neutrons, electrons
That rest on a Sunday
Work on a Monday

- The Cat Empire

Samenvatting

De operationele Large Hadron Collider (LHC) van de Europese Organisatie voor Kernonderzoek, ook bekend als CERN, voert experimenten uit met hoogenergetische botsingen tussen protonen- of zware-ionenbundels. De toekomstige Electron-Ion Collider (EIC), die gebouwd zal worden in het Brookhaven Nationaal Laboratorium (BNL), zal experimenten uitvoeren met hoogenergetische botsingen tussen elektronen en protonen- of zware-ionenbundels. Deze deeltjesversnellers bieden een unieke kans om de fundamentele bouwstenen van materie te onderzoeken. De vraag die ons interesseert is: hoe zijn deze bouwstenen binnen het proton verdeeld?

Ooit dachten we dat de twee kerndeeltjes, het positief geladen proton en het neutrale neutron, de fundamentele bouwstenen van alle materie waren. Inmiddels weten we echter dat deze deeltjes een complexe substructuur hebben. Het klassieke model van een proton beschrijft het als bestaande uit drie valentiequarks: twee up-quarks en één down-quark. Echter blijkt dat door de aanwezigheid van kortlevende quark-antiquarkparen alle zes soorten quarks, naast up en down, ook strange, charm, bottom en top in het proton kunnen voorkomen, waarbij de zwaarste paren het kortst verschijnen. Bovendien bevat het proton gluonen, de dragers van de sterke kernkracht, die niet alleen de quarks via hun kleurlading samenbinden, maar ook onderling interacties aangaan.

De sterke kernkracht wordt beschreven door de veldentheorie kwantumchromodynamica (QCD), die stelt dat er drie kleurladingen zijn (en drie antikleurladingen): rood, groen en blauw. Het is willekeurig welke kleurlading de quarks in een deeltje hebben, zolang ze samen maar kleurneutraal zijn. Bekende voorbeelden hiervan zijn baryonen, zoals protonen en neutronen, die bestaan uit drie valentiequarks met verschillende kleurladingen, en mesonen, die uit een valentie- quark en -antiquark bestaan met bijpassende kleurlading en antikleurlading. De kracht tussen de quarks verdwijnt niet wanneer ze ruimtelijk van elkaar gescheiden worden. Integendeel, de energie neemt toe naarmate ze verder uit elkaar worden getrokken, totdat uiteindelijk nieuwe deeltjes worden gevormd. Dit betekent dat quarks nooit alleen voorkomen, maar altijd sterk gebonden zijn door gluonen. Deze complexiteit maakt het moeilijk om de interne structuur van kerndeeltjes te doorgronden, en er is nog veel dat we niet weten. Wat we wel weten, is dat wanneer een kerndeeltje botst met een ander deeltje, dit kan leiden tot verstrooiing aan een parton van het kerndeeltje, waarbij een parton een quark of gluon is.

Voor dit soort botsingen kunnen we theoretische modellen ontwikkelen die we met experimenten kunnen vergelijken om zo meer inzicht te krijgen in de interne structuur van bijvoorbeeld het proton. Dit gebeurt door gebruik te maken van distributiefuncties, die de waarschijnlijkheid beschrijven dat een botsend deeltje verstrooit aan een specifiek parton in het proton. Door behoud van impuls kunnen we uit de botsingsreactie de longitudinale impulsfractie, de hoeveelheid impuls die een parton van het proton overneemt, bepalen en gebruiken als variabele van de distributiefunctie. Deze eendimensionale functies, genaamd parton-distributiefuncties (PDFs), zijn, waar het mogelijk is om theorie en experiment naast elkaar te leggen, al met grote precisie bekend. Zo weten we dat bij een grote longitudinale impulsfractie een deeltje voornamelijk verstrooit met een van de valentiequarks. Daarentegen, bij lagere longitudinale impulsfracties kunnen ook andere quarks deelnemen in de reactie, maar verstrooit het deeltje vrijwel zeker met een gluon.

Om een vollediger beeld van het proton te krijgen, kan ook de transversale impuls van het parton ten opzichte van de botsingsrichting worden meegenomen als variabele. Dit leidt tot driedimensionale functies, de zogenoemde transverse-momentum-dependent PDFs (TMDPDFs, of kortweg TMDs). Hoewel er al redelijk veel bekend is over quark-TMDs, is onze kennis van gluon-TMDs nog zeer beperkt. Het doel van dit promotieonderzoek is dan ook om meer inzicht te verkrijgen in de gluon-TMDs van het proton door processen te bestuderen die het mogelijk maken deze functies te extraheren. Specifiek richten we ons op de productie van quarkonium in proton-proton- en elektron-protonbotsingen, omdat quarkonium voornamelijk ontstaat uit gluonen.

Quarkonium is een meson, bestaande uit een gebonden toestand van een zware quark en een antiquark van dezelfde soort, waarbij het specifiek verwijst naar charmonium of bottomonium. In dit onderzoek richten we ons op processen die bestudeerd kunnen worden op verschillende hoge energieschalen, zodat we het TMD-evolutieformalisme dat we gebruiken ook kunnen onderzoeken. Dit doen we door voornamelijk te kijken naar J/ψ-paarproductie voor de LHC en J/ψ-productie voor de EIC. De J/ψ-meson is de laagstgelegen vector-toestand van charmonium en is daarnaast eenvoudig waar te nemen in experimenten.

Om distributiefuncties in een specifiek proces te bestuderen, is het noodzakelijk om het proces te kunnen ontbinden in factoren die (perturbatief) berekend of op een andere manier bepaald kunnen worden. Hiermee bedoelen we dat de werkzame doorsnede een convolutie is van de niet-perturbatieve distributiefunctie(s) en een perturbatieve berekening. De werkzame doorsnede vertegenwoordigt de kans voor het specifieke proces en kan worden gemeten in een experiment. De storingsrekening kan worden berekend op basis van de theorie, omdat de koppeling tussen quarks en gluonen bij hoogenergetisch processen klein is, dankzij de asymptotische vrijheid van QCD. Hoewel factorisatie niet specifiek is bewezen voor de processen die wij bestuderen, zijn er ook geen aanwijzingen dat dit niet is geldig is. Daarom gaan we ervan uit dat de processen in factoren kunnen worden ontbonden.

Volgens de definitie geeft de storingsrekening aan dat de eenvoudigste interactie tussen de deeltjes dominant is. Daarom worden in de bestudeerde reacties alleen een quark en een antiquark van dezelfde soort geproduceerd; andere deeltjes die ontstaan bij het opbreken van het proton worden niet gemeten en daarom niet meegenomen in de theoretische berekening. Vervolgens moeten de twee uitgaande quarks worden samengevoegd tot een J/ψ, waarvoor een andere niet-perturbatieve bijdrage vereist is. Dit doen we met behulp van de zogenaamde niet-perturbatieve lange-afstand matrixelementen (LDMEs), die voortkomen uit de theorie van niet-relativistische QCD.

Bij het bestuderen van de J/ψ-productie in elektron-protonbotsingen valt op dat de gebonden toestand van het quarkpaar aanvankelijk niet kleurneutraal is vanwege de kleurencombinatie die het gluon draagt. Om kleurneutraliteit te bereiken, moeten lage-energie gluonen worden uitgezonden. Deze emissie kan afhankelijk zijn van de transversale impuls, wat de introductie van een nieuwe functie, de vormfunctie, vereist in de berekening van de werkzame doorsnede. We hebben de leidende orde vormfunctie voor dit proces bij grote transversale impuls vastgesteld via een matching-berekening. Voor de TMD-beschrijving moet de transversale impuls van het quarkonium klein zijn ten opzichte van de hoge energieschaal, terwijl voor de bekende PDF-beschrijving deze groot moet zijn ten opzichte van de niet-perturbatieve QCD-schaal. In dit laatste geval moet een extra parton worden uitgezonden om de J/ψ een grote transversale impuls te geven. In het overlappingsgebied moeten de TMD- en PDF-beschrijvingen gelijk zijn, waarbij de vormfunctie in de PDF-beschrijving simpelweg de LDME is. De vormfunctie is dan nodig om de beschrijvingen in het overlappingsgebied exact op elkaar af te stemmen. Deze methode is toepasbaar op J/ψ-productie en andere vergelijkbare processen, mits, zoals wij hebben laten zien, singulariteiten in de gluon geïnitieerde PDF-beschrijving correct worden behandeld. We concludeerden verder dat de vormfunctie universeel is, maar wel met een proces-afhankelijke factor gepaard gaat. De verwachting is dat de vormfunctie ook een rol speelt bij direct kleurneutraal geproduceerde quarkonia wanneer hogere orde berekeningen worden uitgevoerd. Onze resultaten met betrekking tot de vormfunctie worden ondersteund door een alternatieve berekening in de zogenaamde eikonale benadering.

Om theoretisch numerieke voorspellingen te doen voor processen kunnen we parametrisaties gebruiken voor de TMDs, of TMD-evolutie toepassen, waarbij de TMDs gerelateerd zijn aan de bekende PDFs zoals in de bovenstaande matching-berekening. Met deze methode hebben we een studie uitgevoerd die de azimutale asymmetrie voorspelt, dat wil zeggen de hoek tussen het elektronvlak en het proton-J/ψ-vlak, wanneer het proton ongepolariseerd is. De asymmetrie die in dit proces optreedt, is evenredig aan de verhouding van twee gluon-TMDs: de lineair gepolariseerde gluon-TMD gedeeld door de ongepolariseerde gluon-TMD. Volgens onze berekeningen is deze asymmetrie, die toeneemt met de transversale impuls, meetbaar in het toekomstige EIC-experiment, zodat nieuwe inzichten kunnen worden verkregen in zowel de gluon-TMDs als de vormfunctie.

Daarnaast hebben we een studie uitgevoerd die zich richt op het deel van TMD-evolutie dat is geparametriseerd, namelijk de zogenaamde niet-perturbatieve Sudakov-factor. Hiervoor wordt vaak een Gaussische functie gebruikt, die echter bepaalde beperkingen heeft. We lossen dit op door de bekende (perturbatieve) functies te extrapoleren naar het niet-perturbatieve gebied en een duidelijke scheiding tussen deze gebieden aan te brengen. Hoewel onze niet-perturbatieve Sudakov-factor een innovatieve benadering biedt voor het verkennen van TMD-evolutie is het mogelijk niet de uiteindelijke oplossing. In bepaalde situaties vinden we namelijk obstakels; het blijft een procesafhankelijke factor die via experimentele gegevens moet worden gevalideerd.

Vervolgens hebben we onze nieuw ontwikkelde niet-perturbatieve Sudakov-factor gebruikt om voorspellingen te doen voor quarkoniumproductie in ongepolariseerde proton-protonbotsingen, evenals voor recent gemeten J/ψ-paarproductie in de LHC. We constateren een goede overeenstemming met de genormeerde werkzame doorsnede van dit proces. De grootste onzekerheid in onze voorspellingen komt voort uit schaalvariatie; dit betekent dat hogere orde correcties moeten worden meegenomen om de theoretische voorspellingen te verbeteren. We merken op dat de beste voorspellingen in overeenstemming met de data worden verkregen door een schaalvariatie die doorgaans niet wordt beschouwd in conventionele studies. Helaas is de experimentele data niet geschikt voor het vergelijken van de azimutale asymmetrie die we hebben berekend. Daarnaast hebben we ook andere voorspellingen gedaan voor de LHC, zowel voor Υ-paarproductie (de bottomonium-tegenhanger van de J/ψ) in hoogenergetische proton-protonbotsingen als voor J/ψ-paarproductie in een configuratie waarbij een van de protonen in rust is. Deze processen kunnen respectievelijk in de toekomst belangrijke inzichten verschaffen over de gluon-TMDs bij hogere energieschalen en grotere waarden van de longitudinale impulsfractie.

Tenslotte hebben we de eerste stap gezet richting een volledig transversaal impulsafhankelijk spectrum voor J/ψ-productie in de EIC. Hierbij passen we opnieuw onze nieuw ontwikkelde niet-perturbatieve Sudakov-factor toe, maar richten we ons uitsluitend op hoek-onafhankelijke bijdragen. Om dit spectrum te verkrijgen, moeten we de TMD-beschrijving en de PDF-beschrijving numeriek op elkaar afstemmen. Dit doen we met behulp van de inverse foutweegmethode, waarvan we aantonen dat deze goed functioneert nadat we het gewicht van de PDF-beschrijving hebben aangepast voor de vormfunctie. Voor de totale onzekerheid van de curves hebben we de perturbatieve onzekerheden van de schaalvariatie gecombineerd met de onzekerheden van de LDMEs en de matching-berekening. Bovendien hebben we de hoge energieschaalafhankelijkheid onderzocht van onze berekeningen, waarbij we hebben gevonden dat de TMD-beschrijving en de PDF-beschrijving aanzienlijke verschillen vertonen. Desalniettemin concluderen we dat ze netjes op elkaar kunnen worden aangesloten, aangezien de TMD-voorspellingen boven de PDF-voorspellingen liggen in het overlappingsgebied.

Résumé

Le Large Hadron Collider (LHC) de l'Organisation européenne pour la recherche nucléaire, aussi appelée CERN, en opération actuellement, réalise des expériences impliquant des collisions à haute énergie entre des faisceaux de protons ou d'ions lourds. Le futur Electron-Ion Collider (EIC), qui sera construit au Laboratoire National de Brookhaven (BNL), réalisera des expériences impliquant des collisions à haute énergie entre des électrons et des faisceaux de protons ou d'ions lourds. Ces accélérateurs de particules permettent d'étudier de manière unique les éléments fondamentaux de la matière. La question qui nous intéresse est la suivante : comment ces éléments se répartissent-ils dans le proton ?

Nous pensions autrefois que les deux nucléons, le proton chargé positivement et le neutron neutre, étaient les éléments fondamentaux de toute matière. Or, nous savons aujourd'hui que ces particules ont une sous-structure complexe. Le modèle classique du proton le décrit comme étant constitué de trois quarks de valence : deux quarks up et un quark down. Cependant, il s'avère qu'en raison de la présence de paires de quarks-antiquarks dont la durée de vie est courte, les six types de quarks, en plus des quarks up et down, peuvent également apparaître dans le proton sous les formes de strange, de charm, de bottom et de top, les paires les plus lourdes apparaissant d'autant plus brièvement. En outre, le proton contient des gluons, porteurs de la force nucléaire forte, qui non seulement lient les quarks entre eux par leur charge de couleur, mais interagissent également les uns avec les autres.

La force nucléaire forte est décrite par la chromodynamique quantique (QCD), qui est une théorie des champs qui stipule qu'il existe trois charges de couleur (et trois charges d'anti-couleur) : le rouge, le vert et le bleu. La charge de couleur des quarks d'une particule est arbitraire, pour autant qu'ils soient neutres ensemble. Des exemples bien connus sont les baryons, tels que les protons et les neutrons, qui sont constitués de trois quarks de valence avec des charges de couleur différentes, et les mésons, qui sont constitués d'un quark de valence et d'un antiquark avec une charge de couleur et une charge d'anti-couleur correspondantes. L'interaction entre les quarks ne diminue pas lorsque l'on les éloigne les uns des autres. Au contraire, l'énergie de liaison augmente au fur et à mesure que l'on les éloigne, jusqu'à ce que de nouvelles particules soient créées. Cela signifie que les quarks ne sont jamais isolés, mais qu'ils sont toujours fortement liés par des gluons. Cette complexité rend difficile la compréhension de la structure interne des nucléons, et beaucoup reste à découvrir. Ce que nous savons, c'est que lorsqu'un nucléon entre en collision avec une autre particule, cela peut entraîner une diffusion au niveau d'un parton, à savoir un quark ou un gluon du nucléon.

Pour ces collisions, nous pouvons développer des modèles théoriques que nous pouvons comparer aux expériences pour mieux comprendre la structure interne du proton, par exemple. Pour ce faire, nous utilisons des fonctions de distribution qui

décrivent la probabilité qu'une particule impliquée dans une collision se diffuse sur un parton spécifique du proton. Grâce à la conservation de la quantité de mouvement, nous pouvons déterminer, à partir de la réaction de collision, la fraction de quantité de mouvement longitudinale, c'est-à-dire la quantité de mouvement qu'un parton prend au proton, et l'utiliser comme variable de la fonction de distribution. Ces fonctions unidimensionnelles, appelées fonctions de distribution des partons (PDFs), sont déjà connues avec une grande précision grâce à des mesures expérimentales précises. Par exemple, nous savons que pour une fraction de l'impulsion longitudinale importante, une particule se diffuse principalement sur l'un des quarks de valence. En revanche, à des fractions d'impulsion longitudinale plus faibles, d'autres quarks peuvent également participer à la réaction, mais la particule se diffuse presque à coup sûr sur un gluon.

Pour obtenir une image plus complète du proton, l'impulsion transversale du parton par rapport à la direction de la collision peut également être incluse comme variable. Cela conduit à introduire des fonctions tridimensionnelles appelées transverse-momentum-dependent PDFs (TMDPDFs, ou TMDs en abrégé). Alors que l'on connaît déjà certaines caractéristiques des TMDs de quarks, notre connaissance des TMDs de gluons est toujours très limitée. Le but de cette thèse est donc d'améliorer notre compréhension des TMDs de gluons dans le proton en étudiant les processus qui permettent l'extraction de ces fonctions. Plus précisément, nous nous concentrons sur la production de quarkonia dans les collisions proton-proton et électron-proton, car le quarkonium est principalement généré à partir de gluons.

Le quarkonium est un méson qui est un état lié d'un quark et d'un antiquark lourds de la même espèce, se référant spécifiquement au charmonium ou au bottomonium. Dans cette thèse, nous nous concentrons sur les processus qui peuvent être étudiés à différentes échelles d'énergie, afin que nous puissions également étudier le formalisme d'évolution TMD que nous utilisons. Pour ce faire, nous nous intéressons principalement à la production de paires J/ψ pour le LHC et à la production de J/ψ pour l'EIC. Le méson J/ψ est l'état vectoriel le plus stable de la famille des charmonia et il est également le plus facile à observer dans les expériences.

Pour étudier les fonctions de distribution dans un processus spécifique, il est nécessaire de pouvoir décomposer le processus en facteurs qui peuvent être calculés (de manière perturbative) ou déterminés d'une autre manière. Nous entendons par là que la section efficace est une convolution des fonction(s) de distribution non perturbatives et d'un calcul perturbatif. La section efficace représente la probabilité du processus spécifique et peut être mesurée lors d'une expérience. Le calcul perturbatif peut être effectué à partir de la théorie, car le couplage entre les quarks et les gluons dans les processus à haute énergie est faible, grâce à la liberté asymptotique de la QCD. Bien que la factorisation n'ait pas été prouvée spécifiquement pour les processus que nous étudions, rien n'indique qu'elle n'est pas valide. Par conséquent, nous supposons que les processus peuvent être factorisés.

Par construction, le calcul en théorie des perturbations indique que l'interaction la plus simple entre les particules est dominante. Par conséquent, dans les réactions étudiées, seuls un quark et un antiquark du même type sont produits ; les autres particules créées par la rupture du proton ne sont pas mesurées et ne sont donc pas incluses dans le calcul théorique. Ensuite, les deux quarks sortants doivent se lier en un J/ψ, ce qui nécessite une autre contribution non perturbative. Pour ce faire, nous utilisons ce que l'on appelle les éléments de matrice à longue portée non perturbatifs

(LDMEs), qui proviennent de la théorie de la QCD non relativiste.

En étudiant la production de J/ψ dans les collisions électron-proton, l'on remarque que l'état lié du couple de quarks n'est initialement pas neutre en couleur à cause de la combinaison des couleurs portées par le gluon. Pour atteindre la neutralité de couleur, des gluons de basse énergie doivent être émis. Cette émission peut dépendre de l'impulsion transverse, ce qui nécessite l'introduction d'une nouvelle fonction, la fonction de forme, dans le calcul de la section efficace active. Nous avons déterminé la fonction de forme d'ordre principal pour ce processus à grand moment transverse par un calcul d'appariement. Pour la description TMD, l'impulsion transverse du quarkonium doit être petite par rapport à l'échelle des hautes énergies, alors que pour la description en termes de PDF, il doit être grand par rapport à l'échelle QCD non perturbative. Dans ce dernier cas, un parton supplémentaire doit être émis pour donner au J/ψ une grande impulsion transverse. Dans la région intermédiaire, les descriptions TMD et PDF doivent être égales, la fonction de forme dans la description en termes de PDF étant simplement la LDME. La fonction de forme doit ainsi correspondre exactement aux descriptions dans la région intermédiaire. Cette méthode est applicable à la production de J/ψ et à d'autres processus similaires, à condition, comme nous l'avons montré, que les singularités dans la description en termes de PDF initiée par le gluon soient traitées correctement. Nous avons également conclu que la fonction de forme est universelle mais associée à un facteur dépendant du processus. On s'attend à ce que la fonction de forme joue également un rôle dans les quarkonia directement neutres en couleur lorsque des calculs d'ordre supérieur seront effectués. Nos résultats concernant la fonction de forme sont étayés par un calcul alternatif dans l'approche dite eikonale.

Pour faire des prédictions numériques théoriques pour les processus, nous pouvons utiliser des paramétrisations pour les TMDs ou appliquer l'évolution des TMD, où les TMDs sont liés aux PDFs connus, comme dans le calcul d'appariement ci-dessus. En utilisant cette méthode, nous avons réalisé une étude qui prédit l'asymétrie azimutale, c'est-à-dire l'angle entre le plan de l'électron et le plan J/ψ du proton, lorsque le proton n'est pas polarisé. L'asymétrie qui se produit dans ce processus est proportionnelle au rapport de deux gluon-TMDs : le gluon-TMD polarisé linéairement divisé par le gluon-TMD non polarisé. Selon nos calculs, cette asymétrie, qui augmente avec l'impulsion transverse, est mesurable dans la future expérience EIC, ce qui permettra de mieux comprendre à la fois les gluon-TMDs et la fonction de forme.

En outre, nous avons mené une étude axée sur la partie de l'évolution des TMD qui doit être paramétrée, à savoir le facteur de Sudakov non perturbatif. Pour ce faire, une fonction gaussienne est souvent utilisée, mais elle présente certaines limites. Nous résolvons ce problème en extrapolant les fonctions (perturbatives) connues à la région non perturbative et en établissant une séparation claire entre ces régions. Bien que notre facteur de Sudakov non perturbatif constitue une approche innovante pour explorer l'évolution des TMD, il ne s'agit pas nécessairement de la solution finale. En effet, nous trouvons des obstacles dans certaines situations ; il reste un facteur dépendant du processus qui doit être validé par des données expérimentales.

Nous avons ensuite utilisé notre nouveau facteur de Sudakov non perturbatif pour prédire la production de quarkonia dans les collisions proton-proton non polarisées, ainsi que la production de paires J/ψ récemment mesurée au LHC. Nous observons un bon accord avec la section efficace normalisée de ce processus. La plus grande incertitude dans nos prédictions provient de la variation d'échelle ; cela signifie que des corrections d'ordre supérieur doivent être incluses pour améliorer les prédictions théoriques. Nous notons que les meilleures prédictions cohérentes avec les données sont obtenues à partir d'une variation d'échelle qui n'est généralement pas prise en compte dans les études conventionnelles. Malheureusement, les données expérimentales ne permettent pas de comparer l'asymétrie azimutale que nous avons calculée. En outre, nous avons également fait d'autres prédictions pour le LHC, à la fois pour la production de paires Υ (la contrepartie bottomonium du J/ψ) dans les collisions proton-proton à haute énergie et pour la production de paires J/ψ en mode cible fixe au LHC. Ces processus, respectivement, peuvent fournir des informations importantes sur les TMDs de gluons à des échelles d'énergie plus élevées et à des valeurs plus grandes de la fraction d'impulsion longitudinale.

Enfin, nous avons fait le premier pas vers une description complète du spectre en impulsion transverse pour la production de J/ψ auprès de l'EIC. Ici, nous appliquons à nouveau notre nouveau facteur de Sudakov non perturbatif, mais nous nous concentrons exclusivement sur les contributions indépendantes de l'angle. Pour obtenir ce spectre, nous devons faire correspondre numériquement la description TMD et la description PDF. Pour ce faire, nous utilisons la méthode de pondération par l'inverse de l'erreur, qui fonctionne bien après avoir ajusté le poids de la description en termes de PDF pour la fonction de forme. Pour l'incertitude globale des courbes, nous avons combiné les incertitudes perturbatives de la variation d'échelle avec les incertitudes des LDMEs et du calcul de correspondance. En outre, nous avons examiné la dépendance à l'échelle de haute énergie de nos calculs, en constatant que la description TMD et la description PDF présentent des différences significatives. Néanmoins, nous concluons qu'il est possible de les faire correspondre, car les prédictions TMD sont supérieures aux prédictions en termes de PDF dans la région de chevauchement.

Acknowledgements

First of all, I would like to thank my supervisors Daniël Boer and Jean-Philippe Lansberg. Daniël, since I truly think that it is due to you that I arrived at this point in my life, I want to start by expressing my gratitude to you. As my second supervisor of my master thesis, you generously wrote recommendation letters for me when I was looking for a PhD opportunity. After months of applications, I had nearly decided that a PhD was not the right path for me, but then something remarkable happened: you recommended me for the international project with the both of you, giving me the chance to pursue my dream. Over the years I have had the privilege of getting to know you much more, including discovering our shared interest in wildlife observation. Despite your busy schedule, you always found time for our discussions. Your trust, help, kindness, precision, and directness have been invaluable, also over long-distance, and it has been an absolute pleasure working under your supervision. Jean-Philippe, after two years in Groningen, it was time to step out of my comfort zone and fully work under your supervision; the aftermath of the COVID-19 pandemic played a significant role in keeping us quite apart for the first year and a half. Although I was aware that your working ethos differs significantly, it still took me some time to adjust to it, while also adapting to my life in Paris. You are a man of action, driven to accomplish tasks with great passion, a quality that truly resonates with me. I fondly remember the insightful and creative discussions we had, particularly those during the summer of 2023. Although our interactions diminished thereafter as I dedicated myself to writing this thesis, your humour often brought a smile to my face during this challenging task. Reflecting on our collaboration, I have gained valuable insights from you that will greatly benefit my future career for which I am truly grateful.

Secondly, I would like to express my gratitude to several colleagues with whom I frequently interacted. Luca Maxia, I value our collaboration on various projects, which has been enhanced by our shared research interests and your valuable assistance. Besides, I am grateful for your companionship in navigating the challenges of the PhD journey. Carlo Flore, you played a crucial role in helping me settle in France and your support meant a lot to me. Additionally, I would like to express my appreciation to other colleagues I met in Orsay: Benjamin Audurier, Alice Colpani Serri, Dimitrios Daskalas, Christopher Flett, Michael Fucilla, Kate Lynch, Dukhishyam Mallick, Laboni Manna, Saad Nabeebaccus, Maxim Nefedov, Melih Ozcelik, Allencris Rajan, Anton Safronov, Yelyzaveta Yedelkina, Vsevolod Yeroshenko and Valeriia Zhovkovska; thank you for all the enjoyable conversations we had over the years.

Furthermore, I would like to acknowledge several other colleagues, Liupan An, Alessandro Bacchetta, Valerio Bertone, Emilien Chapon, Miguel Echevarria, Charlotte Van Hulse, Daniel Kikola, Aleksander Kusina, Piet Mulders, Cristian Pisano, Marc Schlegel, Ignazio Scimemi, Lech Szymanowski, Pieter Taels, Li Xu, Nodoka Yamanaka and Feng Yuan, for the insightful discussions we have had, whether brief or long-lasting, which have enriched my work. I am also very grateful to Umberto D'Alesio for inviting me to the Sardinian workshop on spin in Cagliari; it was a pleasure to connect with the large Italian high-energy physics community. Besides, I would like to thank Asmita Mukherjee for hosting me in Mumbai, where I enjoyed meeting your students and gaining insight into the academic environment there. Moreover, I would like to thank Raju Venugopalan for making my visit to BNL in New York possible.

Also, I would like to thank Florent Scarpa for all the work he accomplished prior to my studies, some of which I have built upon; your codes helped me significantly in the early stages of my research.

Additionally, I would like to give a special thanks to Tom Beumer for assisting in rewriting my article for the NTvN [182]. Communicating my research to a broader audience in Dutch was no easy task, and your help was very valuable. Moreover, I want to express my gratitude to Marieke de Boer for her efforts in preparing this article for publication. Besides, I am grateful to Sophie Jacobs for her valuable assistance in preparing my thesis for printing.

Finally, I would like to express my gratitude to my family and friends for their emotional support over the years in various ways - this thesis is made possible by you. Rosa, your love and encouragement throughout this journey have been invaluable to me. Joost, 'Ouwe', thank you for all the unforgettable trips we have taken together around the world. Those were the moments that allowed me to fully disconnect from everyday life and truly unwind. Besides, I am also thankful for your help with my relocations to Groningen and Paris, which would have been a lot more difficult without you. Janny, 'Moeders', you called me every week to catch up on daily life to help me clear my head for a while, thank you. 'Opa 10', Martin, thank you for always being there for me, even from afar. To my friends from Groningen, especially Pieter Wolff (paranimf primus), Anton and Bradley, thank you for all the unforgettable nights out in the most beautiful student city in the Netherlands - het was gezellig! To my friends from Den Bosch, especially Jasper Quint (paranimf secundus), Dorus B., Dorus W., Karl, Niels and Thanos, thank you for all the 'Brabantse nachten' when I was back home - wat hebben we gelachen! To my friends in Paris, especially Émile and Yannick, thank you for the wine - santé!

This project has received funding from the European Union's Horizon 2020 research and innovation programme under grant agreement No. 824093 (STRONG 2020) and is part of its JRA4-TMD-neXt Work Package. Additionally, it has received funding from the French Agence Nationale de la Recherche through the grant ANR-20-CE31-0015 ("PrecisOnium"). Partial support for this work was also provided by the French CNRS through the IN2P3 project GLUE@NLO.

Bibliography

[1] S. Bailey, T. Cridge, L. A. Harland-Lang, A. D. Martin and R. S. Thorne, "Parton distributions from LHC, HERA, Tevatron and fixed target data: MSHT20 PDFs," *Eur. Phys. J. C* **81** (2021) 341.

[2] D. Boer, [..], J. Bor *et al.*, "Physics case for quarkonium studies at the Electron Ion Collider," `arXiv:2409.03691`.

[3] J. Collins, *Foundations of Perturbative QCD*. Cambridge University Press, 2011.

[4] M. G. Echevarria, A. Idilbi and I. Scimemi, "Factorization Theorem For Drell-Yan At Low q_T And Transverse Momentum Distributions On-The-Light-Cone," *JHEP* **07** (2012) 002.

[5] M. G. Echevarria, A. Idilbi and I. Scimemi, "Soft and Collinear Factorization and Transverse Momentum Dependent Parton Distribution Functions," *Phys. Lett. B* **726** (2013) 795–801.

[6] J. C. Collins, "Light-cone Variables, Rapidity and All That," `arXiv:hep-ph/9705393`.

[7] P. J. Mulders and J. Rodrigues, "Transverse momentum dependence in gluon distribution and fragmentation functions," *Phys. Rev. D* **63** (2001) 094021.

[8] D. Boer, S. Cotogno, T. van Daal, P. J. Mulders, A. Signori and Y.-J. Zhou, "Gluon and Wilson loop TMDs for hadrons of spin ≤ 1," *JHEP* **10** (2016) 013.

[9] D. J. Gross and S. B. Treiman, "Light-Cone Structure of Current Commutators in the Gluon-Quark Model," *Phys. Rev. D* **4** (1971) 1059–1072.

[10] S. Meissner, A. Metz and K. Goeke, "Relations between generalized and transverse momentum dependent parton distributions," *Phys. Rev. D* **76** (2007) 034002.

[11] A. Bacchetta and P. J. Mulders, "Deep inelastic leptoproduction of spin-one hadrons," *Phys. Rev. D* **62** (2000) 114004.

[12] D. Boer, P. J. Mulders, C. Pisano and J. Zhou, "Asymmetries in heavy quark pair and dijet production at an EIC," *JHEP* **08** (2016) 001.

[13] R. Angeles-Martinez *et al.*, "Transverse Momentum Dependent (TMD) Parton Distribution Functions: Status and Prospects," *Acta Phys. Polon. B* **46** (2015) 2501–2534.

[14] J. C. Collins, “What exactly is a parton density?,” `arXiv:hep-ph/0304122`.

[15] J. C. Collins, L. Gamberg, A. Prokudin, T. C. Rogers, N. Sato and B. Wang, “Relating transverse tomentum dependent and collinear factorization theorems in a generalized formalism,” *Phys. Rev. D* **94** (2016) 034014.

[16] M. Diehl, “Introduction to GPDs and TMDs,” *Eur. Phys. J. A* **52** (2016) 149.

[17] M. G. A. Buffing, M. Diehl and T. Kasemets, “Transverse momentum in double parton scattering: factorisation, evolution and matching,” *JHEP* **01** (2018) 044.

[18] M. Diehl and J. R. Gaunt, “Double Parton Scattering Theory Overview,” *Adv. Ser. Direct. High Energy Phys.* **29** (2018) 7–28.

[19] S. Cotogno, T. van Daal and P. J. Mulders, “Positivity bounds on gluon TMDs for hadrons of spin ≤ 1,” *JHEP* **11** (2017) 185.

[20] A. Bacchetta, M. Boglione, A. Henneman and P. J. Mulders, “Bounds on Transverse Momentum Dependent Distribution and Fragmentation Functions,” *Phys. Rev. Lett.* **85** (2000) 712–715.

[21] A. Bacchetta and P. J. Mulders, “Positivity bounds on spin-one distribution and fragmentation functions,” *Phys. Lett. B* **518** (2001) 85–93.

[22] A. V. Belitsky, X. Ji and F. Yuan, “Final state interactions and gauge invariant parton distributions,” *Nucl. Phys. B* **656** (2003) 165–198.

[23] D. Boer, P. J. Mulders and F. Pijlman, “Universality of T-odd effects in single spin and azimuthal asymmetries,” *Nucl. Phys. B* **667** (2003) 201–241.

[24] D. Boer and C. Pisano, “Polarized gluon studies with charmonium and bottomonium at LHCb and AFTER,” *Phys. Rev. D* **86** (2012) 094007.

[25] J.-P. Lansberg, C. Pisano, F. Scarpa and M. Schlegel, “Pinning down the linearly-polarised gluons inside unpolarised protons using quarkonium-pair production at the LHC,” *Phys. Lett. B* **784** (2018) 217–222. [Erratum: Phys. Lett. B 791, 420–421 (2019)].

[26] A. Bacchetta, D. Boer, C. Pisano and P. Taels, “Gluon TMDs and NRQCD matrix elements in J/ψ production at an EIC,” *Eur. Phys. J. C* **80** (2020) 72.

[27] C. J. Bomhof, P. J. Mulders and F. Pijlman, “The construction of gauge-links in arbitrary hard processes,” *Eur. Phys. J. C* **47** (2006) 147–162.

[28] D. Boer, “Gluon TMDs in Quarkonium Production,” *Few Body Syst.* **58** (2017) 32.

[29] T. C. Rogers and P. J. Mulders, “No generalized transverse momentum dependent factorization in hadroproduction of high transverse momentum hadrons,” *Phys. Rev. D* **81** (2010) 094006.

[30] S. Catani, M. Grazzini and A. Torre, “Transverse-momentum resummation for heavy-quark hadroproduction,” *Nucl. Phys. B* **890** (2014) 518–538.

[31] G. A. Chirilli, B.-W. Xiao and F. Yuan, “One-Loop Factorization for Inclusive Hadron Production in p–A Collisions in the Saturation Formalism,” *Phys. Rev. Lett.* **108** (2012) 122301.

[32] P. Kotko, K. Kutak, C. Marquet, E. Petreska, S. Sapeta and A. van Hameren, “Improved TMD factorization for forward dijet production in dilute-dense hadronic collisions,” *JHEP* **09** (2015) 106.

[33] J. C. Collins, D. E. Soper and G. F. Sterman, “Relation of parton distribution functions in Drell-Yan process to deeply inelastic scattering,” *Phys. Lett. B* **126** (1983) 275–278.

[34] C. Lorce, “Wilson lines and orbital angular momentum,” *Phys. Lett. B* **719** (2013) 185–190.

[35] M. Burkardt, “Parton orbital angular momentum and final state interactions,” *Phys. Rev. D* **88** (2013) 014014.

[36] T. Appelquist, A. De Rujula, H. D. Politzer and S. L. Glashow, “Spectroscopy of the New Mesons,” *Phys. Rev. Lett.* **34** (1975) 365.

[37] Particle Data Group Collaboration, S. Navas *et al.*, “Review of Particle Physics,” *Phys. Rev. D* **110** (2024) 030001.

[38] E. Eichten, K. Gottfried, T. Kinoshita, J. B. Kogut, K. D. Lane and T.-M. Yan, “Spectrum of Charmed Quark-Antiquark Bound States,” *Phys. Rev. Lett.* **34** (1975) 369–372. [Erratum: Phys.Rev.Lett. 36, 1276 (1976)].

[39] E. Eichten, K. Gottfried, T. Kinoshita, K. D. Lane and T.-M. Yan, “Charmonium: The Model,” *Phys. Rev. D* **17** (1978) 3090. [Erratum: Phys.Rev.D 21, 313 (1980)].

[40] J.-P. Lansberg, “New observables in inclusive production of quarkonia,” *Phys. Rept.* **889** (2020) 1–106.

[41] F. Halzen, “CVC for gluons and hadroproduction of quark flavors,” *Phys. Lett. B* **69** (1977) 105–108.

[42] H. Fritzsch, “Producing heavy quark flavors in hadronic collisions– A test of quantum chromodynamics,” *Phys. Lett. B* **67** (1977) 217–221.

[43] Y.-Q. Ma and R. Vogt, “Quarkonium production in an improved color evaporation model,” *Phys. Rev. D* **94** (2016) 114029.

[44] J. F. Amundson, O. J. P. Eboli, E. M. Gregores and F. Halzen, “Quantitative tests of color evaporation: charmonium production,” *Phys. Lett. B* **390** (1997) 323–328.

[45] C.-H. Chang, "Hadronic production of J/ψ associated with a gluon," *Nucl. Phys. B* **172** (1980) 425–434.

[46] E. L. Berger and D. L. Jones, "Inelastic photoproduction of J/ψ and Υ by gluons," *Phys. Rev. D* **23** (1981) 1521–1530.

[47] R. Baier and R. Ruckl, "Hadronic production of J/ψ and Υ: Transverse momentum distributions," *Phys. Lett. B* **102** (1981) 364–370.

[48] G. T. Bodwin, E. Braaten and J. Lee, "Comparison of the color-evaporation model and the nonrelativistic QCD factorization approach in charmonium production," *Phys. Rev. D* **72** (2005) 014004.

[49] G. T. Bodwin, E. Braaten and G. P. Lepage, "Rigorous QCD analysis of inclusive annihilation and production of heavy quarkonium," *Phys. Rev. D* **51** (1995) 1125–1171. [Erratum: Phys. Rev. D 55, 5853 (1997)].

[50] A. Petrelli, M. Cacciari, M. Greco, F. Maltoni and M. L. Mangano, "NLO production and decay of quarkonium," *Nucl. Phys. B* **514** (1998) 245–309.

[51] A. Pineda and J. Soto, "Effective field theory for ultrasoft momenta in NRQCD and NRQED," *Nucl. Phys. B Proc. Suppl.* **64** (1998) 428–432.

[52] N. Brambilla, A. Pineda, J. Soto and A. Vairo, "Potential NRQCD: an effective theory for heavy quarkonium," *Nucl. Phys. B* **566** (2000) 275.

[53] Z.-B. Kang, Y.-Q. Ma, J.-W. Qiu and G. Sterman, "Heavy quarkonium production at collider energies: Factorization and evolution," *Phys. Rev. D* **90** (2014) 034006.

[54] Z.-B. Kang, Y.-Q. Ma, J.-W. Qiu and G. Sterman, "Heavy quarkonium production at collider energies: Partonic cross section and polarization," *Phys. Rev. D* **91** (2015) 014030.

[55] Y.-Q. Ma, J.-W. Qiu, G. Sterman and H. Zhang, "Factorized Power Expansion for High-p_T Heavy Quarkonium Production," *Phys. Rev. Lett.* **113** (2014) 142002.

[56] J. H. Kühn, J. Kaplan and E. G. O. Safiani, "Electromagnetic annihilation of e^+e^- into quarkonium states with even charge conjugation," *Nucl. Phys. B* **157** (1979) 125–144.

[57] B. Guberina, J. H. Kühn, R. D. Peccei and R. Rückl, "Rare decays of the Z^0," *Nucl. Phys. B* **174** (1980) 317–334.

[58] R. Baier and R. Rückl, "Hadronic collisions: A quarkonium factory," *Z. Phys. C* **19** (1983) 251.

[59] P. Ko, J. Lee and H. S. Song, "Color-octet mechanism in $\gamma + p \to J/\psi + X$," *Phys. Rev. D* **54** (1996) 4312–4325. [Erratum: Phys. Rev. D 60, 119902 (1999)].

[60] L. D. Landau, "On the angular momentum of a system of two photons," *Dokl. Akad. Nauk SSSR* **60** (1948) 207–209.

[61] C.-N. Yang, "Selection Rules for the Dematerialization of a Particle Into Two Photons," *Phys. Rev.* **77** (1950) 242–245.

[62] P. L. Cho and A. K. Leibovich, "Color-octet quarkonia production," *Phys. Rev. D* **53** (1996) 150–162.

[63] P. L. Cho and A. K. Leibovich, "Color-octet quarkonia production II," *Phys. Rev. D* **53** (1996) 6203–6217.

[64] N. Kato, L. Maxia and C. Pisano, "Spin asymmetries for C-even quarkonium production as a probe of gluon distributions," *Phys. Rev. D* **110** (2024) 034038.

[65] D. Boer and W. J. den Dunnen, "TMD evolution and the Higgs transverse momentum distribution," *Nucl. Phys. B* **886** (2014) 421–435.

[66] M. G. Echevarria, T. Kasemets, P. J. Mulders and C. Pisano, "QCD evolution of (un)polarized gluon TMDPDFs and the Higgs q_T-distribution," *JHEP* **07** (2015) 158. [Erratum: JHEP 05, 073 (2017)].

[67] D. Gutierrez-Reyes, S. Leal-Gomez, I. Scimemi and A. Vladimirov, "Linearly polarized gluons at next-to-next-to leading order and the Higgs transverse momentum distribution," *JHEP* **11** (2019) 121.

[68] S. Fleming and T. Mehen, "Leptoproduction of J/ψ," *Phys. Rev. D* **57** (1998) 1846–1857.

[69] M. Cacciari and M. Krämer, "Color-Octet Contributions to J/ψ Photoproduction," *Phys. Rev. Lett.* **76** (1996) 4128–4131.

[70] M. G. Echevarria, "Proper TMD factorization for quarkonia production: $pp \to \eta_{c,b}$ as a study case," *JHEP* **10** (2019) 144.

[71] S. Fleming, Y. Makris and T. Mehen, "An effective field theory approach to quarkonium at small transverse momentum," *JHEP* **04** (2020) 122.

[72] D. Boer, C. Pisano and P. Taels, "Extracting color octet NRQCD matrix elements from J/ψ production at the EIC," *Phys. Rev. D* **103** (2021) 074012.

[73] A. V. Manohar, "An Introduction to Spin Dependent Deep Inelastic Scattering," in *Lake Louise Winter Institute: Symmetry and Spin in the Standard Model*. 1992. `arXiv:hep-ph/9204208`.

[74] M. Butenschoen and B. A. Kniehl, "Reconciling J/ψ Production at HERA, RHIC, Tevatron, and LHC with Nonrelativistic QCD Factorization at Next-to-Leading Order," *Phys. Rev. Lett.* **106** (2011) 022003.

[75] K.-T. Chao, Y.-Q. Ma, H.-S. Shao, K. Wang and Y.-J. Zhang, "J/ψ Polarization at Hadron Colliders in Nonrelativistic QCD," *Phys. Rev. Lett.* **108** (2012) 242004.

[76] R. Sharma and I. Vitev, "High transverse momentum quarkonium production and dissociation in heavy ion collisions," *Phys. Rev. C* **87** (2013) 044905.

[77] G. T. Bodwin, H. S. Chung, U.-R. Kim and J. Lee, "Fragmentation Contributions to J/ψ Production at the Tevatron and the LHC," *Phys. Rev. Lett.* **113** (2014) 022001.

[78] LHCb Collaboration, R. Aaij *et al.*, "Measurement of J/ψ-pair production in pp collisions at $\sqrt{s} = 13$ TeV and study of gluon transverse-momentum dependent PDFs," *JHEP* **03** (2024) 088.

[79] C.-F. Qiao, L.-P. Sun and P. Sun, "Testing charmonium production mechanism via polarized J/ψ pair production at the LHC," *J. Phys. G* **37** (2010) 075019.

[80] D. Boer, S. J. Brodsky, P. J. Mulders and C. Pisano, "Direct Probes of Linearly Polarized Gluons inside Unpolarized Hadrons," *Phys. Rev. Lett.* **106** (2011) 132001.

[81] A. Bacchetta, F. Delcarro, C. Pisano, M. Radici and A. Signori, "Extraction of partonic transverse momentum distributions from semi-inclusive deep-inelastic scattering, Drell-Yan and Z-boson production," *JHEP* **06** (2017) 081. [Erratum: JHEP 06, 051 (2019)].

[82] A. Bacchetta *et al.*, "Transverse-momentum-dependent parton distributions up to N^{3}LL from Drell-Yan data," *JHEP* **07** (2020) 117.

[83] I. Scimemi and A. Vladimirov, "Non-perturbative structure of semi-inclusive deep-inelastic and Drell-Yan scattering at small transverse momentum," *JHEP* **06** (2020) 137.

[84] MAP Collaboration, A. Bacchetta *et al.*, "Unpolarized transverse momentum distributions from a global fit of Drell-Yan and semi-inclusive deep-inelastic scattering data," *JHEP* **10** (2022) 127.

[85] R. M. Godbole, A. Misra, A. Mukherjee and V. S. Rawoot, "Sivers effect and transverse single spin asymmetry in $e + p^{\uparrow} \to e + J/\psi + X$," *Phys. Rev. D* **85** (2012) 094013.

[86] R. M. Godbole, A. Misra, A. Mukherjee and V. S. Rawoot, "Transverse single spin asymmetry in $e + p^{\uparrow} \to e + J/\psi + X$ and transverse momentum dependent evolution of the Sivers function," *Phys. Rev. D* **88** (2013) 014029.

[87] R. M. Godbole, A. Kaushik, A. Misra and V. S. Rawoot, "Transverse single spin asymmetry in $e + p^{\uparrow} \to e + J/\psi + X$ and Q^2 evolution of Sivers function-II," *Phys. Rev. D* **91** (2015) 014005.

[88] A. Mukherjee and S. Rajesh, "Probing transverse momentum dependent parton distributions in charmonium and bottomonium production," *Phys. Rev. D* **93** (2016) 054018.

[89] A. Mukherjee and S. Rajesh, "J/ψ production in polarized and unpolarized ep collision and Sivers and $\cos 2\phi$ asymmetries," *Eur. Phys. J. C* **77** (2017) 854.

[90] U. D'Alesio, F. Murgia, C. Pisano and P. Taels, "Probing the gluon Sivers function in $p^{\uparrow}p \to J/\psi\, X$ and $p^{\uparrow}p \to D\, X$," *Phys. Rev. D* **96** (2017) 036011.

[91] R. Kishore and A. Mukherjee, "Accessing linearly polarized gluon distribution in J/ψ production at the electron-ion collider," *Phys. Rev. D* **99** (2019) 054012.

[92] F. Scarpa, D. Boer, M. G. Echevarria, J.-P. Lansberg, C. Pisano and M. Schlegel, "Studies of gluon TMDs and their evolution using quarkonium-pair production at the LHC," *Eur. Phys. J. C* **80** (2020) 87.

[93] R. Kishore, A. Mukherjee and M. Siddiqah, "Cos($2\phi_h$) asymmetry in J/ψ production in unpolarized ep collision," *Phys. Rev. D* **104** (2021) 094015.

[94] C. Pisano, D. Boer, S. J. Brodsky, M. G. A. Buffing and P. J. Mulders, "Linear polarization of gluons and photons in unpolarized collider experiments," *JHEP* **10** (2013) 024.

[95] G.-P. Zhang, "Probing transverse momentum dependent gluon distribution functions from hadronic quarkonium pair production," *Phys. Rev. D* **90** (2014) 094011.

[96] W. J. den Dunnen, J. P. Lansberg, C. Pisano and M. Schlegel, "Accessing the Transverse Dynamics and Polarization of Gluons inside the Proton at the LHC," *Phys. Rev. Lett.* **112** (2014) 212001.

[97] J.-P. Lansberg, C. Pisano and M. Schlegel, "Associated production of a dilepton and a $\Upsilon(J/\psi)$ at the LHC as a probe of gluon transverse momentum dependent distributions," *Nucl. Phys. B* **920** (2017) 192–210.

[98] R. Kishore, A. Mukherjee, A. Pawar and M. Siddiqah, "$\cos 2\phi_t$ azimuthal asymmetry in back-to-back J/ψ-jet production in $ep \to e\ J/\psi$ jet X at the EIC," *Phys. Rev. D* **106** (2022) 034009.

[99] R. Kishore, A. Mukherjee, A. Pawar, S. Rajesh and M. Siddiqah, "TMD evolution effect on $\cos 2\phi$ azimuthal asymmetry in a back-to-back production of J/ψ and jet at the EIC," *Phys. Rev. D* **111** (2025) 014003.

[100] D. Chakrabarti, R. Kishore, A. Mukherjee and S. Rajesh, "Azimuthal asymmetries in J/ψ-photon production at the EIC," *Phys. Rev. D* **107** (2023) 014008.

[101] K. Banu, A. Mukherjee, A. Pawar and S. Rajesh, "Azimuthal asymmetries in D-meson and jet production at the EIC," *Phys. Rev. D* **108** (2023) 034005.

[102] K. Banu, A. Mukherjee, A. Pawar and S. Rajesh, "Unraveling gluon TMDs in J/ψ and pion production at the EIC," *Phys. Rev. D* **110** (2024) 054009.

[103] P. Schweitzer, T. Teckentrup and A. Metz, "Intrinsic transverse parton momenta in deeply inelastic reactions," *Phys. Rev. D* **81** (2010) 094019.

[104] D. Boer, W. J. den Dunnen, C. Pisano, M. Schlegel and W. Vogelsang, "Linearly Polarized Gluons and the Higgs Transverse Momentum Distribution," *Phys. Rev. Lett.* **108** (2012) 032002.

[105] M. Anselmino, D. Boer, U. D'Alesio and F. Murgia, "Transverse Λ polarization in semi-inclusive deep inelastic scattering," *Phys. Rev. D* **65** (2002) 114014.

[106] P. Sun, B.-W. Xiao and F. Yuan, "Gluon distribution functions and Higgs boson production at moderate transverse momentum," *Phys. Rev. D* **84** (2011) 094005.

[107] U. D'Alesio, F. Murgia, C. Pisano and S. Rajesh, "Single-spin asymmetries in $p^{\uparrow}p \to J/\psi + X$ within a TMD approach: role of the color octet mechanism," *Eur. Phys. J. C* **79** (2019) 1029.

[108] M. Anselmino, M. Boglione, U. D'Alesio, A. Kotzinian, F. Murgia and A. Prokudin, "Role of Cahn and sivers effects in deep inelastic scattering," *Phys. Rev. D* **71** (2005) 074006.

[109] LHCb Collaboration, R. Aaij *et al.*, "Measurement of the J/ψ pair production cross-section in pp collisions at $\sqrt{s} = 13$ TeV," *JHEP* **06** (2017) 047. [Erratum: JHEP 10, 068 (2017)].

[110] E. R. Nocera, "Collinear Parton Distribution Functions: Precision, Accuracy, and Quarkonia," *Talk presented at Synergies between LHC and EIC for quarkonium physics, Trento, July 8-12* (2024) . `https://indico.ectstar.eu/event/219/contributions/4821/`.

[111] U. D'Alesio, C. Flore, F. Murgia, C. Pisano and P. Taels, "Unraveling the gluon Sivers function in hadronic collisions at RHIC," *Phys. Rev. D* **99** (2019) 036013.

[112] A. Bacchetta, F. Conti and M. Radici, "Transverse-momentum distributions in a diquark spectator model," *Phys. Rev. D* **78** (2008) 074010.

[113] A. Bacchetta, F. G. Celiberto, M. Radici and P. Taels, "Transverse-momentum-dependent gluon distribution functions in a spectator model," *Eur. Phys. J. C* **80** (2020) 733.

[114] A. Bacchetta, F. G. Celiberto and M. Radici, "T-odd gluon distribution functions in a spectator model," *Eur. Phys. J. C* **84** (2024) 576.

[115] J. C. Collins and D. E. Soper, "Back-to-back jets in QCD," *Nucl. Phys. B* **193** (1981) 381. [Erratum: Nucl. Phys. B 213, 545 (1983)].

[116] J. C. Collins and D. E. Soper, "Parton distribution and decay functions," *Nucl. Phys. B* **194** (1982) 445–492.

[117] J. C. Collins, D. E. Soper and G. F. Sterman, "Does the Drell-Yan cross section factorize?," *Phys. Lett. B* **109** (1982) 388–392.

[118] J. C. Collins and D. E. Soper, "Back-to-back jets: Fourier transform from b to k_T," *Nucl. Phys. B* **197** (1982) 446–476.

[119] J. C. Collins, D. E. Soper and G. F. Sterman, "Factorization for one-loop corrections in the Drell-Yan process," *Nucl. Phys. B* **223** (1983) 381–421.

[120] J. C. Collins, D. E. Soper and G. F. Sterman, "Transverse momentum distribution in Drell-Yan pair and W and Z boson production," *Nucl. Phys. B* **250** (1985) 199–224.

[121] F. Scarpa, *Probing the gluon Transverse Momentum-Dependent distributions inside the proton through quarkonium-pair production at the LHC*. PhD thesis, U. of Groningen, U. Paris-Saclay, 2020.

[122] S. M. Aybat and T. C. Rogers, "Transverse momentum dependent parton distribution and fragmentation functions with QCD evolution," *Phys. Rev. D* **83** (2011) 114042.

[123] J. Bor and D. Boer, "TMD evolution study of the $\cos 2\phi$ azimuthal asymmetry in unpolarized J/ψ production at EIC," *Phys. Rev. D* **106** (2022) 014030.

[124] S. Catani, E. D'Emilio and L. Trentadue, "The gluon form-factor to higher orders: Gluon-gluon annihilation at small Q_t," *Phys. Lett. B* **211** (1988) 335–342.

[125] C. P. Yuan, "Kinematics of the Higgs boson at hadron colliders. NLO QCD gluon resummation," *Phys. Lett. B* **283** (1992) 395–402.

[126] S. Melis, M. Boglione, J. O. Gonzalez-Hernandez and A. Prokudin, "Theoretical Uncertainties and Dependence on the C_1, C_2, C_3 Parameters in the CSS Formalism in Drell-Yan and SIDIS," *PoS* **QCDEV2015** 038.

[127] P. Sun, C. P. Yuan and F. Yuan, "Heavy quarkonium production at low $P_\perp$ in nonrelativistic QCD with soft gluon resummation," *Phys. Rev. D* **88** (2013) 054008.

[128] R. F. del Castillo, M. G. Echevarria, Y. Makris and I. Scimemi, "Transverse momentum dependent distributions in dijet and heavy hadron pair production at EIC," *JHEP* **03** (2022) 047.

[129] D. Boer, U. D'Alesio, F. Murgia, C. Pisano and P. Taels, "J/ψ meson production in SIDIS: matching high and low transverse momentum," *JHEP* **09** (2020) 040.

[130] U. D'Alesio, L. Maxia, F. Murgia, C. Pisano and S. Rajesh, "J/ψ polarization in semi-inclusive DIS at low and high transverse momentum," *JHEP* **03** (2022) 037.

[131] R. Zhu, P. Sun and F. Yuan, "Low transverse momentum heavy quark pair production to probe gluon tomography," *Phys. Lett. B* **727** (2013) 474–479.

[132] D. Boer, J. Bor, L. Maxia, C. Pisano and F. Yuan, "Transverse momentum dependent shape function for J/ψ production in SIDIS," *JHEP* **08** (2023) 105.

[133] G. Parisi and R. Petronzio, "Small transverse momentum distributions in hard processes," *Nucl. Phys. B* **154** (1979) 427–440.

[134] D. Boer, "Sudakov suppression in azimuthal spin asymmetries," *Nucl. Phys. B* **603** (2001) 195–217.

[135] S. Rajesh, R. Kishore and A. Mukherjee, "Sivers effect in inelastic J/ψ photoproduction in $ep^{\uparrow}$ collision in color octet model," *Phys. Rev. D* **98** (2018) 014007.

[136] R. Kishore, A. Mukherjee and S. Rajesh, "Sivers asymmetry in the photoproduction of a J/ψ and a jet at the EIC," *Phys. Rev. D* **101** (2020) 054003.

[137] B. A. Kniehl and L. Zwirner, "J/ψ inclusive production in ep deep-inelastic scattering at DESY HERA," *Nucl. Phys. B* **621** (2002) 337–358.

[138] Z. Sun and H.-F. Zhang, "QCD leading order study of the J/ψ leptoproduction at HERA within the nonrelativistic QCD framework," *Eur. Phys. J. C* **77** (2017) 744.

[139] R. Meng, F. I. Olness and D. E. Soper, "Semi-inclusive deeply inelastic scattering at small q_T," *Phys. Rev. D* **54** (1996) 1919–1935.

[140] G. Altarelli and G. Parisi, "Asymptotic freedom in parton language," *Nucl. Phys. B* **126** (1977) 298–318.

[141] S. Catani and M. Grazzini, "QCD transverse-momentum resummation in gluon fusion processes," *Nucl. Phys. B* **845** (2011) 297–323.

[142] A. Bacchetta, D. Boer, M. Diehl and P. J. Mulders, "Matches and mismatches in the descriptions of semi-inclusive processes at low and high transverse momentum," *JHEP* **08** (2008) 023.

[143] A. Bacchetta, G. Bozzi, M. G. Echevarria, C. Pisano, A. Prokudin and M. Radici, "Azimuthal asymmetries in unpolarized SIDIS and Drell-Yan processes: A case study towards TMD factorization at subleading twist," *Phys. Lett. B* **797** (2019) 134850.

[144] H. X. Zhu, C. S. Li, H. T. Li, D. Y. Shao and L. L. Yang, "Transverse-Momentum Resummation for Top-Quark Pairs at Hadron Colliders," *Phys. Rev. Lett.* **110** (2013) 082001.

[145] M. G. Echevarria, S. F. Romera and P. Taels, "Factorization for J/ψ leptoproduction at small transverse momentum," *JHEP* **09** (2024) 188.

[146] G. A. Schuler, "Quarkonium Production: Velocity-Scaling Rules and Long-Distance Matrix Elements," *Int. J. Mod. Phys. A* **12** (1997) 3951–3964.

[147] K. Lee, J.-W. Qiu, G. Sterman and K. Watanabe, "QCD factorization for hadronic quarkonium production at high p_T," *SciPost Phys. Proc.* **8** (2022) 143.

[148] L. Maxia and F. Yuan, "Azimuthal angular correlation of J/ψ plus jet production at the electron-ion collider," *Phys. Rev. D* **110** (2024) 114042.

[149] S. Catani, I. Fabre, M. Grazzini and S. Kallweit, "$t\bar{t}H$ production at NNLO: the flavour off-diagonal channels," *Eur. Phys. J. C* **81** (2021) 491.

[150] W.-L. Ju and M. Schönherr, "Projected transverse momentum resummation in top-antitop pair production at LHC," *JHEP* **02** (2023) 075.

[151] J.-W. Qiu, M. Schlegel and W. Vogelsang, "Probing Gluonic Spin-Orbit Correlations in Photon Pair Production," *Phys. Rev. Lett.* **107** (2011) 062001.

[152] D. Boer and C. Pisano, "Impact of gluon polarization on Higgs boson plus jet production at the LHC," *Phys. Rev. D* **91** (2015) 074024.

[153] D. Boer, P. J. Mulders and C. Pisano, "Dijet imbalance in hadronic collisions," *Phys. Rev. D* **80** (2009) 094017.

[154] E. Laenen, G. F. Sterman and W. Vogelsang, "Higher-Order QCD Corrections in Prompt Photon Production," *Phys. Rev. Lett.* **84** (2000) 4296–4299.

[155] J.-W. Qiu and X.-F. Zhang, "QCD Prediction for Heavy Boson Transverse Momentum Distributions," *Phys. Rev. Lett.* **86** (2001) 2724–2727.

[156] J.-W. Qiu and X.-F. Zhang, "Role of the nonperturbative input in QCD resummed Drell-Yan Q_T distributions," *Phys. Rev. D* **63** (2001) 114011.

[157] A. Bacchetta, M. G. Echevarria, P. J. Mulders, M. Radici and A. Signori, "Effects of TMD evolution and partonic flavor on e^+e^- annihilation into hadrons," *JHEP* **11** (2015) 076.

[158] J. Collins, "Different approaches to TMD Evolution with scale," *EPJ Web Conf.* **85** (2015) 01002.

[159] J. Collins and T. Rogers, "Understanding the large-distance behavior of transverse-momentum-dependent parton densities and the Collins-Soper evolution kernel," *Phys. Rev. D* **91** (2015) 074020.

[160] A. C. Serri, J. Bor, D. Boer and J.-P. Lansberg, "$J/\psi-$pair production at NLL in TMD factorisation at the LHC," *PoS* **EPS-HEP2023** 272.

[161] S. P. Baranov, "Pair production of J/ψ mesons in the k_t-factorization approach," *Phys. Rev. D* **84** (2011) 054012.

[162] A. K. Likhoded, A. V. Luchinsky and S. V. Poslavsky, "Production of $J/\psi + \chi_c$ and $J/\psi + J/\psi$ with real gluon emission at the LHC," *Phys. Rev. D* **94** (2016) 054017.

[163] J.-P. Lansberg, H.-S. Shao, N. Yamanaka and Y.-J. Zhang, "Prompt J/ψ-pair production at the LHC: impact of loop-induced contributions and of the colour-octet mechanism," *Eur. Phys. J. C* **79** (2019) 1006.

[164] L.-P. Sun, H. Han and K.-T. Chao, "Impact of J/ψ pair production at the LHC and predictions in nonrelativistic QCD," *Phys. Rev. D* **94** (2016) 074033.

[165] S. P. Baranov, A. V. Lipatov, M. A. Malyshev, A. A. Prokhorov and P. M. Zhang, "Forward $J/\psi + J/\psi$ and $J/\psi + \psi'$ production with high-energy factorization," *Phys. Rev. D* **110** (2024) 054001.

[166] C. Hadjidakis *et al.*, "A fixed-target programme at the LHC: Physics case and projected performances for heavy-ion, hadron, spin and astroparticle studies," *Phys. Rept.* **911** (2021) 1–83.

[167] M. G. Echevarria, T. Kasemets, J.-P. Lansberg, C. Pisano and A. Signori, "Matching factorization theorems with an inverse-error weighting," *Phys. Lett. B* **781** (2018) 161–168.

[168] M. Boglione, J. O. Gonzalez-Hernandez, S. Melis and A. Prokudin, "A study on the interplay between perturbative QCD and CSS/TMD formalism in SIDIS processes," *JHEP* **02** (2015) 095.

[169] J. O. Gonzalez-Hernandez, T. Rainaldi and T. C. Rogers, "Resolution to the problem of consistent large transverse momentum in TMDs," *Phys. Rev. D* **107** (2023) 094029.

[170] M. Beneke, I. Z. Rothstein and M. B. Wise, "Kinematic enhancement of non-perturbative corrections to quarkonium production," *Phys. Lett. B* **408** (1997) 373–380.

[171] M. Beneke, G. A. Schuler and S. Wolf, "Quarkonium momentum distributions in photoproduction and B decay," *Phys. Rev. D* **62** (2000) 034004.

[172] H1 Collaboration, F. D. Aaron *et al.*, "Inelastic production of J/ψ mesons in photoproduction and deep inelastic scattering at HERA," *Eur. Phys. J. C* **68** (2010) 401–420.

[173] T. Liu, W. Melnitchouk, J.-W. Qiu and N. Sato, "Factorized approach to radiative corrections for inelastic lepton-hadron collisions," *Phys. Rev. D* **104** (2021) 094033.

[174] J.-P. Lansberg, K. Lynch, C. Van Hulse and R. McNulty, "Inclusive photoproduction of vector quarkonium in ultra-peripheral collisions at the LHC," `arXiv:2409.01756`.

[175] M. E. Peskin and D. V. Schroeder, *An Introduction To Quantum Field Theory*. CRC Press, 1995.

[176] M. D. Schwartz, *Quantum Field Theory and the Standard Model*. Cambridge University Press, 2013.

[177] F. Herzog, B. Ruijl, T. Ueda, J. A. M. Vermaseren and A. Vogt, "The five-loop beta function of Yang-Mills theory with fermions," *JHEP* **02** (2017) 090.

[178] H. liu, X. xie and Z. Lu, "Gluon TMDs from J/ψ production in longitudinally polarized deeply inelastic scattering," *Phys. Lett. B* **849** (2024) 138439.

[179] U. D'Alesio, F. Murgia, C. Pisano and P. Taels, "Azimuthal asymmetries in semi-inclusive $J/\psi + \text{jet}$ production at an EIC," *Phys. Rev. D* **100** (2019) 094016.

[180] A. Bacchetta, M. Diehl, K. Goeke, A. Metz, P. J. Mulders and M. Schlegel, "Semi-inclusive deep inelastic scattering at small transverse momentum," *JHEP* **02** (2007) 093.

[181] V. M. Budnev, I. F. Ginzburg, G. V. Meledin and V. G. Serbo, "The two-photon particle production mechanism. Physical problems. Applications. Equivalent photon approximation," *Phys. Rept.* **15** (1975) 181–281.

[182] J. Bor, "De onbekende structuur van het proton ontdekken met behulp van quarkoniumproductie," *Nederlands Tijdschrift voor Natuurkunde* (11, 2023) 26–30.